



HAL
open science

All-optical ultrafast switching of semiconductor micropillar cavities : basics and applications to quantum optics

Emanuel Thomas Peinke

► **To cite this version:**

Emanuel Thomas Peinke. All-optical ultrafast switching of semiconductor micropillar cavities : basics and applications to quantum optics. Materials Science [cond-mat.mtrl-sci]. Université Grenoble Alpes, 2016. English. NNT : 2016GREAY030 . tel-01627309

HAL Id: tel-01627309

<https://theses.hal.science/tel-01627309>

Submitted on 1 Nov 2017

HAL is a multi-disciplinary open access archive for the deposit and dissemination of scientific research documents, whether they are published or not. The documents may come from teaching and research institutions in France or abroad, or from public or private research centers.

L'archive ouverte pluridisciplinaire **HAL**, est destinée au dépôt et à la diffusion de documents scientifiques de niveau recherche, publiés ou non, émanant des établissements d'enseignement et de recherche français ou étrangers, des laboratoires publics ou privés.

THÈSE

Pour obtenir le grade de

DOCTEUR DE L'UNIVERSITÉ DE GRENOBLE

Spécialité : **Physique / Nanophysique**

Arrêté ministériel : 7 août 2006

Présentée par

Emanuel Thomas PEINKE

Thèse dirigée par **Jean-Michel GÉRARD**

et encadrée par **Joël BLEUSE**

préparée au sein de l'équipe mixte **CEA-CNRS « Nanophysique et Semiconducteurs »**, CEA / INAC-PHELIQS , F-38054 Grenoble

à l'École Doctorale de Physique de Grenoble

Commutation tout optique ultra-rapide de micropiliers semi-conducteurs : propriétés fondamentales et applications dans le domaine de l'optique quantique

All-optical ultrafast switching of semiconductor micropillar cavities: basics and applications to quantum optics

Thèse soutenue publiquement le **5 avril 2016**,
devant le jury composé de :

M. Benoît BOULANGER

Président du jury

M. Alfredo DE ROSSI

Rapporteur

M. Philippe ROUSSIGNOL

Rapporteur

M. Willem L. Vos

Examineur

M. Jean-Michel GÉRARD

Directeur de thèse

M. Joël BLEUSE

Encadrant de thèse



REMERCIEMENTS

Pour commencer ce manuscrit, je tiens à remercier toutes les personnes qui m'ont soutenues et inspirées pendant ces trois années de thèse. Grâce à eux, ce fut une expérience enrichissante et inoubliable. J'espère que le résultat, ce manuscrit, saura refléter ceci et convaincre le lecteur.

Mes encadrants m'ont été indispensables. Jean-Michel Gérard, mon directeur de thèse, pour son accompagnement et son engagement tout le long de cette thèse. Ses idées novatrices et son enthousiasme sont certainement deux piliers de cette thèse, et m'ont permis de l'accomplir avec grande satisfaction. Joël Bleuse, mon encadrant, m'a appris à maîtriser les différentes expériences optiques et m'a fortement soutenue pendant la rédaction. A l'écoute de toutes mes questions, soit-elles sur la recherche ou sur le plan personnel, je pouvais toujours me confier à lui — sans oublier nos nombreuses discussions sur la société et la politique. Enfin, Julien Claudon, à qui j'ai pu adresser toutes mes questions sur la physique et discuter des difficultés de programmation rencontrées (ou encore parler d'exploits en montagne).

Je tiens également à remercier les membres du jury qui ont accepté de m'évaluer et m'ont donné un retour précieux sur ce manuscrit : Benoît Boulanger, président du jury, Philippe Roussignol et Alfredo De Rossi, rapporteurs, et Willem L. Vos, examinateur. Merci à vous pour vos remarques et ce moment fort agréable que nous avons passé lors de ma soutenance.

Un grand merci aux techniciens Yann Genuist, Didier Boilot et Yoann Curé. Yann, Didier et moi avons repris ensemble la main sur le bâti d'épitaxie III-As — après que Emmanuel Dupuy m'ait introduit dans ce domaine — et ce fut un grand plaisir de travailler en trinôme : Yann l'expert de la croissance moléculaire, Didier l'expert de la science du vide, et moi le physicien. Nous avons toujours eu le soutien de Yoann. Outre la croissance, j'ai beaucoup apprécié sa complicité et son aide dans la programmation et le développement de codes. Sur ce point je remercie également Jan-Peter Richters, qui au début de ma thèse était mon expert Linux et programmation, et Yohan Désières, qui m'a initié aux simulations FDTD.

Ce travail a été réalisé au sein de l'équipe mixte NPSC, dont je tiens à remercier tous les membres pour l'ambiance exceptionnelle qui y règne — innovante, dynamique, et amicale. Un des moments forts de cohésion et d'amitié était la pause-café matinale. Puis les secrétaires côté CEA, Carmelo Castagna et Céline Conche, qui m'ont fortement facilité toutes les démarches administratives grâce à leur compétence et leur efficacité. Et bien sûr tous les stagiaires, thésards et post-docs, Thomas, Rob, Tobi, Tomek, Quentin, Petr, Mark, Damien+Damien, Manos, Adrien, Pamela, . . . qui sont devenus des amis.

Merci aussi à mes collaborateurs, Gaston Hornecker et Alexia Auffèves (de notre groupe), avec lesquels j'ai travaillé sur le « pulse shaping » et à Willem L. Vos et Henri Thyrrstrup des COPS de l'université de Twente avec lesquels nous avons eu un riche échange autour des expériences de « cavity switching ».

Bien sûr, merci à mon successeur Tobias Sattler pour tout le travail, le rire et les aventures ensemble. Je suis aussi reconnaissant à Adrien Delga qui m'a lithographié des échantillons et à Petr Stepanov avec lequel j'ai eu le plaisir de partager des expériences d'optique.

Finalement tous mes amis de Grenoble et de la région, ma famille, et ma copine Sara.

Merci à vous tous,

votre Emanuel

Introduction	5
1 Physical concepts of optical microcavities	9
1.1 Confinement of the electromagnetic field	9
1.1.1 Spatial confinement	9
1.1.2 Spatial confinement: the mode volume	11
1.1.3 Temporal storage and the quality factor Q	12
1.2 Semiconductor microcavities	14
1.2.1 Properties of distributed Bragg reflectors	16
1.2.2 Planar cavities	19
1.2.3 Micropillars	20
1.3 Applications of semiconductor microcavities	23
1.3.1 Spectral filtering	23
1.3.2 Cavity Quantum Electrodynamics (CQED)	24
1.3.3 Low threshold microlasers	30
1.3.4 Bright single-mode single photon sources	31
1.4 Cavity switching	32
1.4.1 Changing the refractive index of semiconductors	32
1.4.2 Applications of cavity switching	33
1.5 Conclusion	34
2 Sample production and characterization	35
2.1 Conception of a planar microcavity	35
2.2 Molecular beam epitaxy	36
2.2.1 The principle of MBE growth	36
2.2.2 Sample preparation and growth conditions	38
2.2.3 The RHEED	39
2.2.4 Growth of planar cavities	40
2.2.5 Growth of InAs quantum dots	41
2.3 Top-down fabrication of a pillar microcavity	44

2.4	Optical characterisation	46
2.4.1	The FTIR	46
2.4.2	Micro-photoluminescence	47
2.4.3	Time resolved spectral analysis with a streak camera	48
2.5	Numerical methods	50
2.5.1	The transfer matrix method	50
2.5.2	FDTD	54
2.6	Conclusion	55
3	Cavity Switching experiments by all-optical free carrier injection.	57
3.1	Switching microcavities	57
3.2	Our experimental approach: Probing cavity switching with an internal light source	58
3.3	Characterising switching events in micropillar cavities	62
3.3.1	“Switch-on” behaviour	63
3.3.2	Free carrier relaxation and the spectral return of the cavity mode	64
3.3.3	Switching amplitude	73
3.4	Differential switching of micropillar cavity modes	79
3.4.1	Differential switching of a small micropillar	80
3.4.2	Simulation of differential switching	81
3.4.3	Differential switching of an ellipsoid micropillar	84
3.4.4	Differential switching of a big micropillar	86
3.5	Conclusion	90
4	Theory of Purcell switching and related applications	91
4.1	About the real-time control of an emitter in a microcavity	91
4.2	Mathematical description of the time- and energy-dependent coupling of a QD in a cavity	93
4.2.1	Rate equations	94
4.2.2	Quantum Langevin equations for a QD in a cavity	95
4.3	Purcell switching	96
4.4	Temporal shaping of single photon pulses	101
4.4.1	Photon emission fidelity and efficiency	102
4.4.2	Shaping of time-domain Gaussian and exponentially increasing single photon pulses, using cavity switching	103
4.4.3	Efficient emission and consecutive reabsorption of single photon pulses	112
4.4.4	Using emitter tuning to shape single photon pulses	120
4.5	Conclusion	124
5	Experimental applications of cavity switching	125
5.1	Generation of ultrashort spontaneous emission bursts using cavity switching	125
5.1.1	Single burst generation	126
5.1.2	Double burst	130
5.1.3	Dependence of t_{burst} with the amplitude of the switch	132
5.1.4	A test of the light burst coherence	133

5.2	Is there Purcell switching in the experiments?	138
5.3	Switching a planar high- Q cavity with the application to change the colour of the trapped light	140
5.3.1	The high- Q planar cavity	140
5.3.2	The cavity ring-down measurement	142
5.3.3	Changing the colour of the light trapped in a planar cavity	143
5.4	Conclusion	150
	Conclusion and perspectives	153
	Bibliography	157

Semiconductor optical microcavities have been intensively studied since the late 80's, due to their strong interest for basic experiments on light-matter interaction as well as for applications. To give only a few examples, microcavity lasers are nowadays widely used in telecoms and datacoms, while ring microcavities are key components used for filtering and reconfigurable routing in photonic chips.

On a more fundamental side, semiconductor microcavities containing quantum dots (QDs) have been used to reproduce in a solid-state system the famous Cavity Quantum ElectroDynamics (CQED) experiments initially performed on real atoms by the 2012 Nobel Prize laureate Serge Haroche [1]. In these experiments, semiconductor QDs are used as artificial atoms. Major basic effects such as the enhancement or inhibition of the QD spontaneous emission [2, 3, 4], or the strong coupling regime between a single QD and a cavity mode [5, 6], have been demonstrated. Microcavities provide in fact a nearly perfect control of QD spontaneous emission, which opens the way to important novel applications in optoelectronics and quantum information science. Noticeably, highly efficient single-mode single-photon sources have been realized by exploiting the Purcell effect (spontaneous emission enhancement) for a single QD in a GaAs/AlAs microcavity [7, 8, 9].

While tuning techniques have been developed to control the frequency of the cavity modes [10], or the detuning and thus the interaction of cavity modes and embedded emitters, such techniques are usually very slow compared to the relevant time scales of the system (such as the storage time of the light in the cavity, or the emission lifetime of an embedded QD). Cavity switching, i.e. the ability to tune the frequency of the modes of a cavity in an ultrafast way [11, 12, 13, 14], opens far-reaching perspectives, such as the control in real time of the properties of an emitter in a cavity. Another application consists in changing the colour of light trapped in a cavity, and demonstrated experimentally by the group of M. Lipson using ring resonators [11] and later by Tanabe *et al.* using a photonic crystal cavity [15].

The objective of this thesis was to study in a time-resolved way — using a streak-camera with picosecond resolution — all-optical switching of microcavities having integrated solid state emitters. This work is in the continuity of my “Diplomarbeit” [16] and therefore contains some similarities with it. The cavity switching — *i.e.* the energy shift of the cavity mode — was realised in the picoseconds or few tens of picoseconds time-range. The time-dependent interactions of emitter and cavity mode were studied and the final goal was to control in real time the spontaneous emission dynamics of an emitter integrated in a micropillar cavity.

My contribution can be separated in three main parts: growth, simulation and optical analysis.

- With the molecular beam epitaxy (MBE) I grew mainly GaAs, AlAs, AlGaAs bi-dimensional layers and also InAs QDs. On this basis planar microcavities, solid-state emitters, and other structures were grown. In this manuscript I will only focus on the QD and microcavity production.
- I wrote Matlab, Octave and Python scripts to simulate on the transfer-matrix method (TMM), on the Finite-Difference in the Time Domain (FDTD) method, on diffusion, recombination and guided modes in micropillars and on solving differential equations like rate equations and quantum Langevin equations. This ensemble of developed numerical methods allowed me to design cavity samples with the desired properties, to analyse as-grown samples and to predict and study the feasibility of the different cavity switching experiments. Furthermore theoretical studies about the time-dependent coupling of an emitter and a cavity mode could be carried out, leading to results about the temporal shaping of single photon pulses.
- The optical characterisations were mostly about studying microcavities and the photoluminescence of emitters. With Fourier Transform Infra-Red (FTIR) spectroscopy I obtained information about reflectivity and modal structure of as-grown cavities. With macroscopic photoluminescence (excitation and collection of millimetre big structures) I studied ensembles of as-grown InAs-QDs. The micro-photoluminescence enabled me to study emitters integrated in structures on the micrometre scale — *e.g.* micropillar cavities.

The main part of the optical analysis were about cavity switching. They were done by time-resolved micro-photoluminescence measurements. For this purpose we obtained a new streak-camera with a picosecond temporal resolution. I mounted a new setup on the optical table, which was adapted to the switching of micrometre size cavities and could be operated in reflection (*e.g.* to study micropillar cavities) or in transmission (*e.g.* to study planar cavities). A frequency tunable pulsed- and a continuous wave-laser could simultaneously be used as pump or probe. When operating under reflection, the samples could be placed in a cold-finger cryostat and at low temperature (about 7 K), in order to optimise the emission properties of the QDs.

This thesis is organized as follows:

Chapter 1 Optical solid-state microcavities are introduced and their physical concepts discussed. Different types of cavities and their light storage and confinement properties — with the corresponding figures of merit, the quality factor Q and the effective mode volume V_{eff} — will be discussed. Introducing emitters inside the cavities we can speak about spontaneous emission and cavity quantum electrodynamics (CQED). We will see different applications. Finally cavity switching — a dynamic modification of the cavity mode resonance — is introduced. It is the fundamental concept for this work.

Chapter 2 The production of microcavities and the integration of solid-state emitters, notably quantum dots, will be explained. The molecular beam epitaxy (MBE) plays a central role. We will see how to analyse the produced samples optically and introduce the numerical simulations used to concept the samples and predict the cavity switching experiments.

Chapter 3 We present a detailed experimental study of the switching of micropillar modes using all-optical free carrier injection. The spontaneous emission of a QD ensemble is used as internal light source, so as to probe by time-resolved photo-luminescence the switching events. For optimised pumping conditions, we observe very large switching amplitudes and/or clear differential behaviours for the first modes of the micropillar. The switching amplitude and return dynamics are modeled in detail, taking into account the diffusion and recombination of the injected electron hole pairs.

Chapter 4 We will theoretically investigate a real-time control of the emitter–cavity interactions. A single two-level emitter in a microcavity can be dynamically brought in and out of resonance with a cavity mode by tuning the resonance of the cavity mode, *e.g.* by cavity switching. Thanks to Purcell effect the spontaneous emission rate of the emitter will change [17]. Using this behaviour, we will show how to trigger the emission of the two-level emitter and how to shape the time-envelope of an emitted single photon pulse. We will conclude that for a QD in a state of the art semiconductor microcavity, cavity switching could be used to generate, with both a high fidelity and a high efficiency, single photon pulses with a Gaussian time-envelope or with an inverse exponential time-envelope. These pulses are important resources for quantum information processing.

Chapter 5 On the basis of the detailed study of the switching process (presented in chapter 3), we consider here two important potential applications using cavity switching as a resource. On one side, we study the spontaneous emission of QDs embedded in a micropillar. Thanks to their transient coupling to switched cavity modes, the system emits one or several ultrashort light bursts. We show how to control the duration (about 3 to 50 ps) and separation of these bursts and test their coherence properties by studying their propagation through a scattering medium. We also probe and discuss the role of the Purcell effect in this spontaneous emission switching experiments. On the other side, we study another major application of cavity switching: the frequency conversion of the

trapped light. Compared to microdisk and photonic crystal cavities which have been previously used in this context, planar and micropillar cavities are well suited for such experiments thanks to their simple in–out coupling geometry. We present a novel cavity design, including a thick “cavity layer”, which enables to increase the light storage time of the planar cavity up to a few tens of picoseconds. Such a cavity has been grown, and further probed by performing a cavity ring down experiment. FDTD simulations confirm that such a cavity is well suited to trap and change the colour of a 30 ps long Gaussian light pulse (mimicking a typical light pulse used in telecom networks). We finally propose a novel experimental configuration which should enable a perfectly efficient colour change, and could be used for instance to shift the frequency of a single photon without losses.

An optical cavity is a structure that confines an electromagnetic field in a certain region of space, during a certain time. A well-known and simple example is the Fabry-Perot cavity, which consists of two parallel planar mirrors, separated by a certain length. In this chapter, I will focus on cavities made of semiconductor materials. Moreover, the cavities treated here feature at least one dimension on the micrometre scale: they are microcavities.

In this chapter we introduce the cavity quality factor Q and its effective mode volume V_{eff} [18]. These two figures of merit respectively characterise the light storage time and the spatial confinement of light. Those will serve to compare different semiconductor microcavities, such as photonic crystals, microdisks, planar cavities and micropillars. By integrating a solid-state emitter (for example a quantum dot) inside such a microcavity, one can deeply modify and control its spontaneous emission. Furthermore, cavity switching — the possibility to dynamically control the cavity properties — will be discussed, as well as some potential applications.

1.1 Confinement of the electromagnetic field

1.1.1 Spatial confinement

To confine light, the electromagnetic waves must be reflected. There are several kinds of mirrors using different reflection mechanisms. We discuss in the following three reflection mechanisms: metallic reflection, total internal reflection and Bragg reflection.

The metallic reflection Metallic mirrors reflect electromagnetic waves over a broad spectral range. Their production is relatively easy. Their main disadvantage is the absorption

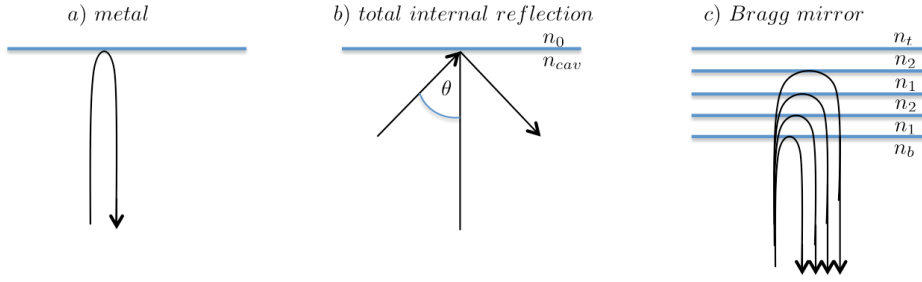


Figure 1.1: Illustration of a) reflection on a metallic mirror, b) total internal reflection and c) reflection on a Bragg mirror for the one wavelength defining its layers. The arrows illustrate the propagation of the electromagnetic waves.

losses in the metal that limit the reflectance to about 95% in the optical domain. Reflection on a metallic mirror is shown schematically in figure 1.1a).

To avoid the use of metals, dielectrics are a possible replacement, in particular semiconductors, below their band gap. The reflection mechanism for dielectrics is either total internal reflection or based on interference effects (distributed Bragg reflectors).

Total internal reflection The interface between a cavity and its external environment can provide a mirror in the context of total internal reflection. We first consider a planar interface between two dielectrics with $n_{cav} > n_0$. For a plane wave incident from the large index side, light will undergo a total reflection if the angle of incidence θ satisfies

$$\sin(\theta) \geq \frac{n_0}{n_{cav}}, \quad (1.1)$$

in accordance with Snell's law. Figure 1.1b) shows the principle of total internal reflection. In the case of a cavity in air, the above equation for total internal reflection reduces to $\theta \geq \arcsin(1/n_{cav})$.

Total internal reflection is used, for example, to guide the light in an optical fibre. In the context of microcavities, total internal reflection is used in circular structures such as spheres or disks, where whispering gallery modes appear on their periphery [19] and in waveguide-like micropillar cavities.

In real cavity structures the internal reflectance on the cavity walls is not exactly $R = 1$ if surface curvature is present. Only if no curvature is present in the direction of propagation, *e.g.* in a flat 2D semiconductor–air interface or in waveguides like a straight optical fibre, total internal reflection may occur. Additional surface roughness of the cavity walls decreases the reflectance in most practical systems in a much stronger way.

Bragg reflection Bragg mirrors, or Distributed Bragg Reflector (DBR), are based on an interference mechanism. For simplicity, we first consider a 1D Bragg mirror, which is built by stacking multiple semiconductor layers having refractive indices n_1 and n_2 and

thicknesses $\lambda_B/4n_i$, where n_i alternates between the two values of n_1 and n_2 and λ_B is the operating wavelength. The surrounding medium above the layer structure has the refractive index n_t (t=top), the medium under the layer structure has the refractive index n_b (b=bottom) as sketched in figure 1.1c. We consider a wave with a normal incidence. At each interface electromagnetic waves are reflected and transmitted. For reflection, a phase shift of π is induced if a wave comes from a material with smaller refractive index than the refractive index of the material on the other side of the interface. In the opposite case, the phase shift upon reflection is by contrast 0. All reflected waves in the $\lambda_B/4n_i$ thick layers are in phase and interfere constructively. Figure 1.1c) shows schematically the reflection on a Bragg mirror. Around the operating wavelength λ_B is a forbidden photonic band with high reflectance, the stopband.

DBR are not limited to one-dimensional confinement. The concept of Bragg reflection is used in photonic crystals, too. Two-dimensional arrays of holes in thin semiconductor slabs are widely used to define 2D photonic crystals. They possess a forbidden band common to all directions of propagation in the plane, and to both polarizations. 3D photonic bandgap materials have also been developed and used for spontaneous emission control [20, 4, 21].

1.1.2 Spatial confinement: the mode volume

If a microcavity confines the light in the three directions of space, the resonant cavity modes form a discrete set and are localised. We speak of 0D cavities. The spatial extent of one mode can be described by its effective volume V_{eff} . V_{eff} is the volume of an equivalent cavity with uniform field distribution which would provide the same maximum field intensity as the actual cavity. Both cavities have to contain the same integrated electromagnetic energy (illustrated in figure 1.2).

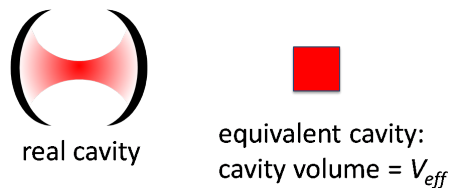


Figure 1.2: The pictures show the extension of a cavity mode in a real cavity (left picture), and the equivalent cavity (right picture) with uniform distribution of the field intensity. The colour intensity corresponds to the electromagnetic field intensity. Both cavities include the same integrated electromagnetic energy, and display the same maximum field intensity.

V_{eff} can be estimated by considering the solutions of the Maxwell equations. The total electromagnetic energy stored in the cavity mode is $W = \iiint \epsilon_0 \epsilon_r |\mathbf{E}|^2 d^3r$. Therefore V_{eff} is defined as $\epsilon_0 \epsilon_{r, \text{max}} |\mathbf{E}|_{\text{max}}^2 \cdot V_{\text{eff}} = W$, with $|\mathbf{E}|_{\text{max}}$ the maximum amplitude of the electric

field \mathbf{E} and $\epsilon_{r,max}$ the relative permittivity on the position of $|\mathbf{E}|_{max}$. Thus

$$V_{\text{eff}} = \frac{\iiint n^2(\mathbf{r}) |\mathbf{E}(\mathbf{r})|^2 d^3r}{n_{max}^2 |\mathbf{E}|_{max}^2} \quad (1.2)$$

$n(\mathbf{r})$ is the refractive index as a function of space and n_{max} is the refractive index at maximum electric field. The effective mode volume is a very useful figure of merit for cavity quantum electro-dynamics (CQED) effects in microcavities.

1.1.3 Temporal storage and the quality factor Q

A perfect cavity, defined by lossless mirrors, would store the light forever. In this ideal case, each cavity resonance represents in the spectral domain one Dirac peak, corresponding to a proper pulsation of the cavity resonance ω_0 , called a cavity mode (see figure 1.3: $R = 1$).

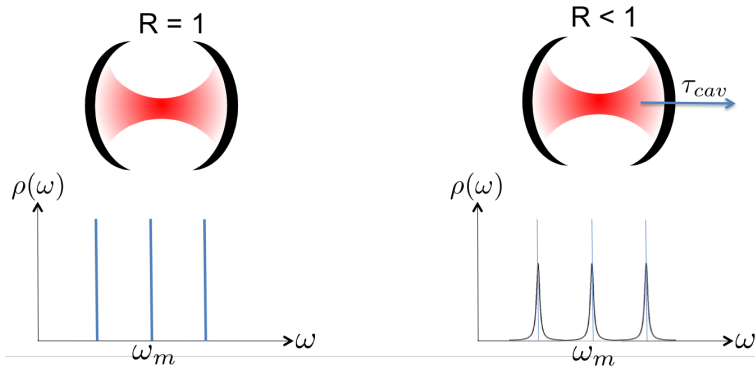


Figure 1.3: The pictures show the confinement of a perfect cavity (left) and the confinement of a real cavity (right) and the corresponding local density of states in the spectral domain. A perfect cavity leads to discrete modes while real cavity modes have a Lorentzian shape.

In reality, light escapes out off the cavity with a characteristic time τ_{cav} , the storage time of light. As a consequence, the energy I of the stored electromagnetic field in the cavity decreases exponentially in time t : $I(t) \propto e^{-t/\tau_{cav}}$, see figure 1.4a). In the spectral domain this results in broadened cavity modes with Lorentzian shape (c.f. figure 1.3: $R < 1$). In practice the light storage can be limited in time by absorption by the mirrors or transmission through the mirrors.

Let us introduce the quality factor of the modes which governs the dynamical and spectral properties of the cavity. We consider a cavity with loss channels which are constant over time and induce weak losses per optical cycle. We assume that some light is injected into a cavity mode m , resonant to ω_m , at $t = 0$. Since τ_{cav} depends, generally speaking, on the mode under study, we note in the following τ_m the decay time from the initially stored electromagnetic energy in the mode I_m to $1/e$ of its value [22]. After $t = 0$, its exponential

decay is defined as

$$I_m(t) \propto e^{-t/\tau_m}, \quad t \in [0, \infty] \quad (1.3)$$

and the corresponding electric field as

$$E_m(t) \propto e^{-t/2\tau_m - i\omega_m t}, \quad t \in [0, \infty] \quad (1.4)$$

In the first order approximation, the stored energy I is

$$I_m(t) = I_m(0) \cdot (1 - t/\tau_m) \quad (1.5)$$

so

$$\Delta I_m = I_m(0) \cdot \Delta t / \tau_m \quad (1.6)$$

To characterise the cavity's capacity to store electromagnetic fields in time, the quality factor Q is introduced:

$$Q = 2\pi \cdot \frac{\text{energy stored in the cavity}}{\text{energy lost per optical cycle}} \quad (1.7)$$

This definition is general and true for every resonator, whether it is electrical, mechanical or optical. We can re-express the energy lost per optical cycle to deduce the final expression of Q_m , the quality factor on a mode m :

$$\begin{aligned} Q_m &= 2\pi \cdot \frac{\text{energy stored in the cavity mode } m}{\frac{\text{energy stored in the cavity mode } m}{\tau_m} \cdot \frac{2\pi}{\omega_m}} \\ &= \tau_m \cdot \omega_m \end{aligned} \quad (1.8)$$

This is the definition of the quality factor in the temporal domain. Q_m can be measured in this domain using a ‘‘cavity ring-down’’ experiment, an example of which is illustrated in the reference [23], by determining τ_m . A short light pulse excites the cavity and the transmitted intensity is observed as a function of time.

I will now introduce the quality factor in the spectral domain. Having the time dependence of the electric field in the cavity, equation 1.4, from a Fourier transformation the spectral distribution can be obtained:

$$\begin{aligned} E_m(\omega) &\propto \int_0^\infty e^{-t/2\tau_m} e^{-i(\omega_m - \omega)t} dt \\ &\propto \frac{1}{\frac{1}{2\tau_m} + i(\omega_m - \omega)} \end{aligned} \quad (1.9)$$

The intensity of the electromagnetic field, proportional to the local density of states, is

$$|E_m(\omega)|^2 \propto \frac{1}{(\omega_m - \omega)^2 + \frac{1}{4\tau_m^2}} \quad (1.10)$$

This is a Lorentzian distribution. Thus the cavity modes have a Lorentzian spectral distribution and are broadened with a characteristic full width at half maximum

$$\Delta\omega_m = \frac{1}{\tau_m} \quad (1.11)$$

(cf. figures 1.3: $R < 1$ and 1.4b)).

The quality factor in the spectral domain is

$$Q_m = \frac{\omega_m}{\Delta\omega_m} \quad (1.12)$$

Q_m is measured in the spectral domain, measuring ω_m and $\Delta\omega_m$ (see figure 1.4b)) in the cavity's reflection or transmission spectrum, see *e.g.* Rivera *et al.* [24].

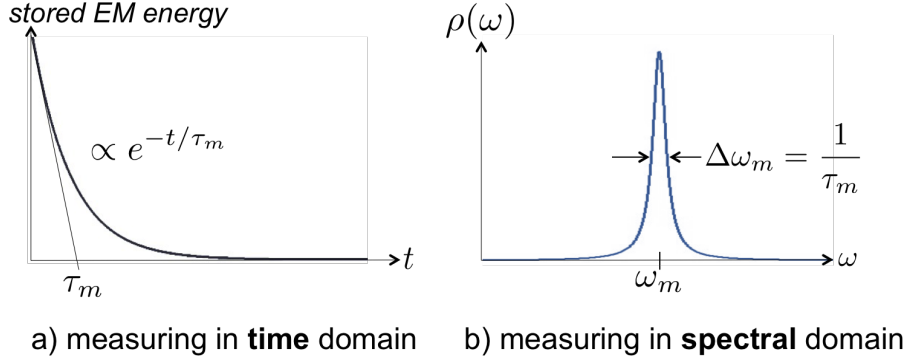


Figure 1.4: a) Exponential decay of the energy stored in the cavity. b) Illustration of the values, which characterise the temporal storage in an optical cavity.

Formula 1.11 shows the equivalence of the measurement of Q_m in the temporal domain and in the spectral domain.

The later discussion illustrates the two different strategies for probing the quality factor of a cavity. Spectral measurements can easily be performed for moderate Q cavities ($Q < 10000$) in the optical domain. By contrast time-resolved ring-down experiments are more easily performed for high Q cavities.

1.2 Semiconductor microcavities

With the mentioned confinement mechanisms, different types of semiconductor microcavities can be obtained and characterised by their figures of merit Q and V_{eff} . Depending on the foreseen application, a high Q , a small mode volume, or a combination of both properties will be looked after. The highest Q combined with the smallest V_{eff} should represent the ideal cavity. In my studies I will focus on cavities based on Bragg mirrors, but for state of completeness let me introduce other cavities, too.

Microdisk cavities are thin circular disks surrounded by air. Figure 1.5a) shows such a microdisk. The stored light is confined by total internal reflection, thanks to the high contrast in the refractive index of the cavity's semiconductor and the surrounding air; once in the plane of the thin disk, once at the disk circumference. Whispering gallery modes

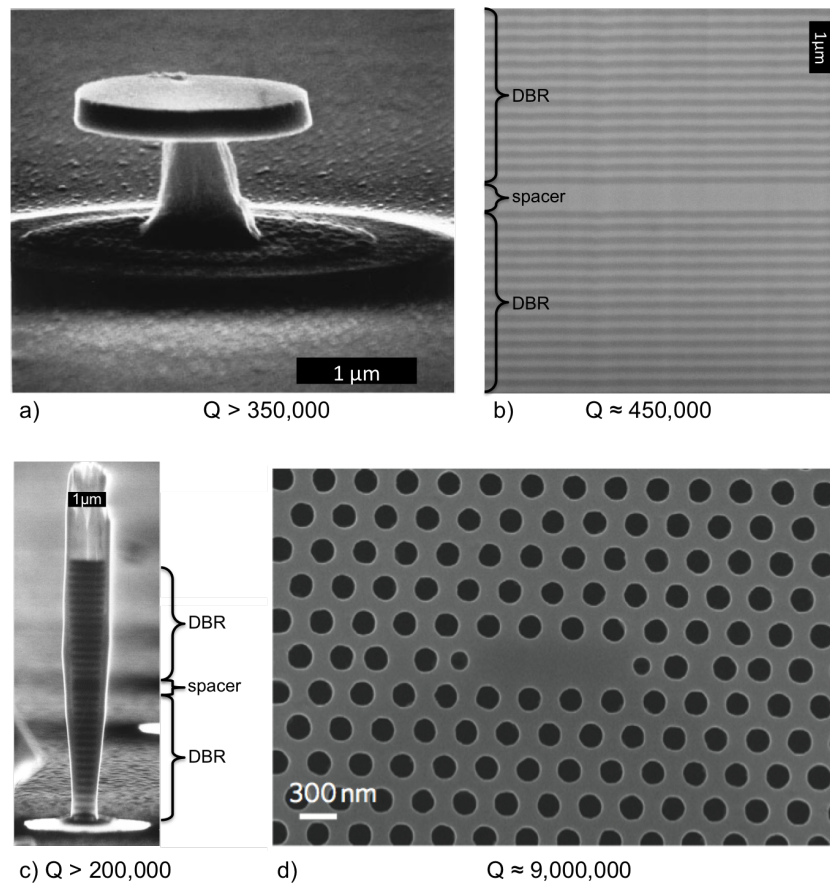


Figure 1.5: SEM (Scanning Electronic Microscope) images of four AlGaAs microcavities with the corresponding maximum Q -values. a) A GaAs microdisk having a $2 \mu\text{m}$ diameter [25]. b) A planar cavity (its cross-section) which was produced in my laboratory. c) A micropillar having a $1 \mu\text{m}$ diameter [2]. In b) and c) the colour of the spacer corresponds to GaAs and the other colour corresponds to AlAs. The central spacer and the Bragg mirrors are well distinguishable. d) A photonic crystal cavity made of GaAs, taken from [26]. GaAs is grey, the holes are black. The cavity mode is localised in the centre of such cavity.

can take place. Quality factors Q up to 360000 were measured [27]. One has to note that Q increases with the radius and is intrinsically limited by radiation losses, mainly induced by the surface roughness [28]. The whispering gallery modes are localised close to the disk circumference and occupy a mode volume much smaller than the disk volume. For a disk of diameter $2 \mu\text{m}$ the effective volume is $V_{\text{eff}} = 4(\lambda/n)^3$ [29]. Microdisk cavities have very high Q and small V_{eff} . However, isolated microdisks display a broad radiation diagram, covering all directions in (and close to) the plane of the microdisk. Out of plane emission is much easier to detect. Various strategies, including the coupling to a nearby waveguide, have been developed to collect the emission from microdisk cavities.

Photonic crystal cavities consist of a very tiny cavity volume surrounded by arrays of periodic holes. The effective volume can be $V_{\text{eff}} < (\lambda/n)^3$ [30]. The holes act as reflection

centres. Interference mechanisms lead to the confinement of the light in the central cavity. The holes can be etched in a thin semiconducting film, producing a 2D photonic crystal [31]. At the cavity surface total internal reflection occurs. Figure 1.5d) shows a 2D photonic crystal cavity made of GaAs. Noda *et al.* measured quality factors up to 9000000 [32]. Three dimensional photonic crystal cavities exist, too. Photonic crystal cavities have very high Q and hold the records of the smallest V_{eff} . Their radiation pattern is more difficult to control.

Microcavities based on Bragg mirrors are relevant for this thesis. The basic cavity is the planar cavity, confining the light in the plane between two Bragg mirrors. The medium in between the DBR is called a spacer. Such a cavity is shown in figure 1.5b). Quality factors up to $Q \approx 450000$ were obtained [33]. The effective volume V_{eff} is much bigger than in the previous cavities as the modes have no real lateral confinement. An advantage of planar cavities is their radiation perpendicular to the cavity surface and quite directive.

Etching planar cavities perpendicular to their surface creates the so called pillar microcavities [34] (see figure 1.5c)). Those micropillars combine two types of confinements. On the sidewalls the total internal reflection confines the light like in waveguides. At the top and bottom of the pillar the Bragg mirrors confine the light like in planar cavities. Q up to 200000 were measured for state of the art processing [33, 35]. The effective volume is more or less small: $V_{\text{eff}} \approx 5(\lambda/n)^3$ for a pillar of $1 \mu\text{m}$ diameter [2]. Their emission is very directive and perpendicular to the cavity surface. This makes them very accessible for the collection and use of the emitted light and very useful as microlasers and single photon sources.

One has to note that the mentioned quality factors are all for cavities based on III-V-semiconductors, mainly made of GaAs and AlAs, the most mature material system beside Si/SiO₂.

The studies I did are all about planar and micropillar cavities, made of aluminum-gallium-arsenide, Al_{*x*}Ga_{1-*x*}As. This material has the advantage of being very well mastered in terms of growth and processing, which are described in section 2.2. It is possible to precisely define the layers of the Bragg mirrors. In addition, it is possible to integrate optical emitters in these structures, such as InAs quantum dots or InGaAs quantum wells. Complicated cavities for sophisticated experiments are feasible. I describe in the next sections in more detail the properties of DBRs and micropillar cavities

1.2.1 Properties of distributed Bragg reflectors

Firstly let us consider only normal incidence. Bragg mirrors are defined for a central wavelength λ_B for which they feature their maximal reflectance. The reflectance R of a Bragg mirror increases with the number of its layers. Having M pairs of quarter-wavelength

layers, the reflectance for the wavelength λ_B , coming from the top, is [36, 37]

$$R_t = \left(\frac{1 - \frac{n_b}{n_t} \left(\frac{n_1}{n_2} \right)^{2M}}{1 + \frac{n_b}{n_t} \left(\frac{n_1}{n_2} \right)^{2M}} \right)^2, n_1 > n_2. \quad (1.13)$$

This value depends on the surrounding media. n_t , n_b , n_1 and n_2 are illustrated in figure 1.6. An interesting property of DBR is that for normal incidence the reflectance does not differ for light impinging from the bottom and for light impinging from the top.

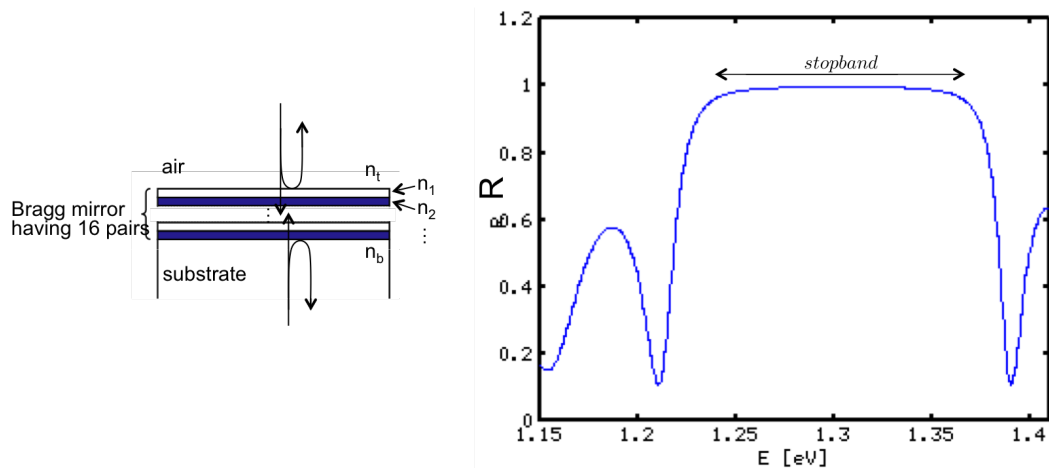


Figure 1.6: A simple Bragg mirror having 16 alternating $\lambda_B/4n_i$ thick layers, placed on a substrate and the corresponding reflectance spectrum for $\lambda_B = 954$ nm. This spectrum is the same, if light impinges from the top (air) or from the substrate, both under normal incidence. The material with the high refractive index is shown in white (layers and substrate), the one with the smaller refractive index in blue. The spectrum is computed for alternating AlAs/GaAs layers placed on a GaAs substrate. At 1.3 eV, so $\lambda = 954$ nm, and for room temperature their refractive indices are $n_{GaAs} \approx 3.55$ and $n_{AlAs} \approx 2.95$ [38]. The refractive index of the air is taken $n_{air} = 1$.

For other than the central wavelength, the Bragg mirror features a high reflectivity on a photonic stopband covering a certain wavelength range $\Delta\lambda$ (*cf.* figure 1.6). The size of stopband does not depend on the number of layers (if they are numerous). All reflectance spectra in this thesis have the same stopband size $\Delta\lambda$, *cf.* the figures, because they are all based on Bragg mirrors of the same materials, aluminum-arsenide (AlAs) and gallium-arsenide (GaAs). For a large number of layers it is approximately [36]

$$\frac{\Delta\lambda}{\lambda_B} = \frac{4}{\pi} \arcsin \left(\frac{n_1 - n_2}{n_1 + n_2} \right), n_1 > n_2. \quad (1.14)$$

The discussed characteristics are identical for transverse electric (TE) and transverse magnetic (TM) electromagnetic waves, provided normal incidence. If we consider other than normal incidence, the results differ. Out of normal incidence it matters from which side light impinges and TE and TM waves behave in a different manner. Their reflectances

as a function of the angle to normal incidence θ are shown for the central wavelength λ_B for different cases in figure 1.7. Where the reflectance reaches unity, total internal reflection appears.

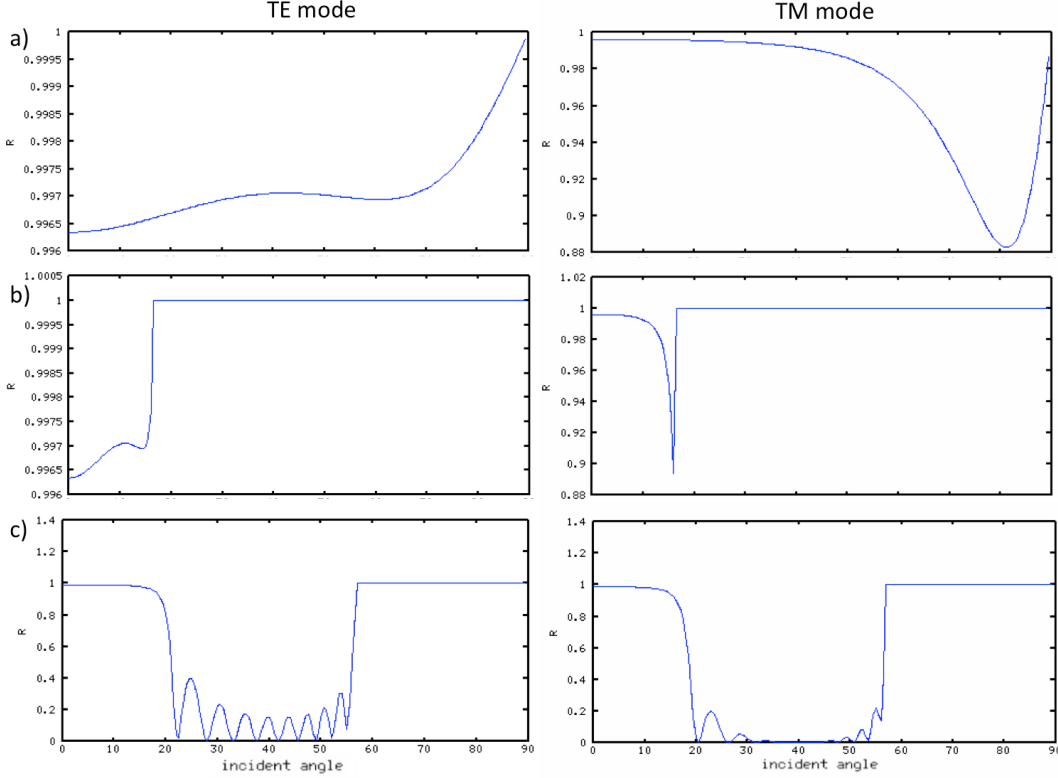


Figure 1.7: Reflectance spectra for TE and TM mode for the central wavelength $\lambda_B = 954$ nm as a function of the incident angle, showing three different cases. The spectra in a) and b) are computed for the mirror of figure 1.6, where $n_t = n_{air} = 1$ and $n_b = n_{GaAs}$; at $\theta = 0$ the reflectivities are equal. a) Light is injected from the air. For $\theta \neq 0$ the reflectivities differ, but remain high. Because of the high refractive index of the mirror compared to the air, light under any angle of incidence in the air continues propagating nearly with normal incidence inside the cavity. Thus the Bragg mirrors are well defined and have good reflection properties for all angles of incidence. b) Light is injected from the substrate. For larger angles total internal reflection appears. Right before that, the TM-mode has a minimum. The global reflectance is very high. c) Now the mirror is modified, by replacing the air with the material with the small refractive index, so $n_t = n_{AlAs}$. Light impinges from the substrate, $n_b = n_{GaAs}$. Compared to b) the refractive index change at the cavity surface, next to n_t , is small. The total internal reflection appears for larger incident angles. For small incident angles the Bragg mirrors are well defined and well reflecting. In between the reflectance is close to zero. This can have important consequences when inserting emitters, such as quantum dots.

1.2.2 Planar cavities

Assembling two parallel infinite Bragg mirrors separated by a spacer leads to a planar cavity, confining the light in spacer between its two DBR. To produce such a planar cavity made of AlAs and GaAs, $\lambda_B/4n_i$ -layers are deposited on a GaAs substrate and construct a Bragg-mirror having the reflectance R_{bottom} . Then a spacer, generally an integer multiple of λ_B/n_i thick, is deposited on the bottom mirror. This selection rule for the thickness of the resonator enables the cavity mode to be centred inside the reflectance's stopband. Each cavity mode has an associated peak in the reflectance spectrum. The optical thickness of the spacer defines the number of resonant modes in the stopband and their positions. Finally a second Bragg mirror, also defined for λ_B , is deposited on the resonator. Its reflectance is R_{top} . The materials are chosen such that n_i alternates between the 2 values at each interface. This assembly leads to a longitudinal (in the growth direction) confinement of the light. Such a cavity is shown in figure 1.5b).

The cavity's main properties are its central wavelength, its quality factor and its functionality. Good extraction and collection properties or filtering properties can be desired, for example. If an emitter is placed in the cavity, the light extraction will play the crucial role. Good upwards extraction will be achieved for $R_{bottom} \gg R_{top}$. If $R_{bottom} \approx R_{top}$ the cavity will have good filtering properties. For $R_{bottom} = R_{top}$ the resonant cavity modes will have a reflectance equal to zero, corresponding to a transmittance equal to 1. For the rest of the stopband the reflectance remains approximately unity. An exemplary spectrum for such filtering cavity is shown in figure 2.1. Section 2.5.1 treats the mathematical description of the planar cavity's reflectance.

The reflectance of the two DBR, R_{bottom} and R_{top} , and the thickness of the spacer L_{cav} define the time τ_{cav} stored light stays in the cavity, and so Q . We can describe the cavity by an equivalent Fabry-Perot cavity (*cf.* figure 1.8), confining the light during the same time τ_{cav} and having two ideal mirrors (no phase shift and no absorption upon reflection) with the DBR's reflectivities R_{bottom} and R_{top} . The corresponding Fabry-Perot resonator thickness is $L_{FP} = L_{eff,top} + L_{cav} + L_{eff,bottom}$. The penetration lengths L_{eff} account for the penetration of the light within the DBRs upon reflection (*cf.* figure 1.8). [39]

$$L_{eff} = \frac{\lambda_B}{n_{cav}} \frac{n_1 n_2}{4n_{cav}(n_1 - n_2)}, n_1 > n_2. \quad (1.15)$$

n_{cav} is the refractive index of the cavity spacer. In there the light source can be placed. L_{eff} depends only on the different refractive indices of the layers, and not on the number of layers. For a planar cavity, consisting of only two different materials, the penetration length in both Bragg mirrors is always equal. For example for a GaAs/AlAs cavity with a GaAs spacer the penetration length is $L_{eff} = 1.23 \frac{\lambda_B}{n_{cav}}$.

Placing a spacer of the thickness $L_{cav} = N \cdot \lambda_B/2n_{cav}$, $N \in \mathbb{N}$, (the resonator) in between the two mirrors, a round-trip of the light in the cavity is $L = N \cdot \lambda_B/n_{cav} + 4 \cdot L_{eff}$ long. We can introduce the order of the cavity $m = \frac{L}{\lambda_B/n_{cav}}$:

$$m = N + 4 \cdot \frac{L_{eff}}{\lambda_B/n_{cav}}. \quad (1.16)$$

cavity modes appear. The small volume is important for the enhancement of spontaneous emission, the Purcell effect, and used for active components.

The resonances of micropillars differ from the ones of the planar cavity [42]. In the ideal planar cavity with two perfect mirrors $R_{top} = R_{bottom} = 1$ and spacer λ_B/n_{cav} thick, the resonant condition is $\lambda_B/n_{cav} = L_{cav}$ leading to one only cavity mode. However micropillars behave like waveguides. The physics of waveguides predict several guided modes m having proper resonances λ_m , described by $\lambda_m/n_{eff}^m = L_{cav}$ with the effective refractive index n_{eff}^m (m is an index) and the unchanged physical length L_{cav} . The DBR confine these modes vertically.

The guided modes are calculated as follows: An electric field which propagates along the z -axis writes $\mathbf{E} := \mathbf{E}(r, \theta, z, t) = \mathbf{E}(r, \theta) \cdot e^{i(\omega t - \beta z)}$, with $\mathbf{E} = (E_r, E_\theta, E_z)$ (same for the magnetic field \mathbf{H}), using the cylindrical coordinates (r, θ, z) . β is the propagation constant along z . It has to be $\frac{\min(n)\omega}{c} < \beta_m < \frac{\max(n)\omega}{c}$ for guided modes. When describing a micropillar cavity, ω is the resonance of the corresponding planar cavity. c is the speed of light in vacuum. n is the refractive index and can depend on r and t .

The wave equation for guided modes along z writes generally:

$$\left(\Delta^2 + \left(\frac{n(r, t) \omega}{c} \right)^2 \right) E_z = 0 \quad (1.20)$$

Thanks to the here cylindrical symmetry $E_z(r, \theta) = E_z(r)e^{\pm il\theta}$, with $l \in \mathbb{N}$, and the Laplacian $\Delta = \partial_r^2 + \frac{1}{r}\partial_r + \frac{1}{r^2}\partial_\theta^2 + \partial_z^2$. The wave equation can be simplified:

$$\left(\partial_r^2 + \frac{1}{r}\partial_r - \frac{l^2}{r^2} - \beta_m^2 + \left(\frac{n(r, t) \omega}{c} \right)^2 \right) E_z(r) = 0 \quad (1.21)$$

and describes now the guided modes in a cylindrical waveguide. Solving this equation results in the propagation constants β_m of the guided modes. These constants are the same in the GaAs section of the micropillar. (If n is a function of the time, β_m is a function of the time, too. This is interesting for later simulations of cavity switching.)

In a micropillar, due to the DBR, each guided mode m gives birth to a confined micropillar mode m . The corresponding effective refractive index is $n_{eff}^m = \beta_m c / \omega$ and the cavity resonance in energy $E_m = \frac{n_{GaAs}}{n_{eff}^m} \hbar \omega$.

When the pillar diameter decreases, the modes get more and more confined by the sidewalls, like the case for waveguides. n_{eff}^m decreases and the cavity resonances are blue-shifted. The resonant condition can be written as $(\lambda_B - \Delta\lambda_m)/n_{eff}^m = L_{cav}$. $\Delta\lambda_m$ is the induced shift of the resonant modes and λ_B is the resonance for an infinitely thick pillar, the planar cavity. For the different modes this shift is shown on the energy scale, so $\Delta E_m = E_m - E_B$, as a function of the pillar radius in figure 1.9.

In addition, a continuum of non-confined modes exists. Those are the leaky modes of the pillar. Two kinds exist. The modes can be not confined in plane, so not confined by total internal reflection. Or they can be not confined by the Bragg mirrors: Initially the

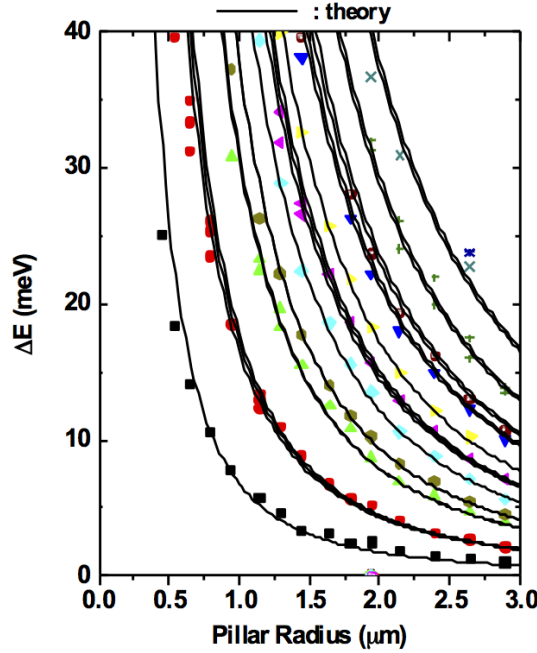


Figure 1.9: The energy blue-shift for the different modes of a GaAs/AlAs micropillar, having a λ_B/n -thick resonator, as a function of the pillar radius. Experimental and theoretical results are taken from [42]. The operating wavelength is $\lambda_B = 960$ nm ($E_B = 1.29$ eV)

DBR are defined for a resonance λ_B with the stopband centred around this value. Every confined mode corresponds to a shifted resonance $\lambda_B - \Delta\lambda_m$ and its stopband is always centred around this shifted resonance. Let us now consider for instance the wavelength λ_B , the resonant wavelength of the planar cavity under normal incidence. λ_B belongs to the stopband of the planar cavity, as well as to the stopbands related to the first guided modes in the micropillar. This is no longer the case for higher order guided modes of the GaAs cylinder, as soon as their effective index n_{eff}^m is reduced by typically 5% with respect to n_{cav} . Such guided modes are no longer confined by the DBR at around λ_B , and give rise to the formation of a continuous density of modes around λ_B .

In general, the quality factors of micropillars are smaller than the quality factor of the original planar cavity. The pillar's effective refractive indices may change in a different way for the different layer materials. For each material $\frac{n-n_{\text{eff}}^m}{n}$ has to be compared. For aluminum-arsenide (AlAs) and gallium-arsenide (GaAs) the relative changes in the refractive indices are nearly equal. The thicknesses of the GaAs and AlAs sublayers in the DBR correspond still to a quarter of the optical wavelength, for the novel resonance E_m . The Bragg mirrors keep their reflection properties and micropillars made of alternating layers of AlAs and GaAs have still high intrinsic quality factors. In the ideal case (and for pillar diameters $> 1\mu\text{m}$), the quality factor of the micropillar equals the quality factor of the

planar cavity [43]. Usually of bigger effect is the reduction of Q by the losses on the pillar's side-wall surface having a certain roughness [24, 44]. The smaller the pillar radius, the bigger is this effect, see figure 1.10 [44].

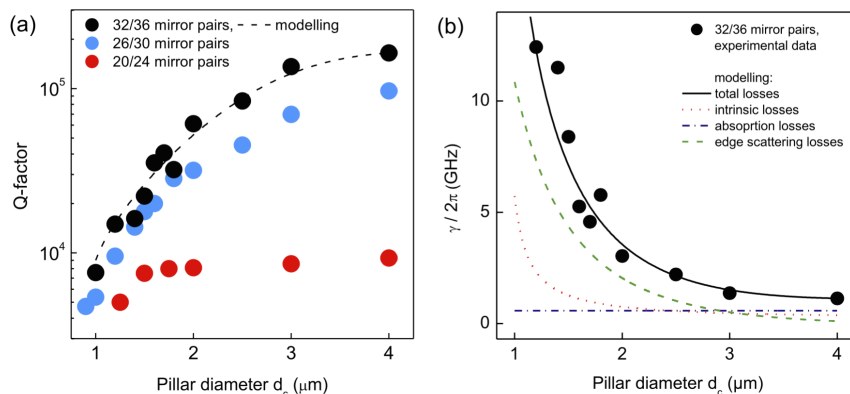


Figure 1.10: Limited quality factor in high Q micropillar cavities, taken from [44]. Three different micropillar cavities, characterised by their number of Bragg layers, are studied. The smaller the micropillar diameter, the more its quality factor is limited by the losses due to imperfections. As shows the second figure, intrinsic losses have limited effect on Q . The dominating losses originate from scattering at the more or less rough pillar surface [44].

1.3 Applications of semiconductor microcavities

Microcavities can be used for passive and active components. First, a microcavity can be used to spectrally filter optical signals. Second, a microcavity can be used to increase the strength of light-matter interactions, with application to the realization of low threshold microlasers and to bright single photon sources.

1.3.1 Spectral filtering

A common filtering cavity consists of a microring in an integrated optical photonic circuit, described in reference [45]. Two waveguides are coupled to a microring like shown in figure 1.11. Only the wavelengths resonant with the microring cavity modes enter from the first waveguide into the microring and are extracted into the second waveguide. Those are in the spectral interval $\Delta\lambda = \lambda/Q$ ($\Delta\lambda/\lambda = \Delta\omega/\omega_0 = 1/Q$). Such resonators are nowadays widely used for photonic integrated circuits on silicon.

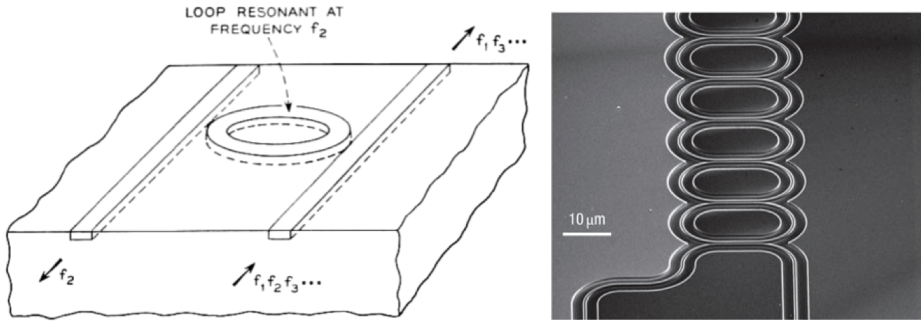


Figure 1.11: To the left, two waveguides coupled to a microring cavity creating a filtering cavity for the wavelength $\lambda_2 = c/f_2$; image taken from [45]. To the right, a recent application showing a delay line, composed of many coupled microrings [46].

1.3.2 Cavity Quantum Electrodynamics (CQED)

Cavity Quantum Electrodynamics describe the interaction between a quantum light emitter and the light confined in a cavity.

Basics of CQED

The insertion of an emitter in a cavity influences the emitter's spontaneous emission, depending on the strength of the coupling between emitter and the available local density of states, strongly related to the available cavity modes. Purcell proposed in 1946 to tailor so the emitter's spontaneous emission rate [17], which became an important tool for cavity quantum electro-dynamics (CQED), even in its early development stages [1, 47]. In the 90s solid state microcavities became more and more important and the Purcell effect became a major research topic for them [48]. The first very successful experimental demonstration of the Purcell effect in a semiconductor microcavity was realised with self-assembled InAs quantum dots (QDs) in a GaAs/AlAs micropillar in 1997 [2]. InAs QDs in GaAs/AlAs micropillar are still an important subject of research in modern CQED, thanks to the maturity of technological processes for this system.

QDs are semiconductor monochromatic two-level emitters (usually called two-level-systems, TLS). Integrated in a microcavity, they can couple to the cavity modes and to the continuum of leaky modes. For the easiness of the purpose I will consider first one TLS in a microcavity with one only cavity mode. A detailed quantum treatment of a two-level emitter in a cavity is given by [49] and [50]. The system can be described in terms of normalised coupling rates κ , $\tilde{\gamma}$ and g . It is spanned in the sub-space $\{|e, 0\rangle, |g, 1\rangle, |g, 0\rangle\}$, indicating the TLS excitation with e the excited state and g the ground state and the cavity mode photon population which can be in between 0 and 1. κ describes the energy relaxation from the cavity mode to the continuum of empty modes in the outer space, $\tilde{\gamma}$ the energy relaxation from the two-level emitter to the mentioned continuum and g the (reversible)

coupling between cavity mode and two-level emitter, as illustrated in figure 1.12.

An ideal loss-less cavity–TLS system would have $\kappa = 0$ and $\tilde{\gamma} = 0$. Emitter and cavity would coherently exchange a single photon, oscillating eternally between the states $|e, 0\rangle$ and $|g, 1\rangle$. These are the so-called Rabi-oscillations. In real systems $\kappa, \tilde{\gamma} > 0$ damp the coherent exchange, as shown in figure 1.12. It is called the strong coupling regime where $g \gg \kappa, \tilde{\gamma}$. The first experimental evidence of the strong coupling regime was realised by Thompson *et al.* for atoms in a cavity [51]. In a solid state system it was obtained in 2004 with InAs QDs in a photonic crystal [52] and in a micropillar-system [5].

For much weaker coupling between emitter and cavity mode the photon exchange can be over-damped and become irreversible. This is the weak coupling regime where $g < \kappa$. The emitter emits with an exponentially decaying signal, as if it was surrounded by bulk material instead of the cavity, but with a modified characteristic time of decay τ_{TLS} . It can be calculated using Fermi’s golden rule. Depending on the strength of the coupling, the spontaneous emission can be accelerated or slowed down.

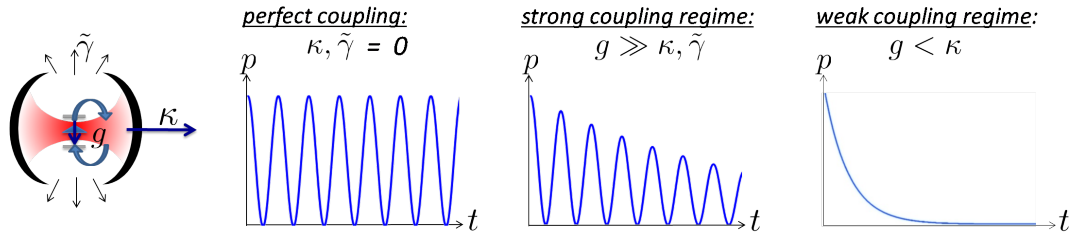


Figure 1.12: Left image: A two-level system in a cavity and the relevant coupling rates. Following images: The emitter’s population p as a function of time t , once for perfect loss-less coupling between emitter and cavity mode, once for the strong coupling regime, and once for the weak coupling regime. In the loss-less case emitter and cavity coherently exchange one single photon, leading to Rabi-oscillations. In the strong coupling regime the envelope of the coherent exchange is damped, reflecting the losses of the cavity. In the weak coupling regime no re-excitation of the emitter occurs. The population of the emitter shows an exponential decay, leading to an exponentially decaying spontaneous emission signal.

The Purcell factor In the weak coupling regime of CQED, the cavity mode coupled to the cavity loss or leaky modes is described as a quasi-mode, with a Lorentzian spectral local density of states $\rho(\omega)$ (*cf.* figure 1.13). The coupling of a monochromatic emitter to this continuous quasi-mode is described by Fermi’s golden rule. It describes the transition from the excited TLS state and zero photon in the cavity $|e, 0\rangle$ to the TLS ground state with one photon in the cavity $|g, 1\rangle$ by the spontaneous emission rate

$$\Gamma_m = \frac{2\pi}{\hbar^2} |\langle e, 0 | -\hat{\mathbf{d}} \cdot \hat{\mathbf{E}} | g, 1 \rangle|^2 \rho(\omega) \quad (1.22)$$

The relaxation of the emitter (initially excited) in the cavity mode m (initially empty) remains irreversible and occurs with the rate Γ_m , related to the emitter's characteristic time of decay $\tau_{\text{TLS}} = 1/\Gamma_m$. $\hat{\mathbf{d}}$ is the dipole operator of the emitter and $\hat{\mathbf{E}}$ the electrical field operator of the cavity mode. $\hat{\mathbf{d}}$ acts on the TLS excited and ground states $|e\rangle$ and $|g\rangle$, respectively, and $\hat{\mathbf{E}}$ on the cavity mode population ($|0\rangle$ or $|1\rangle$). $\hat{\mathbf{E}}$ can be described with the photon creation and annihilation operators, \hat{a}^\dagger and \hat{a} , respectively:

$$\hat{\mathbf{E}}(\mathbf{r}, t) = |\mathbf{E}|_{\text{max}} \left(\hat{a}(t) \mathbf{f}^*(\mathbf{r}) + \hat{a}^\dagger(t) \mathbf{f}(\mathbf{r}) \right) \quad (1.23)$$

$|\mathbf{E}|_{\text{max}}$ is the maximum value of the electric field at the centre of the cavity mode. \mathbf{f} is a complex function describing the spatial distribution of the cavity mode, and normalised to $|\mathbf{f}|_{\text{max}} = 1$. In accordance with the definition of V_{eff} by equation 1.2

$$|\mathbf{E}|_{\text{max}} = \sqrt{\frac{\hbar\omega_m}{2\epsilon_0 V_{\text{eff},m}}} \quad (1.24)$$

The local density of states $\rho(\omega)$ for a cavity with one only cavity mode resonant to ω_m is a Lorentzian

$$\rho(\omega) = \frac{2}{\pi\Delta\omega_m} \frac{1}{1 + 4\left(\frac{\omega - \omega_m}{\Delta\omega_m}\right)^2} \quad (1.25)$$

$\Delta\omega_m = \omega_m/Q_m$ is the cavity line-width.

One generally introduces the Purcell factor F_P as the maximum enhancement of spontaneous emission obtained for an emitter on resonance with the cavity mode, so $\rho(\omega = \omega_m) = \frac{2Q_m}{\pi\omega_m}$, located on the maximum amplitude of the electric field \mathbf{E} , with a dipole aligned along the local mode polarization. Under this conditions we can simplify equation 1.22. With $d^2 = |\langle e|\hat{\mathbf{d}}|g\rangle|^2$, we obtain the final spontaneous emission rate for an emitter perfectly coupled to a cavity mode:

$$\Gamma_m = \frac{2d^2 Q_m}{\hbar\epsilon_0 V_{\text{eff},m}} \quad (1.26)$$

The spontaneous emission rate of the same emitter placed in infinite bulk material is

$$\Gamma_0 = \frac{d^2 \omega^3}{3\pi\epsilon_0 \hbar c^3} \quad (1.27)$$

We can compare both spontaneous emission rates:

$$\frac{\Gamma_m}{\Gamma_0} = \frac{6\pi Q_m}{V_{\text{eff},m}} \frac{c^3}{\omega_m^3} \quad (1.28)$$

The Purcell factor F_P describes the maximal enhancement of spontaneous emission. Therefore

$$\Gamma_m = F_P \cdot \Gamma_0 \quad (1.29)$$

defines the Purcell factor, which is [17]

$$F_P = \frac{3}{4\pi^2} \frac{Q_m}{V_{\text{eff},m}} \frac{\lambda_m^3}{n^3} \quad (1.30)$$

Since it depends only on λ_m , Q_m , and $V_{\text{eff},m}$, F_P is also a figure of merit of the cavity mode m .

Using a microcavity with an effective volume of the order of $(\lambda/n)^3$ and a high quality factor, like for a micropillar, gives a Purcell factor greater than 1; spontaneous emission is enhanced. The spontaneous emission rate of a TLS in a cavity is maximised, if the conditions for equation 1.30 are fulfilled: the TLS is perfectly aligned in the cavity and its transition is at the same frequency as the cavity resonance: $\omega_{\text{TLS}} = \omega_m$.

Besides the emission into the cavity mode, two-level systems emit into leaky modes. The spontaneous emission rate into these leaky modes is $\gamma \Gamma_0$ with $\gamma \approx 1$ for a micropillar cavity [2, 53], and much lower values for photonic crystal cavities. For TLS in a semiconductor cavity the total spontaneous emission rate is generally speaking Γ_{TLS} , the sum of spontaneous emission rate into the cavity mode $F_P \Gamma_0$, and spontaneous emission rate into leaky modes $\gamma \Gamma_0$.

$$\Gamma_{\text{TLS}} = (F_P + \gamma) \cdot \Gamma_0 \quad (1.31)$$

These different contributions to the global spontaneous emission rate are illustrated in figure 1.13. The two formalisms are related:

$$\begin{aligned} \kappa &= \Delta\omega_m \\ g &= \frac{1}{2} \sqrt{F_P \Gamma_0} \kappa \\ \tilde{\gamma} &= \gamma \Gamma_0 \end{aligned} \quad (1.32)$$

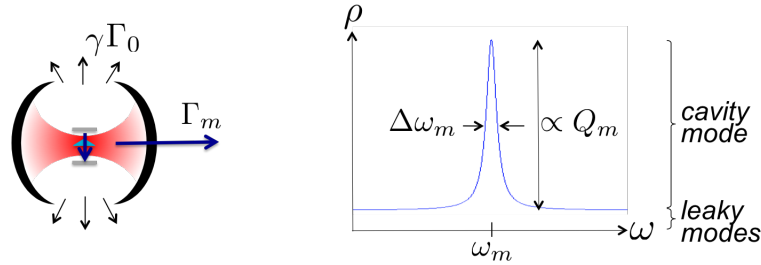


Figure 1.13: The TLS-cavity system in the Purcell regime: To the left is illustrated a TLS inside a cavity. The TLS emits a photon which can populate the cavity mode, before leaving the cavity, or which can couple into the leaky modes. The corresponding rates are indicated. To the right is shown the associated density of modes as a function of the angular frequency. The leaky modes have a constant contribution to the density of modes, the cavity mode a Lorentzian contribution. The full-width at half-maximum of the Lorentzian is equal to $\Delta\omega_m = \omega_m/Q_m$, its height is equal to Q_m divided by its integral.

For an emitter which is in resonance with a cavity mode, one quantifies the fraction of the spontaneous emission that couples into the cavity mode by the factor β .

$$\beta = \frac{F_P}{F_P + \gamma} \quad (1.33)$$

In the Purcell regime, where spontaneous emission is increased, $F_P \gg \gamma$ and $\beta \rightarrow 1$. High β can be exploited for good photon extraction properties, like done in the references [2, 54, 55, 9]. Micropillar cavities are useful for observing the Purcell effect. The figure of merit Q/V_{eff} can be high. The first successful observation of the Purcell effect in a semiconductor microcavity was achieved with a micropillar [2]. This micropillar is shown in figure 1.5c). We will consider in the following two applications of single mode emission using high F_P and high β .

Quantum Dots (QDs): Artificial atoms for solid state CQED

A possible and widely used TLS light source in CQED are solid state semiconductor QDs. Their production is described in section 2.2.5. A semiconductor QD has a low band-gap compared to the surrounding bulk material. It can be described as a few-nanometre small three-dimensional potential-well. Thus it can confine very locally electrons and holes. Due to this strong local confinement, discrete excitonic energy states exist inside the QD. The fundamental excited state, with one electron-hole pair, is called exciton (X). The following injected electron-hole pair is called bi-exciton (XX). The QD size is small and the confined carriers are close to each other. Coulomb-interactions are thus important. Therefore the different excitonic states are separated in energy. The splitting between the discrete exciton- and bi-exciton-state is about a few meV and depends strongly on the QD geometry [56].

The confinement energies of the discrete excitonic states in a QD depend strongly on the QD size and shape. Usually neighbouring and very similar QDs have not the same size and shape. This makes that an ensemble of semiconductor QDs has a broad photoluminescence spectrum, being the sum of all the contributing discrete states. The radiative recombination of an electron-hole pair leads to the emission of one photon, called photoluminescence. A spectral line-width $\Delta\omega_{\text{TLS}}$ can be attributed to each transition.

At low temperature (about 4 K) such line-width is a few tens of μeV , but usually not limited by the radiative lifetime T_1 of the transition: $\Delta\omega_{\text{TLS}} = \frac{1}{T_2^*} + \frac{1}{2T_1}$ is broadened by the dephasing time T_2^* . The broadening exists because the QD — integrated in a semiconductor matrix — couples to its environment. Phonon interactions, for example, broaden its line-width with increasing temperature, *cf.* references [57, 58, 59] and figure 1.14. Fluctuations of the environment, especially of the filling of charge traps, also broaden the line-width. That is why a QD line-width is a few tens of μeV broad if the free carriers are injected in the semiconductor surroundings (for $T \approx 4$ K). But if the QD excitation is resonant to a QD transition, *e.g.* the exciton, no charges are excited in the semiconductor surroundings. With such resonant excitation [60], and at $T \approx 4$ K, the QD line-width can be much closer to the radiative lifetime limit.

In the context of CQED experiments when the Purcell effect is of interest, one needs an emitter line-width much smaller than the line-width of the cavity mode: $\Delta\omega_{\text{TLS}} \ll \Delta\omega_m$. We will focus our studies to this case and have cavity quality factors Q_m of the order of 1000 to 10000. This requires a QD-transition with $\hbar\Delta\omega_{\text{TLS}} < 100 \mu\text{eV}$. As long as the

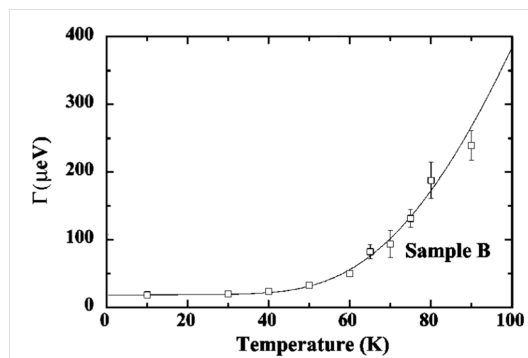


Figure 1.14: The broadening of the line-width of a QD transition — called “Sample B” — in function of the temperature is shown. This figure is taken of reference [57]. The plotted line-width Γ is equal to $\hbar\Delta\omega_{\text{TLS}}$.

temperature $T \lesssim 50$ K such CQED experiments can be feasible.

If one is interested in single photon emission, the different QD-transitions, *e.g.* of exciton and bi-exciton, have to be spectrally separated. Their line-widths have to be smaller than their splitting. The constraint on the temperature is similar as in the preceding case.

The emission of indistinguishable single photons requires lower temperatures and resonant excitation. Under resonant excitation and at the very low temperature of $T \approx 4$ K the line-widths are of only a few of μeV , as we saw. For the emission of indistinguishable single photons the influence of the dephasing, so T_2^* , has to be negligible. The Purcell effect can be used to obtain these conditions: it decreases the radiative lifetime T_1 by the Purcell factor F_P . Therefore the contribution of dephasing is reduced. In this way indistinguishable single photons were generated [61].

CQED experiments with QDs

Generally speaking, the combination of high quality factor microcavities having a small modal volume ($\propto (\lambda/n)^3$) and two-level atomic or atomic-like systems allow the realization of CQED experiments. First demonstrations were realised in the 80s with isolated Rydberg atoms [1]. Those were recently reproduced using quantum dots as “artificial atoms” inserted in semiconductor microcavities. The strong coupling regime between a QD and a discrete mode was observed [5, 6], also the spontaneous emission enhancement of an ensemble of QDs [2]. The quality factor Q is one key factor in most applications.

Other important demonstrations were the inhibition of the spontaneous emission rate of an ensemble of QDs, first realised in photonic crystal cavities [3, 4], the enhancement of the spontaneous emission rate of a single QD [62, 54, 55], and its inhibition [63].

In the following I will mention some possible applications of CQED with QDs in solid state cavities.

1.3.3 Low threshold microlasers

We consider a laser formed by an optical cavity containing a gain medium. To reach the lasers threshold, the mean photon number in the cavity should exceed one. Below the threshold, the cavity mode is essentially fed by the spontaneous emission of the gain medium. In a “macroscopic” cavity, the fraction of spontaneous emission coupled to the mode is typically $\beta \sim 10^{-5}$. In the gain medium more than 10^5 excited resonant QDs are necessary to reach the laser threshold. The threshold current, which compensates the relaxation by spontaneous emission of these QDs, as well as of all QDs which are not in resonance due to the size distribution of the QDs, must be large. For the “macroscopic” diode laser it is about 5 mA, *cf.* figure 1.15a).

In a microcavity having a small mode volume and a high Purcell factor, thus a β -factor close to unity, the laser threshold can be reached with few QDs. The reason is the very effective coupling of spontaneous emission and the cavity mode. Low threshold currents, of the order of $10 \mu\text{A}$, exciting the QDs of microlasers are sufficient to maintain the lasing. This threshold is two orders of magnitudes smaller than that of a standard diode laser. An example of such microcavity laser has a microdisk as resonator, *cf.* figure 1.15c). An other example is the VCSEL (vertical-cavity surface-emitting laser) [64]. VCSEL are physically very similar to micropillars. Planar Bragg mirrors are used to confine the light in the central laser cavity. The semiconductor resonator, often made of AlAs, is reduced in size by selective oxidation in order to locally increase the confinement of the light and to localise current injection. The emission of a VCSEL is very directional. Recently much smaller threshold currents, around 200 nA, were obtained using photonic crystal laser cavities albeit at cryogenic temperatures [26]. These four mentioned types of lasers and typical threshold currents are shown in figure 1.15.

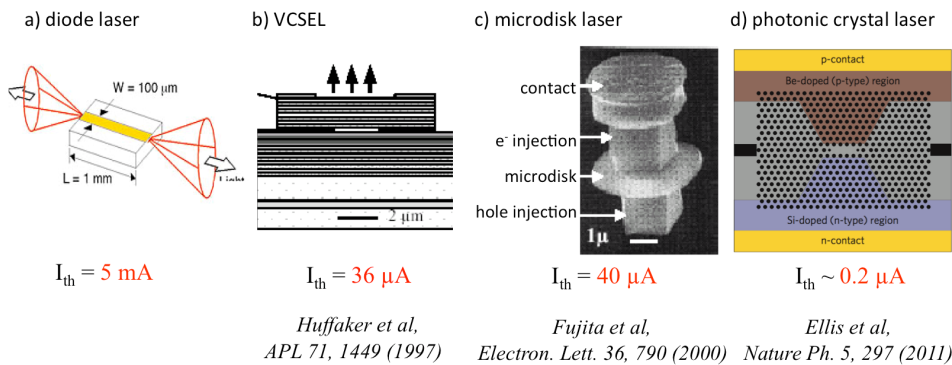


Figure 1.15: Four types of lasers and exemplary threshold currents. a) diode laser. b) VCSEL (vertical-cavity surface-emitting laser) [64]. c) microdisk laser [65]. d) photonic crystal laser [26]. The threshold currents of microlasers are much smaller than those of standard laser diodes, used for example in CD players.

1.3.4 Bright single-mode single photon sources

A single photon source has to emit one single photon after the other, and never two simultaneously. The research about single photon sources has initially been motivated by quantum cryptography, where quantum mechanical principles predict most safely communication protocols [66]. Single photon sources can be obtained by strongly attenuating a pulsed laser. The average photon number per pulse $\langle n \rangle$ follows the Poisson law. To avoid as much as possible pulses containing multiple photons, one can reduce drastically the average photon number per pulse. $\langle n \rangle \sim 10^{-2}$ seems to be ideal for quantum cryptography with attenuated laser pulses [67]. In most pulses $\langle n \rangle = 0$ and the single photon pulse cannot be deterministic.

Efficient solid-state single photon sources would be by far more useful for quantum communication and metrology applications [68]. Solid-state single photon sources were realised, for example, with a colour centre in diamond [69, 70] or with a single QD [54, 71, 61].

Single photon emission from QDs can be obtained at low temperature. An approach is to prepare the QD in a state containing only the exciton X: radiative recombination must result in the emission of a single photon. The preparation can be obtained as follows: a pulsed excitation injects a lot of excitons in the QD. As the number of excitons follows a Poisson statistic, it should always be initially greater than 1. The radiative cascade starts and several photons are emitted. The last remaining excitation in the QD must be the exciton X. This state is obtained, just after the emission from the bi-exciton XX (what can be detected in order to know the corresponding time). Adapted spectral filtering can filter all the photons emitted by the QD, except the exciton X. Following this protocol [72] the QD can be a deterministic and very efficient single photon source. Another possibility is to excite only the exciton X — separated in energy from the other QD excitons — by resonant excitation [60, 61, 73, 74]. In this way the jitter can be reduced, but the preparation is more challenging.

To be a bright single photon source the emission also has to be very directive, in order to make the collection efficient. Solid state TLS in bulk material are barely directive. Integrated in a microcavity they can couple their emission into the cavity mode, described by the factor β ; *e.g.* for $F_P = 10$: $\beta > 90\%$, so nearly signal-mode emission. In a micropillar for example, the cavity mode emission is very directive and perpendicular to the cavity surface.

State of the art single photon sources can be bright and highly efficient, with $\epsilon \approx 75\%$ the probability to find actually one photon in the right pulse [7, 9] and the multiple photon probability reduced by two orders of magnitude compared to a poissonian source. Besides microcavities in the Purcell regime, a very successful approach and one of the brightest single photon sources is realised with an InAs QD in a tapered photonic wire [7, 8].

1.4 Cavity switching

Under cavity switching one understands a fast modification of the cavity properties, especially of the cavity resonance frequency. Fast means of the order of the time-scales of the cavity properties, like its storage time τ_{cav} , or of coupled cavity–emitter systems (*e.g.* period of Rabi-oscillations, lifetime of an emitter in the Purcell regime).

The resonant condition in a cavity is $L_{cav} = N\lambda/2n_{cav}$, where N is an integer. A way to change the cavity resonance λ is to change the cavity length L_{cav} . This is possible for macroscopic cavities (albeit not in a fast way), but hardly for semiconductor microcavities where the mirror positions are fixed. For these, the only accessible parameter to change the resonance is the refractive index n_{cav} , and so the optical cavity length $L_{cav} n_{cav}$. A modification of n_{cav} by Δn modifies λ by $\Delta\lambda$:

$$\frac{\Delta\lambda}{\lambda} = \frac{\Delta n}{n_{cav}} \quad (1.34)$$

and the cavity mode resonance is shifted. The good news is that several ultrafast ways exist for changing the semiconductor material’s refractive index.

1.4.1 Changing the refractive index of semiconductors

The presence of free carriers inside a semiconductor decreases its refractive index. Free carriers can be injected electrically or optically. The free carrier injection is very efficient if the excitation is higher in energy than the bandgap of the semiconductor. Xu *et al.* showed how to inject electrically, with a p-i-n junction, free carriers in a microcavity [10]. The cavity resonance was blue-shifted within several nanoseconds. Important acceleration of the free carrier injection to below the picosecond level was achieved when injecting the free carriers optically [75, 76, 11, 14]. In such all-optical free carrier injection a femtosecond (or picosecond) pumping laser pulse is absorbed in the microcavity and generates free carriers, as illustrated in figure 1.16. The refractive index changes and the spectral positions of the cavity modes are shifted. The cavity is switched. Once injected, the free carriers will recombine. The recombination speed depends on the properties of the semiconductor, which has usually a predominant role for the non-radiative recombination processes. Depending on the quality of the material and its geometry, the related characteristic time can vary from tens of a picosecond up to nanoseconds. These recombination dynamics control the spectral return of the switched cavity resonance.

Reference [14] shows for an injected free carrier density of about 10^{19} cm^{-3} a switch of the cavity resonance from $E_{cav} = 1.278 \text{ eV}$ to 1.29 eV , so $\frac{\Delta E_{cav}}{E_{cav}} = -\frac{\Delta\lambda}{\lambda} \approx 1\%$.

An instantaneous change of the refractive index, in order to switch the cavity mode’s resonance, can be obtained with the electronic Kerr effect [12, 13]. An applied electric field (which can be applied electrically and optically) increases the refractive index proportional to its intensity. Ctistis *et al.* reported a red shift of a cavity mode by more than a half line-width, corresponding to a change in the refractive index of $+0.1\%$ [12]. Between the

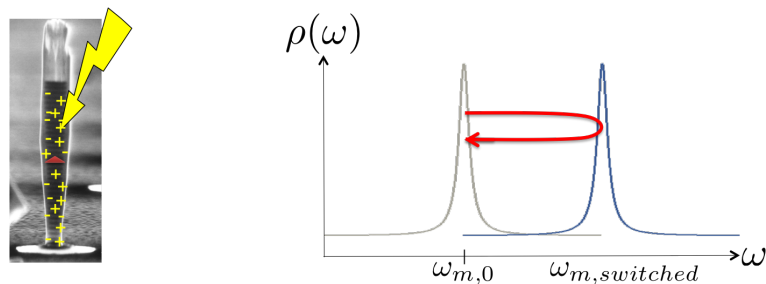


Figure 1.16: Illustration of cavity switching by all-optical free carrier injection. A laser pulse (yellow flash) injects free carriers in the GaAs layers of a micropillar, having possibly QDs in the central spacer. In terms of density of modes $\rho(\omega)$, this translates in a blue-shift of the spectral position of the cavity mode during the free carrier injection, followed by a red-shift: the spectral return to the unswitched cavity mode position $\omega_{m,0}$, governed by the free carriers recombination.

beginning of the switch and the return of the modes to their unswitched value passes less than one picosecond. Repeated and reproducible switching at THz rates can thus be achieved using the Kerr effect [77].

1.4.2 Applications of cavity switching

All-optical switches are studied for telecommunications and optical computing since the 80's [75]. Later all-optical logic gates could be achieved; Rivera *et al.* demonstrated for instance in 1993 all-optical bistability in a micropillar, enabling the development of a single bit all-optical memory [76].

In 2005 Lipson *et al.* switched the filtering properties of a silicon ring cavity [10], similar to the one shown in figure 1.11. A waveguide was coupled to this cavity. By switching the ring, it became possible to change the spectral properties and passband of such an add-drop filter on the nanosecond time-scale.

Notomi *et al.* explained in 2006 that a refractive index change in a microcavity can be used to change adiabatically its resonance and with it the colour of the light which is stored inside the cavity [78]. This adiabatic colour change was realised later by switching a ring cavity [11] or a photonic crystal cavity [15].

Further, one could imagine coupling in a controlled way emitters to cavity modes, thus the Purcell effect. The cavity mode can be brought in resonance with an emitter transition by electromechanical tuning of the cavity resonance [79]. This is a more or less static process. To tailor CQED effects in real time, the coupling between QD and cavity has to be controlled on time-scales shorter than the QD lifetime (sub nanosecond), resulting in a time-dependent spontaneous emission rate [80]. Such control has been realised by

all-optically switching a Fabry-Pérot cavity coupled to a target photonics crystal cavity containing one QD [81] or by tuning the transition of a QD in a photonic crystal cavity using the Stark effect [82]. In a very similar system, even the shape of the emitted photon pulse could be shaped, as theoretically proposed by [80, 83]. This equals the full control of the emission process over its entire duration. In chapter 4 I will propose a procedure to obtain single photon pulses shaped with a high fidelity using cavity switching.

By switching cavities which have more than one resonant cavity mode, as it is the case in most micropillar cavities, the different modes can be switched in a differential way [84]. For example the fundamental cavity mode can be switched more than the following cavity modes of higher order. We obtained recently new results about differential switching of micropillar cavities, see chapter 3.4.

Cavity switching of a micropillar containing an ensemble of QDs enabled us to study the time-resolved properties of the switched modes. The luminescence of the ensemble of QDs was used to probe the spectral positions of the cavity modes. Applying spectral filtering, we were able to generate ultrashort emission bursts, which represent an ultrafast low-coherence source for speckle-free imaging, described in chapter 5.

1.5 Conclusion

In this chapter we introduced microcavities and their physical properties. Especially micropillars will be used for the following theoretical and experimental studies. Micropillar cavities have the advantage of a very directive emission diagram perpendicular to the sample's surface, in contrary to photonic crystal cavities and microdisk cavities. Those three types of microcavities have all a small effective mode volume, very important for spontaneous emission enhancement when solid-state emitter like QDs are integrated.

We saw that in the context of cavity quantum electrodynamics semiconductor microcavities can be used for spectral filtering or for the enhancement of the spontaneous emission if emitters are integrated. Low threshold microlasers and bright single photon sources can be obtained.

We discussed cavity switching, which can be an ultrafast spectral shift of the cavity resonance due to all-optically injected free carriers. Switching of micropillar cavities is the necessary tool for the theoretical and experimental studies of this thesis.

In the following chapter I will explain how to produce and characterise planar cavities and micropillars and explain the necessary tools for the following experimental and theoretical studies.

In this chapter, I discuss the design and fabrication of planar cavities and micropillar cavities. Planar cavities are grown by Molecular Beam Epitaxy (MBE). I will present the clean room processing (including lithographic and etching steps) which are employed to define micropillar cavities. Finally, I will present the optical characterization of those microcavities and present the numerical methods used to simulate the cavity properties and to predict possible cavity switching experiments.

2.1 Conception of a planar microcavity

Each planar cavity (introduced in section 1.2.2) is characterised by its functionality, central resonant wavelength and quality factor. Here, I will consider as an example the design of a narrowband cavity filter with transmission band around $E = 1.3$ eV or $\lambda_B \approx 954$ nm. Such a cavity is well suited for instance for the cavity switching studies in the following chapters. For most of our studies, cavities Bragg-mirrors are composed of alternating GaAs and AlAs $\lambda_B/4n_i$ -layers, the spacer and the substrate of GaAs.

In order to get sharp filtering properties, we need a high Q and balanced top and bottom mirror reflectivities ($R_{top} \approx R_{bottom}$). For example, a top mirror with 16 pairs of Bragg-layers leads to a reflectivity $R_{top} = 0.9963$ for $E = 1.3$ eV at room temperature. In the same conditions the bottom mirror has a smaller reflectivity because of the other surrounding material, *cf.* the formula for reflectivity in section 1.2.1. Several $\lambda_B/4n_i$ -layers are added to the bottom mirror to adjust its reflectivity to R_{top} . The closest reflectivity is $R_{bottom} = 0.9969$ for a bottom mirror having 20 pairs of layers. The most basic filtering cavity has a spacer thick of λ_B/n_{cav} in between the DBRs.

The resulting cavity has a reflectance spectrum with a well defined stopband and a

central resonant mode at $E = 1.3$ eV, where $R|_{min} = 0.007$, *cf.* figure 2.1. The maximum value of reflectance is $R|_{max} = 99.998\%$. Apart from $E = 1.3$ eV, the cavity reflects very efficiently the light over a $\Delta E = 153$ meV wide stopband (equal to $\Delta\lambda = 111$ nm around $\lambda_B = 945$ nm). This theoretical width of the stopband, calculated with the formula of section 1.2.1, confirms the width in the simulated spectrum of figure 2.1. The cavity's quality factor is $Q = 7650$, predicted by the simulation of figure 2.1. Section 2.5.1 treats the mathematical description of the transfer matrix method (TMM), used to simulate the reflectance spectra of planar cavities.

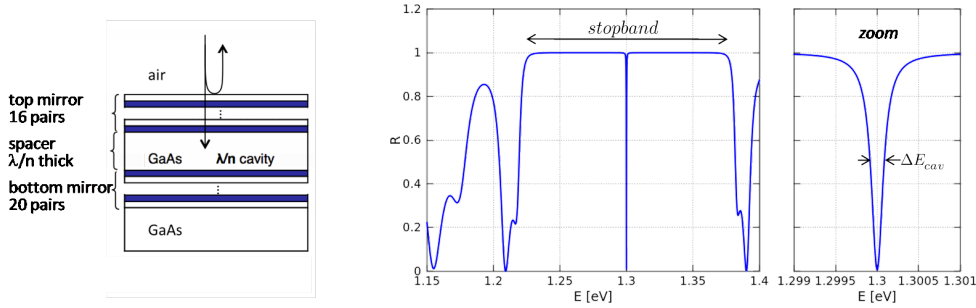


Figure 2.1: A filtering planar microcavity defined for $E = 1.3$ eV, so $\lambda_B \approx 954$ nm, composed of two DBR and a spacer, placed on GaAs substrate. The reflectivity spectrum is shown for light impinging from the top, showing the filtering property for the resonant light. A zoom in the central cavity mode is given, too. GaAs is shown in white, AlAs in blue.

2.2 Molecular beam epitaxy

A very precise way to produce semiconducting structures is the molecular beam epitaxy (MBE). One molecular layer after the other is deposited on a substrate. It is an ideal tool to precisely build complex bi-dimensional structures layer by layer, like a planar microcavity, and to integrate solid state emitters like quantum wells or self-assembled InAs QDs.

I will introduce the principles of the MBE growth and discuss the structures I fabricated, particularly two-dimensional layers and self-assembled InAs QD structures.

2.2.1 The principle of MBE growth

A MBE consists of an ultra-high vacuum chamber with accorded material cells and an introduction chamber. The introduction chamber is necessary to keep an ultra-high vacuum in the growth chamber when introducing a sample. The growth chamber can be cooled down with liquid nitrogen to disable every evaporation from its internal surfaces.

The residual vacuum can be as high as 10^{-10} mbar and is maintained by complementary pumping tools (turbo-molecular pump and titanium sublimator). The material cells, containing each one piece of an ultra-pure element, are heated up to a critical temperature in order to evaporate these elements with a desired flux. They can be opened separately, so that a molecular or atomic flux enters the growth chamber and hits the wafer. This is schematised in figure 2.2.

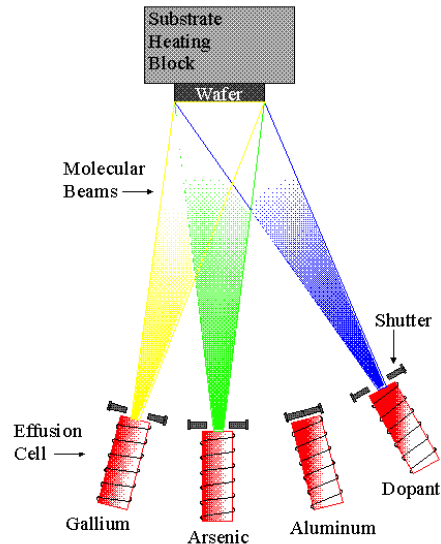


Figure 2.2: Working principle of a MBE-chamber. Heated effusion cells, controlled by shutters, evaporate material. The outgoing material fluxes deposit on the sample surface. Its temperature is controlled to obtain the right atomic mobilities. This figure is taken from [85].

The used MBE is made for III-As material growth. The available materials of the group III are in our case gallium, aluminum and indium. Gallium and aluminum are used to grow GaAs, AlAs or $\text{Al}_x\text{Ga}_{1-x}\text{As}$ 2D layers. Indium is used to grow InAs islands, the future QDs, or InGaAs 2D layers, future quantum wells. For the growth a permanent As flux is needed and provided by a large capacity cell under the form of As_4 molecules.

The sample, in my case it is an undoped crystalline GaAs wafer with orientation (100), is placed on a heating substrate holder in front of the effusion cells. Its temperature can be controlled up to 700°C to allow ideal growth conditions. Different regimes of growth exist:

- The Franck-Van Der Merwe regime describing layer by layer growth, also called 2D or bi-dimensional growth.
- The Volmer-Weber regime describing three-dimensional island growth.
- The Stranski-Krastanov regime, describing a growth being first bi-dimensional, than islands nucleate.

The current regime of growth is determined by the lattice mismatch to the underlying GaAs substrate. The lattice constants of AlAs and GaAs are 5.66 Å and 5.65 Å, respectively. The lattice mismatch is small, $< 0.2\%$, and both GaAs and AlAs growth on GaAs substrate follow the Franck-Van Der Merwe regime. The lattice constant of InAs is 6.06 Å. The mismatch to GaAs is of the order of 7%. InAs growth on GaAs happens in the Stranski-Krastanov regime, resulting in self-assembled InAs islands forming on the top of a one monolayer thick “wetting layer” which covers the GaAs substrate [86, 87, 88, 89].

2.2.2 Sample preparation and growth conditions

Commercial GaAs needs no chemical treatment before the growth. Only the native oxide on the surface has to be removed. This can be done in the MBE chamber by heating the sample up to $T_{ox} = 590^\circ C$, the temperature at which the oxide desorbs. As we will see, this desorption event is used to calibrate the sample temperature measurements.

Before rising the sample temperature to T_{sub} , the introduced sample has to be heated up to about $400^\circ C$, the temperature at which the wafer’s arsenic starts evaporating. Until to this moment, all material cells are closed. At $T_{sub} = 400^\circ C$ the sample is placed in its growth position, as perpendicular as possible in front of the effusion cells. The arsenic cell is opened, and kept open at all times, necessary to supply As for the growth and to compensate eventual evaporation from the sample surface. Under this arsenic flux the deoxidation is observed at $T_{sub} = 590^\circ C$. The sample is rotated permanently to avoid a gradient in its surface temperature and later to homogenise the growth rate. The sample is heated up to $T_{sub} = 610^\circ C$ for ten minutes to evaporate all eventual residuals. Then growth starts at $T_{sub} = 600^\circ C$ with a 500 nm GaAs buffer, to prepare an as perfect GaAs surface as possible for the following growth of the desired structures.

Both gallium and aluminum are trapped on the sample surface. Their desorption is negligible in the temperature range of interest for us. Under As-rich conditions the stoichiometry condition is fulfilled by desorption of excess arsenic for pure GaAs or AlAs growth. When the Ga-cell is opened, crystalline GaAs will be grown, when the Al-cell is opened, crystalline AlAs will be grown. When the Ga and Al-cells are open simultaneously, the two fluxes have to be controlled to have the right composition for the desired crystalline $Al_xGa_{1-x}As$.

The most important parameters for MBE growth are the precise growth rates and the real substrate temperature. Both can be determined with the help of the in situ RHEED diffraction analysis.

2.2.3 The RHEED

The most widely used method for growth monitoring is called RHEED: reflection high-energy electron diffraction. It is a way to probe the sample surface in situ. A RHEED-gun sends a high-energy electron beam (about 25 keV) under grazing incidence on the wafer. The advantage of the use of electrons is that electrons penetrate only a few atomic layers into the material, in contrast to x-rays, and so only the atomic layers close to the surface contribute to the diffraction. The incident electron beam diffracts on the sample. The diffraction pattern is constructed by the intersection between the Ewald sphere and the reciprocal lattice (see figure 2.3). The latter is, for a perfect flat sample surface, a series of vertical lines perpendicular to the sample's surface. The resulting intersections are dots, corresponding to the directions of diffraction. Nevertheless lines are observed on the RHEED screen probing a mostly flat surface. There are two explanations: First, the radius of the Ewald sphere is directly proportional to the incident electron energy. Energy fluctuations lead to an Ewald sphere having a certain thickness. Second, the sample surface is never perfectly flat, which broadens the reciprocal rods.

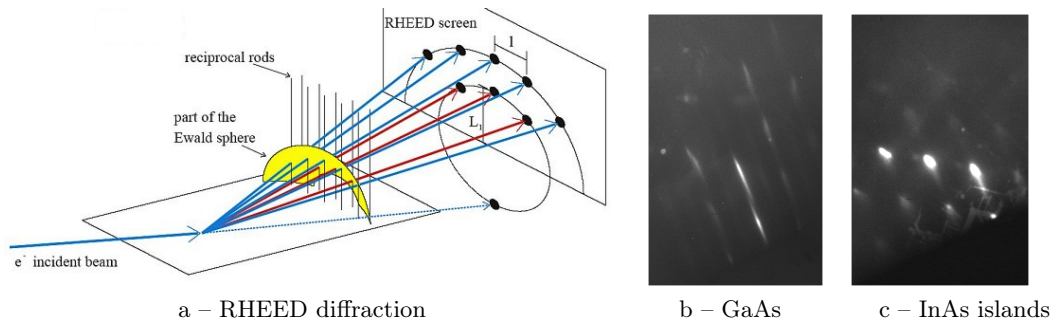


Figure 2.3: (a) Construction of the RHEED's diffraction pattern for an ideal flat surface. The incident electron beam diffracts on the sample. The diffraction pattern on the RHEED screen is constructed by the intersection between the Ewald sphere and the reciprocal lattice (here: rods). This figure is taken from [90]. (b+c) Observed diffraction pattern for a flat GaAs surface and for InAs islands on GaAs.

The RHEED diffraction pattern of an oxidised wafer is blurred and not intense. When the wafer reaches $T_{ox} = 590^{\circ}C$ its surface is deoxidised and the RHEED diffraction pattern becomes spotty and intense. At this moment the displayed wafer temperature, which has often a large offset, can be calibrated to the real wafer temperature of $590^{\circ}C$. Knowing the real temperature of the wafer is very important for controlled growth conditions and resulting high quality samples.

After the deposition of a buffer to flatten the GaAs surface, RHEED oscillations can be used to determine growth rates. Often those are observed with a test sample, before introducing in the MBE chamber the real wafer on which the sample structure will be grown. During 2D-growth, molecular layer after molecular layer is deposited. One can follow the growth with the RHEED by observing by diffraction the number of deposited

layers. The growth rate can be deduced from the RHEED pattern by following the intensity of the directly reflected specular spot. When this spot is not clearly visible, the intensity of a diffraction spot can be observed, too. If the sample surface is entirely flat, the intensity of the specular spot is maximal. If the last molecular layer is just half filled and the surface rough, its intensity is minimal. The diffraction pattern illustrates this behaviour in intensity oscillations, *cf.* figure 2.4a. The intensity of each spot oscillates during the growth, with the period equal to the time of the deposition of one III-V molecular layer. These are the so-called RHEED-oscillations [91].

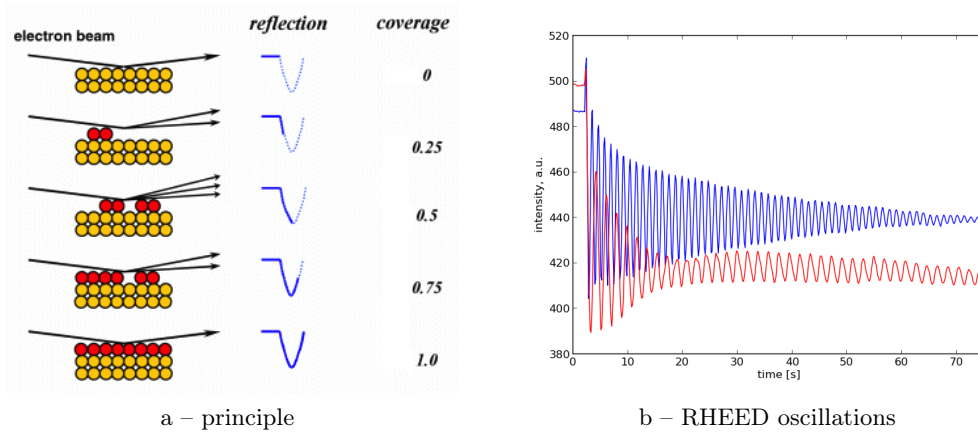


Figure 2.4: RHEED-oscillations. (a) The RHEED-pattern's intensity oscillates with the molecular coverage of the surface. One oscillation corresponds to the deposition of one molecular layer. This figure is taken of [92]. (b) RHEED-oscillation of the deposition of GaAs (blue) and AlAs (red) as a function of time. In this experiment the growth rates of GaAs and AlAs are found to be around $1 \mu\text{m}$ and $0.5 \mu\text{m}$ per hour, respectively.

Knowing the cubic lattice constants of AlAs and GaAs, 5.66 \AA and 5.65 \AA respectively, one knows the height of two molecular layers of the cfc crystalline structure. With the period of the RHEED-oscillations one deduces the growth rate to be a few $\text{\AA}/\text{s}$. Example RHEED-oscillations measured for AlAs and GaAs are shown in figure 2.4b. A very large number of oscillations is observed, enabling a precise estimate of the growth rate, here $1 \mu\text{m}$ per hour for GaAs and $0.5 \mu\text{m}$ per hour for AlAs.

2.2.4 Growth of planar cavities

For the growth of high quality planar cavities the growth rates have to be very precisely known, so that the deposited Bragg layers correspond exactly to $\lambda_B/4n_i$ and the thickness of the cavity spacer to λ_B/n_c . For planar cavities made of GaAs and AlAs, n_i is the refractive index of GaAs or AlAs, respectively. n_c is the refractive index of the spacer, in our case always made of GaAs. To prevent foreseeable deviations of the aimed growth rates, we grow planar cavities on large GaAs wafers. Slight inhomogeneities in the flux depending

on the sample position always exist and vary from effusion cell to effusion cell. Thanks to them always a region of the grown sample should have the desired cavity properties.

I will show as an example the very successful realization of a planar microcavity with moderate quality factor made of GaAs and AlAs. The cavity was desired to be resonant to 1.2 eV, so $\lambda_B = 1033\text{nm}$. After preparation of the substrate a 500 nm thick GaAs buffer was deposited on the GaAs wafer. This was followed by the growth of 14 alternating GaAs and AlAs $\lambda_B/4n_i$ -thick Bragg layers, each respectively 74.0 nm and 87.8 nm thick. Then a $\lambda_B/n_{\text{GaAs}}$ -thick GaAs spacer was grown, followed by 10 alternating AlAs and GaAs $\lambda_B/4n_i$ -thick Bragg layers. The entire cavity structure is 4.2 μm high and its growth with growth rates for GaAs and AlAs of 1 μm and 0.5 μm per hour, respectively, takes more than 6 hours.

The theoretical reflectance spectrum is simulated with the transfer matrix method (TMM) and shown in figure 2.5a. Top and bottom mirror are equilibrated, $R|_{\min} = 0.003$ and $Q = 715$. The spectrum of the actual cavity is acquired by Fourier Transform Infra-Red (FTIR) spectroscopy and shown in figure 2.5b. At a first glance simulated and acquired spectra are very similar. The reflectances have the same envelope. The real cavity has a flat stopband, the cavity mode is centered, $R|_{\min} = 0.12$, $Q = 685$ and $E_{\text{cav}} = 1.23$ eV. $R|_{\min}$ is most probably limited by the FTIR resolution. The only real difference is that the entire acquired spectrum is slightly shifted to higher energies. We can conclude that overall less material was deposited as planned (in the same way for AlAs as for GaAs) as all other cavity properties are very well reproduced.

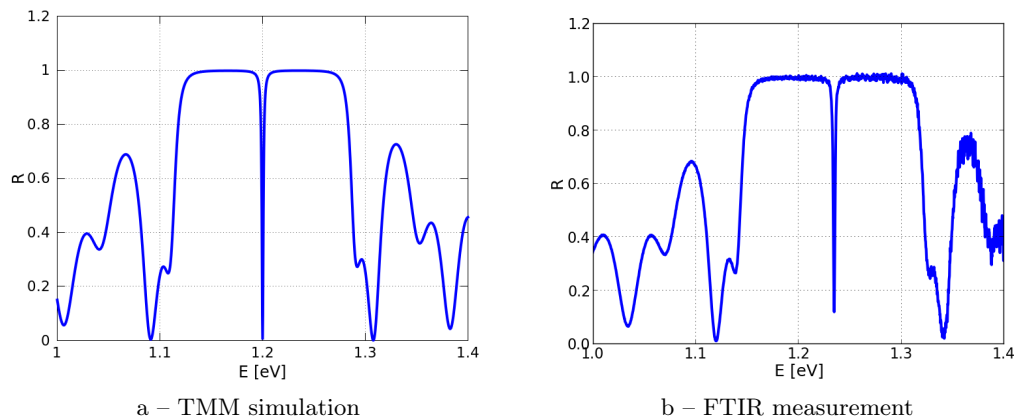


Figure 2.5: Result of the growth of a planar cavity. The simulated and the acquired spectra are shown. Both are very similar, the cavity growth was very successful.

2.2.5 Growth of InAs quantum dots

In section 1.3.2 self-assembled InAs QDs were introduced as emitters in the centre of a GaAs/AlAs cavity. Those self-assembled semiconductor QDs are formed by InAs is-

lands of nano-metric size surrounded by GaAs [86, 87, 88, 89] (see figure 2.6a), confining electron-hole pairs in all three directions of space. These pairs form excitonic states. Their energies depend on the factor of occupation and are discrete, like the atomic energy levels. Luminescence can be observed after excitation and at cryogenic temperature. Cryogenic temperature is used to well confine the excitons inside the QDs.

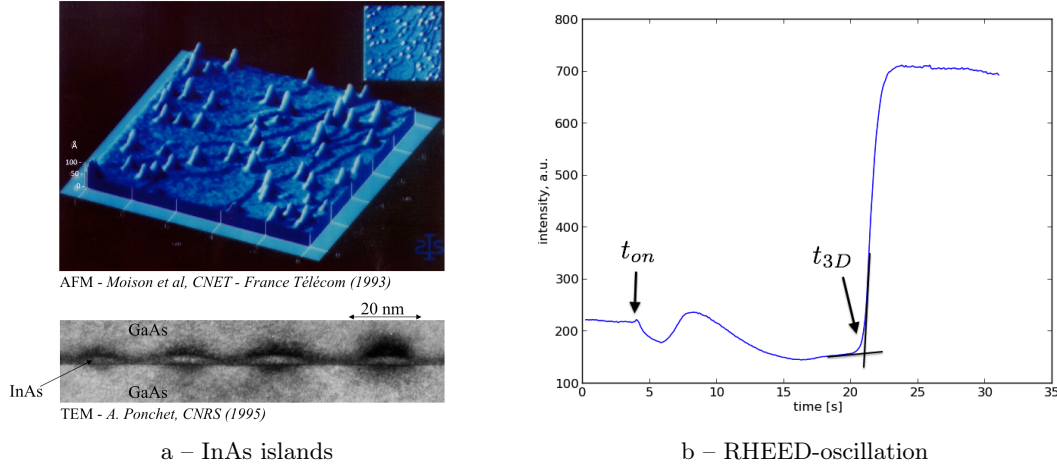


Figure 2.6: InAs growth. (a) The first image shows InAs islands on GaAs [87], acquired by atomic force microscopy (AFM). The inset is the top view of same image. The second image shows a side-view of InAs-QDs in GaAs [93], acquired by transmission electron microscopy (TEM). (b) RHEED-oscillation during the formation of InAs-islands on GaAs. The signal's intensity, corresponding to the island formation, is shown as a function of time. When the oscillation starts, InAs deposition starts (t_{on}), and when the signal reaches its maximum, the island formation is completed.

To place the QDs into the cavity's spacer, at half time of the growth of the cavity's central GaAs spacer the growth is interrupted and the InAs islands are grown. Once grown, they are capped by GaAs.

For InAs deposition on GaAs the temperature of the sample has to be decreased below 540°C . Otherwise the deposited InAs would evaporate. I reduced the sample temperature right before the InAs deposition to $T_{sub} = 530^\circ\text{C}$ and inversed it immediately afterwards back to $T_{sub} = 600^\circ\text{C}$, the usual growth temperature. The GaAs surrounding the InAs, which is grown in between $530^\circ\text{C} < T_{sub} < 600^\circ\text{C}$ might have slightly decreased crystalline quality.

The lattice constant of InAs is 6.06 \AA . The huge difference compared to the GaAs lattice constant induce a large strain in a 2D InAs layer, so that InAs growth on GaAs follows the Stranski-Krastanov regime [94, 95]. For small amounts of deposited InAs the growth is bi-dimensional. If 1.7 molecular layers of InAs, or more, are deposited on GaAs, the formation of InAs islands becomes energetically favourable. If the growth is stopped before the 1.7 molecular layers of InAs are deposited the result will be a quantum well (QW) [96].

The transition QW–QD is shown in figure 2.7.

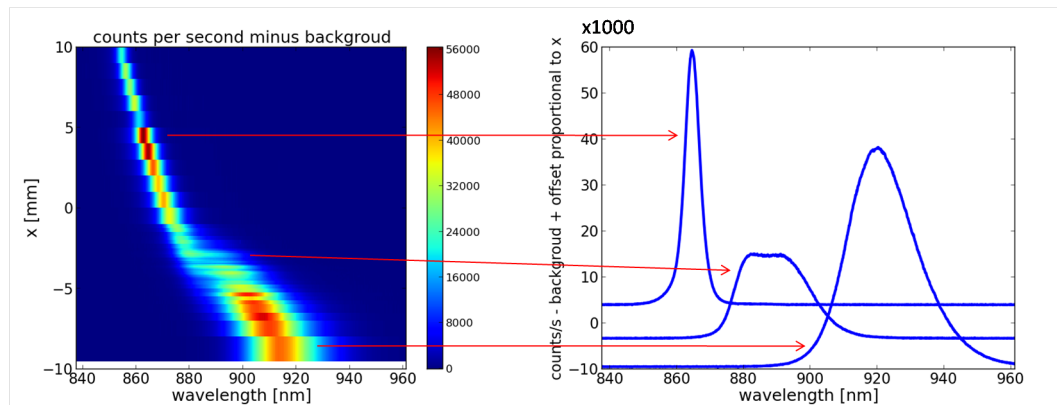


Figure 2.7: Study of a QD sample, for which a lateral gradient of the quantity of InAs has been introduced on purpose. The thickness of the InAs layers varies here approximatively from 1.2 to 2 molecular layers across on the wafer. Shown are photo-luminescence (PL) spectra of InAs QDs and QWs, obtained with the sample at 4 K. The left image shows the PL spectra (colour intensity) as a function of the wavelength (x-axis) and the spatial probed position indicated “x” (y-axis). The right image shows three exemplary spectra of the left image. The total scanned length is ± 10 mm, from the sample centre on. Three regimes can be identified. For $x > -1$ mm we detect a spectrally narrow InAs QW, for $x < -5$ mm we detect a spectrally broad ensemble of InAs QDs, and in between is a mixed regime of transition, where both QW and QD PL are present [89]. The more InAs was deposited, the higher the wavelength of the photo-luminescence. When less than 1.7 molecular layers are deposited, the InAs growth is still bi-dimensional and QW-like emission is observed. At the critical quantity of 1.7 molecular layers the island formation appears, corresponding to the transition regime from QW to QDs in the PL signal. If more than 1.7 molecular layers of InAs are deposited, a high density ensemble of QDs is formed on top of a one molecular layer thick wetting layer. The PL signal shows only the QDs and not the surrounding 2D InAs wetting layer, as the confinement potential of the QDs is deeper than the confinement potential of the surrounding QW.

The island formation can be observed by RHEED, my measurements are shown in figure 2.6b, following the intensity of one spot of the InAs diffraction pattern (*cf.* figure 2.3c). Around 0.4 s the indium deposition starts (t_{on}), this means the In-cell is opened. When the signal reaches a maximum, the islands are formed. t_{3D} corresponds to the time, when 1.7 monolayers of InAs are deposited and islands appear. For further InAs deposition the shape of the sample’s surface does not change any more, the islands just increase in size. The RHEED diffraction pattern does not change anymore in time. This time needed to reach the onset of the island-formation, here around 18.5 s, is used to calibrate InAs growth rate and the QD growing parameters. Here the growth is quite slow to have a very illustrative RHEED oscillation. Usually we want QDs where 1.8 InAs molecular layers are deposited in one second. A fast deposition gives less time for diffusion of the InAs and the islands will be smaller. Thus the QDs exhibit larger bandgap energies, around 1.3 to

1.37 eV at low temperatures (4 K) [18, 97] (*cf.* figure 2.8a).

Once the islands reach the desired size, the In-cell is closed and a GaAs cap is deposited on top of the islands. Due to the growth of this layer, the small band-gap InAs islands are surrounded by larger band-gap GaAs, thus forming QDs. The temperature of the sample is increased to the standard growth temperature for GaAs and the growth of the GaAs spacer goes on without growth interruption. If there was a growth interruption after the InAs deposition, the PL of the future QDs would red-shift. During the growth interruption, indium adatoms can diffuse and increase the island sizes [89] (see figure 2.8b).

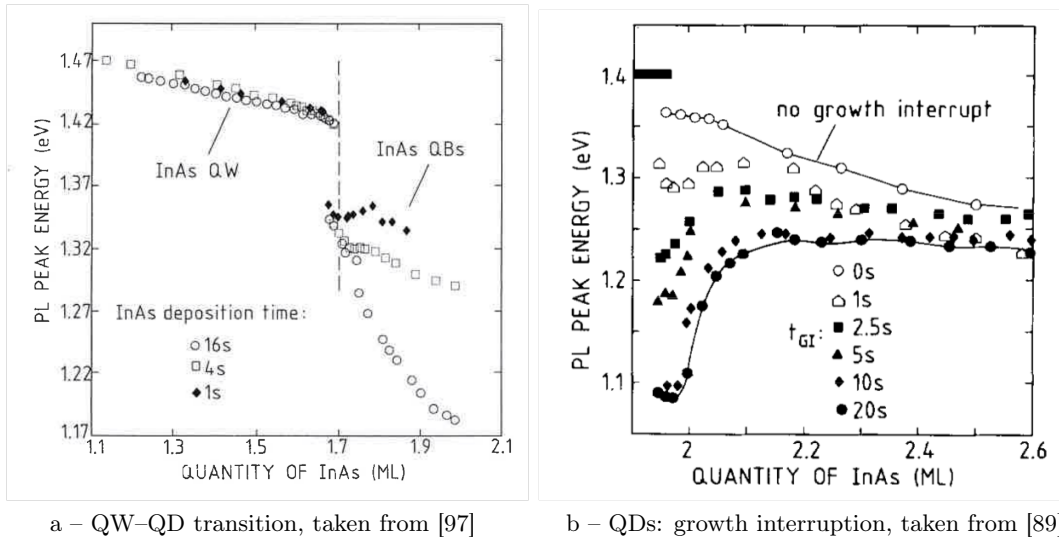


Figure 2.8: Those two figures, taken from literature, show how the size of the deposited InAs islands (and so the PL peak energy of the QDs) depends on the deposition rate of the InAs [97] and on a eventual growth interruption before encapsulating the InAs islands with GaAs [89]. In (b) the InAs deposition time is one second.

2.3 Top-down fabrication of a pillar microcavity

Starting from a planar cavity, micropillars have been fabricated by using electron-beam lithography and reactive ion etching (RIE) with a Si_3N_4 hard mask. The processing steps are detailed on the following.

To produce the mask about 900 nm of Si_3N_4 are deposited by PECVD (plasma enhanced chemical vapour deposition) on the planar cavity. Next, about 400 nm of resist are deposited by spin coating. The resist is developed by electron-beam lithography, leading to holes in the resist at the locations of the future micropillars. Directive aluminum deposition (about 100 nm) fills the remaining holes, and covers the resist. The resist is lifted off with acetone. An aluminum mask in form of disks now covers the Si_3N_4 (figure 2.9). Reactive ionic etching of Si_3N_4 using SF_6 etches the mask down to the planar cavity. Next,

reactive ionic etching with Ar and SiCl_4 defines the micropillars and allows straight etching and smooth surfaces on long distances compared to the mask size. Finally, the Si_3N_4 is removed with reactive ion etching, using SF_6 gas chemistry. These processes are illustrated in figure 2.10.

Julien CLAUDON and Adrien DELGA, both members of the team, did this work.

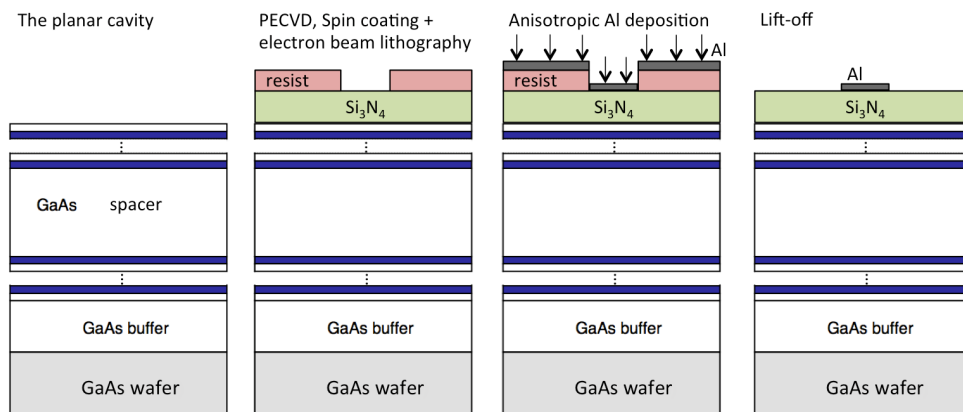


Figure 2.9: Definition of a hard mask to etch a micropillar from a planar microcavity. GaAs is shown in white, AlAs in blue, forming the cavity.

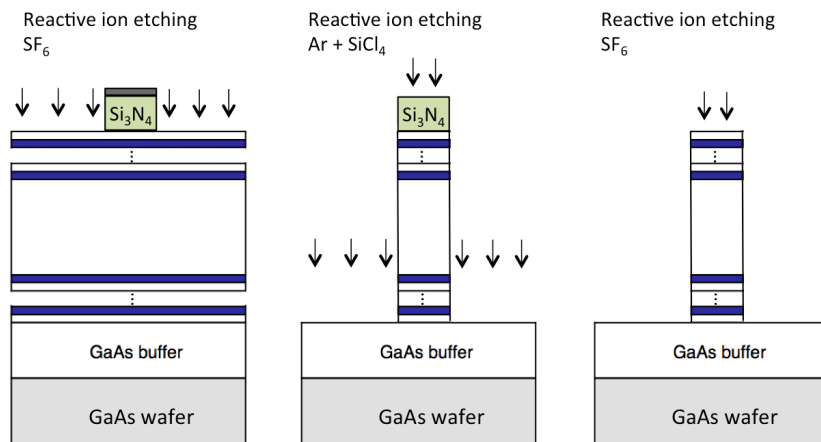


Figure 2.10: Etching the micropillars. The Al top mask is totally etched during the etching of the micropillar. GaAs is shown in white, AlAs in blue, forming the cavity.

2.4 Optical characterisation

In order to analyse and evaluate the quality of as-grown samples and to conduct experiments, like cavity switching, I will use optics. In this section I will introduce the optical techniques I used.

2.4.1 The FTIR

The Fourier Transform Infra-Red (FTIR) spectroscopy is a very efficient technique to measure reflectance or transmittance spectra. Its main characteristics are a very high signal to noise ratio (SNR), which allows short acquisition times (typically a few second for planar cavities), and an automatic, built-in spectroscopic calibration property. The FTIR principle of operation is to use a spectrally broad light source, the light of which is sent through a Michelson interferometer where this light is modulated at a frequency that is proportional to the photon energy¹. Figure 2.11 shows the setup.

So the signal measured by a single-element detector after transmission through or reflection from a sample depends on time, in a way that makes it the Fourier transform of the transmitted or reflected spectrum. Recording this time-dependent signal and computing its inverse Fourier transform gives access to the spectrum itself.

The FTIR spectroscopy has two advantages over dispersive spectroscopy that uses gratings. The first one is the so-called “multiplex” one, also called Fellgett’s advantage, since all of the light is measured at all times, at contrast with the dispersive spectroscopy using a single-element detector, where only a very narrow photon energy range, selected by the exit slit, is measured at a time. This “multiplex” advantage is shared with dispersive spectroscopy using multiple-element detectors, such as CCD cameras, but a second advantage, known as the “throughput” one, or Jacquinot’s advantage, comes from the fact that one does not need to let the light go through an entrance slit in order to ensure spectral resolution², as it is for dispersive spectroscopy (with single- as well as multiple-element detectors).

These very good noise characteristics can be seen in the FTIR measurement shown in figure 2.5b. The FTIR enables to measure rapidly reflectance spectra and thus to evaluate the used growth parameters. Analysing planar cavities, their quality factor can be deduced,

¹To set things: if the interferometer mobile mirror is driven at a speed v , the light at energy $E = h\nu = hc/\lambda$ will be modulated at a frequency $f = \frac{2v}{hc} \cdot E$; this modulation frequency lies around 10^4 Hz in our photon energy range of interest, since v is of the order of $1 \text{ cm}\cdot\text{s}^{-1}$. In practice, the light beam from a high-coherence length laser (usually a stabilised He-Ne laser) at an energy E_0 is fed into the same Michelson arrangement, therefore modulated at a frequency $f_0 = \frac{2v}{hc} \cdot E_0$. Located in a corner of the Michelson, this laser interference is independently measured and serves as a calibrated reference through the proportionality relation $E_0 f = f_0 E$.

²For Fourier transform spectroscopy, the spectral resolution ΔE depends only on the maximum path difference ΔL between the two arms of the Michelson interferometer through the relation $\Delta E = hc/\Delta L$. We have $\Delta L \approx 1 \text{ cm}$ in our instrument, which leads to $\Delta E \approx 0.1 \text{ meV}$ or $\Delta \lambda \approx 0.1 \text{ nm}$, but high-resolution FTIR spectrometers could present path differences of the order of a few metre.

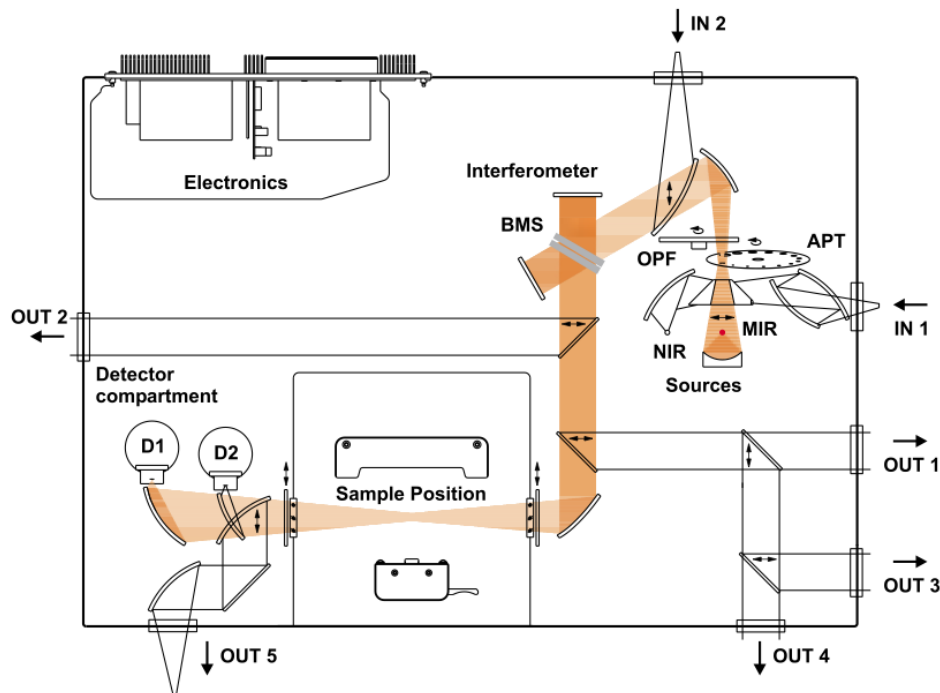


Figure 2.11: Beam-path of the used FTIR. This figure is taken of [98]. The white light source is brought on a beam-splitter (BMS), passes the Michelson interferometer with the oscillating mirror and enters in the sample chamber. There the signal is reflected on the sample with an impinging angle of 13° and is detected in the detector compartment.

if not limited by the FTIR resolution (here $\Delta E \approx 0.1$ meV). The figure 2.5b shows such a spectrum.

2.4.2 Micro-photoluminescence

The micro-photoluminescence (μ PL) is a method to detect luminescence signal with a spatial resolution of the order of one micrometre. It is used to study isolated nano- and micro-objects. I will use it to study micropillars.

The excitation of a small object and the collection of the emitted photoluminescence signal is realised through a microscope objective. A white light source and a CCD camera for visualization are necessary to superpose exciting laser beam and sample structure and to properly focus the laser. This requires a micro-metric control of the sample position in the three directions of space. Often the measurements are conducted at cryogenic temperatures. So the sample has to be in a cryostat; in our case a cold-finger cryostat. The detection of the light signal is done by a monochromator, resolving the signal spectrally, plus a CCD camera. Optionally a streak camera or avalanche photon diodes (APDs)

can figure as detector. I built a new μ PL setup adapted for the switching experiments, schematised in figure 2.12.

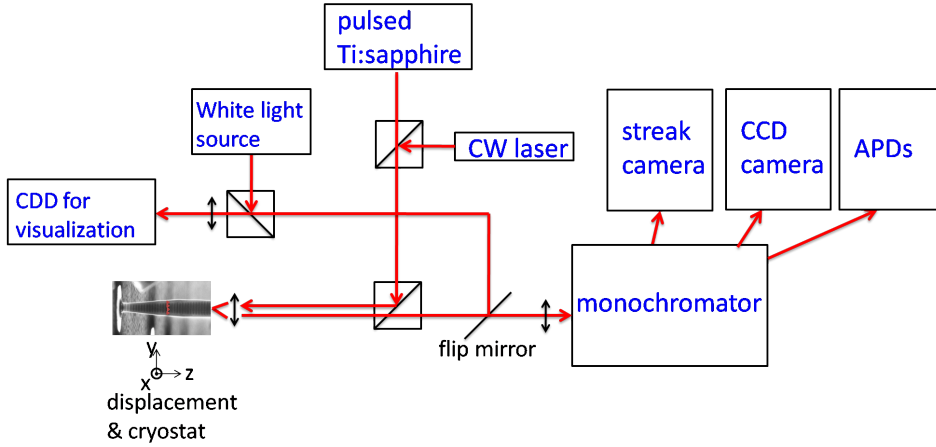


Figure 2.12: The micro-photoluminescence setup. A micropillar illustrates the sample in the cryostat.

2.4.3 Time resolved spectral analysis with a streak camera

A powerful instrument to measure an ultrafast signal resolved in the time domain and in the energy domain in one acquisition is the so-called streak camera. The time resolution Δt has its limit at 0.9 ps. This analysis is used to study the temporal response of a sample to an ultra short laser pulse.

A “femtosecond” laser, in our case a Coherent MIRA 900-F, Ti:sapphire laser, delivers an approximately 200 fs long light pulse³ that is focused on the sample. It can, for example, excite quantum dots or atoms, or be coupled into resonances of a semiconductor microcavity. From there, the light is sent into the monochromator and dispersed — depending on its wavelength or photon energy — along the horizontal axis at the output, and then fed to a photocathode to transform the photons into electrons. These electrons travel from this photocathode into a vacuum tube. They cross a space zone where they are deviated by a vertical oscillating electric field that is synchronised with the laser pulse rate. Finally, these electrons impinge a phosphor screen⁴ where they create a light spot. The proper phase synchronization of the oscillating field with the laser pulse signal ensures that this light spot is vertically located at a position that depends only on the time delay between the laser pulse and the arrival of the photon on the photocathode. The horizontal position of the spot is given by the photon energy. If that delay is the same for each period, the signal piles up at the same position where it is integrated by a CCD camera that records the

³This laser delivers light pulses thanks to the mode-locking of the many longitudinal modes that are amplified within a 3.9 m long cavity, with an approximately 10 meV wide energy band.

⁴After going through a micro-channel plate amplifier that multiplies the electrons number, in order to get a measurable signal from each original photon.

phosphor screen image. Such a streak camera and its setup are illustrated in figure 2.13. An exemplary acquisition is shown in figure 2.14.

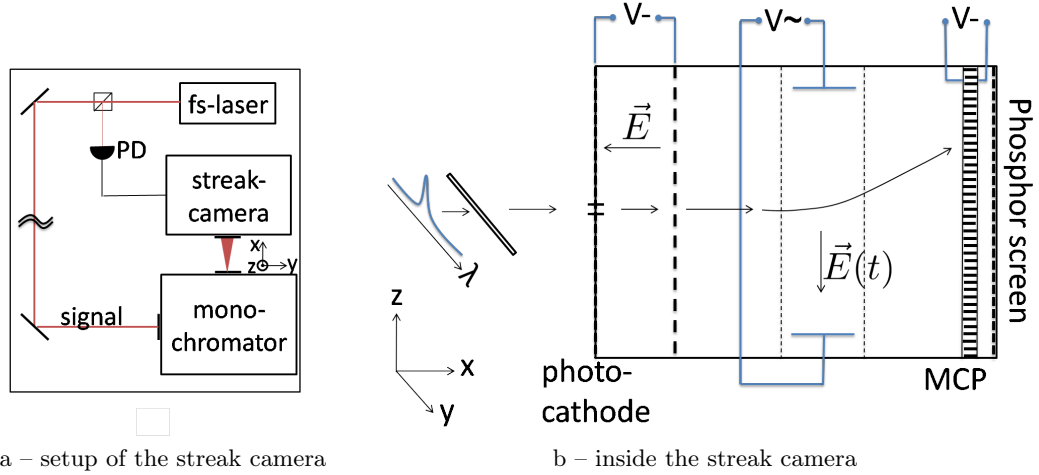


Figure 2.13: Setup of a streak camera. (a) The laser source generates fs-laser pulses. A beam-splitter takes a very small part of the pulses light; it is detected by a photodiode (PD) to synchronise the detection in the streak camera with the laser’s repetition rate. The big part of the signal will follow the beam-path of detection. It may, for example, excite or transmit through a sample. The resulting light signal is spectrally resolved in a monochromator and detected in the streak camera. (b) Streak camera, resolving the signal in time. MCP stands for microchannel plate. The signal, travelling along x , wavelength resolved along y , is transformed in electrons, accelerated, resolved in time along z , again accelerated and detected.

The time resolution is limited by several parameters, the main one being the number of lines on the diffracting grating, since the first order diffraction direction corresponds to a single λ delay between neighbouring lines, *i.e.* $\lambda/c \approx 3$ fs time delay per line. We use mostly a 1200 lines per mm grating, illuminated over a 3 mm wide, narrow rectangle. This therefore limits the time resolution Δt_{mono} to about 10.8 ps. Combined with the streak camera intrinsic resolution $\Delta t_{SC} = 0.9$ ps, and a laser pulse duration $\Delta t_{LP} \leq 0.2$ ps, this leads to an expected time resolution $\Delta t_{exp} = \sqrt{\Delta t_{mono}^2 + \Delta t_{SC}^2 + \Delta t_{LP}^2} \approx 11$ ps. In the experiments, the time resolution was a few picosecond better. This could be due to an inhomogeneous illumination of the grating. If needed, the width of the grating was reduced to increase the temporal resolution down to a few picosecond, or increased so that more signal arrived on the detector.

In this work, the excellent time-resolution of the streak camera has been used to perform experiences on high- Q cavities (see section 5.3), cavity switching induced by free carrier injection (chapter 3) and related applications to colour change experiments and real time control of CQED effects (see chapter 5).

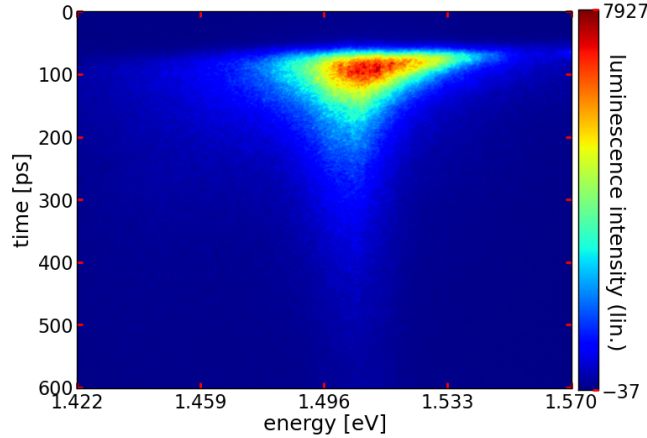


Figure 2.14: Exemplary streak camera acquisition. The figure shows a time (y-axis) and spectrally (x-axis) resolved luminescence signal, acquired with a streak camera. The colour-scale corresponds to the detected luminescence intensity. At $t \approx 80$ ps the luminescence signal starts and decays in the following. The monochromator is centred around 1.496 eV and a grating with 150 lines/mm was used to obtain the spectral resolution.

2.5 Numerical methods

In order to predict experiments and to understand the Physics behind I will use numerical simulation. In this section I will introduce the mathematical models I used to calculate reflectance spectra and to simulate ring-down and cavity switching experiments.

2.5.1 The transfer matrix method

Before a cavity sample is produced, its expected properties (such as mode energies and quality factors) can be optimised using numerical simulations. With the transfer matrix method (TMM) reflectance spectra can be computed [36, 99]. The TMM describes how electromagnetic waves propagate, are transmitted and reflected, while passing through a planar dielectric structure.

The idea of the TMM is to separate the structure into elements, each described by a matrix. The multiplication of those results in the propagation properties of the entire dielectric structure. The idea is illustrated in figure 2.15.

More precisely, the elements may be divided in two alternating groups, the layers with constant refractive index having a certain thickness and the interfaces (or surfaces) without a thickness. For each element of the structure a matrix describing the propagation is established. The matrix for each interface contains the information for the entering and outgoing electromagnetic field, on both sides of the interface. Each matrix describing a

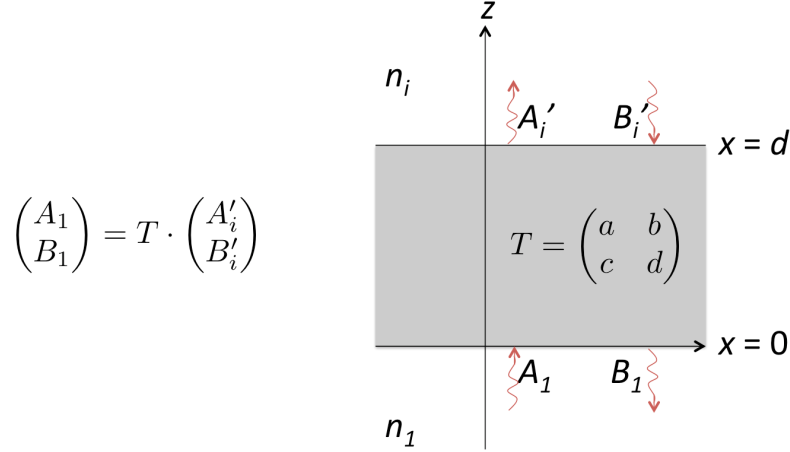


Figure 2.15: Illustration of the TMM principal for a propagation along the z -axis. The amplitudes of the electromagnetic waves A_1 and B_1 on the one side of the structure are related by a matrix T with the amplitudes of the electromagnetic waves A'_i and B'_i on the other side of the structure.

layer accounts for dephasing and possible absorption induced by the propagation through this layer. A useful mathematical description is the formulation in 2x2 matrices. Their simple multiplication, in the order of the elements, result in one 2x2 matrix containing the information of the incoming and outgoing electromagnetic waves on both sides of the entire structure.

In the following I will develop, in accordance with the approach of P. Yeh [36], the mathematical formalism I used in my simulations to compute reflection and transmission properties of dielectric structures.

The Model Having widely extended symmetric microstructures, such as planar cavities, the propagation can be described in two dimensions. The first is the z -direction, perpendicular to the planar cavity surface, the second the x -direction, in the plane of the cavity (the (x, z) -plane). Considering a TE-wave (transverse electric), the electric field oscillates in the y -direction. For a TM-wave (transverse magnetic), the magnetic field oscillates in the y -direction. I will explain the establishment of the matrices for the TE-case. The refractive index n does not change in the x -direction, $\frac{\partial n}{\partial x} = 0$. Solving Maxwell equations gives the electric field for the wave in the the (x, z) -plane

$$E = E(z)e^{i(\omega t - k_x x)}. \quad (2.1)$$

E is the electric field, ω its angular frequency, t the time and k_x the x -component of the wave vector \vec{k} .

$$E(z) = C_1 e^{-ik_z z} + C_2 e^{ik_z z} = A(z) + B(z) \quad (2.2)$$

C_1 and C_2 are constants characterizing the waves propagating upwards and downwards along z , described by the amplitudes A and B , respectively. Next to the interfaces, at zero

distance, I define the wave amplitudes: below the interfaces they are A_i and B_i and above the interfaces A'_i and B'_i . The index i corresponds to i -th layer with refractive index n_i . These definitions are visualised in figure 2.16.

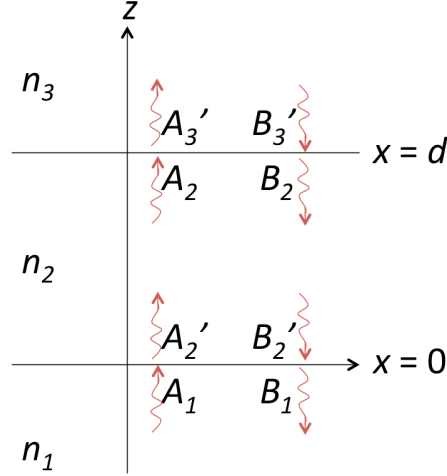


Figure 2.16: Illustration of the different amplitudes of electromagnetic waves for a propagation along the z -axis. Interfaces are at $x = 0$ and $x = d$.

Now we can describe the propagation with the transfer matrices. Coming from the layer l , going upwards to the following layer m , so $m - l = 1$, the propagation through one interface is described by

$$\begin{pmatrix} A_l \\ B_l \end{pmatrix} = D_{lm} \begin{pmatrix} A'_m \\ B'_m \end{pmatrix}, \quad (2.3)$$

where

$$D_{lm} = D_l^{-1} D_m \quad (2.4)$$

is the matrix describing the reflection and transmission through one interface in both directions. Assuming an incident angle θ_l to the z -axis, in the layer l , each matrix D_l is

$$D_l = \begin{pmatrix} 1 & n_l \cos(\theta_l) \\ 1 & -n_l \cos(\theta_l) \end{pmatrix}. \quad (2.5)$$

This is for the TE-case. In the TM-case it is

$$D_{l,TM} = \begin{pmatrix} \cos(\theta_l) & \cos(\theta_l) \\ n_l & -n_l \end{pmatrix}. \quad (2.6)$$

In a layer l , the incident angle θ_l is related to z -component of the wave vector: $k_{l,z} = n_l \frac{\omega}{c} \cos(\theta_l)$ with c the velocity of light in vacuum.

Same description can be done for the propagation through a layer l with the thickness d_l , describe by the matrix P_l :

$$\begin{pmatrix} A'_l \\ B'_l \end{pmatrix} = P_l \begin{pmatrix} A_l \\ B_l \end{pmatrix} \quad (2.7)$$

$$P_l = \begin{pmatrix} e^{i\phi_l + \alpha_l d_l} & 0 \\ 0 & e^{-i\phi_l - \alpha_l d_l} \end{pmatrix}, \quad (2.8)$$

where $\phi_l = k_{l,z} \cdot d_l$ is the accumulated phase and α_l the layer's absorption coefficient. Instead of α_l an imaginary part of the refractive index n_i also describes the absorption.

The propagation of electromagnetic waves from a medium n_0 to a medium n_s through $N \in \mathbb{N}$ layers can thus be described as

$$\begin{pmatrix} A_0 \\ B_0 \end{pmatrix} = T \begin{pmatrix} A'_s \\ B'_s \end{pmatrix} \quad (2.9)$$

$$T = D_0^{-1} \left[\prod_{l=1}^N D_l P_l D_l^{-1} \right] D_s = \begin{pmatrix} a & b \\ c & d \end{pmatrix} \quad (2.10)$$

Reflectivity and transitivity coefficients r and t can be deduced. Under the condition $B'_s = 0$, which means that light enters the structure only as A_0 and leaves the structure as B_0 and A'_s , it is

$$r = \frac{B_0}{A_0} = \frac{c}{a} \quad (2.11)$$

$$t = \frac{A'_s}{A_0} = \frac{1}{a} \quad (2.12)$$

Therefore reflectance and transmittance are

$$R = |r|^2 = \left| \frac{c}{a} \right|^2 \quad (2.13)$$

$$T = |t|^2 = \frac{n_s \cos(\theta_s)}{n_0 \cos(\theta_0)} \left| \frac{1}{a} \right|^2 \quad (2.14)$$

$\frac{n_s \cos(\theta_s)}{n_0 \cos(\theta_0)} = k_{s,z}/k_{0,z} = \det(T)$ is the correction in the phase velocity, necessary to calculate the transmittance.

The Simulation I implemented these TMM-equations in an Octave script to compute reflection spectra for arbitrary planar $\text{Al}_x\text{Ga}_{1-x}\text{As}$ cavities. The simulation runs for TE- and TM-mode, absorption is taken into account, the desired angle of incident can be chosen and the dispersion of the refractive index $n(\lambda)$ is included. To take the right values of the refractive index as a function of wavelength and temperature for any $\text{Al}_x\text{Ga}_{1-x}\text{As}$ composition, I implemented the results of Gehrsitz *et al.* [38].

In figure 2.17 is shown a simulated reflection spectrum and the corresponding cavity. Around 1.3 eV is the stopband with the resonant modes of the planar cavity. The central mode has $R|_{\min} = 0.007$. The other modes have slightly higher values. Each mode's quality factor is equal to the inverse of the relative width of the corresponding peak.

$$Q_m = \frac{\omega_m}{\Delta\omega_m} = \frac{E_m}{\Delta E_m} \quad (2.15)$$

Zooming into the spectrum allow to deduced the quality factors of the modes, as shown. They result by adjustment to a Lorentzian. In the centre of the reflectance band the quality factor is the highest. In my case $Q = 65000$. Q decreases to the outer modes of the stopband. The structure is defined for the central energy; there the Bragg mirrors have their best reflectance. For other energies the reflectance of the Bragg mirrors decreases.

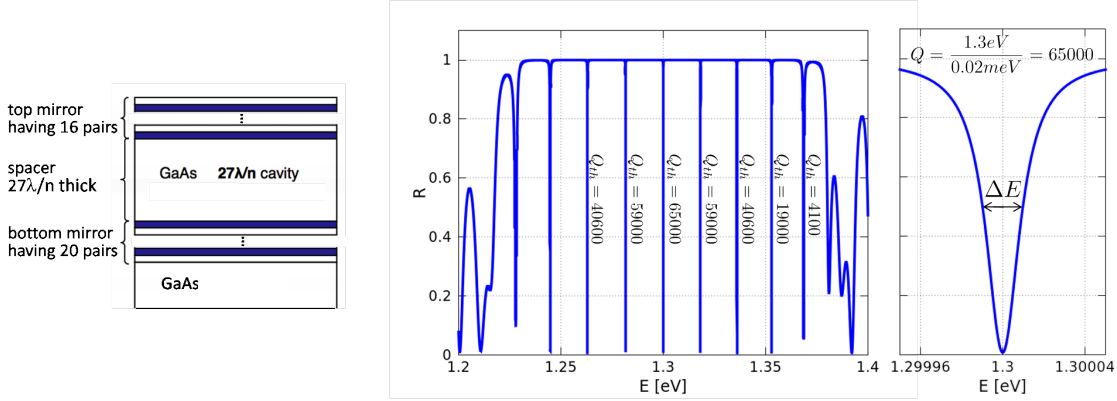


Figure 2.17: A planar multi-mode cavity, characterised by a thick spacer, and its calculated reflectance spectrum. The graphs show the reflection band as a function of energy and indicate the quality factors of several cavity modes. A zoom into the central cavity mode reveals its Lorentzian shape, its FWHM and its quality factor.

2.5.2 FDTD

The finite-difference time-domain formulation allows solving the Maxwell equations in the time domain, thus an ideal tool to compute the propagation of light pulses through dielectric structures. Electric field is calculated for a time-step, then the magnetic field for half a time step later, continuing all time like this. Yee developed this algorithm, opening the door to efficient and accurate numerical resolution of Maxwell's equations in the time domain [100].

I use the FDTD to compute the propagation through planar microcavities, in order to predict or support analysis of experimental results. The restriction on planar microcavities, which are isotropic in plane, allows to reduce the propagation in one direction perpendicular to the cavity surface. Normal incidence is mainly used for my experiments, too. The FDTD formulation can be reduced to one dimension. This makes the code easier to write and the simulation much faster.

Taking the FDTD formula from a MATLAB code, written by Yohan DÉSIÈRES of CEA Grenoble, I established my own one-dimensional FDTD Python code. The principals of the one-dimensional FDTD-simulation are well explained by Loui [101]. In the FDTD, boundary conditions play a crucial role. I use those formulated by Mur [102].

2.6 Conclusion

In this chapter I described how to design, fabricate and analyse high Q planar cavities and high Q micropillar cavity.

Elementary is the molecular beam epitaxy. With a III-As MBE-machine I grew two-dimensional layers of GaAs and AlAs, needed to construct the cavities DBRs and spacer. A very good precision is required to obtain cavities of high quality. I inserted solid-state emitters, namely self assembled InAs QDs. As internal light source, they will be essential for the CQED experiments in the following chapters.

I explained the optical analysis methods. The FTIR to check the properties of the as-grown planar cavities and the time-resolved photo-luminescence for the coming sophisticated cavity switching experiments.

As last I introduced simulation tools for reflectance spectra and cavity switching experiments.

With this knowledge, I will introduce in the next chapter the real cavity and conduct all-optical switching experiments.

CHAPTER 3

CAVITY SWITCHING EXPERIMENTS BY ALL-OPTICAL FREE CARRIER INJECTION.

Via linear absorption, a short light pulse can generate free carriers in the semiconductor material of a microcavity. These free carriers induce a refractive index change that dynamically modifies the optical length of the cavity, and thus its resonance frequency. This change is reversible: the resonance frequency comes back to its original value when the carriers recombine. Such a cavity switching process has numerous potential applications. To mention a few examples, the filtering properties of the cavity can be switched in time [10]; The colour of a light field stored in the cavity could be changed [11, 15]; That can be used to introduce a time-dependent coupling between emitters in the cavity and the optical cavity modes [80, 81].

In this chapter, we study the switching of micropillar cavities. I will discuss the dynamics of the switched cavity mode due to the free carrier density evolution. In particular, we will see that different pillar modes can experience different switching dynamics, provided a non-uniform free carrier injection is used.

3.1 Switching microcavities

All-optical cavity switching can be realised by free carrier injection [11, 14] or by the electronic Kerr effect [12, 13]. For the Kerr switching, for example, Ctistis *et al.* used a femtosecond pulsed laser pumping at $\lambda = 2400$ nm having a pulse intensity of $70 \text{ pJ}/(\mu\text{m})^2$ [103] to obtain refractive index changes of $+0.1\%$ [12]. This method is of great advantage if the fastest switches are desired, but its realisation is quite challenging and large switching magnitudes, well above one mode linewidth, seem presently out of reach [104]. Herein I will focus on the switches obtained by free carrier injection, which are much easier to realise.

Cavity switching by all-optical free carrier injection has been known since the early days of microcavity physics [75]. It has the advantage of being much faster than electronic switches and was historically investigated for ultrafast telecommunication and optical computing [75]. Harding *et al.* have recently provided a nice demonstration of large amplitude cavity switching of a planar cavity. They obtained a switch of thirteen mode linewidths, corresponding to a refractive index change of about -1% [14]. They injected the free carriers in the cavity's GaAs layers by two-photon absorption, using a fs-pulse laser at $\lambda = 1720$ nm. The energy of each laser photon was slightly larger than the half of the GaAs bandgap. The weak probability of two-photon absorption leads to a very homogeneous free carrier distribution in space, thus avoiding the possible broadening of the switched cavity mode. But this implies that high pulse intensity is needed to inject a significant density of free carriers. For the switch in reference [14], the pulse intensity was $300 \text{ pJ}/(\mu\text{m})^2$.

In order to reduce the needed excitation pulse energy, our strategy is to inject the free carriers by linear, one-photon absorption. The exciting laser has therefore to operate above the energy of the GaAs bandgap. A pulse intensity of around $1 \text{ pJ}/(\mu\text{m})^2$ becomes sufficient for cavity switching, thanks to the large absorption coefficient of GaAs, which is easily obtained with a Ti:sapphire laser.

The large absorption coefficient however seems to be in conflict with a homogeneous spatial free carrier distribution in the GaAs layers. But it turns out that two strategies can be used to overcome this problem: The exciting laser can operate very close to the energy of the GaAs bandgap, so that the absorption coefficient is weak enough to avoid a pump depletion along the depth of the cavity; The other possible trick is based on absorption saturation. A very homogeneous spatial free carrier distribution can be obtained for both ways. For one-photon absorption, the overall number of injected free carriers is proportional to the laser pulse energy (as long as no saturation occurs), which allows the induced resonance wavelength switch to be easily controlled.

An additional route towards smaller switching energies is to reduce the physical size of a microcavity, as Jewell *et al.* did with micropillar cavities [75]. We will also switch micropillar cavities, and therefore use an excitation of a few pJ per pumping pulse.

3.2 Our experimental approach: Probing cavity switching with an internal light source

The injection of free carriers shifts the resonant modes of a microcavity towards higher energies. For this purpose, we use linear one-photon absorption and micropillar cavities with small physical size (diameter of a few micrometres) to limit the required laser energy. We use a pulsed Ti:sapphire laser with the repetition rate of 76 MHz. A typically used average power of 1 mW (measured in front of the micropillars) corresponds to 13 pJ per

laser pulse, which will impinge on a micropillar¹.

The most common approach to study such ultrafast events is the pump–probe spectroscopy, as done *e.g.* in the references [76, 11, 14]. The rather intense pump laser pulse switches the cavity modes. The probe laser pulse, covering the spectral range of interest (usually the switched cavity modes), probes the cavity mode positions at a given delay relative to the pumping event. The signal of the reflected or transmitted probe, depending on the experiment, is spectrally resolved and detected. In this way, probing one delay after the other, the pump–probe–delay dependent spectral position of the cavity mode can be detected and a time- and spectrally resolved map of the cavity mode time-wise constructed.

Here we use a different approach. QD emitters are embedded in the microcavities and figure as internal light source. They can probe the time- and spectral-dependent density of the cavity modes. (The figure 3.3 evidences that the QDs probe the spectral cavity mode positions.) We detect the emitted signal with a streak camera, with the great advantage to detect for all required delays and frequencies simultaneously. In that way, we observed temporally and spectrally resolved switches, usually within a few minutes long experiments.

For these cavity switching experiments we used a sample with many micropillar cavities of different diametres having each an ensemble of InAs QDs in the central GaAs spacer as an internal light source. An important advantage of micropillars is that light emitted through the modes of a micropillar cavity has a very directive emission diagram and can be collected with a high efficiency.

The micropillars made of GaAs and AlAs have a bottom DBR of 25 periods and a top DBR of 15 periods and are resonant between 1.37 eV and 1.42 eV, depending on the position on the sample. We studied micropillars with diameters between 1.1 μm and 5 μm and quality factors between 1000 and 4000. Such micropillars are sketched in figure 3.1. The thicker bottom mirror has a higher reflectance than the top mirror. The light of the cavity modes therefore escapes essentially through the top mirror and can be detected. The five QD layers in the cavity spacer constitute an intense photo-luminescence source that probes the cavity modes.

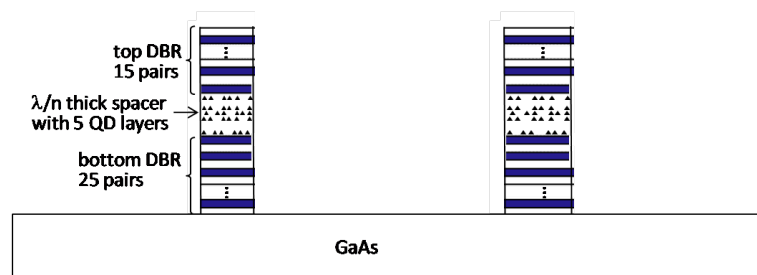


Figure 3.1: Exemplary micropillar sample — a sketch. GaAs is shown in white, AlAs in blue.

¹Usually the exciting laser spot is of the order of — or smaller than — the micropillar diameter. About 30% of the impinging laser intensity is reflected off the pillar surface, the remaining 70% enter the micropillar and can excite the free carriers and switch the cavity modes.

The micropillars that are studied in this thesis are listed in the following table, together with their diameters d , the energies of their fundamental cavity modes $E_m|_{\text{fund.}}$, the corresponding quality factors $Q_m|_{\text{fund.}}$, their theoretical Purcell factor $F_{P,\text{th}}$, and the measured characteristic decay times τ_{QD} of the QD transitions resonant with the fundamental cavity modes:

pillar name	d	$E_m _{\text{fund.}}$	$Q_m _{\text{fund.}}$	$F_{P,\text{th}}$	τ_{QD}
G2_02	5 μm	1.395 eV	4200	2.7	800 ps
G2_04	3 μm	1.397 eV	3700	6.5	530 ps
G2_05	2.5 μm	1.399 eV	2800	7.1	480 ps
G2_06	2 μm	1.402 eV	2100	8.4	330 ps
G2_07	1.6 μm	1.406 eV	1700	10.8	310 ps
G2_08	1.4 μm	1.411 eV	1100	9.3	290 ps
G2_09	1.1 μm	1.418 eV	900	11.4	240 ps
D2_04	3 μm	1.372 eV	3200	5.7	—
F2_02	5 μm	1.388 eV	~ 4000	2.6	—
F2_04	3 μm	1.390 eV	~ 3500	6.2	—

For the different experiments, we used the setup of the time-resolved micro-photoluminescence, presented in figure 2.12, with the streak camera as detector.² The pulsed Ti:sapphire laser was focused on one micropillar to excite the QDs and, if wanted, to switch the modes at the same time.

In the first experiments, we only excited the QDs from one micropillar, without switching it. The goal was to extract the decay times τ_{QD} and the intrinsic lifetime of the excitons τ_X . We paid attention not to saturate the luminescence signal, in order to measure correctly τ_{QD} . The results are listed above. The intrinsic lifetime of excitons in self-assembled InAs QDs in GaAs is typically about $\tau_X = 1.2$ ns. The emission shown on figure 3.3a, close to 1.4 eV, shows a reduced decay time of $\tau_{QD} = 530$ ps (*cf.* preceding table). There may be two reasons: the observed emission on the 1.4 eV resonance could come from excited states of the QD transitions; their intrinsic lifetime would be reduced compared to the value of the intrinsic exciton lifetime $\tau_X = 1.2$ ns. Furthermore, the Purcell effect reduces the decay time of QD transitions in resonance with a cavity mode, as discussed in chapter 1.3.2.

Having measured the decay times τ_{QD} of the QD transitions resonant to the fundamental cavity modes, we want to determine the corresponding intrinsic lifetimes τ_X . To this aim, we can write equation 1.31 as:

$$\frac{1}{\tau_{QD}} = \frac{F_P + \gamma}{\tau_X} \quad (3.1)$$

In order to fit τ_X , the Purcell factor we need to put into this equation is not the theoretically predicted one ($F_{P,\text{th}}$). In micropillars which contain an ensemble of in-plane spatially

²The streak camera present, depending on the detection conditions, more or less distinct vertical line defects. The decrease in the detected signal is thus an artefact of the streak camera and not signature of the emitted light.

dispersed QDs, one measures an averaged Purcell factor $\overline{F_P}$. This one is four time smaller than the actual Purcell factor: $\overline{F_P} = F_P/4$. That can be explained by the spatial overlap of the in-plane cavity mode profile with the dispersed QDs (see the definition of the Purcell factor in section 1.3.2). Therefore we can rather extract τ_X from the modified relation

$$\frac{1}{\tau_{QD}} = \frac{\overline{F_P} + \gamma}{\tau_X} \quad (3.2)$$

where $\overline{F_P} = F_{P,th}/4$, and γ is equal to about 1 in micropillar cavities.

We plotted the data of the table shown above in figure 3.2 and fitted τ_X under the assumption $\gamma = 1$. We obtained an intrinsic lifetime of about 1.1 ns. This is very close to the intrinsic lifetime of excitons in self-assembled InAs QDs in GaAs. That means that the probed QD transitions at 1.4 eV are most probably not excited, but fundamental QD excitonic states. We can conclude that the Purcell effect is at the origin of the reduced values for τ_{QD} , thus of the accelerated spontaneous emission.

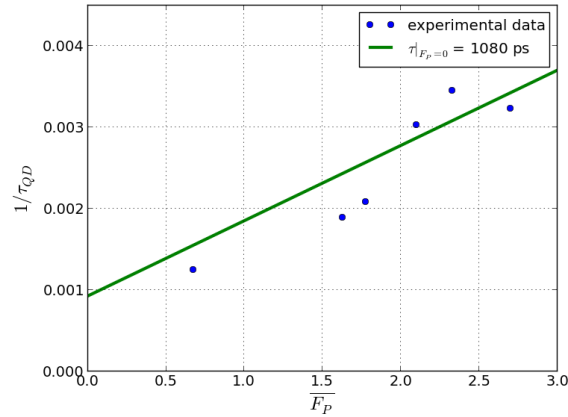


Figure 3.2: Inverse characteristic decay time of the QDs resonant to fundamental micropillar modes, in function of their averaged Purcell factor. This graph let us extract the intrinsic lifetime of the observed QD transitions. It is here 1.08 ns.

Having introduced the micropillar sample, the properties of the studied micropillars, and the experiment, we will discuss in the following the cavity-switching.

In this chapter all the photoluminescence was measured at 7 K. The pulsed Ti:sapphire femtosecond laser was focused and the luminescence collected with a 40x Zeiss objective with a 0.6 numerical aperture. A 830 nm long-pass filter from Semrock protected the streak camera from the reflected laser light (except for excitation at 850 nm in the InAs wetting layer).

3.3 Characterising switching events in micropillar cavities

The photoluminescence signal of an unswitched micropillar is shown in figure 3.3a. The laser excites only the QDs via the InAs wetting layer, with the laser tuned to 850 nm; that avoids exciting of carriers in the GaAs cavity. In order to switch the cavity, the laser is then tuned above the GaAs bandgap at 7 K ($\lambda < 816$ nm) to excite simultaneously both the QD transitions and a free carrier plasma in the GaAs layers of the micropillars. The cavity resonances blue-shift and subsequently relax back to their unswitched positions, see figure 3.3b. We call that process “cavity switching”. The laser power may be increased — or its wavelength tuned — to control the injected free carrier density and therefore the amplitude of the initial blue-shift.

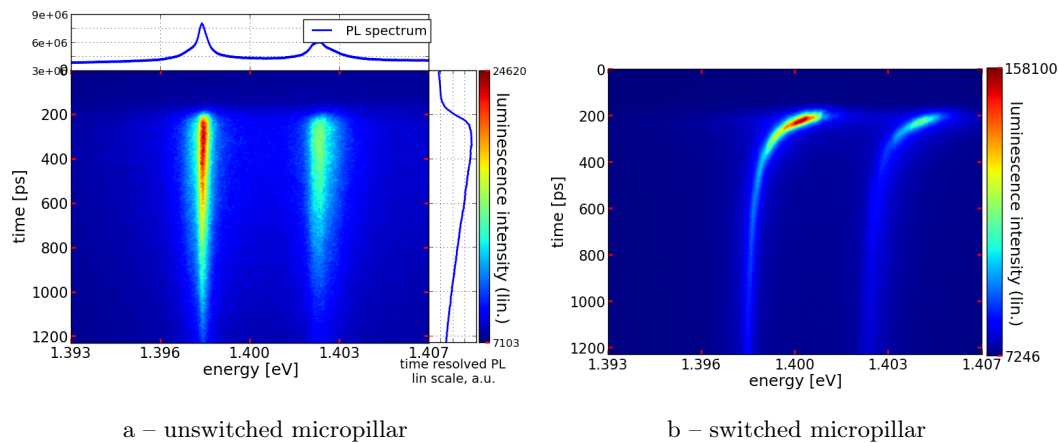


Figure 3.3: Time and spectrally resolved luminescence of an ensemble of InAs QDs embedded in an GaAs/AlAs micropillar cavity of $3 \mu\text{m}$ diameter (pillar G2_04), obtained with a streak camera. The QDs are excited with a pulsed Ti:sapphire laser and probe the cavity mode positions. The fundamental and the first high order pillar modes are visible. The exciting laser operates first set at 850 nm with a power of $60 \mu\text{W}$ to excite only the QDs and the InAs wetting layer (a), and second set at 805 nm and $800 \mu\text{W}$ to excite the GaAs and switch the micropillar cavity (b).

The main features of the cavity switching are: the establishment time of the switch (*i.e.* the time needed to reach that maximal shift), we call it “switch on” time, the time needed for the spectral return of the cavity modes to their unswitched value, governed by the free carrier relaxation, the amplitude of the switch (*i.e.* the maximal value of the energy-shift), and a possible different behaviour of neighboured cavity modes. I will discuss these features in the following.³

³Here we cannot study experimentally a possible modification of the cavity mode’s quality factors due to the switching. The spectral resolution (linked to the temporal resolution) was not sufficient to resolve the width of the cavity modes. Simulations show that the effects on Q should be negligible for a Q of about a few thousands.

3.3.1 “Switch-on” behaviour

The displacement of the cavity mode when the femtosecond laser pulse hits the micropillar is not instantaneous. It takes a few picoseconds to establish the switch — the time that the excited free carriers need to cool down through phonon emission. The refractive index depends on the energy distribution of the free carriers, *cf.* the Kramers-Kronig relation [105].

To illustrate the “switch-on”, in addition to the pulsed Ti:sapphire laser exciting QDs and switching the cavity, we used a continuous wave (CW) laser set at 808 nm to excite also the QDs, but without switching the cavity. This CW laser ensures that some QDs are excited at all times and the cavity mode resonances are continuously probed. Before the laser pulse impinges on the micropillar, luminescence resonant with the unswitched cavity modes is detected, as shown in figure 3.4, even though it is hardly visible in the streak camera images. The red lines illustrate the time dependent spectral mode positions and were obtained by fitting for each time step the corresponding spectra to a Lorentzian peak.

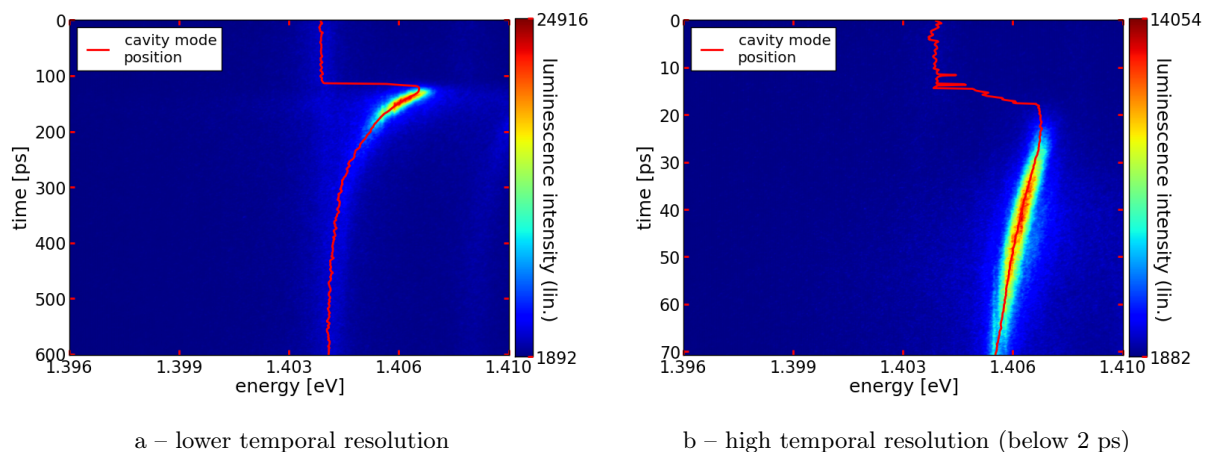


Figure 3.4: Time- and spectrally-resolved luminescence of an ensemble of InAs QDs embedded in a switched micropillar (G2_04). A CW laser (operating at 808 nm and 1 mW) and the pulsed Ti:sapphire laser (operating at 800 nm and 1.14 mW) excite QDs, wetting layer, and GaAs. The fundamental pillar mode is shown for two different temporal resolutions. Its instantaneous spectral position is highlighted with the red lines⁴. The lower time resolution (a) shows the entire switching process while the high temporal resolution (b) enable to resolve the “switch-on”, the duration of which is measured as 7.3 ps.

⁴One has to note that there is some unswitched contribution to the switched signal. This signal is an artefact of the streak camera. In the used, “synchro-scan” mode an electric field oscillates sinusoidally inside the streak camera at the 76 MHz repetition rate of the Ti:sapphire laser. This field translates temporal retardation in the signal to spatial vertical displacement, thus generating the temporal resolution. The detection happens around the zero-crossing of the sinusoidal oscillating field. There exist therefore two possible moments to detect the time-resolved signal: once for the zero-crossing having positive slope, once having negative slope. The signal resulting from the pulsed excitation can only be detected in one of these cases, while the signal emitted because of the CW excitation is detected in

The fast “switch-on”, *i.e.* the time elapsed between the moment when the cavity mode starts switching and the moment when the cavity mode reaches its spectral maximum, amounts here to 7.3 ps. Afterwards, luminescence resonant to the switched cavity mode is detected. This mode relaxes with the free carrier recombination in a few hundred picoseconds, that is discussed in the following.

3.3.2 Free carrier relaxation and the spectral return of the cavity mode

The spectral return of a cavity mode to its unswitched value is a function of the free carrier recombination. In order to describe the cavity switching, we have to describe the temporal and spatial evolution of the once injected free carrier distribution. With this knowledge, we will be able to calculate the corresponding time-dependent cavity mode resonance and predict how switches occur in micropillar cavities.

The evolution of the free carrier distribution can be described by the diffusion processes, by the recombination on the pillar surface with the characteristic speed S , and by the characteristic lifetime of free carriers in the bulk material τ_{bulk} . We take the diffusion constant from literature and furthermore, we need to know S and τ_{bulk} in our micropillars.

In this subsection, we will first introduce the free carrier recombination in GaAs and show how to model micropillar modes for a time-dependent inhomogeneous free carrier distribution. Then we will conduct a numerical experiment to define a strategy how to extract S and τ_{bulk} from the experimental data. Finally we analyse the experimental data — which are spectral returns of switched cavity modes from micropillars with different diameters — and extract S and τ_{bulk} using the developed strategy.

Knowing S and τ_{bulk} , we can model the switching experiments which are presented in the following sections.

Carrier recombination in GaAs

The recombination of free carriers in GaAs is the basis for the time dependence of the switched cavity modes.

In agreement with the Drude model for free carrier dispersion [106], the refractive index change Δn is proportional to the free carrier density N :

$$\Delta n = -\frac{e^2}{2n_0\epsilon_0\omega_{\text{pump}}^2} \left(\frac{\Delta N_e}{m_e^*} + \frac{\Delta N_h}{m_h^*} \right) \quad (3.3)$$

where e is the elementary charge, n_0 the unperturbed refractive index, ϵ_0 the vacuum permittivity, ω_{pump} the frequency of the exciting laser, ΔN_e (ΔN_h) the injected electron

both cases, therefore twice.

(hole) density, and m_e^* (m_h^*) the effective mass of electron (hole). So:

$$\Delta n_{\text{GaAs}}(t) \propto N(t) \quad (3.4)$$

where n_{GaAs} is the refractive index of GaAs and $N(t)$ the total free carrier density.⁵

In order to describe properly the spectral position of the cavity mode, we have to study the free carrier dynamics in GaAs. The free carrier relaxation dynamics in thin GaAs layers are described by the equation [107]:

$$-\frac{dN}{dt} = \frac{N}{\tau_{e,h}} + BN^2 + CN^3. \quad (3.5)$$

Depending on the instantaneous carrier density N , different effects dominate: the non-radiative recombination with the characteristic lifetime $\tau_{e,h}$, the radiative bimolecular recombination characterized by B or the Auger recombination characterized by C . For bulk GaAs, $\tau_{e,h}$ lies typically between 1 ps and 1 ns depending on the growth conditions and the sample geometry, $B \approx 2 \cdot 10^{-9} \text{cm}^3/\text{s}$ at 15 K [108], and $C = 3.1 \cdot 10^{-31} \text{cm}^6/\text{s}$ at room temperature [109] and is known to decrease with temperature [110].

Being undoped, our MBE-grown micropillars will experience nearly equal electron (N) and hole (P) densities when photo-pumped.

For an electron density of $10^{18}/\text{cm}^{-3}$, Bennett *et al.* [111] predict a relative GaAs refractive index change of 1%, so a maximal switch of the cavity mode $\Delta E|_{\text{max}}/E_m$ of 1%. The in the experiments injected free carrier density should lie far below 10^{19}cm^{-3} . Auger recombination can be neglected as higher densities would be required; Strauss *et al.* [112] mentions $N \geq 2.5 \cdot 10^{19}\text{cm}^{-3}$ for a significant contribution of the Auger recombination. Assuming $\tau_{e,h} \approx 100$ ps the linear and quadratic terms in equation 3.5 will be comparable for $N \approx 5 \cdot 10^{18}\text{cm}^{-3}$. (For $\tau_{e,h} \approx 1$ ns: $N \approx 0.5 \cdot 10^{18}\text{cm}^{-3}$.) Radiative bimolecular recombination may be present in the experiments. Neglecting the Auger term, the solution of equation 3.5 is then:

$$N(t) = \frac{N(0)}{1 + (N(0)B\tau_{e,h} + 1)(e^{t/\tau_{e,h}} - 1)}. \quad (3.6)$$

That equation can be rewritten as:

$$N(t) = \frac{n_0}{e^{t/\tau_{e,h}} - n_0 B \tau_{e,h}}, N(0) = \frac{n_0}{1 - n_0 B \tau_{e,h}}. \quad (3.7)$$

At short times after excitation, if N is high, radiative bimolecular recombination can dominate. At long times, as N decreases in the meantime, the non-radiative exponential decay will always dominate.

First of all, we want to focus on the non-radiative exponential decay, in order to describe the spectral return of the cavity mode at long times. This spectral return will show

⁵In a planar cavity, if the free carrier distribution is homogeneous in space, the relative refractive index change equals the relative blue shift of the cavity mode: $\frac{E_m(t) - E_{m,0}}{E_{m,0}} = \frac{\Delta n_{\text{GaAs}}(t)}{n_{\text{GaAs}}}$. But in a micropillar cavity the nearby and strongly recombining surfaces make this relation invalid.

an exponential decay with the characteristic time $\tau_{e,h}$, as it is proportional to N (see equation 3.4). The main contributions to $\tau_{e,h}$ are the recombination in the bulk GaAs and on the pillar surfaces⁶ [113, 114]. For a thin slab of thickness l , it writes [115]:

$$\frac{1}{\tau_{e,h}} = \frac{1}{\tau_{\text{bulk}}} + \frac{2S}{l} \quad (3.8)$$

where τ_{bulk} is the characteristic recombination time in bulk material and S the surface recombination speed.

By analogy, we write for a micropillar of radius R

$$\frac{1}{\tau_{e,h}} = \frac{1}{\tau_{\text{bulk}}} + \alpha_S \frac{S}{R} \quad (3.9)$$

where the geometry-dependent, dimensionless pre-factor α_S has to be determined, as well as τ_{bulk} and S for our experiments. Thyrestrup *et al.* estimated S to be $2.8 \cdot 10^3$ m/s in a similar framework [84] (they worked at room temperature and not at cryogenic temperature, as it is here the case). In order to check the validity of the expression 3.9, estimate α_S , and find a strategy to extract τ_{bulk} and S from our experimental data, we firstly conducted a numerical experiment.

Modeling micropillar modes for a time-dependent inhomogeneous distribution of free carriers

In our numerical experiment we need to describe how the cavity modes evolve in time. Therefore we simulate the time-dependent inhomogeneous distribution of free carriers and calculate the spectral positions of the cavity modes. For the ease of our purpose we use cylindrical symmetry — which is well adapted to describe circular micropillars. This limits ourselves to the symmetrical injection of the free carriers. Furthermore, we assume a homogeneous free carrier injection along the vertical pillar axis.

The lateral free carrier distribution in micropillar cavities is not uniform. Even if homogeneously injected, the surface recombination will make the distribution inhomogeneous. We simulated the time-evolution of the free carrier distribution considering diffusion, surface and bulk recombination. With the help of the diffusion equation (also known as second Fick's law):

$$\partial_t N = D_a \Delta N - \frac{N}{\tau_{e,h}}, \quad (3.10)$$

we obtained the radial free carrier profile $N(r, t)$. Using the cylindrical coordinates (r, θ, z) , the Laplacian Δ — with $\partial_\theta N = 0$ — and the diffusion equation write

$$\partial_t N = D_a \left(\partial_r^2 + \frac{1}{r} \partial_r \right) N - \frac{N}{\tau_{e,h}} \quad (3.11)$$

⁶One has to note that the exponential decay can be a combination of radiative exciton recombination and all non-radiative recombination processes. All of them are proportional to N : $dN/dt \propto N$. In GaAs, the radiative exciton recombination does not have an important contribution.

D_a is the ambipolar diffusion coefficient in bulk GaAs. Zhao *et al.* [116] determined it in bulk GaAs at 10 K to be $D_a = 170 \text{ cm}^2/\text{s}$. Their result was obtained for an injected free carrier density of 10^{17} cm^{-3} , close to our experiments.

In terms of diffusion and the first Fick's law, we can express the surface recombination:

$$-\frac{\partial N}{\partial r} D_a = NS \quad (3.12)$$

In the simulation, we take into account the surface recombination via an increased recombination rate $\tau_{e,h} = \Delta r/S$ on a $\Delta r = 100 \text{ nm}$ thick layer next to the pillar surface; everywhere else $\tau_{e,h} = \tau_{\text{bulk}}$. Furthermore, I used the boundary condition of zero flux at the pillar surface, $\partial_r N|_{r=\pm d/2} = 0$, meaning that no free carrier can cross the surface of the micropillar cavity; d is the pillar diameter.

The figure 3.5 shows the radial profile of the refractive index change, related to the free carrier density by equation 3.4, as a function of time for a micropillar with $d = 3 \mu\text{m}$. In this example I used a characteristic recombination time in the bulk material $\tau_{\text{bulk}} = 560 \text{ ps}$, the recombination speed on the surfaces $S = 7 \cdot 10^3 \text{ m/s}$, and the diffusion coefficient $D_a = 170 \text{ cm}^2/\text{s}$. Initially the free carrier are injected in a homogeneous way, so that the refractive index change is constant in space. The amplitude of the initial refractive index change — as well as of the switch — is $\Delta n_{\text{GaAs}}/n_{\text{GaAs}} = 0.006$. The temporal and spatial evolution of this distribution are calculated using equation 3.11. Because of the highly recombining surfaces, the free carrier density decreases much faster on the pillar surface than elsewhere, influencing the shape of the free carrier distribution as one can see in the following figure.

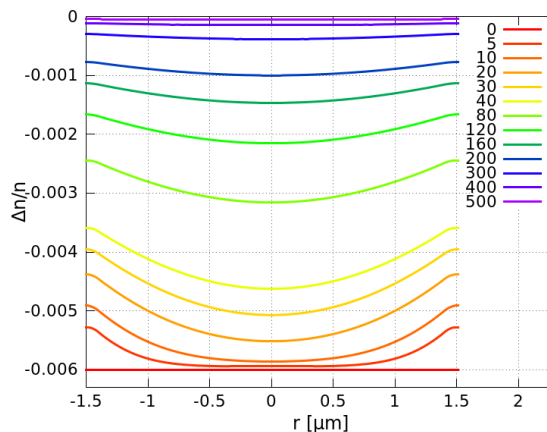


Figure 3.5: Evolution of the relative radial refractive index change under free carrier diffusion and recombination. The delay after the free carrier injection is indicated in the legend in picoseconds.

Knowing the spatial profile of the refractive index, we don't know the resonant energies of the switched micropillar modes yet. As introduced in chapter 1.2.3, every micropillar mode is constructed by a guided mode m and has the proper resonances λ_m , described by $\lambda_m/n_{\text{eff}}^m = L_{\text{cav}}$. n_{eff}^m is the effective refractive index of the guided mode m and L_{cav} the

physical length of the cavity. The DBRs confine these modes vertically. Thanks to a cylindrical symmetry, those resonances can be determined by solving the wave-equation 1.21 for a radial refractive index profile $n(r, t)$.

I solved the equation 1.21 numerically for different fixed values of time — taking the corresponding refractive index profiles $n(r, t)$ — and obtained the propagation constant $\beta_m(t)$ of the guided modes in the GaAs section of the micropillar and the corresponding cavity resonances $E_m(t)$.

As an example, I show in figure 3.6 the result of the calculation for the fundamental cavity mode HE_{11} and the first higher order cavity mode TE_{01} .⁷ The micropillar and refractive index profile of figure 3.5 were used for the simulation; parameters were $d = 3 \mu\text{m}$, $n|_{r \leq d/2} = n_{\text{GaAs}}(r, t)$ as calculated above and $n|_{r > d/2} = n_{\text{air}} = 1$, $\tau_{\text{bulk}} = 560 \text{ ps}$, and $S = 7 \cdot 10^3 \text{ m/s}$.

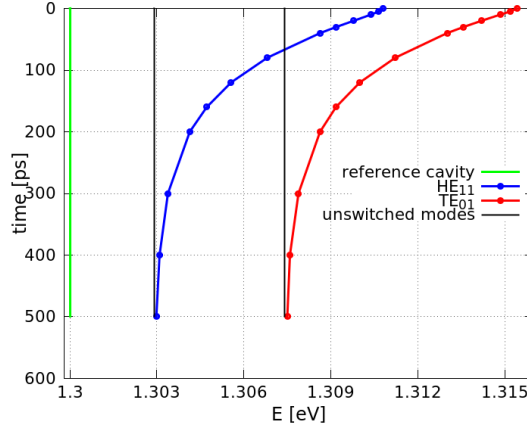


Figure 3.6: Evolution of the fundamental and first higher order micropillar modes for the time- and radial-dependent refractive index profiles (shown in figure 3.5). The resonance of the corresponding unswitched planar cavity is drawn in green, the unswitched mode positions of the two switched modes in black, and the time-dependent fundamental (HE_{11}) and first higher order (TE_{01}) micropillar modes in blue and red, respectively.

With the here initial uniform free carrier injection, the shown cavity modes present similar, almost identical, behaviour. The slight differences result from the different matching of the mode-profiles with the time dependent free carrier density shown in figure 3.5. Much more important differences will be observed in the section 3.4, where a non-uniform free carrier injection is used.

⁷The mode TE_{01} , together with the two following modes HE_{21} and TM_{01} , forms a triplet. In the shown experiments this triplet is not spectrally resolved as the separation in energy is small (*cf.* chapter 1 figure 1.9).

Numerical study of the non-radiative recombination rate in micropillars

Simulations of cavity switching, similar to the above shown one, taking into account free carrier diffusion, surface- and bulk-recombination, enabled us to fit the characteristic time $\tau_{e,h}$ of the spectral return of the cavity mode as a function of the micropillar diameter. $\tau_{e,h}$ characterises the non-radiative free carrier relaxation. We did so, and obtained data for $1/\tau_{e,h}$ as a function of $1/d$, for fixed values of the parameters $\tau_{\text{bulk}} = 560$ ps and S . For each set of simulations having a constant S , we were able to extract the coefficient α_S of equation 3.9.

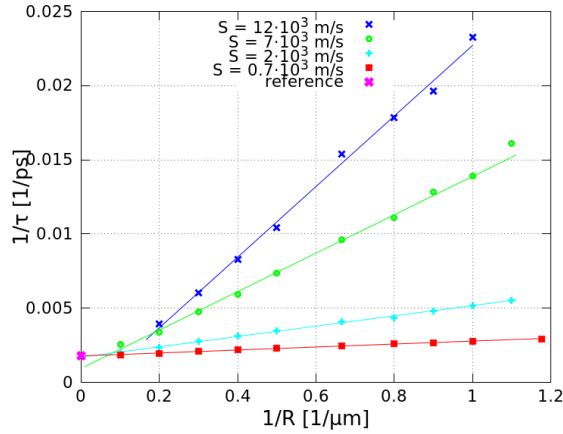


Figure 3.7: Simulation of the characteristic free carrier relaxation time $\tau_{e,h}$ as a function of the inverse of the pillar radius R for four different surface recombination speeds S . The point called “reference” corresponds to the inverse of the bulk recombination time, where $\tau_{\text{bulk}} = 560$ ps. The lines correspond to an interpolation of the datapoints of same colour, in order to deduce the four slopes $\alpha_S S$.

The figure 3.7 shows $1/\tau_{e,h}$ as a function of the pillar radius $R = d/2$ for four different surface recombination speeds S . These simulations show that $1/\tau_{e,h}$ can be well described by a linear function of $1/R$. The fit of the simulated datapoints to equation 3.9 results in:

S	α_S	$\tau_{\text{bulk,fit}}$
$12 \cdot 10^3$ m/s	1.98	-929 ps
$7 \cdot 10^3$ m/s	1.85	1070 ps
$2 \cdot 10^3$ m/s	1.74	588 ps
$0.7 \cdot 10^3$ m/s	1.43	562 ps

Interestingly, the factor α_S is a function of the surface recombination speed S , which is slowly varying, and here always smaller than 2, which corresponds to the slab case (*cf.* equation 3.8). Only for small S ($\lesssim 3 \cdot 10^3$ m/s) does the data converge to $1/\tau_{\text{bulk}}$ in a linear way at $R = 0$. For larger values of S , even for very thick micropillars, the surface recombination dominates the bulk recombination, so that there seems to be some offset at $R = 0$. Nevertheless, $1/\tau_{e,h}$ stays always greater than $1/\tau_{\text{bulk}}$ (for $S > 0$).

Coming back to the case of moderate surface recombination speeds, below $3 \cdot 10^3$ m/s, the clear linear behaviour of $1/\tau_{e,h}$ as a function of $1/R$ provides a simple strategy to estimate material properties of our micropillars. Let us assume that we have a series of experimental data for variable pillar diameters. If we plot the non-radiative decay rate $1/\tau_{e,h}$ as a function of $1/R$, the extrapolated values of $1/\tau_{e,h}$ for infinitely large pillars correspond to $1/\tau_{\text{bulk}}$, the recombination rate in bulk GaAs. The slope of the line gives us $\alpha_S S$. Using the previous calibration of $\alpha_S S(S)$, we can estimate S . This calibration is shown in figure 3.8.

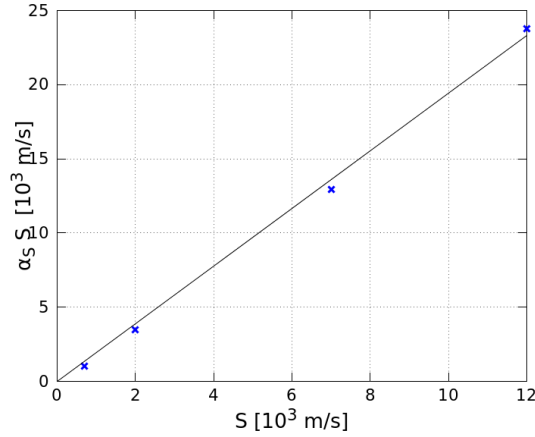


Figure 3.8: Calibration of $\alpha_S S$ as a function of S . The four datapoints (blue crosses) are equal to the slopes $\alpha_S S$ of figure 3.7. Knowing $\alpha_S S$ for experimental data, we will be able to estimate the real S of our micropillars. The slope of the interpolation (black line) equals here 1.94.

Experimental study of the non-radiative recombination rate in micropillars

Five neighbouring micropillar cavities with different diameters were switched one after the other. The resulting streak-camera images are shown in figure 3.9. They are at the origin of the experimental study of the non-radiative recombination rate. From each streak-camera image the spectral position of the fundamental micropillar modes were extracted and plotted in the last subfigure. The spectral shift of the cavity mode is proportional to the free carrier density. To obtain $1/\tau_{e,h}$ — which is the non-radiative decay rate of the free carriers — the long-time components of the spectral positions were fitted to an exponential decay (from 200 ps after the switching event on). At these delays, the once injected free carriers should be redistributed through diffusion. Furthermore, the bimolecular recombination processes should be negligible. The mono-exponential non-radiative decay should thus be the dominating one. The corresponding fits were superposed in the subfigure 3.9f.

The obtained experimental data for $1/\tau_{e,h}$ are shown in figure 3.10. The linear fit of the experimental data points gives $\alpha_S S = 0.0022 \mu\text{m}/\text{ps} = 2.2 \cdot 10^3$ m/s and $\tau_{\text{bulk}} = 424$ ps. With that value for τ_{bulk} , we can now estimate the unknown S with the calibration in

figure 3.8. Interpolating the two datapoints surrounding $\alpha_S S = 2.2 \cdot 10^3$ m/s, we can attribute the value $1.33 \cdot 10^3$ m/s to S .

In the work done here, we observe that cavity modes of smaller micropillars return faster to their unswitched spectral positions. The smaller a micropillar, the more the nearby micropillar surfaces must influence the nature of the recombination dynamics and accelerate them⁸. The pillar surface acts as an efficient trap for electrons and holes; which is much more efficient than heterostructure interfaces and bulk semiconductor that present much smaller defect densities. For small micropillars, the probability of recombination on the pillar surface increases, reducing $\tau_{e,h}$. This is at least the case for long times where non-radiative recombination dominates.

For short times the initial injected number of free carriers and possible inhomogeneous injection played an important role for the dynamics of the return of the micropillar mode. For larger free carrier densities N the recombination could be faster if bimolecular recombination was present. For inhomogeneous injection the mode dynamics can be accelerated until the carriers were diffused, *i.e.* their average density decreased. Ideally, the spot size of the exciting laser should have been much larger than the biggest studied micropillar, so that the initially injected free carrier density would have been the same for all micropillars. In reality we had a focused laser spot. For different micropillars, we tried to inject the same free carrier density. But once the free carriers were distributed inside the micropillar, thanks to diffusion, the free carrier density N might vary from pillar to pillar. We had difficulties to control the injected free carrier density N , a fact that is shown by the initial switching amplitude.

In this context, it may be of interest to know how much time the initially injected free carriers take to diffuse inside the different micropillars. Zhao *et al.* [116] described the time dependance of the width w of a Gaussian free carrier spatial distribution to be:

$$w^2(t) = w_0^2 + 16 \ln(2) D_a t . \quad (3.13)$$

The initial value of the width is w_0 . In our case, $w_0 \approx 1\mu\text{m}$; except for the $5\mu\text{m}$ pillar, where it was a few μm . The width of the free carrier distribution $w_0 = 1\mu\text{m}$ will equal the pillar diameter in about $\tau_{\text{spread}} \approx 43$ ps (16 ps, 80 ps) for a pillar of $3\mu\text{m}$ diameter, ($2\mu\text{m}$, $4\mu\text{m}$ respectively). This process is very fast, so that it will not affect the long-time components of the spectral return of cavity modes.

Studying the recombination mechanism and diffusion processes of free carriers in micropillar cavities, we showed and explained how the free carrier recombination dynamics and, as a consequence, the time dependent spectral cavity mode positions behave as a function of the micropillar diameter. The possible free carrier recombination dynamics were identified to be the radiative bimolecular recombination at short delays after the switching pulse, and an exponential decay with characteristic time $\tau_{e,h}$ at long delays. Bimolecular recombination should only be present, if the injected free-carrier density was very large,

⁸This gets obvious while comparing the ratio of pillar surface to pillar volume, which is $2\pi R h / \pi R^2 h = 2/R$, where h is the pillar height.

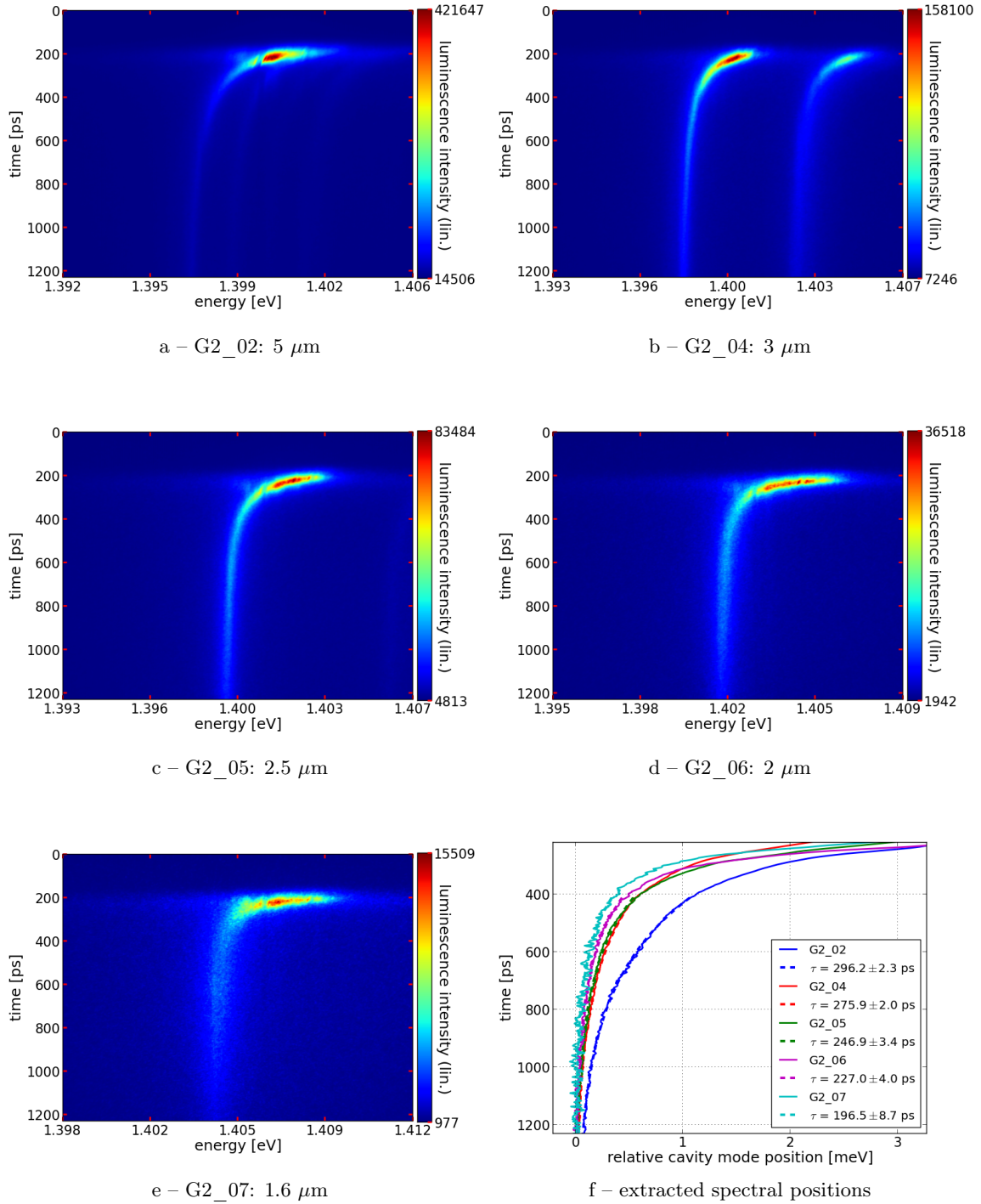


Figure 3.9: Switching micropillar cavities: showing the spectral return of the fundamental (and higher order; a-b) micropillar mode as a function of the pillar diameter. (a-e) Streak camera images; pillar name and diameter are indicated. Those images were taken under very similar conditions, with pulsed excitation using low average power, of about 1 mW (except for the 5 μm pillar, where we used 3 mW). (f) Extracted spectral positions of the fundamental micropillar modes (x-axis) of the five experiments, shown as a function of time (y-axis). The axes are analogous to the streak camera images. The dashed lines are interpolations of mono-exponential decays for long times (from $t \approx 400$ ps on). The resulting characteristic time $\tau = \tau_{e,h}$ is indicated for each fit. We observe that the smaller the micropillar, the faster the switched cavity mode returns to its spectral unswitched position.

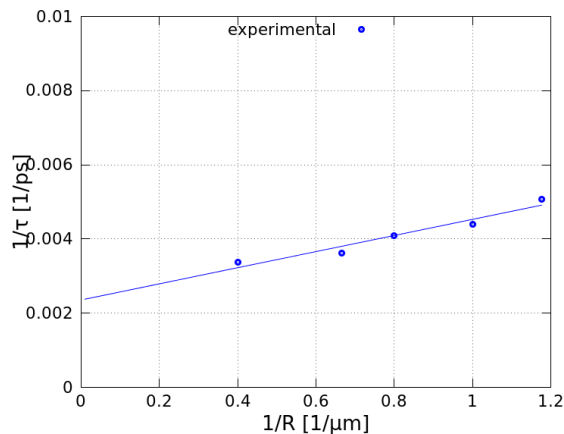


Figure 3.10: Measurement of the characteristic free carrier relaxation time $\tau_{e,h}$ as a function of the inverse of the pillar radius R . The datapoints are extracted from figure 3.9f. The line is the linear interpolation of the datapoints, in order to deduce $t_{\text{bulk}} = 424$ ps and the slope $\alpha_S S = 0.0022 \mu\text{m}/\text{ps} = 2.2 \cdot 10^3$ m/s.

what was rarely the case. The main contribution to $\tau_{e,h}$ should be the nonradiative recombination on the pillar surface. We found a surface recombination speed $S = 1.33 \cdot 10^3$ m/s and a characteristic time of the free carrier relaxation in bulk material of $\tau_{\text{bulk}} = 424$ ps, observed at the sample temperature of 7 K.

3.3.3 Switching amplitude

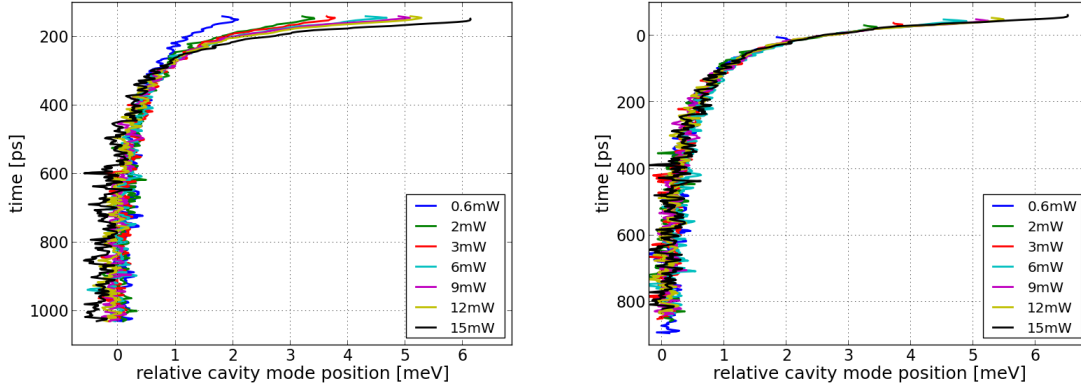
In a switching experiment, the maximal value of the energy-shift of the cavity modes — we call it switching amplitude — can increase with the exciting laser power and its photon energy. In this section we want to study this behaviour.

In a first study, we switched a micropillar with varying average laser powers, and observed how the fundamental cavity mode behaves. We used the pulsed Ti:sapphire operating at 800 nm. The figure 3.11 shows in the subplot (a) the time-dependent spectral positions of the fundamental cavity mode, as it was extracted from streak-camera images. The studied pillar is D2_04 and has a diameter of $3 \mu\text{m}$. The average laser power is indicated. The higher the average laser power, the larger the switching amplitude.

In the subplot (a), the lines for the different laser powers do not superpose. Two effects have to be taken into account in order to superpose them: First, for high laser power, above about 8 mW, the micropillar is heated, and that redshifts the unswitched cavity mode position. Second, the maximal energy shift of the lines — the switching amplitude — differs from line to line, but occurs at the same time. Therefore these lines — if they follow the same decay — do not superpose. We can correct the red-shift and delay the lines so that they cross at a given moment a certain energy-shift: We shifted the lines in time in order to cross the relative cavity mode position of 2.54 meV at $t = 0$ ps. If the lines

show all the same decay — as we expect — they should superpose after these corrections.

This result is depicted in the subplot (b). The time-dependent spectral positions of the fundamental cavity mode superpose now very well. This proves that they follow the same decay. With increasing laser power, we only changed the initially injected free carriers density, which is proportional to the switching amplitude.



a – spectral cavity mode position as extracted from streak-camera images

b – the lines of subplot (a) are superposed

Figure 3.11: Spectral cavity mode position (x-axis) as a function of the time (y-axis), shown for switching experiments of the micropillar D2_04. The axes are chosen in analogy to streak camera images. The laser power is indicated in the legends. One can identify the power depending switching amplitude.

It is now of interest to extract the switching amplitude and plot it against the laser power. This is shown in the figure 3.12. Two other micropillars are also shown: G2_04 and G2_06. They were excited with the same pulsed laser as used for the previous micropillar, and still operating at 800 nm. The properties of the three micropillars are listed in the table beneath. We denote the switching amplitude with $\Delta E|_{max}$.

The figure shows for all micropillars that, for low laser power, the switching amplitudes increase linearly with the excitation power. With increasing laser power — from a few milliwatt on — every dataset shows saturation. The saturations and the maximal reached switching amplitudes are very similar for the different micropillars.

The maximal obtained values for the switching amplitude $\Delta E|_{max}$ were extracted from the figure and are listed in the following together with the characteristics of the micropillars:

pillar	d	E_m	$\Delta E _{max}$	ΔE_m	$\Delta E _{max}/\Delta E_m$
G2_04	3 μm	1.397 eV	6.16 meV	0.379 meV	16.3
D2_04	3 μm	1.372 eV	6.60 meV	0.425 meV	15.5
G2_06	2 μm	1.402 eV	6.70 meV	0.673 meV	10.0

where d is the pillar diameter, E_m the unswitched cavity mode position, and ΔE_m the

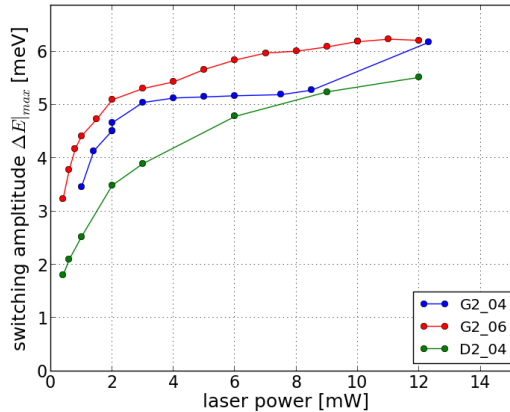


Figure 3.12: The maximum switching amplitude as a function of the laser power. Each circle corresponds to one switching experiment with the laser set at 800 nm. Three different micropillar cavities were shown.

cavity linewidth. Energy shifts of up to 16 cavity linewidths were observed, while the maximum value for the relative switching amplitude $\Delta E|_{max}/E_m$ is about 0.48%.

As we saw, the switching amplitude increases as a function of the pump intensity and saturates above a certain threshold intensity. Its maximum value, obtained at saturation, is very similar for different pillar sizes. This reflects a saturation of the density of the free carriers in the pillar's GaAs layers. We will explain and estimate this saturation in the following.

Estimation of the switching amplitude

We want to estimate the maximal reachable switching amplitude with pulsed excitation. To this purpose we will study the free carrier density — to which the energy-shift in cavity-switching is proportional — depending on the laser wavelength and average power.

The absorption of a photon by a semiconductor material can be described with the help of the semiconductor's dispersion diagram. In this diagram, the absorption of a laser photon corresponds to a vertical transition of an electron from the valence band to the conduction band. (Before any excitation, the valence band was completely filled with electrons and the conduction band empty.) This transition has to be quasi-vertical and resonant to the photon energy, so that wavevector (*i.e.* \mathbf{k}) and energy are conserved. Such transition locally fills the conduction band and depletes the valence band, and can saturate. In order to absorb further photons to further fill the conduction band with electrons, the now empty electron state in the valence band, *i.e.* a hole, has to be filled and the filled electron state in the conduction band has to be emptied. Electrons can relax to lower energies by phonon emission and will therefore fill the bottom of the conduction band and the holes fill the top of the valence band, making room for new excitation. This is precisely what electrons experience as they cool down after excitation with photons at an energy

larger than the bandgap. In GaAs it happens on the few-picosecond time-scale and may explain the time for the “switch-on” (*cf.* section 3.3.1). If the laser excitation is above an intensity threshold and long compared to the cooling of the electron-bath, the conduction band can be completely filled, up to the resonant transition (or the valence band completely depleted)⁹. Therefore the absorption of the laser saturates.

It seems that this happened in our experiments, as showed by the following calculations. A useful consequence is that the injected free carrier distribution in the GaAs layers could easily be very spatially homogeneous. This can be of interest for cavity switching experiments and other applications.

We can calculate the maximal excitable electron density N_e under the assumption of filling all available electron states in the conduction band up to a given energy E . With the help of this calculation also the switching amplitude $\Delta E|_{max}$ could be estimated. We calculate the electron density N_e in the conduction band via the density of states in three dimensions:

$$D_{3D}(E) = \frac{dN_e}{dE} = \frac{\sqrt{2m_e^*{}^3(E - E_{CB})}}{\pi^2\hbar^3}. \quad (3.14)$$

where E_{CB} is the energy of the conduction band and m_e^* is the effective mass of electrons. Integration leads to the accessible N_e for the given energy E , ($E > E_{CB}$):

$$N_e = \frac{\sqrt{2m_e^*(E - E_{CB})}^3}{3\pi^2\hbar^3}. \quad (3.15)$$

The same calculation can be done for the hole density N_h in the valence band. This results in:

$$N_h = \frac{\sqrt{2m_{hh}^*(E_{VB} - E)}^3}{3\pi^2\hbar^3}. \quad (3.16)$$

where E_{VB} is the energy of the valence band and m_{hh}^* is the effective mass of the heavy holes.¹⁰ In order to calculate the accessible total free carrier density, we introduce the effective mass $\frac{1}{m^*} = \frac{1}{m_e^*} + \frac{1}{m_{hh}^*} = \frac{1}{0.067m_e} + \frac{1}{0.45m_e} = \frac{1}{0.058m_e}$ (the electron mass $m_e = 9.11 \cdot 10^{-31}$ kg). The accessible total free carrier density N_{max} , describing the density of the linked electron-hole states, is in good approximation¹¹:

$$N_{max} \approx \frac{\sqrt{2m^*(E_{laser} - E_{GaAs})}^3}{3\pi^2\hbar^3} \quad (3.17)$$

where the laser is set at the energy E_{laser} . At 7 K the GaAs band-gap $E_{GaAs} \approx 1.52$ eV. For a narrowband laser resonant to E_{laser} , one obtains

- for $E_{laser} = 1.55$ eV ($\lambda = 800$ nm): $N_{max} \approx 3.3 \cdot 10^{17}/\text{cm}^{-3}$,

⁹For GaAs, the valence band is flat compared to the conduction band. That means that for a given energy-width much more \mathbf{k} -states exist in the valence band than in the conduction band. We can therefore concentrate on the limitation coming from the electron density in the conduction band.

¹⁰Light holes exist, too, but in the case of GaAs barely influence N_h compared to the heavy holes. We can here neglect them.

¹¹As the experiments are conducted in the regime of large free carrier injection, many other effects (*e.g.* band-gap shrinkage and band-filling) can influence the actual GaAs band-gap. Those effects partially compensate each others and can be neglected in a first approximation.

- for $E_{\text{laser}} = 1.59$ eV ($\lambda = 780$ nm): $N_{\text{max}} \approx 1.2 \cdot 10^{18}/\text{cm}^{-3}$,
- for $E_{\text{laser}} = 1.70$ eV ($\lambda = 730$ nm): $N_{\text{max}} \approx 4.9 \cdot 10^{18}/\text{cm}^{-3}$.

This result suggests that larger shifts should be obtained by decreasing the excitation laser's wavelength, so as to be able to inject a larger density of free carriers.

In the experiments, our femtosecond Ti:sapphire excitation laser has a spectral width of around 10 nm. One has to note that energies higher than the resonant one are accessible with the tail of the laser spectrum. This can slightly increase N_{max} .

For an electron density of $N_e \approx 10^{18}/\text{cm}^{-3}$ Bennett *et al.* [111] predicted a relative GaAs refractive index change of 1%, which should be equal to $\Delta E|_{\text{max}}/E_m$ following equation 3.4. With the laser set at $\lambda = 800$ nm, the predicted maximal free carrier density is $N_{\text{max}} \approx 0.33 \cdot 10^{18}/\text{cm}^{-3}$. Thus the expected maximal relative refractive index change should be 0.33%, as well as the maximal relative switching amplitude $\Delta E|_{\text{max}}/E_m$.

To resume, we expect for a laser set at $\lambda = 800$ nm to observe a maximal relative switching amplitude of $\Delta E|_{\text{max}}/E_m \approx 0.33\%$. Above, we experimentally observed $\Delta E|_{\text{max}}/E_m \approx 0.48\%$. As the used pulsed laser is not monochromatic, but has a certain spectral width, this result is in good agreement with the explained saturation process.

In the following, I will estimate the average laser power $\overline{P_{\text{sat}}}$ necessary to saturate the free carrier injection. The number of free carriers that can be injected in one micropillar — which is $n_{\text{e,h}} = N_{\text{max}}V_{\text{GaAs}}$ — has therefore to be compared with the number of photons per laser pulse n_{ph} entering the micropillar. For an average laser power $\overline{P} = 1$ mW the laser beam transports 1 mJ = $6.2 \cdot 10^{15}$ eV per second (*i.e.* $\overline{P} = 6.2 \cdot 10^{15}$ eV/s). With a repetition rate of $f = 76$ MHz, each laser pulse contains — for the laser resonant at $E = 1.55$ eV — $n_{\text{ph}} = \frac{\overline{P}}{fE} = 53 \cdot 10^6$ photons (if $E = 1.7$ eV: $n_{\text{ph}} = 48 \cdot 10^6$). A part of those photons ($\sim 30\%$) will be reflected at the pillar surface. Most of the remaining $n_{\text{ph}} \approx 35 \cdot 10^6$ photons should be absorbed in the micropillar cavity, as long as the absorption is not saturated. We estimate $\overline{P_{\text{sat}}}$ for a 3 μm micropillar¹² for different wavelengths of the exciting laser to be:

- for $E = 1.55$ eV ($\lambda = 800$ nm): $n_{\text{e,h}} \approx 5 \cdot 10^6 \Rightarrow \overline{P_{\text{sat}}} = 0.13$ mW,
- for $E = 1.59$ eV ($\lambda = 780$ nm): $n_{\text{e,h}} \approx 19 \cdot 10^6 \Rightarrow \overline{P_{\text{sat}}} = 0.5$ mW,
- for $E = 1.70$ eV ($\lambda = 730$ nm): $n_{\text{e,h}} \approx 73 \cdot 10^6 \Rightarrow \overline{P_{\text{sat}}} = 2.1$ mW.

Those values were found using the relations $n_{\text{e,h}} = N_{\text{max}}V_{\text{GaAs}}$ and $\overline{P_{\text{sat}}} = \frac{n_{\text{e,h}}}{0.7} fE$ (equal to the amount of the needed photons for the saturation $n_{\text{ph}} = \frac{n_{\text{e,h}}}{0.7}$ times the repetition rate f times the photon energy E). They are of the same order of magnitude as the experimentally obtained values for saturation (*cf.* the figures 3.12 and 3.13).

¹²A pillar with a diameter of 3 μm has GaAs volume $V_{\text{GaAs}} \approx 1.5 \cdot 10^{-11} \text{cm}^3$.

Switching amplitude in function of the wavelength of the exciting laser

Above we found that a decreasing wavelength of the exciting laser should increase the maximal amplitude of the switch $\Delta E|_{max}$. We want to confirm this experimentally: In the figure 3.13 we illustrate the switching amplitude as a function of the laser power for different wavelengths of the exciting pulsed laser. Two different micropillars are studied, as indicated.

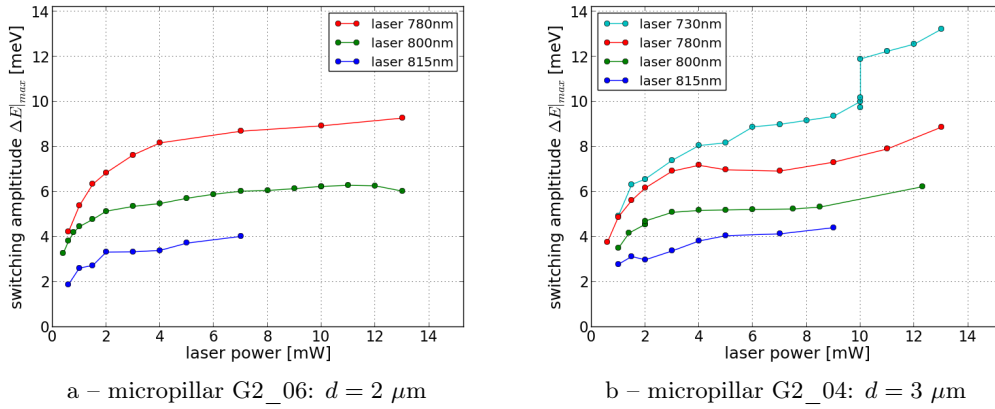


Figure 3.13: The switching amplitude as a function of the laser power for different wavelengths of the exciting pulsed Ti:sapphire laser. Each circle corresponds to one switching experiment. Two different micropillars are studied.

Both micropillars reveal that, in the regime of low excitation power, the switching amplitude is larger and increases faster, when the excitation wavelength is smaller. This can be explained by the fact that the photon absorption probability increases with decreasing wavelength. In the regime of high excitation power, the switching amplitude always saturates. The smaller the excitation wavelength, the larger the maximal injectable free carrier density can be, and the switching amplitude saturates at a higher value.

The maximal switching amplitude that I observed is shown in the streak-camera image of figure 3.14. It is as high as 13 meV, equal to 34 cavity linewidths. It was obtained with the micropillar G2_04 and the pulsed laser operating at 730 nm with an average power of 10 mW.

We studied here the maximal accessible switching amplitude and the related free carrier density. We found that the absorption of laser photons can saturate — and with it the injectable free carrier density. This process depends on the wavelength and power of the exciting laser pulse. An interesting consequence is that in the regime of saturation of the absorption, the injected free carrier distribution can be very spatially homogeneous. Under optimal conditions, the maximal observed energy shift for cavity switching was 13 meV or 34 cavity linewidths.

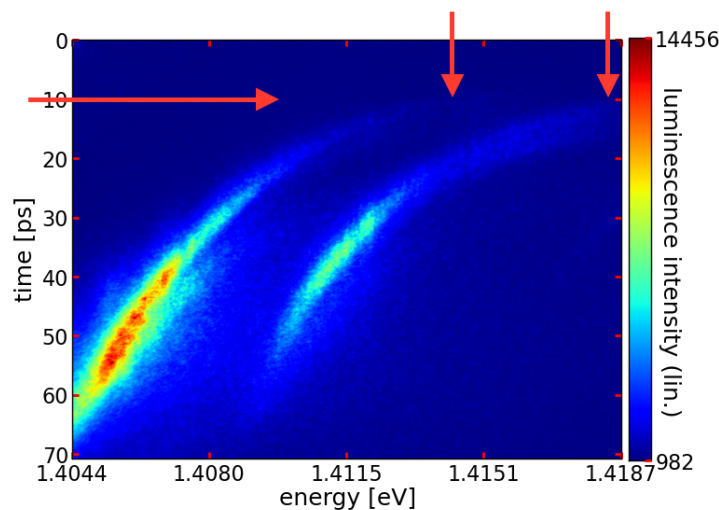


Figure 3.14: A very large switch. The fundamental and first high order cavity modes are shown. Their maximal reached spectral positions and the moment of the switch are indicated with the red arrows. The return of the modes back to their unswitched values is out of the window. The high temporal resolution evidences that it takes between 30 and 45 ps for the QD emission to reach its maximum, similar to the value given in reference [97].

In this section we studied cavity switching by all-optical free carrier injection of micropillar cavities and identified the main characteristic properties. Those were the “switch-on” (*i.e.* the time needed to reach the maximal energy shift), the following free carrier recombination which governed the time-dependent spectral cavity mode positions, and the amplitude of the energy shift induced by the switch. The main characteristics that is still to be discussed is a possible differential behaviour of neighbouring cavity modes, and is presented in the next section.

3.4 Differential switching of micropillar cavity modes

Up to now the shown cavity switching experiments of micropillars present homogeneous switches. The fundamental and higher order modes have exhibit very similar switching amplitudes and time-evolutions. Differential switching means that different cavity modes behave in different ways.

As the switch of the cavity modes originates from the all-optical injected free carriers, the differential switching can be understood by considering the spatial overlap of the injected free carriers with the cavity mode’s field distribution. A local perturbation of the refractive index, via an increased free carrier concentration, will only influence a cavity mode resonance if its mode field is relatively intense in the perturbed region. A free carrier

injection which is localised at the centre of the micropillar will preferentially switch the fundamental cavity mode, as well as all other modes which possess an antinode on the pillar axis.

Thyrrestrup *et al.* tested this idea [84]. They probed the reflectivity of the switched micropillar in a pump–probe experiment and observed a stronger initial blue-shift for the fundamental cavity mode than for the first higher order cavity mode, addressing the switch preferentially to the fundamental cavity mode. Here, we want to study differential switching using QDs which can probe the ensemble of the micropillar cavity modes at the same time (same sample and procedure as in the previous sections). Thanks to the QD transition lifetimes of several hundred picoseconds, the entire dynamics of the time-dependent cavity mode positions can be probed and observed by the streak camera. Proceeding as mentioned, we exploited different regimes of differential switching.

The pulsed Ti:sapphire laser was used to both excite the QD transitions and generate the free carriers inside the micropillar's GaAs (so as to switch the cavity modes). It operated at 733 nm and at the indicated powers. To enable a localised excitation, the laser spot size was about 0.84 μm (FWHM diameter), much smaller than the diameters of the studied micropillars.

Three different micropillars were studied:

- A circular micropillar with small diameter (3 μm). The fundamental and first higher order cavity mode were spectrally well separated and fit inside the spectral window of the detection. A differential switch similar to the observation in reference [84] was obtained.
- An ellipsoid micropillar. The minor axis is 3 μm long and the major axis about 6 μm long. The field distributions of the fundamental and first higher order cavity modes are very different. Selective switching of one or the other mode can be more easily realised. These results are the most illustrative ones.
- A circular micropillar with large diameter (5 μm). The spectral separation of the cavity modes was small and many of them fit inside the spectral window of the detection. New, differential switching effects were observed.

Simulations were conducted to support our analysis of the experimental results obtained with the small circular micropillar.

3.4.1 Differential switching of a small micropillar

A relatively small circular micropillar was switched with a localised central excitation. The focused laser FWHM spot diameter was measured to be about 0.84 μm . This was much smaller than the micropillar diameter of about 3 μm . According to the reference [84], the fundamental cavity mode should switch with larger amplitude than the first higher order mode. This is indeed what we observe experimentally, as shown in the figure 3.15.

The fundamental cavity mode experienced a stronger initial blue-shift (maximal energy-shift 2.6 meV) than the first higher order cavity mode (maximal energy-shift 2.1 meV). Furthermore, the spectral return during the first hundred picoseconds is faster for the fundamental cavity mode than for the first higher order cavity mode. Afterwards both cavity modes show a very similar spectral relaxation.¹³

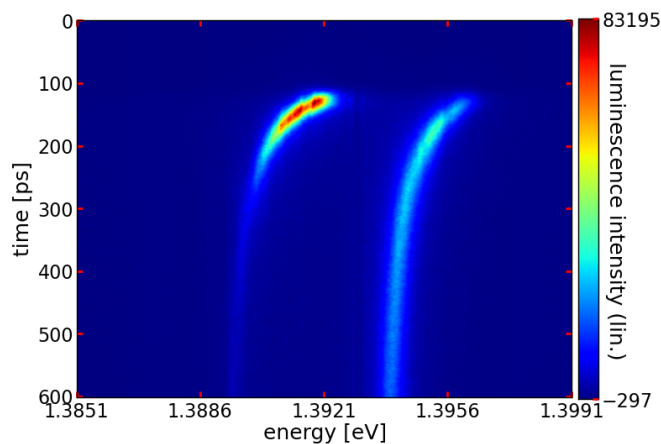


Figure 3.15: Differential switch of a micropillar (diameter $3 \mu\text{m}$, pillar F2_04). The exciting laser having the average power 0.6 mW hits the centre of the micropillar. The fundamental cavity mode is more switched than the first high order cavity mode and its initial relaxation is faster. This can be explained by the spatial overlap of the cavity modes and free carrier distribution inside the micropillar.

Both features of the differential switching — the different switching amplitudes and the different spectral returns — can be understood by considering the overlap of the spatial distributions of the cavity modes and of the free carriers. The switching amplitude depends on the initial overlap of the local free carrier density and mode profile, while the initial decay rate depends on the free carrier diffusion.

3.4.2 Simulation of differential switching

In order to understand the differential switching, I computed the cavity mode profiles, the injected spatial free carrier density, and the temporal evolution of the spatial free carrier density. With this, I could simulate the time-dependent cavity mode positions.

The central in-plane cavity mode profile is like the mode profile of a guided mode in an infinite circular waveguide with the same diameter d as the micropillar. The derivation of such mode profiles is described in [117] and in many textbooks. In figure 3.16 are shown

¹³The difference in the signal intensity of both modes result from the detection. The streak camera is very sensitive to the directionality of the signal. Depending on the position of the lens at the entrance of the monochromator the different modes are more or less detected.

the in-plane mode profiles of the first four modes of an infinite circular waveguide with diameter $3 \mu\text{m}$, made of GaAs and surrounded by air, like the micropillar. These modes are called HE_{11} , TE_{01} , HE_{21} and TM_{01} . HE_{11} has the same lateral profile as the fundamental cavity mode. TE_{01} , HE_{21} and TM_{01} give rise to the first higher order cavity mode, which is a triplet. The contribution of TE_{01} is resonant to lower energy, HE_{21} in the centre, and TM_{01} to higher energy. The intensities of their mode profiles are almost identical, as illustrated. Differences are hardly visible, but exist.

The maps shown of the mode profiles clearly evidence that a central free carrier excitation will strongly influence the fundamental cavity mode and much less the next mode (before the free carrier diffusion homogenise their distribution). This is in complete agreement with the differential switching in figure 3.15.

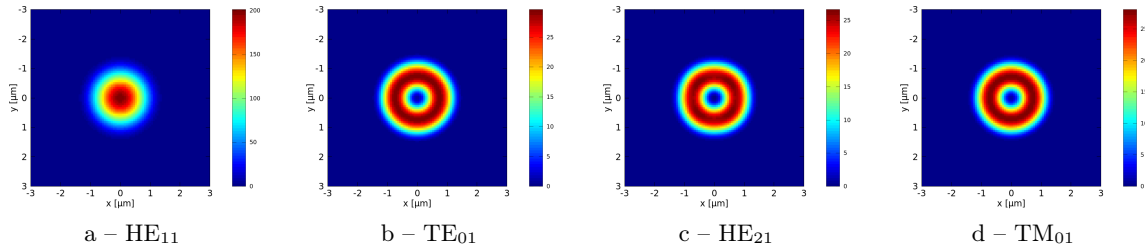


Figure 3.16: Intensity of the in-plane mode profiles ($|E_r|^2 + |E_\theta|^2 + |E_z|^2$) of an infinite circular waveguide with diameter $3 \mu\text{m}$, made of GaAs and surrounded by air, like the studied micropillar. The guided mode HE_{11} gives rise to the fundamental cavity mode and the three other guided modes give rise to the first higher order cavity mode, which is a triplet.

Now we want to study the time dependent free carrier distribution during the switching.

The initial free carrier distribution is determined by the excitation laser pulse. No saturation of the free carrier absorption should occur, as long as the exciting laser power does not exceed a few milliwatt (for the laser set at 733 nm). Thus in the experiment the initially injected free carrier concentration was inhomogeneous along the micropillar axis and decayed exponentially with the penetration depth of the laser. But, in order to simplify the computation, and to show that the effect comes from the lateral variations of the spatial free-carrier distribution, the simulations will consider that free carrier distribution is homogeneous along the pillar axis. In-plane, the initial free carrier distribution is proportional to the Gaussian-like shape of the laser spot. Once injected, the carrier distribution evolved by diffusing and recombining. This is described by the equation 3.11. We assumed a cylindrical symmetry. No bimolecular recombination needs to be considered as the injected free carrier density was low enough (about $2 \cdot 10^{17} / \text{cm}^3$ in the experiment of figure 3.15).

In the section 3.3.2, I found a surface recombination speed $S = 1.33 \cdot 10^3 \text{ m/s}$ and a characteristic free carrier lifetime in bulk GaAs of $\tau_{\text{bulk}} = 424 \text{ ps}$. I used this as input for the simulation of the cavity mode positions of figure 3.15. In addition, I used again

$D_a = 170 \text{ cm}^2/\text{s}$ as determined in the reference [116]. The pillar diameter — calculated from the separation of the unswitched fundamental and first higher order mode — is $d = 3.05 \text{ }\mu\text{m}$, and thus slightly larger than the expected one. The computed mode profiles superpose best with the experimental data in figure 3.15 for an exciting laser spot FWHM diameter as large as $1.8 \text{ }\mu\text{m}$.¹⁴

Using those parameters, I calculated the temporal and spatial evolution of the radial free carrier density N in the micropillar. This is shown in the figure 3.17, together with the corresponding radial profile of the relative refractive index change $\Delta n/n$. $\Delta n/n$ is negative, so the cavity modes are blue-shifted.

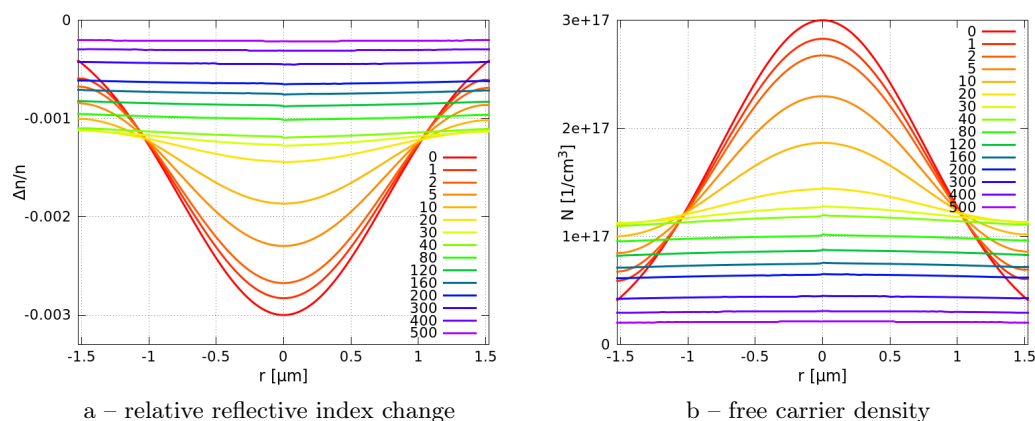


Figure 3.17: Evolution of the radial relative refractive index change and the radial free carrier density under free carrier diffusion and recombination. The corresponding moment of each trace is indicated in the legend in the unity of picoseconds.

After injection of the free carriers at $t = 0$, the shape of $\Delta n/n$ is given by the shape of the exciting laser beam. At short times the carriers diffuse and the shape of $\Delta n/n$ becomes wider. At longer times the shape of $\Delta n/n$ becomes more or less stable, but continues to decrease in amplitude. The stable shape results from the combination of the surface recombination and the carrier diffusion.

At all times, the profile of $\Delta n/n$ is much closer to the mode profile of the fundamental cavity mode than to the mode profile of the first higher order cavity mode (*cf.* figure 3.16). This explains the observed energy-shifts in figure 3.15, which are always stronger for the fundamental cavity mode than for the first higher order cavity mode.

To reproduce the experimental data of figure 3.15, the micropillar mode resonances were calculated for the estimated time-dependent and radial refractive index of figure 3.17, by solving the equation 1.21 numerically. The result is shown in figure 3.18. The theory describes well the temporal evolution of the switched cavity modes in the experiment: the differential switching amplitude and the different decays are reproduced.

¹⁴The estimated FWHM of $0.84 \text{ }\mu\text{m}$ was obtained by measuring the focused laser spot size. Probably, inside the spacer of the micropillar, the laser is not the ideally focused. Thus, the spot diameter in the plane of the spacer might be bigger.

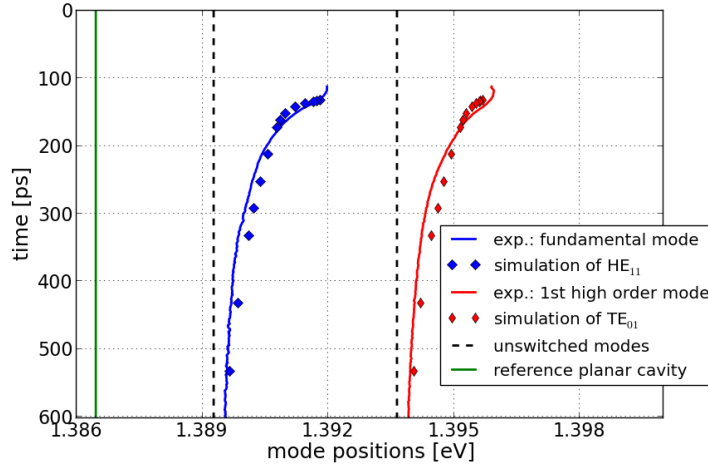


Figure 3.18: Differential switching in a circular, $3 \mu\text{m}$ diameter micropillar. The blue and red lines (representing fundamental and first higher order micropillar mode, respectively) show the extracted cavity mode positions of figure 3.15. The blue and red dots are the simulation results and fit well the experimental lines. After the switching event, the two micropillar modes return to their unswitched values, which are indicated by the black dashed lines. The green line shows the resonance of the corresponding planar cavity. (Let me note that there is a zero offset of 133 ps compared to figure 3.17.)

Up to now, I showed a first demonstration of differential cavity switching and could explain this with a model describing carrier diffusion, bulk- and surface recombination. In the following I will further discuss differential switching exhibiting new differential behaviours.

3.4.3 Differential switching of an ellipsoid micropillar

In a strongly elongated ellipsoid micropillar the fundamental cavity mode is concentrated in the central part of the ellipse. The first higher order cavity mode is concentrated close to the antipodal points of the ellipse. Their spatial selection by free carrier injection is much easier than for a circular micropillar. We study an ellipsoid micropillar with a $3 \mu\text{m}$ minor axis and a $6 \mu\text{m}$ major axis. Positioning the exciting laser at the centre of the micropillar surface resulted in the streak camera image shown in figure 3.19a. As expected, the fundamental cavity mode was much more switched than the higher order cavity modes. Positioning the exciting laser close to one antipodal point of the micropillar resulted in the streak camera image shown in figure 3.19b. The higher order cavity modes were more switched than the fundamental cavity mode. We were therefore able to control the switching preferentially to the desired cavity mode.

The extracted time-dependent spectral positions of the three observed cavity modes illustrate nicely the differential switching (see figure 3.19c). The power of the exciting laser was adjusted to keep the initial blue-shift of the first high-order cavity mode constant

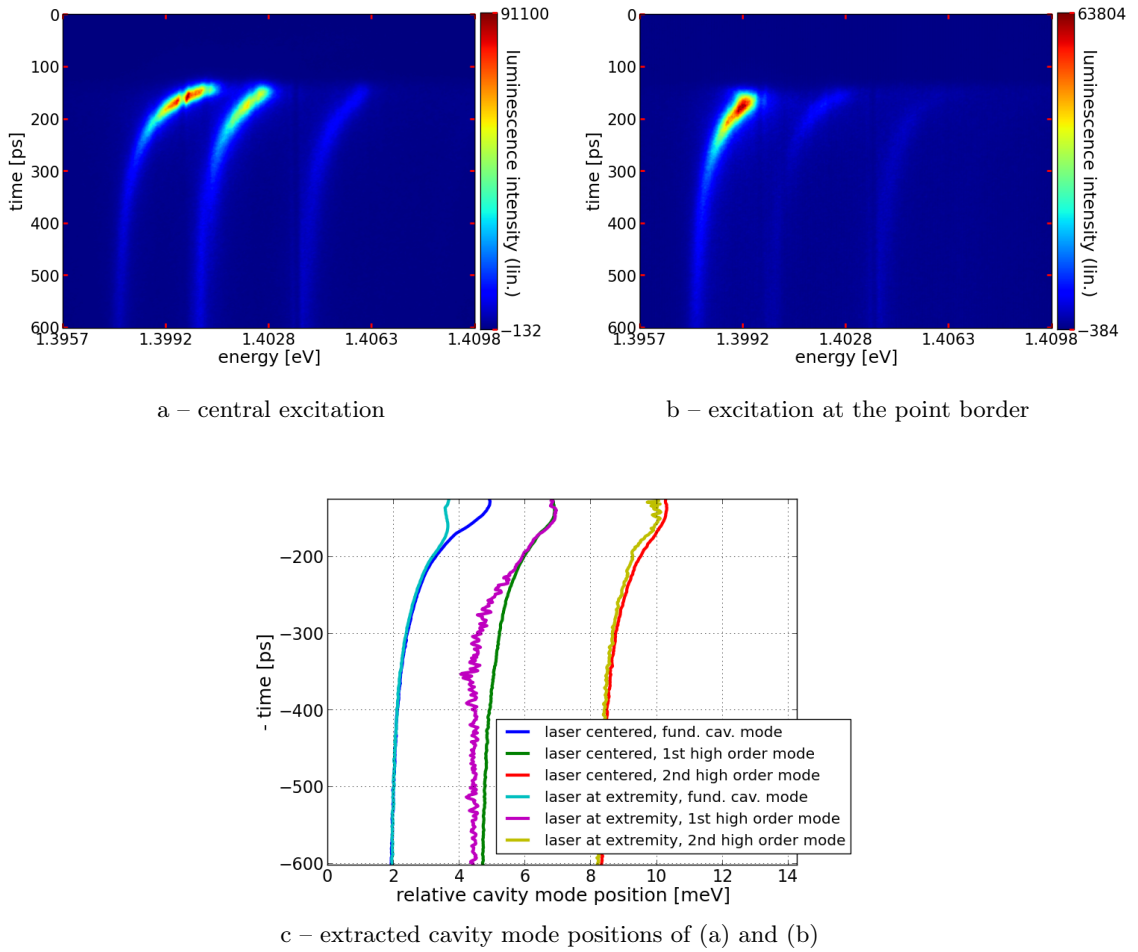


Figure 3.19: Differential switch of an ellipsoid micropillar. Streak camera images are shown for central excitation (a) and excitation around one of the antipodal points (b) of the ellipsoid micropillar. Once the fundamental, once the higher order cavity modes were more switched, respectively. The cavity mode positions are extracted and plotted (c). The spot diameter of the exciting laser was about $0.84 \mu\text{m}$ at FWHM and its average power was 0.6 mW (a) or 3.7 mW (b). In (b) the laser spot impinges in part next to the micropillar. The laser power was adjusted to make the experiments comparable. We chose the first higher order cavity mode to have a constant initial blue-shift, here approximately 2.3 meV .

and equal to 2.3 meV , in order to ease the comparison of both differential switches.

The fundamental cavity mode experienced a strong switch for the central excitation of the ellipsoid micropillar. The maximal blue-shift was 3 meV and was reached at $t = 127.6 \text{ ps}$. For excitation at one antipodal point the maximal blue-shift was only 1.7 meV and was reached at $t = 160.5 \text{ ps}$, thus 33 ps later than in the first case. The injected free carriers had to diffuse to the centre of the ellipsoid micropillar in order to make the fundamental

mode switch maximal. This took some time. As they could recombine in the meantime, and due to their diffusion, the local free carrier concentration switching the fundamental cavity mode is reduced, as well as the maximal obtainable blue-shift. The diffusion process was described with equation 3.13 and examples were given. The 33 ps difference agrees with that. The free carriers do not take much more time to be homogeneously distributed inside the cavity. The two decays of the fundamental mode confirm this, as they follow the same trace for $t \gtrsim 180$ ps.

We set the experimental conditions so that the first higher order cavity mode had twice an initial blue-shift equal to 2.3 meV. This maximum was reached in both cases at about $t = 140$ ps, slightly (12 ps) after the fundamental mode reached its maximum for the case of central excitation. This means that for both spatial excitations the initial carrier diffusion increased the overlap of free carrier distribution with the mode profile of the first higher order cavity mode. The time-dependent decays of this mode can hardly be compared as the magenta line in figure 3.19c shows a considerable noise for $t > 200$ ps.

The second high order cavity mode behaved very similarly for both spatial positions and corresponding powers of the exciting laser. The maximum blue-shift was twice 2.0 meV and the spectral return followed the same trace. The maximal blue-shifts were reached at $t = 140$ ps and coincide with the maxima for the first higher order cavity mode. This second high order cavity mode seems to be barely influenced by the applied differential switching. This can be traced back to the fact that such modes have antinodes both at the centre and close to the edges of the micropillar [118].

Using an ellipsoid micropillar we were able to control the switching in a selective way to the first two micropillar modes: central excitation favoured the fundamental mode switching, while antipodal point excitation favoured the first higher order cavity modes.

3.4.4 Differential switching of a big micropillar

A larger number of cavity modes can be studied by switching a bigger micropillar. The cavity mode separation is smaller and many nearby cavity modes can enter the spectral window detected by the streak camera. We used a circular micropillar with $5 \mu\text{m}$ diameter. A spatial homogeneous switch affects all the cavity modes in the same way. We defocused the exciting laser so that it illuminated a much larger area than the pillar size with a nearly flat constant value. Higher laser power was needed to keep similar switching amplitudes. Other light-emitting structures were sufficiently far away and the signal from them was not detected. The in-plane free carrier excitation inside the micropillar should be much more homogeneous than in the previous studies. Figure 3.20a illustrates the resulting, quite homogeneous switch of the cavity modes for this micropillar. The fundamental cavity mode was the one resonant to the smallest energy. All the modes shown behaved similarly, the signature of a homogeneous switch.

Switching this micropillar locally might affect many of its cavity modes in a different

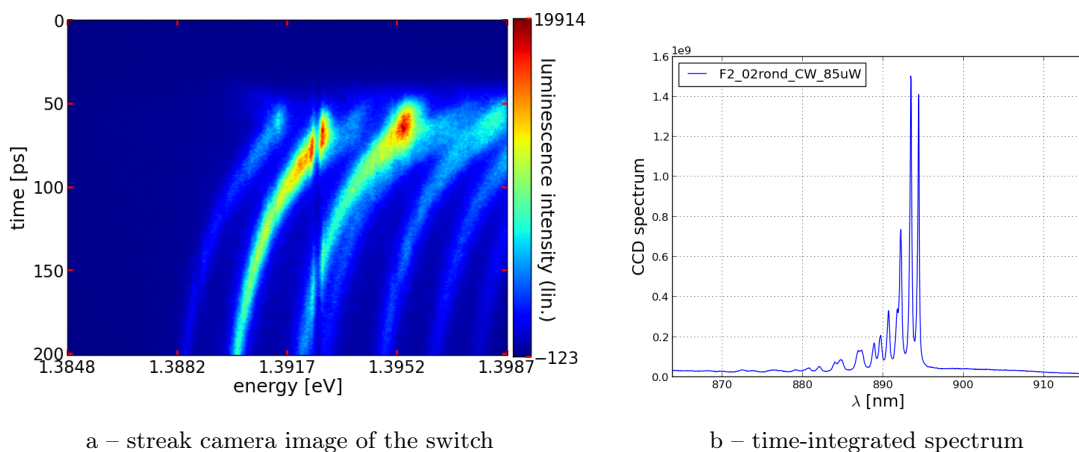


Figure 3.20: Homogeneous switch of a big circular micropillar (diameter $5 \mu\text{m}$, pillar F2_02) and its spectrum. For the switch, all micropillar cavity modes behaved almost in the same way. To this purpose the exciting pulsed laser was strongly defocused (spot diameter \gg pillar diameter) and excited the entire micropillar as homogeneously as possible. The average laser power was 15 mW. In this image one line-defect of the streak camera with decreased detection sensitivity is very visible. For the time-integrated spectrum, taken with a CCD detector, a CW laser (operating at 808 nm and $85 \mu\text{W}$) excited the QD transitions far below saturation. It shows all the nearby unswitched cavity modes of this micropillar.

way. We want to present two particular interesting and clear phenomena. The first is a behaviour of the switched modes depending on their symmetries: Even modes will behave in one manner and odd modes in another. The second is a splitting of the first higher order cavity modes.

With even modes we mean the second, fourth and sixth sets of cavity modes and with odd mode the first, third, fifth and seventh sets of cavity modes. We want to address selectively one class of those modes with differential cavity switching. Again the small exciting spot with diameter about $0.84 \mu\text{m}$ was used and excited the micropillar cavity off the central axis. At the right spatial position all even modes showed the common behaviour of a switched cavity mode. They were blue-shifted in an ultrafast way and relaxed back to their unswitched position. All odd modes showed a different behaviour (*cf.* figure 3.21). The odd modes first experienced an increase of their detuning during roughly 50 ps, reached their maximal blue-shift, and then relaxed back to their unswitched position. The initially injected and very localised free carriers are located close to an antinode (node) of the profiles of the even (odd) cavity modes. Their subsequent diffusion enabled, at later times, to switch all cavity modes in the same way. A typical diffusion time of 50 ps seems to be in agreement with the equation 3.13 for a micropillar of diameter $5 \mu\text{m}$.

The splitting of the first higher order cavity modes was observed for a very asymmetric switch of the micropillar. These modes are in fact a triplet. The three contributions have

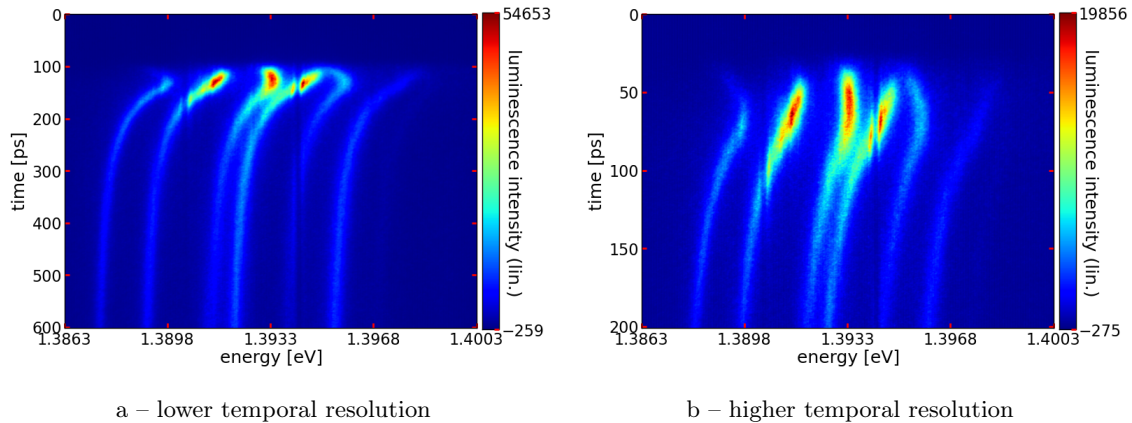


Figure 3.21: Differential switch of a big micropillar (diameter $5 \mu\text{m}$, pillar F2_02). The exciting laser (spot diameter $\sim 0.84 \mu\text{m}$) impinges on the micropillar off its central axis. Its average power was 1.5 mW . The same experiment is shown for two different temporal resolutions, resulting from two subsequent acquisitions. The high temporal resolution gives some detailed illustration of the beginning of the switch. All the odd cavity modes experienced an unusually slow “switch on” before relaxing back as usual to their unswitched value. The even cavity modes behaved as usual. (One has to note that the central energy was a different one compared to figure 3.20a.)

very similar spatial mode profiles, but their components of the electrical field differ. Mode splitting under an asymmetric switch is possible. The exciting pulsed laser was slightly defocused so that its spot diameter was comparable to the pillar diameter and hit the micropillar off-axis. Under this configuration the excitation could be highly asymmetric, switching only one side of the micropillar. The experiment result is shown in figure 3.22. A clear and strong splitting of the first higher order cavity modes was detected during the switching event. The initially strong splitting vanished within the following 40 to 50 ps. This corresponds to the time the free carriers needed to diffuse until they were homogeneously distributed inside the micropillar, establishing a homogeneous switch.

All the other cavity modes illustrate an inhomogeneous switch, too, but no additional mode-splitting was detected. The asymmetric free carrier excitation made that establishing the maximal blue-shift was delayed for all cavity modes. Once the free carriers were homogeneously distributed (at $t \approx 100 \text{ ps}$), the spectral returns of the cavity modes followed a common trend.

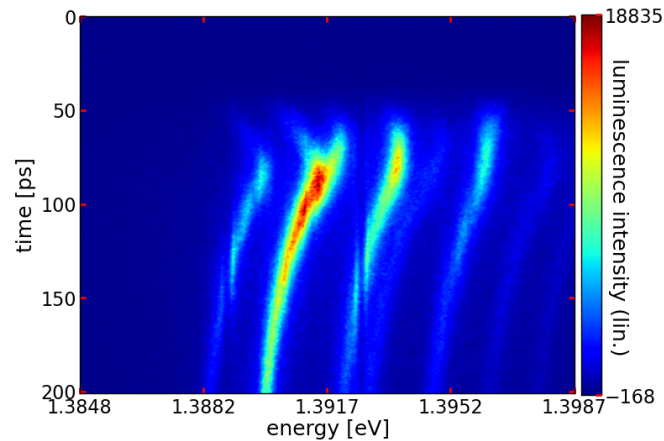


Figure 3.22: Differential switch of the big micropillar F2_02 (diameter $5 \mu\text{m}$). All visible micropillar modes were switched in a differential way and the first higher order micropillar mode split when the switch occurred. The exciting laser was slightly defocused (spot diameter comparable to the pillar diameter) and hit the micropillar off-centre to produce a very asymmetric switch. Its average power was 2.2 mW. Only part of the laser could excite free carriers inside the micropillar as some part of the laser spot hit the sample out of the micropillar.

In this section we studied the differential switching of micropillar modes. A spatial inhomogeneous free carrier injection allowed differential switching. The local perturbation of the refractive index (the local switch) affected selectively the cavity modes having different mode profiles. With the small circular and the ellipsoid micropillars we were able to control in a selective way the switching of cavity modes. The selected cavity mode, may it be the fundamental or the first higher order one, experienced a stronger initial blue-shift than all the other modes of the micropillar cavity. The big micropillar cavity with its numerous nearby cavity modes was switched in two regimes: First, the switch was addressed to all the even cavity modes which behaved as usual. All the odd cavity modes experienced an unusually slow “switch on” taking about 50 ps. Second, the free carrier injection was very asymmetric resulting in the splitting of the first higher order cavity mode triplet.

3.5 Conclusion

The characterization of switching micropillar cavities by all-optical free carrier injection using one-photon absorption lets us identify some characteristic properties of the switch, all observed at cryogenic temperatures.

The “switch-on” was very fast and took about 7 ps. The following recombination of the free carriers happened in a few hundred picoseconds and was governed by a combination of diffusion, bimolecular recombination and non-radiative recombination. The latter was a combination of surface and bulk recombination. We obtained a surface recombination speed $S = 1.33 \cdot 10^3$ m/s and a characteristic time of the free carrier relaxation in bulk material of about $\tau_{\text{bulk}} = 420$ ps.

The switched and time-dependent spectral micropillar mode positions are governed by these recombination and diffusion processes. We studied them as a function of the micropillar diameter and saw that the spectral return is faster for smaller micropillar cavities. The nearby pillar surfaces are the key parameter for recombination and spectral return.

The injected free carrier distribution could be very homogeneous in space, thanks to saturation of the absorption. The injected free carrier density and the resulting switching amplitude were estimated. We observed a maximal switch of about 13 meV energy shift, equal to 34 cavity linewidths for a 3 μm diameter micropillar with $Q = 3700$ quality factor cavity.

A spatial inhomogeneous free carrier injection allowed differential switching. The local perturbation of the refractive index (the local switch) affected the different cavity modes in a different way and we were able to switch selectively the cavity modes of circular and ellipsoid micropillars. Under particular conditions a splitting of the first higher order cavity mode triplet was detected. The differential switching of cavity modes could be simulated for the experimental configuration preserving circular symmetry, when taking into account the free carrier diffusion and recombination.

In the following chapter, the QD emitters will no longer figure as simple light source probing the cavity mode. We will study the real-time interactions between QD emitters and a switched cavity mode in the context of the Purcell effect.

In this theoretical chapter, we will see how to trigger a spontaneous emission process and how to shape the time-envelope of single-photon wave packets emitted by a two-level emitter. For example, single photons with Gaussian envelopes have interesting assets for linear optics quantum computing [119]. Furthermore, considering a simple time-reversal argument, a time-inverted exponential wave-packet can be absorbed with optimal probability by a second identical emitter, with potential application to the realization of an elementary quantum network [120].

In the static regime, cavity quantum electrodynamics effects, in particular the Purcell effect, can be used to control the spatial mode in which a single photon is emitted by a two-level emitter. In this chapter, we consider a dynamic situation, in which a time-dependent spectral detuning between the emitter transition and the cavity mode resonance introduces a time-dependent emission rate into the cavity mode. Such a supplementary degree of control allows one to dynamically shape the time envelope of the emitted photon, or to trigger its emission *i.e.* Purcell switching. In particular, this requires a control of the emitter-cavity mode coupling on a time scale shorter than the typical spontaneous emission dynamics.

4.1 About the real-time control of an emitter in a micro-cavity

The spontaneous emission rate of a two-level emitter depends on the available photon states. The integration in a cavity can strongly influence the emitter's photonic environment, leading to an inhibition or enhancement (Purcell effect) of the spontaneous emission

rate. Such modulation of the spontaneous emission rate is often used in QD-CQED (quantum dot-cavity quantum electro dynamics) to control the lifetime of the QD exciton. This lifetime can be probed with pulsed excitation of the emitter and results in either short or long spontaneous emission pulses, with an associated characteristic lifetime.

We can introduce a detuning dependent spontaneous emission enhancement factor $F(\delta)$. It describes how an energy detuning $\hbar\delta = E_m - E_{\text{QD}} \neq 0$ between the cavity mode E_m and the emitter transition energy E_{QD} influences the emitter's spontaneous emission rate. A QD in perfect resonance with a single cavity mode has the spontaneous emission rate $F_P\Gamma_0$ (Purcell effect with the Purcell factor F_P and the spontaneous emission rate in bulk material Γ_0). A non-zero detuning $\delta \neq 0$ reduces the spectral density of modes at the emitter's frequency. Hence this rate becomes $F(\delta)\Gamma_0$, the spontaneous emission rate for the detuned QD coupling to the cavity mode [121]. As the cavity mode has a Lorentzian form with spectral linewidth $\Delta\omega_m$, the enhancement factor F is in good approximation

$$F(\delta) = \frac{\Delta\omega_m^2}{\Delta\omega_m^2 + 4\delta^2} F_P . \quad (4.1)$$

This formulation is true as long as the emitter is placed at the maximum of cavity mode's electric field and if its dipole is oriented parallel to the field's polarisation, assumed to be so all along this chapter. Furthermore the line-width of the emitter transition has to be thin compared to the line-width of the cavity mode, true in the weak-coupling regime. A full description for an arbitrary orientated emitter is given in [2]. Reducing (increasing) the detuning δ increases (inhibits) the spontaneous emission into the cavity mode.

A time-dependent detuning, applied between QDs or other two-level emitters — like atoms — and the surrounding cavity results in a dynamic control of the spontaneous emission and opens wide applications for CQED. QDs are of particular interest as they possess fixed positions in solid-state cavities, whereas in early CQED experiments [1], it were atoms that were sent with a precise speed and interacted only a certain time with the cavity. All the simulations of this chapter are valid for any kind of two-level emitters, even if I will use mostly the example of QDs.

There are different approaches to control the detuning. The cavity mode can be brought in resonance with an emitter transition by electromechanical tuning of the cavity resonance [79]. This is a more or less static process. To tailor CQED effects in real time, the coupling between QD and cavity has to be controlled on time-scales shorter than the QD lifetime, resulting in a time-dependent spontaneous emission rate [80]. Such control has been realised by all-optically switching of a Fabry-Pérot cavity coupled to a target photonics crystal cavity containing one QD [81]¹ or by tuning the transition of a QD in a photonic crystal cavity using the Stark effect [122, 82] (*i.e.* by applying an electrical field). When using the Stark effect the frequency of the emitted photons shifts, which is a drawback for most applications. Furthermore it is experimentally very difficult to achieve such emitter tuning in an ultrafast way, *i.e.* on time-scales of the order of tens of picoseconds. Our strategy is to change the cavity mode's energy via cavity switching, as discussed

¹They also discussed the possibility to emit shaped single photon pulses with this system [83].

in section 1.4. In this context, optical free carrier injection provides an ultrafast way to tune in and out the resonance of a QD and a cavity mode (sub-picosecond control could be possible). The instantaneous free carrier density defines the detuning between the QD transition and the cavity mode as a function of time, and can be regulated by the intensity *vs.* time shape of the pumping laser pulses. Exploiting this, one can control the dynamics of the spontaneous emission rate with time in the weak coupling regime. In a similar way, Kerr switching [12, 13] could be used for example to control in the strong-coupling regime the beginning and/or the end of Rabi oscillations [51, 52, 5].

In this chapter, I will model the effects of a time-controlled coupling of a two-level emitter (*e.g.* a QD) and a cavity mode (*e.g.* from a micropillar). In the weak-coupling regime this correspond to modeling the dynamics of the Purcell effect. In this framework, I will first explain how to accelerate and trigger spontaneous emission by “plugging” the Purcell effect at a well defined time. Then I will show some further theoretical studies on the possibility to shape the temporal envelope of single photon pulses; that means controlling the spontaneous emission probability during the whole QD relaxation in order to shape the intensity of the outgoing single photon pulse. Well-defined shaped single photon pulses might play an important role in future quantum information processing. Perfect absorption properties would be only achieved when an absorbing dipole (or QD) would receive a time-reversed version of the pulse that it could emit. I will discuss that process. Gaussian time-symmetrical pulses would be ideal for optical quantum information processing, as was theoretically proven by Rohde *et al.* [119]. I will present how to produce such pulses in a robust way.

We will develop in the following the theoretical description of the emission dynamics with rate equations and quantum Langevin equations.

4.2 Mathematical description of the time- and energy-dependent coupling of a QD in a cavity

Theoretical investigations of the time-dependent spontaneous emission enhancement will elucidate and deliver useful informations for possible applications and experiments. In a first time a very simple description of the emission processes is formulated with classical rate equations. They describe the temporal evolution of the populations for a two-level emitter in a cavity, which is valid in the weak-coupling regime. The time-dependent intensity of an emitted light pulse can be deduced. The essential, derivated result is a formulation of the time-dependent enhancement factor $F(\delta(t))$ as a function of the cavity parameters and the temporal envelope of an emitted light pulse.

For a more detailed study of the emitted light pulses, which are all single photon pulses, the information about the temporal envelopes of the pulses is not sufficient. The calculation of the emitted electric field provides further informations, like the instantaneous

frequency. This will be described by quantum Langevin equations. Realistic interference and absorption processes of the computed emitted photon pulses can be studied. As the quantum Langevin equations are not limited to the weak-coupling regime, this analysis will also be used to test the validity of the classical rate equations approach, which shows its limits at the boarder of the weak- and strong-coupling regimes.

4.2.1 Rate equations

Population equations, or rate equations, are differential equations describing the temporal evolution of system variables. In the present case they describe a single QD in a cavity, coupled to the unique cavity mode m and to the leaky modes. The description is valid for the cavity–QD system in the weak-coupling regime. The system variables are

- the instantaneous exciton population of the excited quantum dot: p_{QD}
- the instantaneous photon population in the cavity mode: p_m
- the instantaneous photon population in the leaky modes (without losses): p_{leaky} .

The values are all positive and real. The set of differential equations for the spontaneous emission dynamics of a two-level emitter in a cavity is:

$$\frac{dp_{\text{QD}}(t)}{dt} = -p_{\text{QD}}(t) (F(\delta, t) + \gamma) \Gamma_0 . \quad (4.2)$$

$$\frac{dp_m(t)}{dt} = p_{\text{QD}}(t) F(\delta, t) \Gamma_0 - \frac{p_m(t)}{\tau_m} \quad (4.3)$$

$$\frac{dp_{\text{leaky}}(t)}{dt} = p_{\text{QD}}(t) \gamma \Gamma_0 \quad (4.4)$$

where $1/\tau_m = \kappa$ the cavity mode line-width, τ_m the lifetime of the cavity mode, and $\gamma\Gamma_0$ the coupling to the leaky modes. Here the time- and detuning-dependent enhancement factor $F(\delta, t)$ replaces the Purcell Factor F_P found in more common formulations. The first equation describes the decrease of the QD exciton population emitting into the cavity mode and the leaky modes while the second (third) equation gives the cavity (leaky) mode population fed by the QD excitons and depleted by cavity losses. With this set of equations the influence of a dynamic detuning between cavity mode and emitter transition on the photon emission can be studied. In this chapter, the initial conditions are $p_m|_{t=0} = p_{\text{leaky}}|_{t=0} = 0$ and $p_{\text{QD}}|_{t=0} = 1$, which accounts for one excited QD containing one exciton. In the weak-coupling regime, the QD dynamics are slow compared to the cavity dynamics. Consequently, the stimulated emission and photon reabsorption processes can be neglected and do not appear in the set of equations.

We are interested in the time-envelope of a (single-) photon pulse emitted from a QD via the cavity mode. As the cavity dynamics is much faster than the QD dynamics — here the system is in the weak-coupling regime — the cavity mode population p_m stays at the same, negligibly small value. We may then write that $\frac{dp_m(t)}{dt} \equiv 0$. The envelope of the

emitted photon of interest is therefore approximatively

$$n(t) = \frac{p_m(t)}{\tau_m} = p_{\text{QD}}(t) F(\delta, t) \Gamma_0 . \quad (4.5)$$

A simple relation between pulse time-envelope n and enhancement factor F can be found by replacing $p_{\text{QD}} = \frac{n(t)}{F(\delta, t)\Gamma_0}$ and its decay rate $\frac{dp_{\text{QD}}(t)}{dt} = \frac{\dot{n}(t)F(\delta, t) - n(t)\dot{F}(\delta, t)}{F(\delta, t)^2\Gamma_0}$, where $\dot{x} := \frac{dx}{dt}$, in equation 4.2. One obtains:

$$\frac{dF(\delta, t)}{dt} = F(\delta, t) \left(\frac{1}{n} \frac{dn}{dt} + \gamma\Gamma_0 \right) + F(\delta, t)^2 \Gamma_0 \quad (4.6)$$

From that, I can compute the enhancement factor $F(\delta, t)$ corresponding to a given pulse shape having the time-envelope $n(t)$ (*e.g.* of a single photon). The reformulation of equation 4.1 gives the time-resolved detuning $\delta(t)$ appropriate to $n(t)$.

$$\delta(t) = \pm \sqrt{\frac{F_P}{F(\delta, t)} - 1} \frac{\Delta\omega_m}{2} \quad (4.7)$$

I wrote an Octave code and solved these time-dependent differential equations numerically. The results are predictions of CQED experiments for QDs in solid state microcavities. A full quantum treatment is useful to confirm the mathematical model and to extend the simulations to the strong-coupling regime.

4.2.2 Quantum Langevin equations for a QD in a cavity

A detailed quantum treatment of a two-level emitter in a cavity is given by [49] and [50]. The following theoretical description and corresponding simulations were done in collaboration with Gaston HORNECKER and Alexia AUFFÈVES [123]. We considered a system spanned in the sub-space $\{|e, 0\rangle, |g, 1\rangle, |g, 0\rangle\}$, *i.e.* one (zero), zero (one), or zero (zero) exciton in the emitter (photon in the cavity mode), respectively. The coupling rates are κ , which describes the energy relaxation from the cavity mode to the continuum of empty modes in the outer space, $\tilde{\gamma}$ which is the energy relaxation from the two-level emitter to the mentioned continuum, and g , which is the coupling between the cavity mode and the two-level emitter. The relations between the Langevin formalism and the rate equation formalism are:

$$\begin{aligned} \kappa &= \Delta\omega_m = \frac{E_{\text{QD}} + \delta}{\hbar Q_m} \\ g &= \frac{1}{2} \sqrt{F_P \Gamma_0} \kappa \\ \tilde{\gamma} &= \gamma \Gamma_0 \end{aligned} \quad (4.8)$$

The quantum Langevin equations [124, 125] give the temporal evolution of the wave amplitudes of the exciton and the cavity mode. Under the rotating wave approximation,

and assuming that the couplings are independent of frequency, these equations are

$$\begin{aligned}\dot{\alpha} &= -i\omega_1\alpha + g\beta \\ \dot{\beta} &= -i\omega_2\beta - g\alpha - \sqrt{\kappa}\beta_{in}\end{aligned}\tag{4.9}$$

$$\begin{aligned}\omega_1 &= \omega_{QD} - i\tilde{\gamma}/2 \\ \omega_2 &= \omega_{QD} + \delta - i\kappa/2\end{aligned}\tag{4.10}$$

where $|\alpha|^2$ is the population of the two-level emitter transition, and β is the electric field inside the cavity. The electric field outside the cavity is $\beta\sqrt{\kappa}$ and $|\beta|^2\kappa$ is the outgoing photon pulse intensity. β_{in} is the electric field of a pulse entering the cavity, if present. ω_{QD} is the angular frequency of the two-level emitter transition and δ the detuning between the two-level emitter transition and the cavity mode. Those equations hold for emission and absorption. The typical initial conditions for emission are $\alpha|_{t=0} = 1$, $\beta|_{t=0} = 0$ and $\beta_{in} = 0$. For absorption it is $\alpha, \beta|_{t=0} = 0$ and $\beta_{in}(t) \neq 0$.

This quantum mechanical description — in addition to the rate equations — give the necessary tools to simulate the CQED experiments.

4.3 Purcell switching

After charging a QD with one exciton, it might be of interest to trigger the emission of one photon at a deterministic time. In most QD-CQED studies, a pump pulse excites the QD and the photon emission follows. The outgoing light pulse, *e.g.* a single photon, has a characteristic time-length given by the lifetime of the QD transition τ_{QD} . It is interesting to control separately both the times of the excitation by the pump and of the beginning of the emission, for example to limit the temporal jitter induced by a slow excitation with a temporally long pump pulse. A possible realization with cavity switching was first proposed by Vos *et al.* [126]. Here, by using cavity switching or emitter tuning, a cavity mode and an emitter transition will be brought into resonance to trigger the emission at a well defined time, as proposed by Thyrestrup *et al.* in the reference [80].

Let us consider a system composed of one emitter in a cavity, being in the weak-coupling regime. This emitter transition may have a large spectral offset to the cavity mode, and therefore couples its spontaneous emission only to the leaky modes. Switching the cavity brings the emitter transition in resonance with the cavity mode (illustrated in figure 4.1). Then, thanks to the Purcell effect as we established it, the emitter excitation will decay preferentially in the cavity mode and the emission rate will increase.²

This can be simulated by solving the rate equations: For a time-dependent cavity mode, *i.e.* for cavity switching, the figure 4.2 shows the cavity and QD resonances, the QD exciton population (plus the proportional leaky mode signal) and the collected signal, all

²Let us remind that the coupling rate to the leaky modes γ is assumed to be constant.

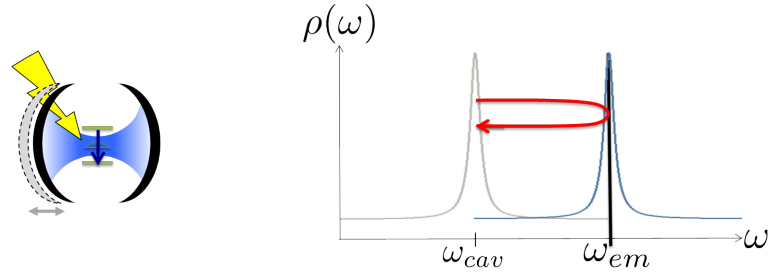


Figure 4.1: Concept of Purcell switching (in analogy to figure 1.16). Cavity switching will bring the cavity mode in resonance with the emitter transition and increase the photon emission rate.

as a function of time. While the emitter transition and the cavity mode are detuned (before 50 ps and after 100 ps in the graphs), the QD exciton population decreases barely and the collected signal is very weak. When the emitter transition and the cavity mode are in resonance (between 50 ps and 100 ps), the emission is accelerated, clearly detected by a decrease of the emitter population, which is proportional to the leaky mode signal. Simultaneously, the collected signal increases dramatically, thanks to the efficient collection of the cavity mode signal. With the logarithmic scale, this collected signal reflects the reduced emitter population after switching (>100 ps), as compared to the unswitched case. But this signature of the Purcell effect is much more obvious if one looks at the QD exciton population or at the leaky mode signal. The population of the QD-transition does not show a mono-exponential decay any more. The emission signal pulse was triggered by inducing a large, temporary increase of the spontaneous emission rate.

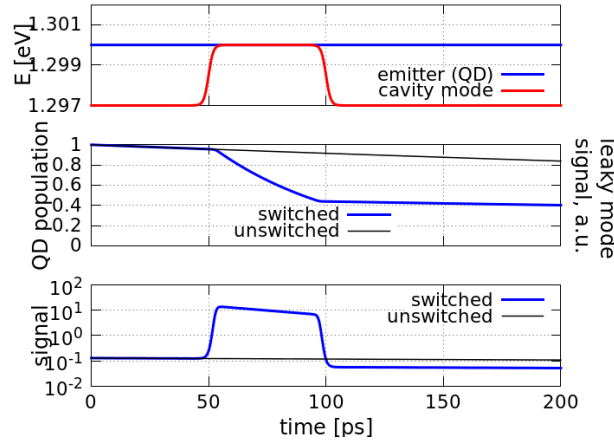


Figure 4.2: Purcell switching for $F_P = 20$. The cavity mode and emitter transition are brought into resonance, which increases the photon emission rate.

In accordance to the emission diagram of a micropillar cavity, I assumed all along this section a directional emission of signal resonant to cavity modes which was collected with an efficiency of 90%, and a more or less isotropic emission from the leaky modes collected with an efficiency of 10%. This explains the increase of the collected signal when the QD is in resonance with the cavity mode. Furthermore the parameters γ , Γ_0 and Q are set to

the values $\gamma = 1$, $\Gamma_0 = 1/1.2 \text{ ns}^{-1}$ and $Q_m = 4000$ all along this section.

Bringing the emitter transition and the cavity mode for tens of picoseconds into perfect resonance, like in the simulation above, could be very challenging to realize experimentally. To study a more realistic case, the detuning will now evolve as for a fast all-optical free-carrier injection, followed by their recombination. As a result of such cavity switching, the cavity mode will dynamically cross twice the emitter transition, as sketched in figure 4.3 and plotted in the first graph of figure 4.4. Experimentally a pump pulse could inject free carriers inside the cavity and blue-shift the cavity mode in a few picoseconds. An initially detuned emitter transition can then enter a first time into resonance with the cavity mode, but only very briefly. The injected free carriers will later recombine with a characteristic time of tens to hundreds of picoseconds, inducing a red-shift of the cavity mode back to its unperturbed spectral position: The QD transition therefore comes a second time into resonance. As the recombination process is slower than the injection process, this second time for interaction is much longer. Four cases are simulated and shown in figure 4.4: a) off-resonant spontaneous emission, corresponding to $F_P = 0$, b) Purcell switching for a QD perfectly aligned with the cavity mode, for small $F_P = 1.25$, c) for a modest $F_P = 5$, and d) for large $F_P = 20$. so still in the weak-coupling regime.

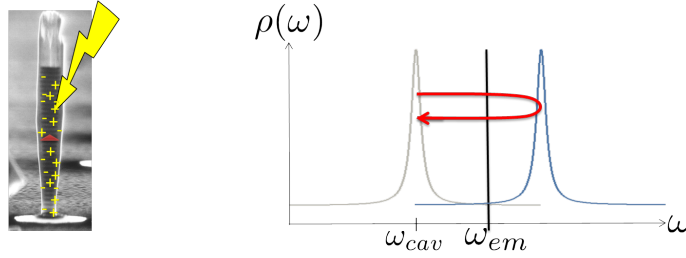


Figure 4.3: Realistic Purcell switching. Cavity switching will bring the cavity mode of a micropillar cavity dynamically in and off resonance with the emitter transition.

Initially the cavity mode and the QD transition are detuned, as shown in the first sub-plot of figure 4.4. At $t = 20 \text{ ps}$ occurs a fast blue-shift of the cavity mode (switching event due to free-carrier injection), followed by the spectral relaxation of the switched cavity mode having an exponential decay with the characteristic time $\tau = 40 \text{ ps}$, corresponding to the free-carrier decay. The second sub-plot shows the QD population, proportional to the leaky mode signal, and the third sub-plot shows the intensity of the collected signal, only for $F_P = 1.25$ and $F_P = 5$. When the QD transition and the cavity mode are not resonant, the QD population decreases barely (with characteristic time $\tau_{QD} = 1.2 \text{ ns}$) and the collected signal is very small. On the first time the QD transition and the cavity mode come into resonance, the cavity mode moves very fast, such that the time in resonance is very short.³ The collected signal increases strongly, but its time-integral is very small, so that the QD population shows nearly no decrease. The second time in resonance is much longer, so that there is an effect on the QD population. The expected step in the population is significant only for the high Purcell factor $F_P = 20$. That can be estimated,

³What actually counts, is the time the spectral line-widths of the cavity mode and the QD transition overlap.

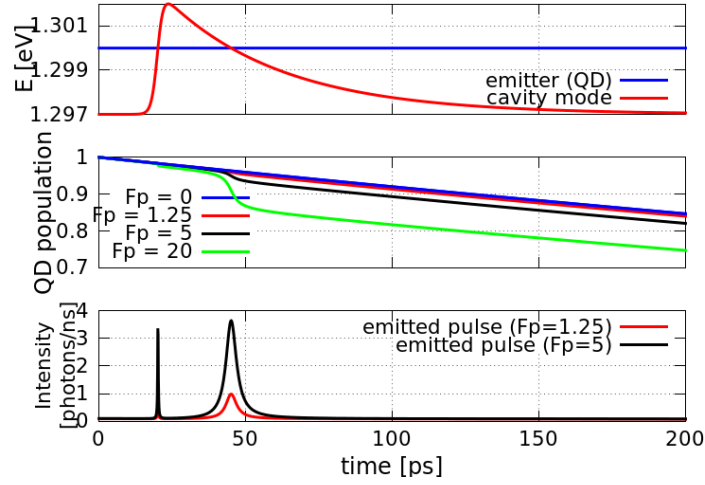


Figure 4.4: Purcell switching for four different F_P . The first plot shows the resonances of the switched cavity mode and the unswitched QD transition. The second plot shows the QD population, and the third plot shows the collected signal for $F_P = 1.25$ and $F_P = 5$. One has to note that the QD population is shown from 0.7 to 1.

as the time in resonance is

$$\Delta t_{res}(E_m) \approx \frac{\Delta E_m}{\partial E_m / \partial t} = \frac{E_m / Q}{1 / \tau (E_m - E_{cav,0})} = \frac{\tau / Q}{1 - E_{cav,0} / E_m} \quad (4.11)$$

so here $\Delta t_{res}|_{E_m=E_{QD}} = 4.33$ ps. In this equation τ is the characteristic time of the spectral relaxation of a switched cavity mode having an exponential decay, here $\tau = 40$ ps. Furthermore we made the assumption that the line-width of the emitter transition is much smaller than the line-width of the cavity mode. The relative population decay while passing in resonance is approximatively $\Delta t_{res} F_P \Gamma_0 = 7.2\%$ for $F_P = 20$ ($< 2\%$ for $F_P = 5$).

During this second resonance event the collected signal increases again strongly. Even for a small F_P , an intense burst is emitted. The ratio of the maximal amplitudes equals the ratio of the corresponding F_P : $5/1.25 = 4$. This is a signature of the Purcell switching, but experimentally not very convincing. Rather, the increased intensities are mainly caused by the collection efficiencies and not by the Purcell effect. In the off-resonant case the signal is proportional to 0.1γ , in the resonant case to $0.9F_P + 0.1\gamma$. As long as $F_P \gtrsim \gamma$, there will always be an emission burst. Hence the collected signal is not a good criterion for detecting Purcell switching, but can be used to observe bursts of spontaneous emission. A better signature of Purcell switching is the fast decrease of the QD population when the cavity and the QD enter into resonance. As the figure shows, a high Purcell factor is needed for this signature of Purcell switching to be clearly observed.

This simulation did not show the triggering of an efficient emission process. Even for $F_P = 20$, the QD population decreased only by a few percent. The interaction between the cavity mode and the QD transition has to be strongly increased, in order to obtain in resonance an efficient emission together with a strong decrease of the QD population. Without

changing the coupling parameters, this can be obtained by increasing the interaction time.

The previous simulation is conducted again, but with a changed spectral relaxation of the cavity mode: now $\tau = 200$ ps and 500 ps. The results are shown in figure 4.5. The plots of the time-dependent energies reflect the increased relaxation time. Out of resonance and for the first fast resonance crossing, the QD exciton population and the collected signal behave as in the previous case. For the second resonance event, the interaction time changes and with it the behaviour of the QD exciton population and collected signal. The longer the interaction time, the stronger the decrease of the QD exciton population. The decrease is efficient even for modest F_P and becomes visible for small F_P . The study for $\tau = 500$ ps and $F_P = 20$ illustrates the triggering of a very efficient emission process, even more efficient than the case of perfect resonance during 50 ps (*cf.* figure 4.2), and is much more realistic to implement. The corresponding detected emission bursts have still the same peak intensities as before, governed by the Purcell factor, but the burst durations increase with a slower spectral relaxation of the cavity mode (*i.e.* with larger τ).

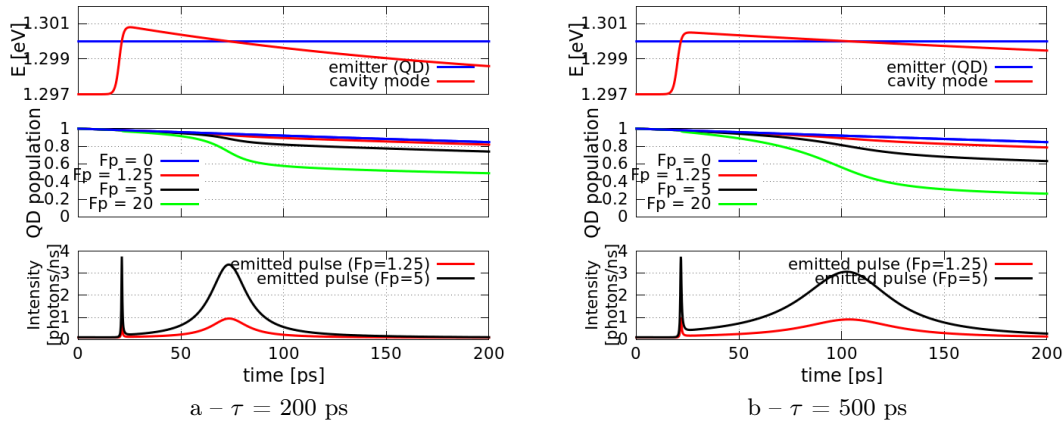


Figure 4.5: Purcell switching for four different F_P , like in figure 4.4. The characteristic time of the cavity mode relaxation changed from 40 ps to 200 ps (a) and 500 ps (b). One has to note that the QD exciton population is now shown from 0 to 1.

With the latter study, where the cavity mode is brought into resonance with the QD transition for a longer time, it became possible to trigger properly the QD's photon emission at a well defined time with highly efficient emission. With the chosen cavity-QD parameters, the QD exciton population could be decreased of about 60%, a clear signature of Purcell switching. The signal emitted through the leaky modes of the cavity is directly proportional to the QD exciton population — its detection, possible with the right spatial selection, would also evidence Purcell switching.

4.4 Temporal shaping of single photon pulses

Single photon pulses of well-defined shape may play an important role in future quantum information processing. One fundamental principle of scalable quantum information processing is the coalescence of two indistinguishable single photons on a beamsplitter [127, 128]. The necessary condition is that both photons impinge simultaneously on the beamsplitter, to temporally overlap as much as possible. The Gaussian time-envelope presents the perfect shape for robust coalescence properties when a jitter in the photon arrival times exists [119]. For efficient optical quantum links, two key components are required: a first system needs to be a reliable single photon emitter, and a second system has to present very good absorption properties for single photons. Perfect reabsorption could be obtained if a spontaneously emitted photon is reversed in time and sent back to its emitter. Unfortunately, the time-envelope of a spontaneously emitted photon is not symmetric in time, but exponentially decreasing, and its absorption probability is limited, as pointed out by [120]. The best time-envelope for absorption would be here the exponentially increasing one. In this context of spontaneous emission the time-envelopes of emitted and best absorbed single photon differ and decrease the efficiency of optical quantum links. Shaping the time-envelope of the emitted single photon matching the best exponentially increasing time-envelope for absorption may be a solution, schematized in figure 4.6.⁴

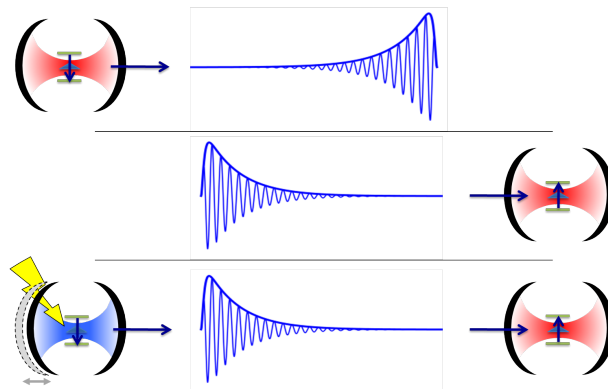


Figure 4.6: Example of pulse shaping. First line: spontaneous emission of a single photon by a cavity-QD system. Second line: the time-reversed single photon is perfectly absorbed by the QD in a cavity. Third line: Using cavity switching, the photon time-envelope can be re-shaped. In this example an efficient emission-absorption process might become possible.

I will present how to produce in a robust way such pulses with a Gaussian or an exponentially increasing time-envelope. Using cavity switching, to go beyond the possibility to just play with the Purcell effect and trigger spontaneous emission, I want to control the enhancement factor during the whole QD relaxation in order to shape the time-envelope of the outgoing single photon pulse.

To be an ideal pulse, the single photon must be emitted in the right spatial mode, so

⁴We will discuss the photon absorption and corresponding probabilities in section 4.4.3.

that its propagation is well defined and directional, and it can be efficiently detected. In addition, the single photon must have perfect properties in amplitude and frequency. This can be described by two figures of merit: the efficiency of the source $\tilde{\beta}$ and its fidelity f , that I will define below. The goal of my work is to produce single photon pulses with both high fidelity and efficiency.

Similar studies were done: Fernée *et al.* did theoretical studies using the Stark effect and an atomic three-level emitter in a cavity. They shaped a Gaussian pulse in the weak-coupling regime with an asymmetric time-varying Stark tuning, but didn't discuss its frequency properties [129]. Johne *et al.* did similar studies with a QD instead of a three-level emitter [122]. Their studies were done in the limit between strong- and weak-coupling regime. They shaped a Gaussian-like single photon pulse and reported about reabsorption difficulties due to a frequency chirp, or in other words to the low fidelity. The Stark effect, used by [129] and [122], indeed modifies the emitter's energy transition in order to change the coupling between the emitter transition and the cavity. This provokes a considerable frequency chirp of the emitted photon. The novelty of my approach will be the use of cavity switching to control in time the spontaneous emission enhancement. The frequency chirp can be significantly reduced and the fidelity f therefore increased. Again, I will use the time-resolved detuning, *i.e.* $F(\delta, t)$, to compute the outgoing pulses. The use of a two-level QD emitter would make solid-state integration much easier than with the atomic emitters mentioned above.

A completely different strategy to shape the time-envelope of a single photon pulse was also reported by Keller *et al.* [130]. A $^{40}\text{Ca}^+$ atom in a cavity was excited with a resonant laser pulse. The instantaneous intensity of the laser pulse, which lasts as long as the emitted photon pulse, directly influences the temporal shape of the emitted photon pulse.

After introducing the figures of merit, I will present the highly efficient generation of single photon pulses with Gaussian and exponentially increasing time-envelopes. Using cavity switching, those results can be obtained for a wide range of cavity and QD parameters. Absorption probabilities will be discussed and the results of temporal shaping with cavity switching will be compared to the Stark tuning approach.

4.4.1 Photon emission fidelity and efficiency

In the following are criteria to evaluate the quality of the generated single photon pulses. The fidelity f describes the temporal overlap between an emitted single photon pulse and a target single photon pulse having well-defined, requested constant frequency and temporal envelope [122].

$$f = \frac{|\int \mathbf{E}^* \cdot \mathbf{E}_{\text{ref}} dt|^2}{\int |\mathbf{E}|^2 dt \int |\mathbf{E}_{\text{ref}}|^2 dt} \quad (4.12)$$

\mathbf{E}_{ref} is the electric field of the suited reference pulse as a function of time, \mathbf{E} is the electric field of the simulated pulse as a function of time and \mathbf{E}^* its complex conjugate; all are

classical fields⁵. This scalar product describes the temporal matching of frequency and time-envelope of the simulated and reference pulses. The values of f can vary between 0 and 1, meaning zero and perfect matching in frequency and time-envelope, respectively.

If only the time-envelopes are of interest, and no frequency properties are considered, this can be described by a second figure of merit \tilde{f} , which is obtained by replacing \mathbf{E}^* and \mathbf{E}_{ref} by their moduli in the previous expression:

$$\tilde{f} = \frac{\int |\mathbf{E}| |\mathbf{E}_{\text{ref}}| dt}{\int |\mathbf{E}|^2 dt \int |\mathbf{E}_{\text{ref}}|^2 dt} \quad (4.13)$$

In this work, the reference field \mathbf{E}_{ref} oscillates with constant angular frequency ω_{ref} . In most cases f is not maximal when ω_{ref} matches the emitter's angular frequency ω_{QD} , but can be maximised by varying ω_{ref} around ω_{QD} .

The efficiency of the photon emission is described by

$$\tilde{\beta} = \frac{\int F(t) \Gamma_0 dt}{\int (F(t) + \gamma) \Gamma_0 dt} \quad (4.14)$$

equal to the ratio of all the emission into the cavity mode to the entire emission in cavity and leaky modes. Emission through the cavity mode is very directional and can be detected with high efficiency. $\tilde{\beta}$ can vary between 0 and 1, meaning zero and full emission into the cavity mode, respectively. This equation corresponds to the generalization of equation 1.33 for non-resonant cases.

Finally we introduce the integral of the photon which is emitted into the cavity mode:

$$I = \int |\mathbf{E}|^2 dt = \tilde{\beta}(1 - p_{\text{QD,end}}) \quad (4.15)$$

where $p_{\text{QD,end}}$ is the QD excitation probability at the end of the simulation. If I is less than one, the photon emission probability is reduced. The upper limit to I is the value of $\tilde{\beta}$, the probability of emission into the cavity mode. If I is smaller than $\tilde{\beta}$, the QD has some residual probability for being excited at the end of the simulated emission event.

4.4.2 Shaping of time-domain Gaussian and exponentially increasing single photon pulses, using cavity switching

To predict the emission of a single photon pulse with a particular time-envelope $n(t)$ by a cavity-QD system, the equations 4.6 and 4.7 of the classical population approach are solved with the desired $n(t) = |\mathbf{E}_{\text{ref}}(t)|^2$ as input, and result in the corresponding enhancement factor $F(t)$ and detuning $\delta(t)$. The computed detuning $\delta(t)$ can be applied by cavity switching or emitter tuning (*e.g.* Stark tuning) to the relevant cavity-QD system in the

⁵From the quantum Langevin equations, one obtains $\mathbf{E} = \beta\sqrt{\kappa}$. This “ β ” must not be mistaken with β in equation 1.33 of chapter 1.

excited QD-state. The subsequent emission from this system will be computed with the quantum Langevin equations (equations 4.9), which present a more complete description⁶ of the emission process than the rate equation approach, and result in the time-dependent photon envelope and photon frequency. The comparison with the desired photon (time-envelope $n(t)$ and constant frequency) is quantified with the figures of merit $\tilde{\beta}$ and f .

My simulations use all the following parameters (except when specified otherwise): at $t = 0$, the emitter (*e.g.* the QD) is in its excited state (one exciton), the cavity is in its ground state and the photon density in the cavity mode and leaky modes is zero. The reference energy equals 1.3 eV and is constant in time. It represents either the emitter transition E_{QD} for cavity switching or the cavity mode resonance E_m for emitter tuning (through *e.g.* Stark effect). The reference spontaneous emission rate in bulk GaAs is $\Gamma_0 = 1/1.3 \text{ ns}^{-1}$. The spontaneous emission rate into the leaky modes is $\tilde{\gamma} = \Gamma_0/20$ (*e.g.* $\gamma = 1/20$). The Purcell factor F_P and cavity quality factor Q will depend on the simulation, and are typical values that can be achieved in semiconductor photonic crystal cavities [4], as well as in superconducting microwave resonators.

The Gaussian time-envelope and the study of \tilde{f} . The first simulation I want to present is the emission of a single photon with Gaussian time-envelope. I am only interested in the reproduction of the target time-envelope, quantified by \tilde{f} . The parameters of the cavity–QD system and the target Gaussian pulse envelope $n(t)$ have to be defined. As the rate equations are formulated for the weak-coupling regime, the cavity–QD system should be in a first instance in the same regime. I chose as an example $\kappa/g = 11$, here realised with $F_P = 42.9$ and $Q = 1979$. (The system will be in the weak-coupling regime for $\kappa/g > 4$, and in the strong-coupling regime for $\kappa/g < 4$. [49]) The duration of the Gaussian target pulse cannot be chosen arbitrarily. A necessary condition is that its duration is longer than the photon lifetime in the cavity (here 1 ps), longer than the emitter transition lifetime in perfect resonance $1/F_P\Gamma_0$ (here 30 ps), and much shorter than the emitter transition lifetime off-resonance $1/\tilde{\gamma}$ (here 26 ns). I chose a 150 ps FWHM for the target pulse. The target Gaussian time-envelope for the photon population is $n(t) = \frac{1}{\tau\sqrt{\pi}} e^{-\frac{(t-195 \text{ ps})^2}{\tau^2}}$ with $\tau^2 = \frac{(150 \text{ ps})^2}{4\ln(2)}$. Its integral is one, to represent a single photon. With this input, solving the differential equation 4.6⁷ results in the corresponding enhancement factor $F(t)$ and detuning $\delta(t)$, and further solving the associated quantum Langevin equations (equations 4.9) with a time-dependent cavity resonance and constant emitter transition (*i.e.* cavity switching) results in the time-envelope of the emitted pulse. When choosing the mentioned parameters for the simulation, one has to find the right set of values, so that the simulations work. For example, one important criterion is that F is always smaller than F_P .

⁶An important difference to the rate equation approach is that the information about the instantaneous frequency are included.

⁷It can be of interest to reduce the integral of the target single photon pulse by $\sim 1\%$ if the solving does not converge. The length of the simulated time interval has to be chosen so that the solving converges, too. Further the initial enhancement factor has to be chosen. I use always $F(t=0) = n(t=0)/\Gamma_0$.

The figure 4.7 illustrates the results. As we see, a suitable set of parameters has been found and the time-envelopes are nearly identical with $\tilde{f} = 0.9998$. The corresponding enhancement factor and detuning illustrate the shaping process of the Gaussian time-envelope. When the emitted photon intensity is small, the detuning is large and the enhancement factor is weak (inhibition of the spontaneous emission). When the photon amplitude is large, the detuning is small and the enhancement factor approaches the Purcell factor. The spontaneous emission is accelerated. But the maximum of the enhancement factor (here $F = 33$) and the minimum detuning do not match with the time of maximum intensity. The decreasing quantum dot population has to be compensated for by an increasing coupling between the QD transition and the cavity mode. As the variations of the detuning are smooth, the experimental realization should be possible. $\delta(t)$ can be applied to a cavity-QD system either electrically (Stark tuning of the emitter) or optically (cavity switching via continuous and tailored free carrier injection).

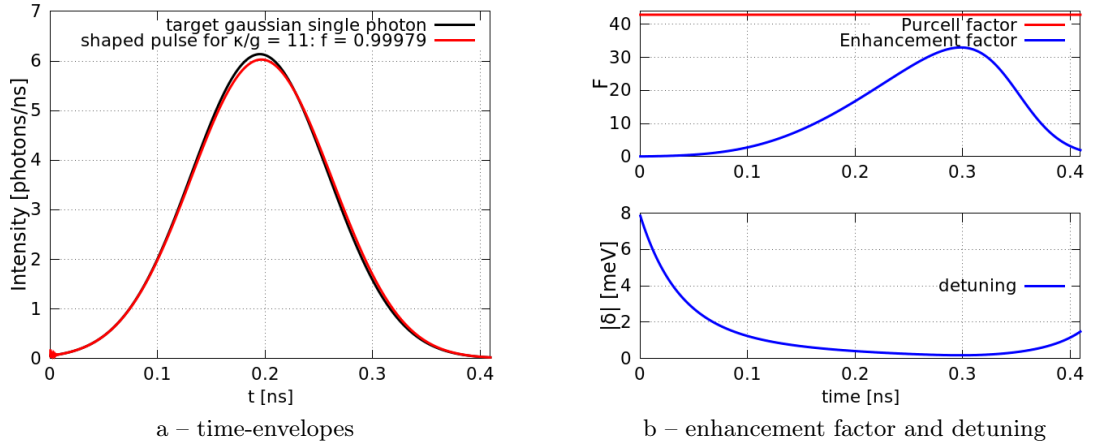


Figure 4.7: Shaping a Gaussian single photon pulse in the weak-coupling regime using cavity switching. (a) The target pulse is shown in black, the shaped pulse in red and reproduce the target time-envelope with $\tilde{f} = 0.9998$ (f in the graph). (b) The corresponding time-dependent enhancement factor and detuning.

This first simulation shows that in the weak-coupling regime the established equation for F (equation 4.6) and the corresponding shaping concept work very well, as is confirmed by the quantum mechanical model predicting a pulse time-envelope with nearly unit \tilde{f} .

In the following, I want to test if this approach for pulse shaping, based on rate equations, still works as well close to the limit between the weak- and strong-coupling regime. The last simulation will again be conducted while changing only the value of Q , therefore of κ/g . I chose the values $Q = 38317$, 14968 or 6652 that correspond to $\kappa/g = 2.5$, 4 or 6 , respectively, and compared the obtained results with the last simulation where $Q = 1979$, $\kappa/g = 11$, see figure 4.8.

The larger κ/g , the better the reproduction of the target time-envelope works and far in the weak-coupling regime the reproduction is almost perfect. At the limit between the weak- and strong-coupling regime ($\kappa/g = 4$) the result is still very satisfying with

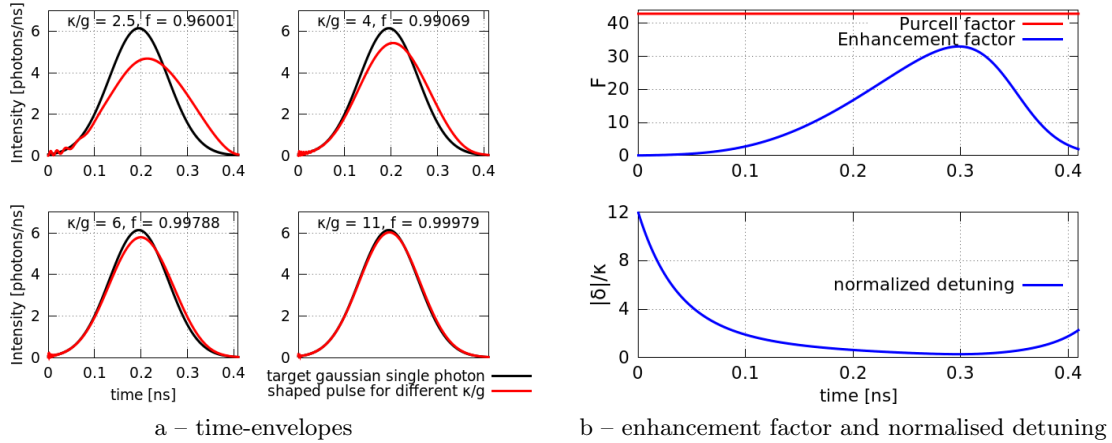


Figure 4.8: Shaping of Gaussian single photon pulses for four values of κ/g , using cavity switching. (a) The target single photon pulse is shown in black, the shaped pulses are shown in red. The overlap of the time-profiles is given by \tilde{f} (f in the graph). (b) Corresponding enhancement factor and normalised detuning δ/κ as a function of time, valid for all four cases: The equation 4.6 depends only on the coupling to the bulk and the external modes, and not on cavity or QD properties; $F(\delta, t)$ is therefore independent of κ and g ; this is the same for δ/κ .

$\tilde{f} = 0.991$. In the strong-coupling regime (example $\kappa/g = 2.5$) the target time-envelope is much less well-reproduced and $\tilde{f} = 0.96$. Oscillations appear at small times, a signature of the strong-coupling regime.

Those simulations reflect the validity of the rate equations-based approach for the detuning and enhancement factor in the weak-coupling regime. The approach allows the efficient reproduction of a target single photon time-envelope for the entire range of the weak-coupling regime ($\kappa/g \geq 4$), where \tilde{f} is always larger than 0.99.

Beyond the rate equation approach: an iterative optimization of the detuning. Up to now the detuning was determined with the help of the equations 4.6 and 4.7, which are obtained from rate equations. For $\kappa/g < 4$ the simulations of pulse-shaping with cavity switching were then not able to perfectly reproduce the target time-envelopes. Nevertheless almost unity \tilde{f} can be obtained in the strong-coupling regime (and close to it), if the detuning $\delta(t)$ is slightly modified. I will explain how to increase so \tilde{f} .

As example the simulation was performed for $\kappa/g = \sqrt{2\pi} \approx 2.51$. We take here $\gamma = 0$ which simplifies the calculations and does not change the idea of this paragraph. Figure 4.9, red lines, shows the results for pulse shaping with a detuning obtained as before. This resulted in $\tilde{f} = 0.961$ and reproduced more or less the target shape. The blue lines show a modified detuning and a corresponding emitted pulse shape which is very similar to the target one. The factor \tilde{f} is therefore greater than 0.999.

This modified detuning was obtained by an iterative approach: Starting with the detun-

ing computed with the help of the equations 4.6 and 4.7 (shown in red) and the corresponding pulse shape as input, we reduced slightly the time-dependent detuning proportional to the time-dependent difference of target pulse shape (shown in black) and the computed pulse shape (shown in red). This increased, if necessary, the instantaneous spontaneous emission enhancement, with the goal to approach the emitted pulse shape towards the target pulse shape. We computed again the emitted pulse shape with the quantum Langevin equations, using the modified detuning as input, and verified if the pulse shape become closer to the target shape. Then, again the emitted pulse shape (the “new” one) was compared with the target pulse shape and the detuning was again adjusted proportional to their difference, so that a new pulse shape could be computed. Repeating this procedure around 50 to 100 times, we could obtain an emitted time-envelope which was very close to the target one, as shown by the blue lines in the figure 4.9. We obtained $\tilde{f} > 0.999$.

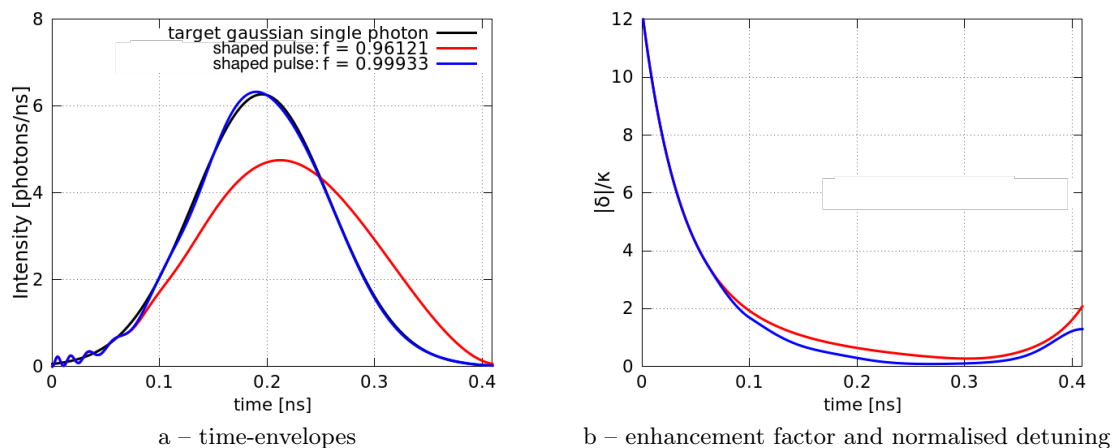


Figure 4.9: Shaping of Gaussian single photon pulses for $\kappa/g = \sqrt{2\pi}$ and $\gamma = 0$, thus in the strong-coupling regime. Using cavity switching, the 150 ps target pulse (black line) is the goal. The results on pulse-shaping, for two different ways to determine the time-dependent detuning $\delta(t)$, are studied. The first way (red lines) is based on rate equations and is not very satisfying. The similarity of emitted time-envelope and target is described by $\tilde{f} = 0.961$. This is because this way to determine $\delta(t)$ loses its validity in the strong-coupling regime. Whereas the second way (blue lines), which is the iterative approach, is very successful to reproduce the target time-envelope and $\tilde{f} > 0.999$.

This shows that an appropriate detuning for the shaping of high-quality Gaussian pulses can also be found in the strong-coupling regime.

We can compare the quality of the emitted, shaped Gaussian pulses over a wide range of κ/g for both ways to determine $\delta(t)$. The emitted pulses, computed with the quantum Langevin equations, contain information about the time-envelope as well as the instantaneous frequency. Up to now, we considered only the time-envelopes. With the frequency information, the other figures of merit can also be calculated.

Figure 4.10 gives a full comparison of the computed pulses. The fidelity f between

shaped pulses and target pulse, the photon integral I , the pure shape (time-envelope) matching \tilde{f} and the pure frequency-, or phase-matching with the target pulse (equal to f/\tilde{f}) are shown in the different subfigures. The graphs illustrate an overall success of the iterative approach; f and the phase matching are always above 0.988, the matching of the time-envelope above 0.998, and the integral of the outgoing photon is about 0.998. The reduced photon integrals for κ/g close to 2 can be ignored, because part of the photon pulse lies outside of the simulation time interval. The rate equation approach differs from the iterative approach: \tilde{f} and f are reduced in the range for which κ/g is smaller than 6. The photon integral is always reduced by 0.01 purposely, to ease the finding of a solution to the differential equations. Therefore $p_{\text{QD, end}}$, which should be close to zero, is increased by 0.01. The pure phase matching shows almost the same values as for the iterative approach. As we chose $\gamma = 0$, the photon efficiency $\tilde{\beta}$ is necessarily 1 for both approaches.

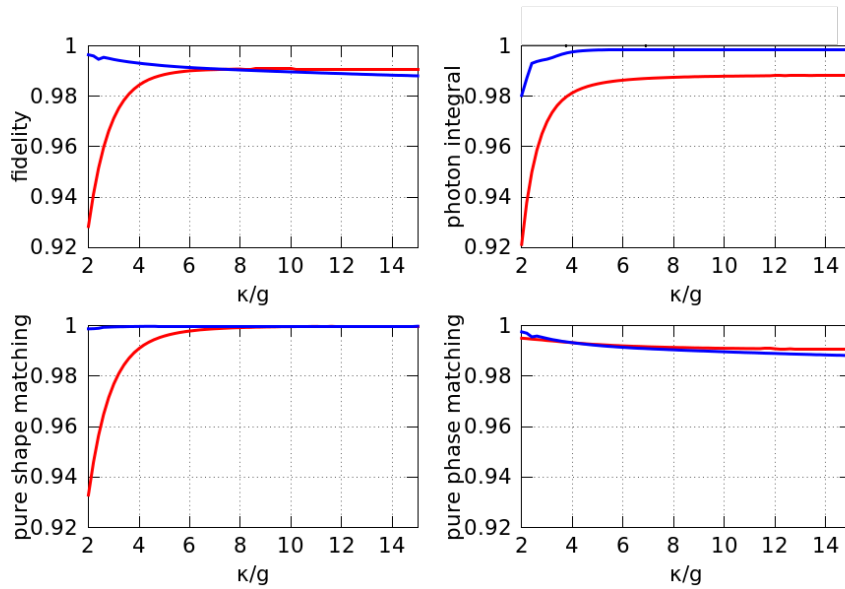


Figure 4.10: Study of the quality of shaping Gaussian single photon pulses as a function of κ/g for cavity switching, compared to a 150 ps long (FWHM) target Gaussian single photon pulses. Red (blue) lines: the pulses were shaped using the rate equation (iterative) approach in order to determine the detuning $\delta(t)$.

In the weak-coupling regime, both approaches lead to single photon pulse shaping with good values for all figures of merit. In this case, the rate equation approach is advantageous, as it is numerically easier to implement and faster to run. On the other hand, in the strong-coupling regime, the rate equation approach fails to achieve high-fidelity pulses. One reason for the failure is that in the rate equations the emitter population is strictly decreasing. In reality it can oscillate when being in the strong-coupling regime. The iterative approach represents here a very good alternative.

Study of f and the pulse spectrum. As a last ingredient to the analysis of the single photon with Gaussian time-envelop, one may also be interested in the photon's spectrum

and its temporally resolved evolution. The following simulation is done with the rate equations to determine $F(t)$ and $\delta(t)$. In analogy to the first — successful — simulation and to the study in figure 4.10, I chose $\kappa/g = 11$, $\tilde{\gamma} = \Gamma_0/20$, $F_P = 58.5$ and $Q = 1452$. The results are shown in figure 4.11.

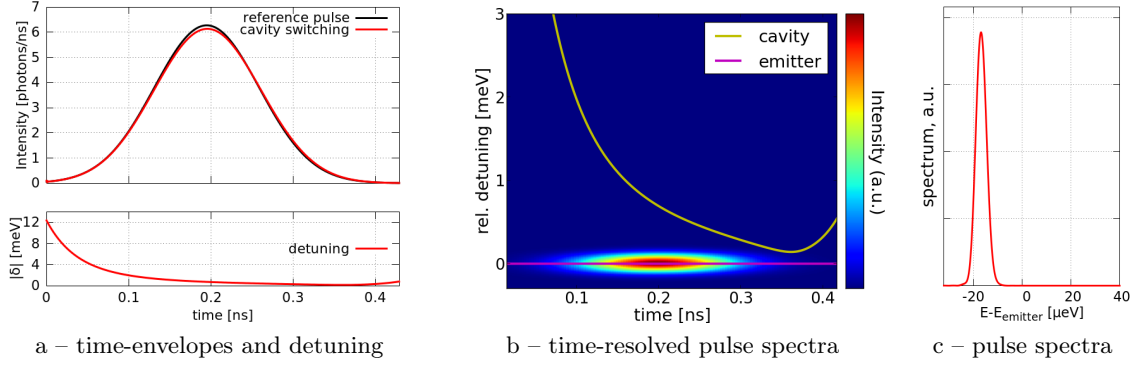


Figure 4.11: Shaping a Gaussian single photon pulse with cavity switching. The time-envelopes and the corresponding detuning (a), the temporally and spectrally resolved pulse (b) and the pulse spectra (c) are shown. In (b) are superposed the time-dependent spectral cavity mode position (yellow line) and emitter transition (magenta line) — one has to note that for short times the spectral cavity mode position is out of the energy window.

Again the Gaussian pulse shape is perfectly reproduced: $\tilde{f} = 0.9999$ (*cf.* subfigure 4.11a). The pulse time-envelope illustrates that for a large detuning, the emission is strongly inhibited. With decreased detuning the spontaneous emission enhancement becomes larger and the emission is accelerated. The photon intensity is modulated by the decreasing QD exciton population, so that the minimum detuning and maximum intensity do not coincide. As $\gamma \ll 1$, the QD exciton population does barely decrease by emission into the leaky modes and the resulting emitted photon has an integral close to unity: $I = 0.992$. This integral is equal to $\tilde{\beta}$ times 0.993 the reduced target integral in order to avoid divergence. With $\tilde{\gamma} = \Gamma_0/20$, the efficiency $\tilde{\beta} = 0.998$.

The time-resolved spectrum (subfigure 4.11b) shows that the emission occurs at the QD-transition frequency and without frequency chirp. Thus the emission should not be spectrally influenced by the time-dependent cavity mode position. This is necessary to obtain the high fidelity compared to the target photon with constant frequency. The entire photon spectrum (subfigure 4.11c) is obtained by a fast Fourier transformation (FFT) of the entire electric field of the computed photon pulse. It shows a Gaussian shape, as expected for a Gaussian time-envelope. As the pulse's time-envelope and spectrum are Gaussian, the fidelity is high: $f = 0.987$.

The time-resolved spectrum was obtained from a FFT on a 30 ps long sliding Hamming window of the electric field, and defined as follows:

$$\text{spectrum}(t_0) = \text{FFT} \left(\mathbf{E} \Big|_{t_0 < t < t_0 + 30 \text{ ps}} \left(0.54 - 0.46 \cos \left(2\pi \frac{t - t_0}{30 \text{ ps}} \right) \right) \right) \quad (4.16)$$

This time-window determines the temporal and spectral resolution, related by Fourier transformation. A higher temporal or spectral resolution can be of interest. Here the 30 ps long window seems to be a good compromise to illustrate the spectral and temporal properties of the shaped single photon pulse. In the following, the time-resolved spectra are obtained using this same time window.

The figure 4.11 shows an overall great success for the shaping of a Gaussian single photon pulse with cavity switching in the weak-coupling regime. The fidelity is close to unity and spectral chirp is negligible. The figure 4.10 shows that similar results could be obtained with most cavity-QD systems, as long as γ is small. Depending on the value of κ/g , the method to determine the time-dependent detuning could be shifted to the iterative method described above. Consequently, by applying cavity switching to different cavity-QD single photon sources, one should be able to produce almost identical Gaussian single photon pulses, making scalable quantum information processing applications possible with different emitters. In this context, it could be necessary to apply a static shift to one QD transition frequency in order to tune it in resonance with the second emitter transition; that requirement could be satisfied through the use of the Stark effect.

To sum up the results obtained about shaping Gaussian single photon pulses: I showed how using an appropriate detuning through cavity switching, one can produce nearly perfect Gaussian single photon pulses for a wide range of κ/g . Other pulse durations could as efficiently be obtained. In the weak-coupling regime a mathematical formulation for the time-dependent enhancement factor (equation 4.6) was found. For the range of the κ/g -ratio that was studied — between 2 and 15:

- The resulting pulses have nearly perfect Gaussian time-envelope, *i.e.* $\tilde{f} > 0.998$.
- The emission efficiency is around $\tilde{\beta} = 0.996$ (assuming $\gamma = 0.05$).
- The fidelity f is better than 0.99.
- As overall efficiency, the photon integral times fidelity If varies between 0.986 and 0.99.

Exponentially increasing time-envelope The second shape for the time-envelope that I am interested in is the exponentially increasing one, which is of particular interest for quantum optical interfaces. In analogy to the Gaussian time-envelope, I want to describe its shaping using the rate equations to determine $\delta(t)$ and apply cavity switching to simulate the emission process with the quantum Langevin equations.

As target photon pulse, I chose the time-reversal of the single photon pulse that is spontaneously emitted by the cavity-emitter system with $F_P = 6$, $Q = 2000$ (*i.e.* $\kappa/g = 29.3$) and $\gamma = 0.05$. Its emitter transition and cavity mode are in perfect resonance. To aim the emission of this target time-envelope, one needs a second cavity-QD system with a time-dependent detuning $\delta(t)$. Initially the system must be off-resonant to inhibit the spontaneous emission and in the following the spontaneous emission rate must be continuously increased in order to emit a photon with an exponential increasing shape. The amplitude of the photon has to increase exponentially while the emitter population decreases exponentially, so that the photon pulse should reach its maximum amplitude

when the emitter transition reaches its ground state. The exponentially increasing time-envelope of a single photon turns out to be one of the most challenging time-envelopes to realise. The shaping can be possible, only if the Purcell factor of the switched and emitting system is much larger than the Purcell factor of the target system — *i.e.* when the spontaneous emission rate in resonance is much larger. In the present case, the emitting cavity–QD system, which aims to reproduce the target time-envelope, has $F_P = 79.8$ to fulfil this criterion. In addition we chose $Q = 1000$, *i.e.* $\kappa/g = 11.3$, to be far inside the weak-coupling regime.

The figure 4.12a shows the target pulse with integral 1 and its successful reproduction with $\tilde{f} = 0.947$, $\tilde{\beta} = 0.993$ and $I = 0.984$. The detuning that is used is also shown. Before $t = 0.6$ ns, the time at which the maximum target amplitude is reached, the detuning corresponds to the solution of the rate equation approach and the obtained emission with the quantum Langevin equations shows good matching with the target time-envelope. The slightly reduced amplitude of the shaped time-envelope corresponds exactly to the reduced photon integral for the easier solution of the differential equation for $F(t)$. Afterwards, for $t > 0.6$ ns, the solution for the detuning proposes to increase strongly δ so that the emission is strongly inhibited and the target shape is the best reproduced. As the QD exciton population is not zero at this moment and to avoid a very fast variation in the detuning (which would increase the difficulty for realization), I forced the detuning to be zero so as to empty the QD as fast as possible. The resulting signal is an exponential decay with a characteristic time equal to $1/(F_P\Gamma_0)$, as shown in the graph. Thanks to this procedure the detuning is smooth for the entire emission process, a feature that is important for experimental realization. A benefit is a slight increase of all the figures of merit.

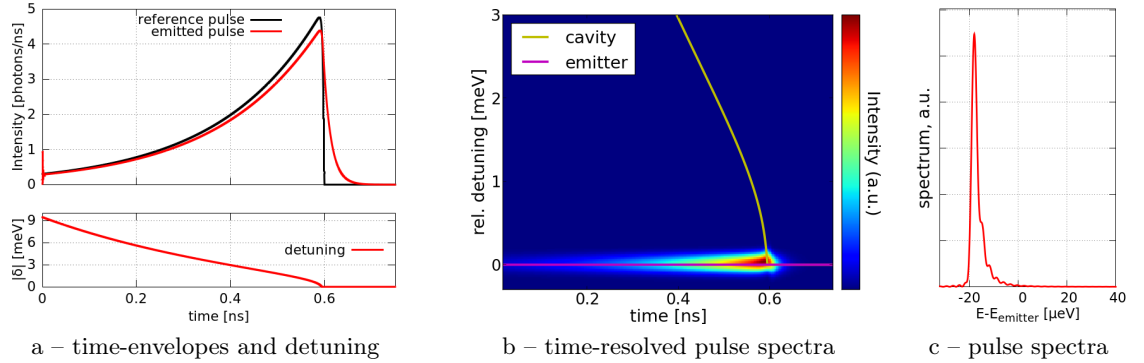


Figure 4.12: Shaping an exponentially increasing single photon pulse with cavity switching. (a) The target time-envelope, the detuning obtained with the rate equation approach and the emitted time-envelope simulated with the quantum Langevin equations. (b) The time-resolved pulse spectrum and superposed the emitter transition and the time-dependent cavity mode position. (c) The spectrum of the emitted pulse.

The corresponding spectral analysis (subfigures 4.12b and 4.12c) provides some infor-

mation about the fidelity. The spectrum that is here obtained deviates from the expected Lorentzian shape that corresponds to an exponential time-envelope. This is in contrast with the simulation of the Gaussian time-envelope (figure 4.11). This deviation can be explained by the slightly differing time-envelope and by induced frequency chirp, which is visible in the time-resolved spectrum. This chirp coincides with the maximum amplitude of the photon pulse, increasing its influence and broadening the photon spectrum. It is probably the accelerated variation of the spectral cavity mode position together with the small detuning, $\delta \ll \kappa = 1.3 \text{ meV}/\hbar$, which provokes this frequency chirp. These frequency properties limit the obtained fidelity f , much more than the reduced temporal overlap \tilde{f} . In the end, $f = 0.788$, which is still a remarkable value for the generation of time-reversed photon pulses.

Other cavity parameters would lead to very similar performances in terms of producing single photon pulses with exponentially increasing time-envelopes, as it was shown with the example of the Gaussian time-envelope. The approach that was discussed is not limited to the shapes shown — no limits are set to the imagination, as long as the variations of the single photon time-envelope are smooth.

Having demonstrated the possible emission of a single photon pulse with an exponentially increasing time-envelope, naturally follows the question of its reabsorption probability.

4.4.3 Efficient emission and consecutive reabsorption of single photon pulses

The use of two identical cavity-QD systems for the emission of a single photon and its consecutive reabsorption ensures that the emission-reabsorption process can be reversible. If the protocol is efficient, communication in both directions is possible. This would be a significant progress for optical quantum links. Using two different cavity-QD systems, the emission-reabsorption process cannot be made reversible. Nevertheless, a highly efficient unidirectional (*i.e.* asymmetric) link might be feasible. Its realization would also constitute a great progress for optical quantum links. We will discuss both possibilities, for either unswitched cavity-QD systems, or switched cavity-QD systems emitting temporally shaped single photon pulses.

Similar studies can be found in the literature. The absorption of a Gaussian shaped single photon and the consecutive emission is discussed in [122]. Therein was exploited the fact that the particular cavity-QD system with $\kappa/g = \sqrt{2\pi}$ emits the most time-symmetric single photon pulse for spontaneous emission; Johne *et al.* studied the absorption of a Gaussian (*i.e.* time-symmetric) single photon by this system (where $\gamma = 0$): If the Gaussian photon had a constant frequency and the right duration, the QD population could reach 0.97. The subsequent spontaneously emitted photon had a 97% Gaussian-like shape. The presented total “efficiency” was $0.97^2 = 0.94$.

This study of the photon absorption and its consecutive emission is different from the

emission–absorption process which is studied in this thesis, and can hardly conclude on communication between two cavity–QD systems. Johne *et al.* compared photon pulses, while I compare exciton populations: I will study the efficiency of quantum-optical links, where a first cavity–QD system — initially prepared in the excited QD state — emits a single photon pulse which will be sent to and absorbed by a second cavity–QD system.

Our criterion to evaluate the efficiency of this emission–reabsorption process, is the maximal reached QD exciton population of the absorbing system: $p_{\text{QD}}|_{\text{max}}$. The simulation is conducted as follows: We consider two cavity–QD systems (not necessary identical), named A and B. At $t = 0$, the system A is prepared in the $|e, 0\rangle$ state (*i.e.* in the excited QD state and in the cavity ground state). All other populations are zero, namely the QD and cavity population in B and the leaky mode population. Subsequently a photon is emitted. All QD emission which coupled into the cavity mode of A (with the efficiency $\tilde{\beta}$) arrives on the cavity B and can be potentially injected in the cavity mode of B. The temporal evolution of A and B is computed with the quantum Langevin equations and the maximal QD exciton population that is reached in B is $p_{\text{QD}}|_{\text{max}}$.

Photon exchange between identical unperturbed cavity–QD systems To ensure the most efficient photon exchange, the QD transitions and the cavity mode frequencies are all in perfect resonance with another. Possible static detuning between emitter transition and cavity mode in A would induce oscillations in the emitted photon’s time-envelope, essentially at the beginning of the emission (*cf.* [50]).⁸ These oscillations would become more and more large with increasing detuning. Simultaneously the pulse spectrum would get broader and couple badly inside the cavity of B, so $p_{\text{QD}}|_{\text{max}}$ can only be reduced. Applying a detuning to B would also reduce the exchange efficiency, therefore $p_{\text{QD}}|_{\text{max}}$.

We want here to study the unperturbed emission and consecutive reabsorption of a single photon between two identical cavity–QD systems (illustrated in figure 4.13). In the first example we study two systems A and B which are both characterised by $F_P = 6$, $Q = 2000$ (*i.e.* $\kappa/g = 29.3$) and $\gamma = 0.05$. These parameters are in analogy to the study shown in figure 4.12a, black line, where we showed the time reversed spontaneously emitted photon pulse. Here A will spontaneously emit a photon pulse with exponential decreasing time-envelope (in contrast to figure 4.12a). Let us study its reabsorption properties by the same cavity–QD system B .

The time-evolution of A and B is computed with the quantum Langevin equations and the resulting absorption properties are shown in figure 4.14. The electricmagnetic field entering the cavity B is the one spontaneously emitted by A (the part that couples inside its cavity mode). The time-dependent cavity population is proportional to the square of the absolute value of the entering electric field. The QD exciton population is fed by the cavity population and decays at the same time back in the cavity mode and in the leaky modes. It reaches the value $p_{\text{QD}}|_{\text{max}} = 0.577$, making the efficiency of this protocol weak.

⁸The single photons with shaped time-envelopes are emitted with non-zero detuning and do not show those oscillations. This is not contradictory, as a time-dependent detuning influences the emitted pulses differently from a static detuning.

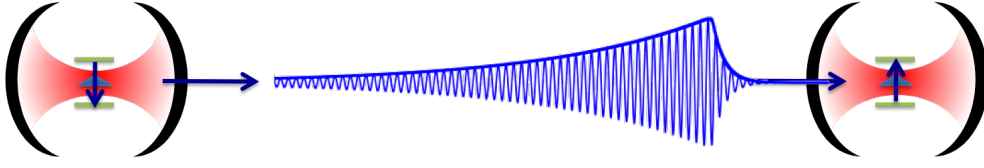


Figure 4.13: Concept of an emission-reabsorption process with two identical unperturbed cavity-QD systems. All QD transitions and the cavity mode frequencies are in perfect resonance to another. The left cavity-QD system has initially an excited QD and emits a single photon with exponentially decreasing time-envelope and constant frequency. (The shown oscillations are only schematic and don't represent the much faster actual ones. The pulse envelope is shown as a function of space and not as a function of time.) The right cavity-QD system absorbs the impinging single photon and the initially unexcited QD transition gets excited.

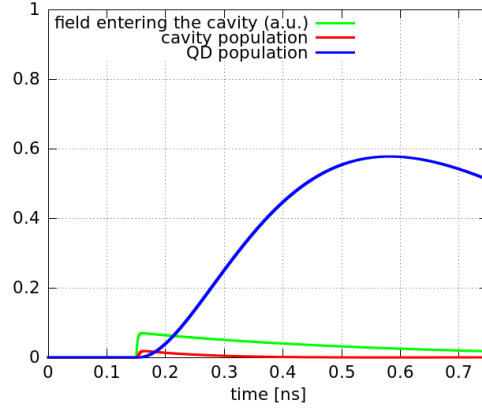


Figure 4.14: Absorption of a single photon pulse, emitted by an identical cavity-QD system. The absolute value of the entering electric field is shown in green. This field populates the cavity mode (its population is shown in red) which excites the QD transition. The QD exciton population is shown in blue.

An increased $p_{\text{QD}}|_{\text{max}}$ is necessary for the efficient photon exchange between identical unperturbed cavity-QD systems. According to the principle of the time-reversibility of emission, the best reabsorption properties are obtained when the emitted pulse time-envelope is the most time-symmetric, so that the fidelity between the emitted pulse and its time-reversal is maximised. The shorter the emitted pulses are, *i.e.* the smaller κ/g , the more time-symmetric they are, up to a certain limit where Rabi oscillations appear in the time-envelope. We want to find the optimal value of κ/g which leads to the largest $p_{\text{QD}}|_{\text{max}}$. As in the previous simulation, A will again emit spontaneously a single photon which will be absorbed by B (as illustrated in figure 4.13 but with a different pulse envelope). γ is taken to be zero.

In the figure 4.15a are shown the time-envelopes of the spontaneously emitted single photon pulses for four different systems A, characterised by $\kappa/g = 1, 2.34, 4.5$ and 7 ,

respectively; figure 4.15b shows the corresponding photon spectra. The emitter transitions and cavity modes are in perfect resonance. For $\kappa/g > 4$, in the weak-coupling regime, the time-envelopes are long and not very time-symmetric. For $\kappa/g < 4$, in the strong-coupling regime, the Rabi oscillations appear and the photon spectrum split into a doublet with two equivalent eigenfrequencies (discussed by [49] and [50]). When the Rabi oscillations are still very weak, the time-envelope is the most time-symmetric. The best reabsorption probability was obtained for $\kappa/g = 2.34$, as we will see beneath.⁹

Simulating the absorption of those pulses (each with its corresponding system B having the same κ/g as A) evidences the best absorption properties for $\kappa/g = 2.34$ (see figures 4.15c-e). When Rabi oscillations are present — for $\kappa/g < 4$ — the population of the absorbing QD (blue lines) also oscillates. Only with very weak Rabi oscillations can large $p_{\text{QD}}|_{\text{max}}$ be reached. For larger κ/g , the emitted photon envelope is less time-symmetric (it becomes exponential-like, see the green lines) and the efficiency of the reabsorption is decreased (see also figure 4.14 with $\kappa/g = 29.3$). The cavity mode population (red lines) provides some further information about the intensity of the entering and re-emitted field — the increase at long times of the cavity population is due to the re-emission of the once excited QD transition, in addition to the still entering field.

The optimal value of κ/g for an efficient emission–reabsorption process can be computed. This give a limit to the efficiency $p_{\text{QD}}|_{\text{max}}$ of the photon exchange between identical unperturbed cavity–QD systems. The evolution of $p_{\text{QD}}|_{\text{max}}$ as a function of κ/g is shown in figure 4.15f. The most efficient photon exchange occurs for $\kappa/g = 2.34$ with $p_{\text{QD}}|_{\text{max}} = 0.905$.¹⁰ For smaller values of κ/g , so far in the strong-coupling regime, the efficiency $p_{\text{QD}}|_{\text{max}}$ decreases strongly, but still stays above 0.5. Increasing κ/g makes the efficiency $p_{\text{QD}}|_{\text{max}}$ also decrease: as a reminder, for $\kappa/g = 29.3$ and $\gamma = 0.05$ we obtained $p_{\text{QD}}|_{\text{max}} = 0.577$.

I showed that the emission–reabsorption of a single photon between two identical unperturbed cavity–QD system can reach $p_{\text{QD}}|_{\text{max}} = 0.905$ for a very particular parameter set ($\kappa/g = 2.34$). Experimentally, it is very difficult to realise two identical cavity–QD systems with precise κ/g values. Applying in this context cavity switching to A and thus shape the emitted pulse envelope cannot increase $p_{\text{QD}}|_{\text{max}}$: The fastest emission occurs when the QD and the cavity mode are in perfect resonance — the condition of the unperturbed emission; any detuning between the QD and the cavity, which is necessary to shape the emitted time-envelope, slows down the emission process and the target pulse for ideal absorption in B (B is identical to A) can never be reproduced. For identical cavity–QD systems, allowing reversible quantum optical links, the unperturbed protocol is the better one.

An initial detuning of B could nevertheless lead to a longer target pulse and, combined with temporal pulse-shaping applied to A, may increase the maximum $p_{\text{QD}}|_{\text{max}}$. The bigger

⁹This differs from $\kappa/g = \sqrt{2\pi} = 2.51$, which was the ideal case for the absorption–emission protocol. Here we discuss the different emission and consecutive reabsorption.

¹⁰This value for the maximal reached QD population is smaller than the fidelity reached in [122] for the absorption–emission process, but difficult to compare, as discussed.

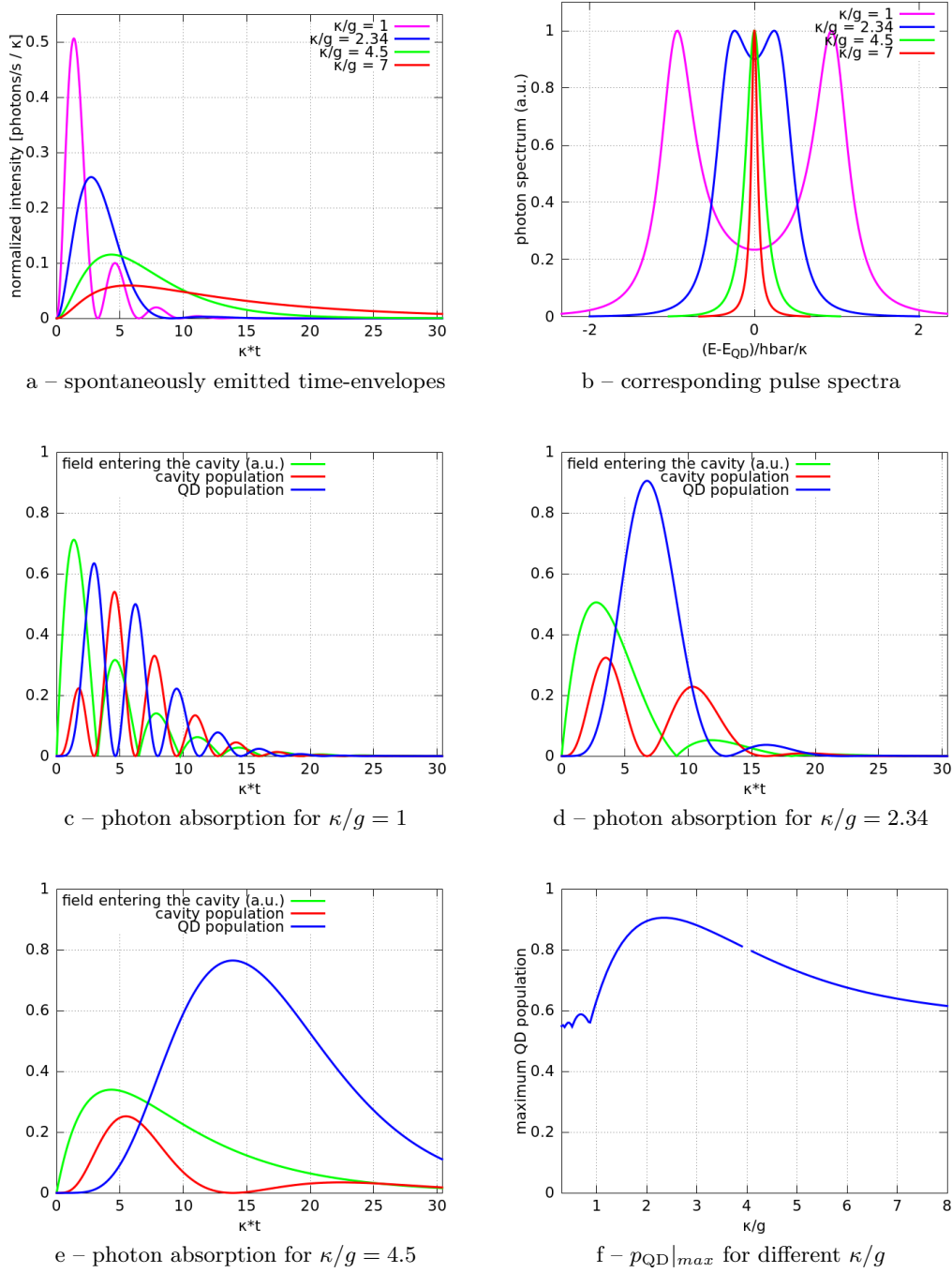


Figure 4.15: Emission–reabsorption process of a single photon with two identical unperturbed cavity–QD systems. Different cavity–QD systems, characterised by κ/g , are studied. The coupling to leaky modes γ is taken to be zero. For four values of κ/g , (a) and (b) show the properties of the spontaneously emitted single photon. (c), (d) and (e) show for given κ/g the reabsorption of the corresponding photons. (a–e) are generic studies, thanks to the normalised time-axes showing κt , and valuable for all combinations of $F_P \propto 1/Q \propto \kappa \propto g$ which keep κ/g constant. Finally (f) shows the maximal excitation probability $p_{\text{QD}}|_{\text{max}}$ of the two-level emitter transition (*e.g.* QD exciton) in the absorbing system as a function of κ/g . The maximum of $p_{\text{QD}}|_{\text{max}}$ is 0.905 for $\kappa/g = 2.34$. At $\kappa/g = 4$ the eigenfrequencies of the spontaneous emission split, as pointed out by [49], causing a discontinuity in the simulation, whereby the missing value.

the detuning, the longer the target pulse and oscillations appear and become more and more large with increasing detuning. A target pulse with sufficient duration would have no more an exponential time-envelope and its reproduction would become even harder due to the oscillations. This protocol is again less efficient than the unperturbed one.

A third approach may be the switching of both cavity-QD systems. The switch of B would have to be perfectly synchronised with the incoming single photon. Even for small jitter, the value of $p_{\text{QD}}|_{\text{max}}$ will decrease, and the absorption won't be efficient. In A the jitter is easier to control: the QD can be prepared in the excited state in a regime of strongly inhibited spontaneous emission, and subsequently cavity switching will start the emission and shaping process of the single photon with the desired time-envelope. The jitter can be large without negative consequences. Experimentally the switching of both cavity-QD systems — most probably two different switching pulses would be necessary to obtain high $p_{\text{QD}}|_{\text{max}}$ — is more challenging than only switching the system A, where we focus on.

To conclude, if one does not want to switch both cavity-QD systems, the perfect exchange of a single photon requires an initially fast cavity-QD system A, perturbed (therefore slowed down) to shape the time-envelope of the emitted pulse, and a slower static perfectly absorbing cavity-QD system $B \neq A$, making the photon exchange unidirectional. The perfect (*i.e.* $p_{\text{QD}}|_{\text{max}} = 1$), reversible exchange of single photons between two identical cavity-QD systems seems not possible. The best results were obtained with unperturbed and identical cavity-QD systems operating at the onset of the strong-coupling regime. Under those conditions, values above 0.9 for $p_{\text{QD}}|_{\text{max}}$ were obtained for the reversible photon exchange.

Photon exchange between different cavity-QD systems using pulse shaping Here we study the unidirectional exchange of a single photon: the emission of a temporally shaped single photon pulse by a first cavity-QD system (A) and the consecutive absorption of this photon by a static cavity-QD system (B). The overall efficiency of the protocol will again be given by $p_{\text{QD}}|_{\text{max}}$, the maximal population of the QD transition in B, initially equal to zero. The absorbing cavity-QD system B sets the target time-envelope, equal to the time-reversal of its hypothetical spontaneous emission. To reproduce this target time-envelope with A, rate equations are used to determine the $\delta(t)$ and $F(t)$ functions which will be applied for switching the cavity-QD system A. The absorbing cavity-QD system B will have constant δ and F , usually $\delta = 0$ and $F = F_P$. It could be imagined to apply cavity switching to B in order to increase the absorption probability, but this would make the protocol much more complex and more difficult to realise. Applying a constant detuning to B is easily feasible, and may be useful, as long as the system stays resonant with the impinging shaped pulse. All temporal evolutions of the systems A and B are computed with the quantum Langevin equations.

Cavity switching will shape the time-envelope of an emitted single photon pulse, as done in the preceding. In figure 4.12, I studied the emission of a shaped, exponentially increasing photon pulse with the cavity-QD system A having $F_P = 79.8$, $Q = 1000$, thus

$\kappa/g = 11.3$, and $\gamma = 0.05$. It reproduced the target pulse spontaneously emitted by the cavity–emitter system $F_P = 6$, $Q = 2000$ (*i.e.* $\kappa/g = 29.3$) and $\gamma = 0.05$ (here equal to the system B) with the fidelity $f = 0.788$. I want to study the absorption of this pulse by the unswitched system B, as illustrated in the figure 4.16. This is simulated with the quantum Langevin equations and the corresponding absorption properties are shown in figure 4.17. The absorption became better compared to the spontaneously and not time-reversed pulse shown in figure 4.14, but the value of $p_{\text{QD}}|_{\text{max}}$ — now slightly larger than 0.7 — is still too modest to conclude on efficient quantum optical links.

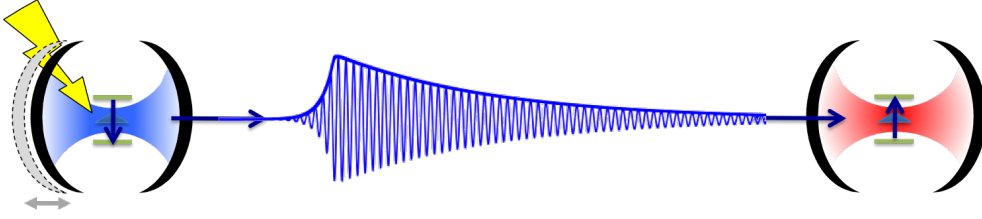


Figure 4.16: Concept of a unidirectional quantum optical link between two different cavity–QD systems. The left cavity–QD system has initially an excited QD. Being switched, it emits a shaped single photon pulse with exponentially increasing time-envelope. This pulse can be reabsorbed by the second and static cavity–QD system. (The pulse envelope is shown as a function of space and not as a function of time.)

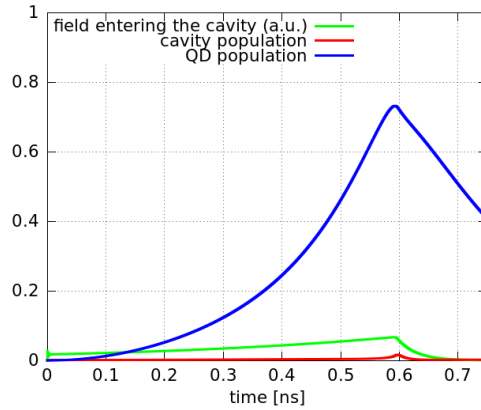


Figure 4.17: Absorption of the shaped single photon pulse studied in figure 4.12. The absolute value of the entering electric field is shown in green. This field populates the cavity mode (its population is shown in red) which excites the QD transition. The QD exciton population is shown in blue.

$p_{\text{QD}}|_{\text{max}}$ has to be further increased to have an efficient emission–absorption protocol. Up to now the best result was $p_{\text{QD}}|_{\text{max}} = 0.905$ for the unperturbed emission–reabsorption with two identical cavity–QD systems having $\kappa/g = 2.34$ and $\gamma = 0$. Based on this result I chose the system B to be in a similar state to insure good absorption properties. Its parameters are therefore $F_P = 109$ and $Q = 15000$, thus $\kappa/g = \sqrt{2\pi}$ and $\gamma = 0.05$. The spontaneously emitted and time-reversed target pulse is quite short and symmetric in time.

Following the principle of time-reversibility, the time-reversed target is perfectly reabsorbed by the identical cavity–QD system B, if initially not excited. We will see if such a pulse can be reproduced with A. The process is schematized in figure 4.18. The best parameter I found for A — concerning the reabsorption probability in B — are $F_P = 235.28$, $Q = 5000$, thus $\kappa/g = 2.95$, and $\gamma = 0.05$. As $\kappa/g < 4$, the detuning and enhancement factor have to be calculated with the iterative approach; the time evolutions leading to these results are computed with the quantum Langevin equations 4.9.

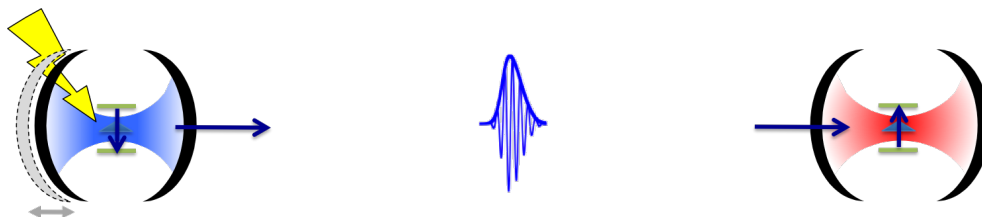


Figure 4.18: Schematic realization of an efficient asymmetric quantum optical link. The left cavity–QD system, having initially one exciton in the QD, is switched and emits a very short, and almost time-symmetric single photon pulse. This pulse is efficiently absorbed by the right and unswitched cavity–QD system so that $p_{\text{QD}}|_{\text{max}}$ approaches unity. (The pulse envelope is shown as a function of space and not as a function of time.)

Applying the computed detuning $\delta(t)$ using cavity switching to A, the target photon with unit integral can be very well reproduced (see figure 4.19a). The comparison of shaped and target pulses gives $f = 0.971$, $\tilde{f} = 0.988$, $\tilde{\beta} = 0.9993$ and $I = 0.998$. Sent to the cavity–QD system B, this photon is well absorbed. The figure 4.19b shows the absolute value of the entering electric field of the shaped pulse, the population of the cavity mode and the population of the QD exciton. The QD exciton population goes up to $p_{\text{QD}}|_{\text{max}} = 0.967$ ¹¹, which represents a very efficient asymmetric quantum optical link.

This subsection states the ability to shape in the time-domain, using cavity switching, nearly perfect single photon pulses — aiming the shape of time-reversed spontaneously emitted single photon pulses — and shows their potential utility for quantum optical links. In an unidirectional quantum optical link a maximal overall efficiency for the emission–absorption process of about 97% was obtained. For a reversible quantum optical link — obtained with unperturbed and identical cavity–QD systems operating at the onset of the strong-coupling regime — an overall efficiency of about 90% was obtained.

¹¹This is the maximum efficiency for an emission–absorption process that I found. Other parameter may even lead to larger $p_{\text{QD}}|_{\text{max}}$. A wide and systematic study varying all the accessible parameter would be interesting but out of the scope of this thesis. I am here solely giving a roadmap for highly efficient unidirectional quantum optical links.

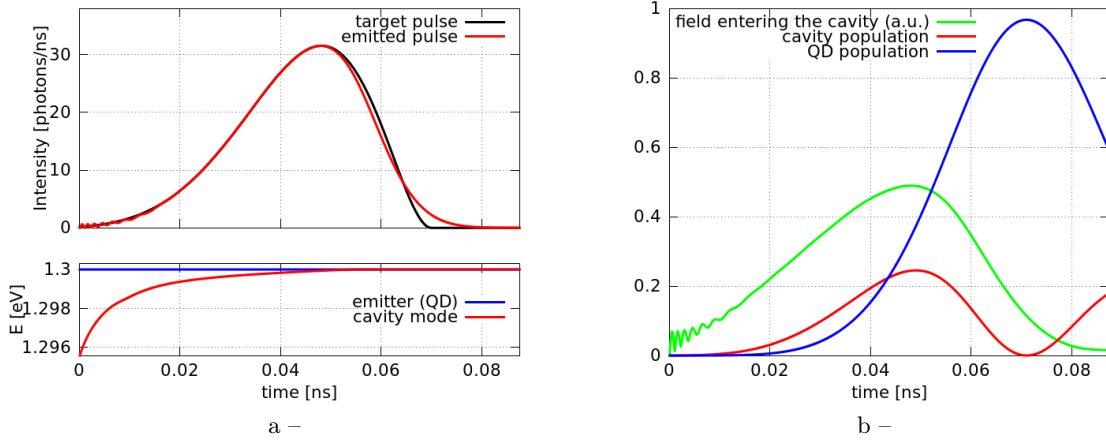


Figure 4.19: Best obtained emission and reabsorption of a single photon. Two different cavity–QD systems communicate with a short exponentially increasing single photon pulse. The emitting system A is perturbed by cavity switching to emit the photon with optimal time-envelope for absorption by the second static cavity–QD system B. (a) The black line shows the target pulse, being the time-reversed unperturbed spontaneous emission of B, very well reproduced by the emitted shaped pulse (red line). The corresponding time-dependent cavity mode resonance and emitter transition are shown below. (b) Absorption of the emitted single photon with the cavity–QD system B. The green line shows the absolute value of the incoming field of the shaped pulse. The red line shows the cavity population and the blue line the QD exciton population. The increase at long times of the cavity population is due to the re-emission of the once excited QD transition. The maximum QD excitation, so the largest reabsorption probability, is $p_{\text{QD}}|_{\text{max}} = 0.967$.

4.4.4 Using emitter tuning to shape single photon pulses

Up to now, all simulations were conducted under the assumption of cavity switching. The time-envelopes of single photon pulses can also be shaped with emitter tuning. For example, Stark tuning provides a good tool. The rate equations lead to identical results for emitter tuning and cavity switching (but not the quantum Langevin equations). All the computed time-dependending detuning can be applied with emitter tuning instead of cavity switching in order to compute the time-evolution of the cavity–QD systems with the quantum Langevin equations. The obtained shaped pulses can be compared to the pulses obtained with cavity switching. The differences between both approaches will be highlighted.

As an example, I will study the emission of shaped single photon pulses with 1) a Gaussian time-envelope, 2) an exponentially increasing time-envelope, in analogy to the studies in the figures 4.11 and 4.12. All the simulations will be done as in the previous sections. For emitter tuning, the cavity mode resonance will be fixed in time and the time-dependent detuning will be applied to the emitter transition alone. As we will see, the photons shaped with emitter tuning experience a strong frequency chirp. The smaller the

variations of the detuning, the smaller this chirp. Cavity-QD systems with small κ/g need less absolute detuning for pulse shaping compared to cavity-QD systems with larger κ/g . Thus to be in a regime of limited frequency chirp, in order to compare emitter tuning with cavity switching and to reproduce the target pulses shown in the figures 4.11 and 4.12, I will use here smaller κ/g than before (5 and 6.55, respectively, instead of 11 and 11.33, respectively).

In the first study, a target single photon pulse with Gaussian time-envelope and a FWHM of 150 ps should be produced with the cavity-QD system where $Q = 7027$ and $F_P = 58.5$, thus $\kappa/g = 5$ (and $\gamma = 0.05$). The corresponding detuning is computed with the rate equation approach (since $\kappa/g > 4$; for smaller κ/g the iterative approach would have been necessary). The detuning and the corresponding time-envelopes are shown in figure 4.20a. The target pulse is very well reproduced and $\tilde{f} = 0.997$ for emitter tuning, as well as for cavity switching. Both methods lead actually to the same time-envelope, as predicted by the rate equations, but the confirmation by the quantum Langevin equations was not guaranteed.

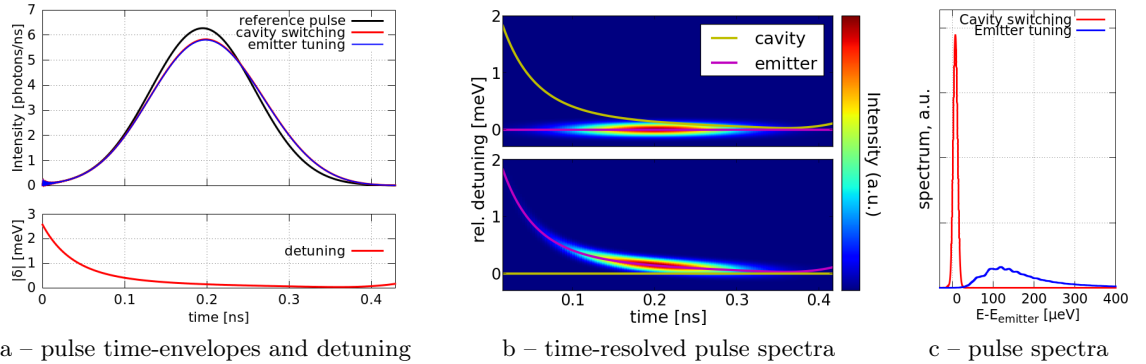


Figure 4.20: Shaping a Gaussian single photon pulse for cavity switching and emitter tuning. (a) The target and the shaped time-envelopes and the corresponding detuning. (b) The temporally and spectrally resolved pulses. Superposed are the time-dependent spectral cavity mode position (yellow line) and emitter transition (magenta line). The top figure corresponds to cavity switching, the bottom figure to emitter tuning. The emission occurs always resonant to the emitter transition. (Again the 30 ps long Hamming window determines temporal and spectral resolution.) (c) The corresponding pulse spectra.

The big difference in emitter tuning and cavity switching lies in the spectral properties of the emitted photon. The time-resolved spectra of both shaped pulses (figure 4.20b) is clearly different. The instantaneous spectral position of the photon always follows the spectral position of the QD transition. This is particularly true as the variations of the detuning are very smooth. The photon emitted using emitter tuning experiences a large spectral chirp, in contrast with the photon emitted using cavity switching. The time-integrated photon spectra reflect this (shown in the figure 4.20c): the spectrum of the photon emitted using emitter tuning is broad, while the spectrum of the photon emitted

using cavity switching is narrow and Gaussian shaped. As the spectral properties directly influence the fidelity, $f = 0.983$ for cavity switching and $f = 0.135$ for emitter tuning. As usual, the reference pulse has a constant frequency.

In this study ($\kappa/g = 5$) cavity switching reproduces with high fidelity the target photon, while, because of the frequency chirp, the emitter tuning fails completely in terms of fidelity.

The second study is the production of a shaped single photon with exponentially increasing time-envelope. The target pulse is the same as in figure 4.12: the time-reversal of the spontaneous emission by the system where $F_P = 6$, $Q = 2000$ and $\gamma = 0.05$ (thus $\kappa/g = 29.3$). The emitting cavity-QD system has $F_P = 79.8$ and $Q = 3000$, thus $\kappa/g = 6.55$, and again $\gamma = 0.05$. The results are presented in figure 4.21, in the same way as in the previous case of shaping a Gaussian time-envelope.

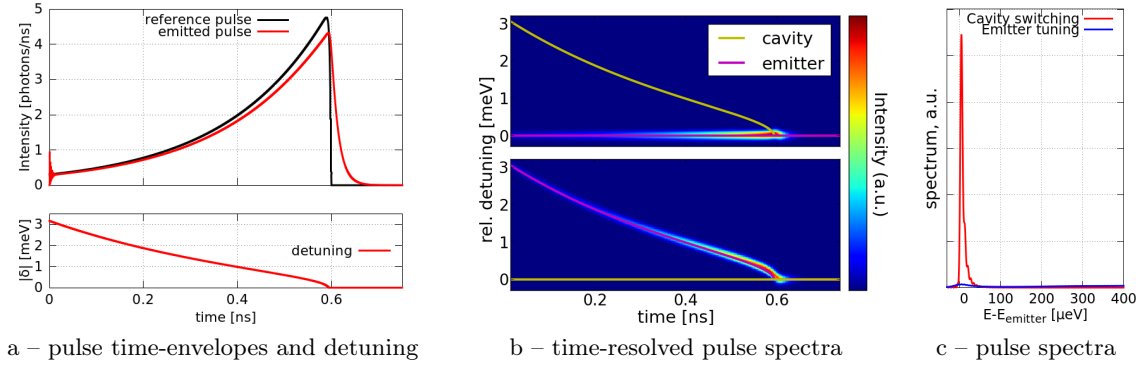


Figure 4.21: Shaping the same exponentially increasing single photon pulse as in figure 4.12, but with another cavity-QD system. Cavity switching and emitter tuning are studied, exactly like in figure 4.20.

The emitting cavity-QD system ($\kappa/g = 6.55$) reproduces the target pulse with $\tilde{f} = 0.937$ and $\tilde{\beta} = 0.993$. Emitter tuning and cavity switching shape the same time-envelope for the emitted photon. The shape is as well reproduced as in the first reproduction with the cavity-QD system $\kappa/g = 11.33$ (*cf.* figure 4.12), showing the versatility of the adapted cavity-QD systems.

The photon emission is again resonant to the spectral position of the emitter transition in time. But only when the detuning reaches zero and its variations become the fastest are there again slight deviations. Cavity funnelling or similar effects may play a role. Consequently the spectrum of the shaped photon emitted with cavity switching is slightly broadened. The spectrum of the shaped photon emitted with emitter tuning is strongly broadened, nearly flat, due to the strong frequency chirp it experiences. The resulting fidelities are $f = 0.79$ for cavity switching and $f = 0.014$ for emitter tuning. Again this illustrates the superiority of cavity switching to shape single photon pulses in the weak-coupling regime.

In the weak-coupling regime the emitter tuning does not seem to be able to shape single photon pulses with high fidelity. To get a better knowledge about pulse shaping with

emitter tuning, I want to present a study of the fidelity f obtained with emitter tuning for cavity-QD systems in the range of $2 < \kappa/g < 15$, with $\gamma = 0$. The target time-envelope to reproduce is the Gaussian shaped single photon pulse as used all along this chapter, having a FWHM of 150 ps. The corresponding detuning in normalised units δ/κ is shown in figure 4.9. It is obtained with the iterative approach, since small κ/g are also studied. Solving the quantum Langevin equations, one can obtain the dependence $f(\kappa/g)$. Such a study was conducted for cavity switching and the results were shown in figure 4.10. Conducting the same simulations for emitter tuning, one can compare both approaches.

Figure 4.22 shows f and I as a function of κ/g for emitter tuning and cavity switching. As expected cavity switching reproduces very well the target photon for all criteria. Emitter tuning reproduces very well the photon time-envelope (not shown here, but discussed in the previous studies) but the fidelity is limited by the spectral properties of the shaped photon. In the weak-coupling regime $f < 0.3$ making the approach unsuited. Additionally for κ/g larger than 8, the photon integral tends toward zero and no photon is emitted for κ/g larger than 11. Under these conditions, the absolute variations of the detuning are very large, which may play a role. In the strong-coupling regime ($\kappa/g < 4$) the emitter tuning is more successful, especially for the smallest κ/g . The detuning varies less, reducing the frequency chirp. f varies between 0.8 and 0.3 for κ/g between 2 and 4, respectively.

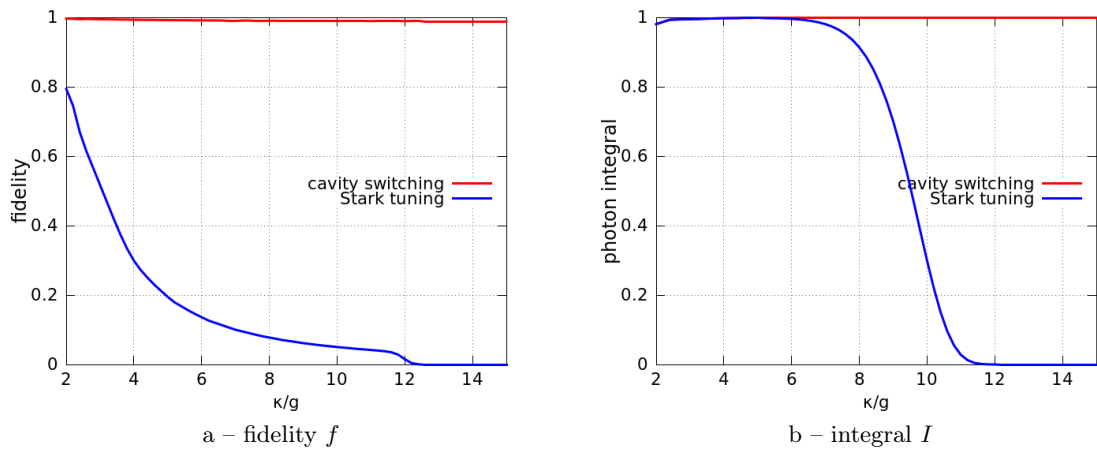


Figure 4.22: Comparison of cavity switching and emitter tuning to shape a single photon pulse with Gaussian time-envelope, in terms of figures of merit. (a) The obtained fidelity depending on κ/g ; κ/g describe the cavity-QD systems. An overall success for cavity switching is shown, while emitter tuning works only for the smallest κ/g thanks to the limited frequency chirp. (b) The integral I of the emitted single photons. For emitter tuning problems appear for κ/g larger than 8. For κ/g larger than 11, the quantum Langevin equations predict that no photon can be emitted anymore inside the cavity mode during the switching process.

One has to note that an ultrafast modification of the detuning is much easier to realise with all-optical cavity-switching (what can be on the (sub-)picosecond time-scale), than by

applying an electric field to tune an emitter transition (reference [82] for example realised a sub-ns control of the emitter transition in a similar context).

Emitter tuning may be interesting for temporal pulse shaping in the strong-coupling regime, even if its performances are very limited compared to cavity switching. But in the weak-coupling regime, emitter tuning is definitively not adapted to shape high-fidelity, single-photon pulses.

4.5 Conclusion

In this chapter I simulated CQED experiments in the context of cavity switching.

I described with rate equations, as well as with quantum Langevin equations, the temporal evolution of a two-level emitter in a cavity having a time-dependent energy detuning. Reabsorption by a second cavity-QD system was also studied. A mathematical formulation, relating the emitted photon's time-envelope and the cavity-QD parameters detuning and spontaneous emission enhancement factor, was found.

First, I simulated how to trigger efficiently, using cavity switching, the spontaneous emission of a two-level emitter in a cavity. We call this "Purcell switching".

Then I discussed how to control the emission process of a single photon over its entire duration. This implied a control of the shape of the time-dependent single photon amplitude. With cavity switching, the effective production of high quality single photon pulses with Gaussian or exponentially increasing time-envelope was realised. Such photons have very stable spectral properties, *i.e.* an almost constant frequency. This is in contrast to single photon pulse shaping by Stark tuning, where the emitted photon experiences a large frequency chirp. I obtained for the studied cavity-QD systems, characterised by κ/g in the range from 2 to 15, an overall shaping efficiency between 0.986 and 0.99 (equal to the emitted photon integral times the fidelity) when cavity switching was used to shape the time-envelope. With very different cavity-QD systems (in terms of κ/g) almost identical, high-quality, single-photon pulse could be produced.

Finally, the subsequent reabsorption process was studied and a maximal overall efficiency for the emission-absorption process of 0.967 was found. This corresponds to an efficient asymmetric quantum optical link. Efficient, reversible quantum optical links could also be simulated; in that case a maximal efficiency of 0.9 was obtained — using two identical and unperturbed cavity-QD systems operating at the onset of the strong-coupling regime.

In this chapter, we discuss several possible applications of cavity switching. In a first experiment, we consider a micropillar cavity that contains an ensemble of QDs. A light pulse simultaneously excites the QDs and induces a switch of the cavity mode. With a proper filtering, ultrashort (~ 10 ps) spontaneous emission bursts can be generated. Beyond this first example of spontaneous emission switching, we also discuss experimental prospects to realize Purcell switching. Furthermore applying cavity switching to high- Q planar cavities — without emitters — can be used to change the colour of the stored light. We model such experiments for switching planar cavities, and propose an experimental procedure which should enable a perfect frequency conversion of light pulses.

5.1 Generation of ultrashort spontaneous emission bursts using cavity switching

Light pulses shorter than a few picosecond are usually emitted by pulsed laser sources and consist of coherent light. They are used — among others — for ultrashort illumination and imaging. But the resulting images are often difficult to interpret because of the presence of interferences in transparent systems, or speckles in diffusing media. Speckle-free imaging is much easier to interpret, as the speckles introduce unwanted structure in the data [131]. To be speckle-free, the illuminating light source has to be of incoherent nature. It may therefore be of interest to have ultrashort pulses with incoherent light for ultrafast imaging. Solid state emitters as QDs can operate in the coherent and in the incoherent regime. Depending on their environment and excitation their emission can be stimulated or spontaneous; in this latter case, they are incoherent light sources. Such spontaneously emitted incoherent light consists of long light pulses (provided that the excitation of the

emitter is pulsed) and the duration of which is given by the lifetime of the transition¹. Such emission can be accelerated if the Purcell effect is present, for example in microcavities. But one would need a very large Purcell factor in order to reduce the lifetime to a few picoseconds. In such case an ultrashort burst of spontaneous emission would be emitted, but the experimental production of such a light source is very challenging.

The present approach is to switch a micropillar cavity with modest quality factor Q (a few thousands) containing an ensemble of QDs. This ensemble constitutes a broadband light-source inside the cavity, that probes the instantaneous cavity mode positions. Provided that the QD luminescence signal is spectrally filtered, a small part of the switched signal can be selected, which leads to few picosecond-long emission bursts, that can be orders of magnitude shorter than the QD's transition's lifetime. The Purcell factor F_P does not influence the pulse duration any-more, but the amplitude of the burst signal is proportional to F_P . For the studied micropillars F_P is small. In this approach, the pulse duration depends on its spectral position and spectral width, which can both be controlled. Multiple bursts can be generated if more than one cavity mode successively crosses the passband of the spectral filters.

In this section, I will present how to generate ultrashort emission bursts and explain two adapted spectral filtering methods. Then I will show how to generate double bursts and discuss their burst durations and their temporal separation. Having described the burst generation, I have to test and prove the spontaneous emission nature of the burst light.

5.1.1 Single burst generation

We want to generate emission bursts by switching a micropillar cavity containing an ensemble of light-emitting QDs. The spectral filtering of the luminescence signal will result in emission bursts. To start, we can attribute a burst duration t_{burst} to the unswitched luminescence signal of a micropillar: $t_{\text{burst}} = 640$ ps, taking the unswitched signal shown in figure 3.3². This spontaneously emitted burst is quite long. We defined t_{burst} to be the full-width at half maximum in time of the spectrally integrated and time-dependent PL signal. The signal emitted by a switched micropillar has a much shorter t_{burst} , *e.g.* in the experiment of figure 5.1 $t_{\text{burst}} \approx 25$ ps.³ An increased PL-intensity for large switching amplitude provokes this effect, while all long time components are still present but their relative amplitudes weak. Several reasons exist for this increase of signal, among which two may dominate: The streak camera response is much better on the high energy side⁴, but this can be corrected, and lasing can occur for high excitation powers, as we will see later.

¹*e.g.* InAs QDs: 1.2 ns for the fundamental transition, few hundred ps for excited states.

²Emitted by the micropillar G2_04 with a $3 \mu\text{m}$ diameter.

³Here we excite the micropillar G2_06 having a diameter of $2 \mu\text{m}$ at 800 nm with 9.7 mW average laser power, just below the limit of lasing.

⁴This effect can be more or less strong, depending on the very sensitive alignment of the streak camera. With few exceptions, it was not possible to align perfectly.

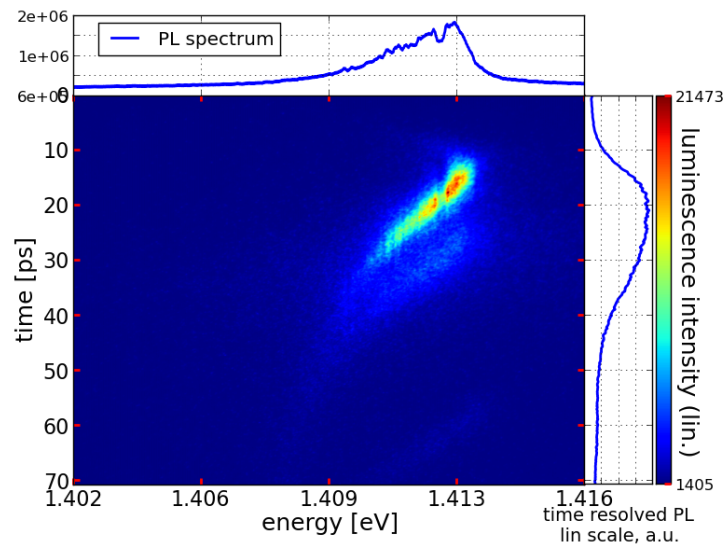
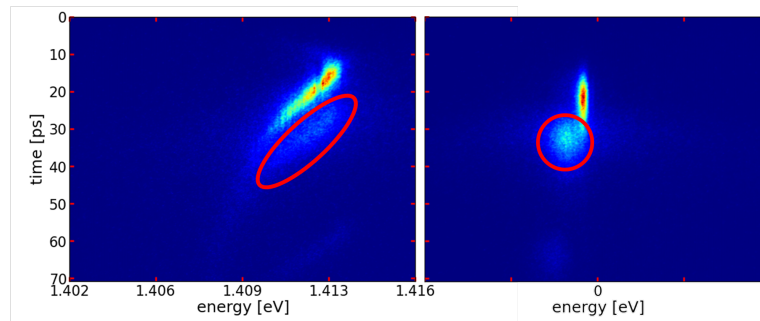


Figure 5.1: Temporally and spectrally resolved luminescence of an ensemble of InAs QDs embedded in a switched GaAs/AlAs micropillar of diameter of about $2 \mu\text{m}$. The few picosecond-long “switch-on” is visible. A ‘ghost’ is detected, too, presenting an artefact of the streak camera and can be neglected. The corresponding PL spectrum is also shown, as well as the spectral integration of the entire detected image, which results in the time resolved PL signal.

The ‘ghost’

The ‘ghost’ presents an artefact of the streak camera measurements. It appeared spectrally and temporally shifted to the real signal. With high spectral and temporal resolution the ‘ghost’ became visible, as it is shown on the two following exemplary streak camera images, with and without energy dispersion, respectively. The red circles highlight this ‘ghost’. The amplitude of this ‘ghost’ could change with the spectral position on the streak camera and could be reduced by optimizing the alignment. But we couldn’t eliminate it in a reproducible manner. As the ‘ghost’ presents an artefact, it can be neglected in the analysis of streak camera images.



In the following I will show how to process such switched signal in order to produce an even shorter burst without any long-time components by applying spectral filtering.

Spectral filtering of the switched luminescence. Selecting a spectral window to which some QD transitions of a switched micropillar are resonant (so that no other QD transitions are detected anymore), can result in one ultrashort spontaneous emission burst, repeated at the laser repetition rate. In the experiment, this is realised by installing sharp, low and high passband filters in between the sample and the detection. The streak camera image of figure 5.1 changes and becomes the one of figure 5.2. All the emitted light at higher (*i.e.* preceding times) or lower (*i.e.* subsequent times) photon energies is filtered out and does not appear any more in the streak camera image. The corresponding PL spectrum (obtained by numerical integration of the complete signal image) gets sharper and the pulse duration gets shorter: $t_{\text{burst}} = 16$ ps. This demonstrates the emission of a true ultrashort burst.

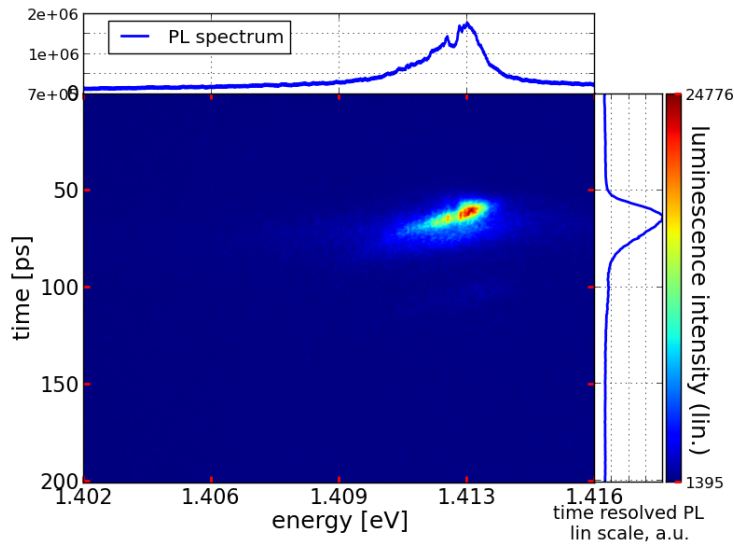


Figure 5.2: After the acquisition shown in figure 5.1, two sharp passband filter are installed, in order to reduce the signal to a narrow spectral window and create a veritable ultrashort emission burst. One has to note that the time-scale has changed compared to figure 5.1.

To further prove that an ultrashort burst was emitted, we tested that there were no contributions to the signal at energies out off the shown spectral window. To that purpose, the burst was observed without energy dispersion on the streak camera (see figure 5.3). This is possible if the grating in the monochromator is turned to its zeroth diffraction order so that it acts as a mirror. The obtained burst duration is again $t_{\text{burst}} \approx 16$ ps.

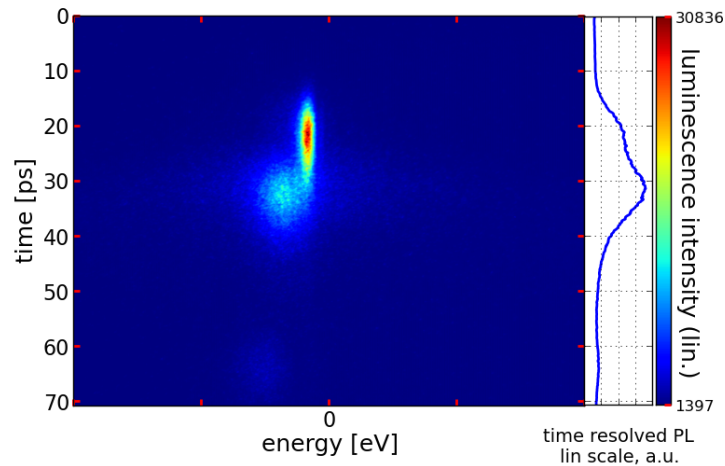


Figure 5.3: Proof of an ultrashort emission burst: The signal shown in figure 5.2 is now detected without energy dispersion. (The grid of the monochromator acts as a mirror.) Eventual light contributions out off the former energy window of the streak camera are now detected, too. The ‘ghost’, contributing to the time-resolved PL, is an artefact of the detection. Neglecting it, the pulse has again $t_{\text{burst}} = 16$ ps.

Second filtering method: spatial spectral filtering. The passband filters that were used, though quite sharp (10 nm passband), were not sharp enough for our purpose and gave too smooth attenuation on both sides of the passband⁵, which resulted in extending the burst duration. Removing the filters, we came to use the monochromator to spectrally filter the signal. Since the output of the monochromator spatially disperses the spectral components of the light in the horizontal plane, we added a narrow vertical slit at the entrance of the streak camera to stop all signal which was not in the wanted narrow spectral range. As a result, a spectrally very clearly defined burst with $t_{\text{burst}} = 6$ ps was detected with the streak camera in that configuration (see figure 5.4).

⁵See the PL-spectrum in the figure 5.2 above the streak image. At high energies, the cut-off is sharper than at low energies, because the corresponding filter was placed to cut off just above the maximum amplitude of the switch.

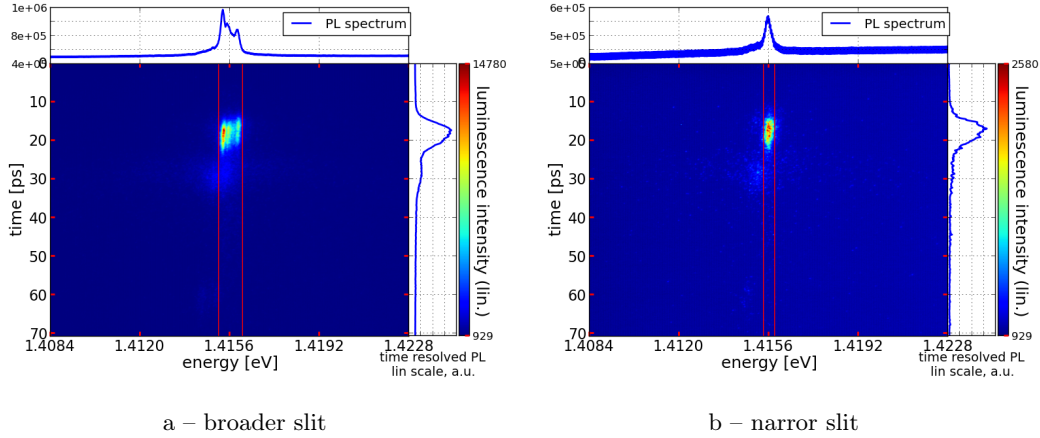


Figure 5.4: Optimised experiment: the signal is now filtered by a narrow vertical slit at the entrance of the streak camera. The red box is the selected area for the time-profile in order to exclude the ‘ghost’, an artefact of the streak-camera. It results in a spectrally well-defined burst with $t_{\text{burst}} = 6$ ps.

5.1.2 Double burst

The presented methods are not limited to the generation of a single burst. The same spectrally selected QD transitions can probe two neighbouring cavity modes, provided that the initial blue-shift of the cavity modes exceeds the spectral separation of the neighbouring cavity modes. Several QD transitions will probe one cavity mode after the other, and therefore emit two consecutive emission bursts with a certain delay (*cf.* figure 5.5). Filtering at different spectral positions can address different QD transitions to emit a double burst. The delay between the bursts will depend on the selected frequencies. For large switching amplitudes, the delay can be decreased down to a few picoseconds (*cf.* figure 5.6a), and be increased for smaller switching amplitudes, theoretically without limitation. The burst durations of both pulses behave similarly: the larger the detuning of the probed cavity mode, the faster its spectral return and the shorter the burst (*cf.* figure 5.6b). Because of that, the first burst is always shorter than the second one.

To conclude, the emission of two consecutive bursts with durations down to 3 ps and 6 ps, separated by only 11 ps, was demonstrated. The delay can easily be increased in a controlled way, if one accepts slightly increased burst durations.

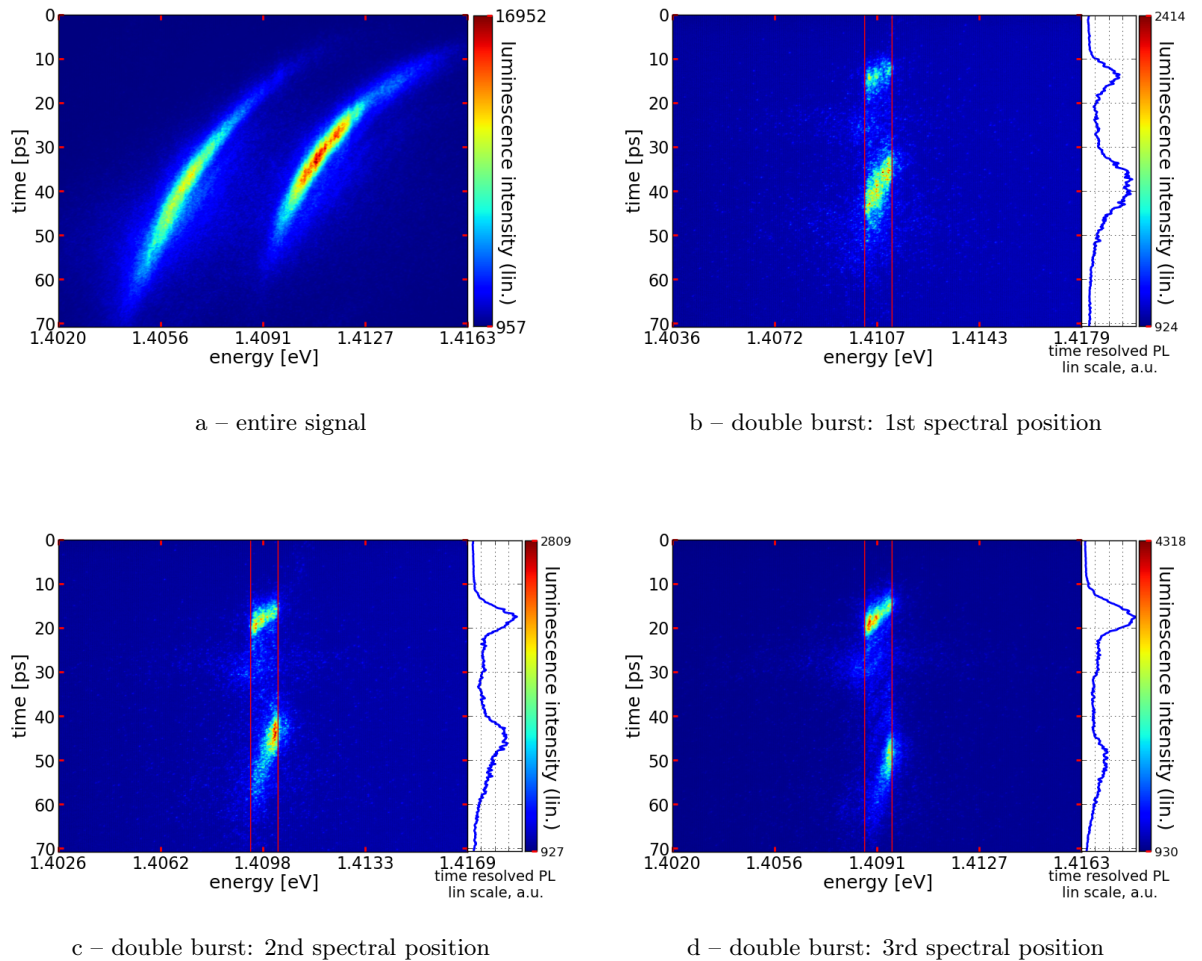


Figure 5.5: Streak camera images of the double burst: switching strongly a micropillar (G2_04) with two close-by cavity modes, several QD transitions probe both cavity modes and emit two consecutive few picosecond-long pulses. Spectral selection applied to the entire signal (a) results in the double bursts (b), (c) and (d). The three different spectral selections result in changing delay between both pulses and in changing pulse durations (data in figure 5.6). The exciting laser operated at 730 nm with 6.5 mW average power (lasing of the signal may occur).

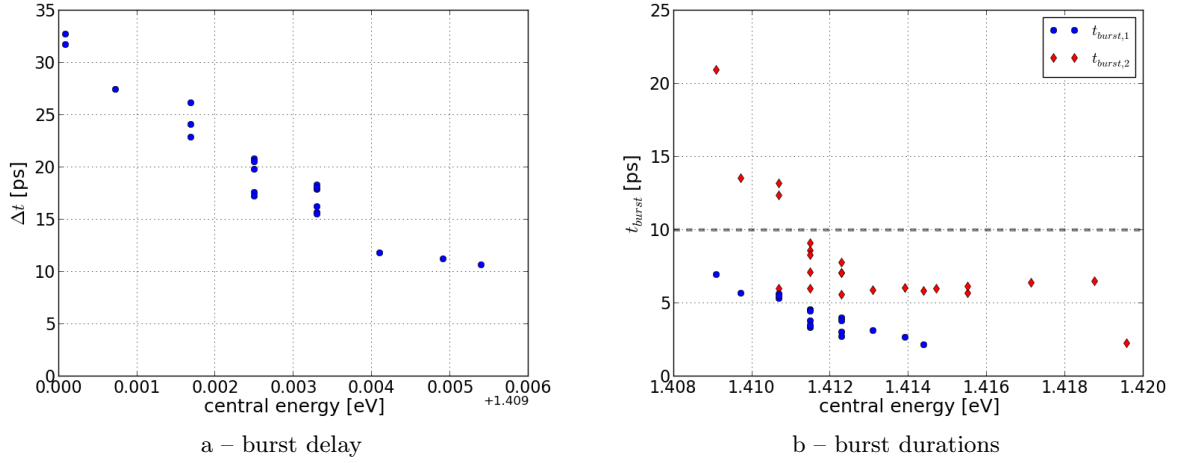


Figure 5.6: Double burst: analysis of the delay between the two consecutive bursts (a) and the burst durations (b). Each datapoint represents one experiment and the x-axis indicates the central energy of the corresponding emission burst. $t_{\text{burst},1}$ ($t_{\text{burst},2}$) corresponds to the first (second) emitted pulse. In (b), above a certain energy, spectral filtering addresses only the first order cavity mode and no more the fundamental cavity mode. For small energies the opposite happens, but is not shown here. Under such conditions, only a single burst is produced.

5.1.3 Dependence of t_{burst} with the amplitude of the switch

After the successful preparation of ultrashort emission bursts, we turned our interest to the limits to their duration. The spectral filtering is now realised by numerically selecting many narrow spectral windows in an acquired streak camera image, like figure 5.5a. For each spectral window a burst duration is computed. One has to note that t_{burst} is now the burst duration at a given energy and no more the burst duration of the entire detected signal. The value of t_{burst} is obtained by adjusting every time-dependent signal to a Lorentzian peak.

Figure 5.7 shows the burst duration as a function of the instantaneous energy-shift. The higher the energy-shift, the shorter the duration of the burst. The minimal burst duration is here ~ 4 ps and limited by the maximum amplitude of the switch. The two underlying streak camera images were obtained using a temporal resolution better than 2 ps and the exciting pulsed Ti:sapphire laser operated at 800 nm and high power (12.3 mW) to maximise the switching amplitude. The pillar G2_04 is studied. Both traces follow nicely the relation (red line):

$$t_{\text{burst}}(E_m) = \frac{\Delta E_m}{\partial E_m / \partial t} \approx \frac{\Delta E_m}{E_m - E_{m,0}} \tau_{e/h} \quad (5.1)$$

The cavity mode is resonant to E_m (E_m is a function of time), in the unswitched case to $E_{m,0}$. ΔE_m is the spectral half-width of the cavity mode and is here limited by the experiment's spectral resolution. The spectral return of the cavity mode, when being a

mono-exponential decay, happens with the characteristic time $\tau_{e/h}$. Only if this condition is fulfilled, the second equality is exact. In general, this is not the case, as we saw in chapter 3, but the approximation holds for the beginning of the spectral return with large energy-shift (for times $\lesssim 100$ ps).⁶ In this regime, the initial fast spectral return of the cavity mode — described with the free-carrier lifetime $\tau_{e/h}$ — is governed by differential switching and free carrier diffusion (*cf.* chapter 3); bimolecular recombination may influence, too.

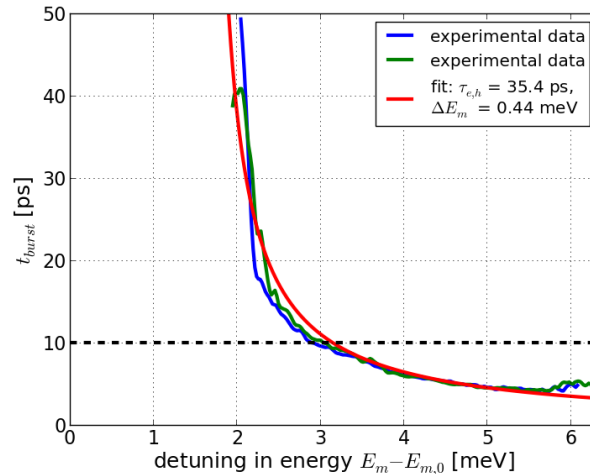


Figure 5.7: Ultrashort emission burst as extracted from two streak camera images (blue and green lines). Maximal temporal (< 2 ps) and spectral (1 pixel) resolution were used. The experimental data match very well equation 5.1 (red line), wherefore the parameters $\tau_{e/h} = 35$ ps and $\Delta E_m = 0.44$ meV were found. The minimal burst duration is here 4 ps.

5.1.4 A test of the light burst coherence

As discussed in the introduction, the generation of short pulses of incoherent light is attractive in view of ultrafast interference-free and speckle-free imaging. In this experiment, the emission from the quantum dot ensemble can be either governed by spontaneous emission or stimulated emission, depending on the experimental conditions. The light coherence has been tested using the burst signal to illuminate a diffusor and image the transmitted, scattered light, which consists in speckles or in a homogeneous illumination, depending on the coherence of the emitted light. For these reasons, we have conducted a set of preliminary experiences, to test the coherence of the emitted light bursts. These tests are combined with PL experiences so as to probe independently the spontaneous or stimulated nature of the QD emission.

The analysed bursts, are generated by filtering the switched emission of the micropillar G2_06 (diameter $2 \mu\text{m}$) with the two sharp pass-band filters. To get an sufficiently intense

⁶Under this conditions a mono-exponential fit results in a shifted value of $E_{m,0}$, different from the actual one. This value has not to be considered.

signal on the diffusor, the filtered spectral width is slightly increased, compared to the previous studies. The burst duration will therefore be slightly longer. The studied burst is shown in figure 5.8. Switch and QD excitation were realised with the same pulsed Ti:sapphire laser operating at 800 nm. Its average power will be tuned for the power-dependent studies. It is 5 mW for the shown image. An 18 ps-long FWHM burst is realised. In such configuration the detected bursts are far above the Fourier limit (here $\Delta\omega\Delta t \approx 1000 \gg 1$), necessary to detect incoherent light.

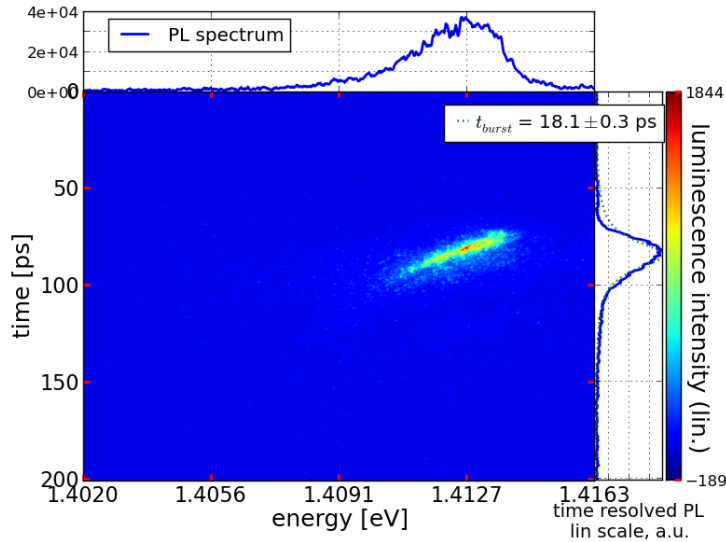


Figure 5.8: Ultra-short emission burst for light coherence analysis. A laser pulse excites the ensemble of QDs and switches the micropillar’s cavity mode resonance. The studied pillar is G2_06 with diameter 2 μm . Provided spectral filtering of the signal results in the emission burst. Its detection with a streak camera is shown, as well as the corresponding photoluminescence spectrum and time-profile. The burst duration is 18 ps. The used average laser power for excitation is 5 mW.

The first analysis of the nature of the burst light comes from power series. Comparing the intensity of the emitted light versus the power of the exciting laser informs us about the nature of the emission process. For spontaneous emission the intensity increases in a linear way with the laser power and can saturate. Further increasing the laser power, the emission gets stimulated, starting lasing, and the intensity increases dramatically. The peak power of a burst, detected with the streak camera, is plotted as a function of the exciting laser power in figure 5.9. It seems that the transition between spontaneous emission and stimulated emission comes around 7 mW.⁷ Thus for this sample and exciting wavelength, below 7 mW the bursts should be spontaneous emission bursts and present no speckles, while above 7 mW the bursts should be of stimulated emission nature and present speckles. This has to be tested.

To test whether the ultrashort emission bursts show speckles or not, the collimated burst

⁷The additional gain for stimulated emission may be provided by transitions between QD excited states and/or the InAs wetting layer.

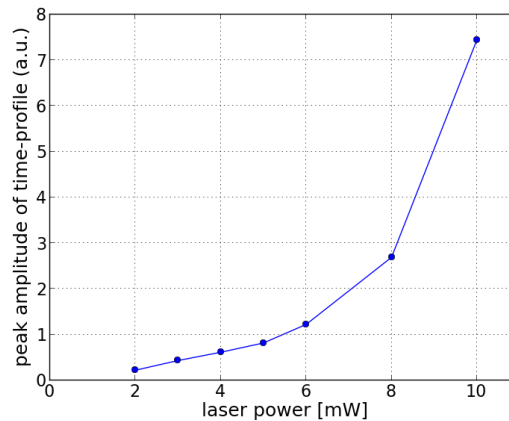


Figure 5.9: Study of the peak amplitude of ultra-short emission burst as a function of the exciting laser power. The peak amplitude is extracted from streak camera images of the bursts (one is shown in figure 5.8). Two regimes can be identified: For small excitation power the regime of spontaneous emission, for high excitation power the regime of stimulated emission. The studied pillar is G2_06 with diameter $2\ \mu\text{m}$ and the exciting laser operated at 800 nm.

signal was detected on a 0.5 mm-thick teflon plate (*cf.* figure 5.10). Teflon is transparent for infrared light, and will scatter it. Thus the image of transmitted coherent light should exhibit speckles, while incoherent light should exhibit a homogeneous distribution. The backside of the teflon plate was imaged with a CCD camera via a 10x objective. Either speckled signal or homogeneous signal, plus noise, was detected. The following images (in figure 5.11), studying the scattered burst light for different excitation powers, represent each the detection on the same 80×80 pixel region of CCD camera. Each set of two figures represents two consecutive acquisitions under the same conditions. The background was subtracted and only positive values are shown, showing the amplitude of the signal. The corresponding excitation power is indicated.

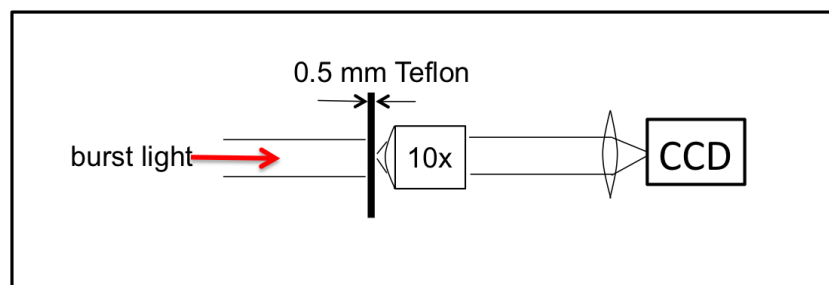


Figure 5.10: Experimental setup of the imaging of the burst light. The collimated burst light impinges on the 0.5 mm thick teflon plate and illuminates an area of about $1\ \text{mm}^2$. The transmitted scattered light is detected with the CCD camera. The visualized area on the teflon backside equals $50\ \mu\text{m} \times 50\ \mu\text{m}$.

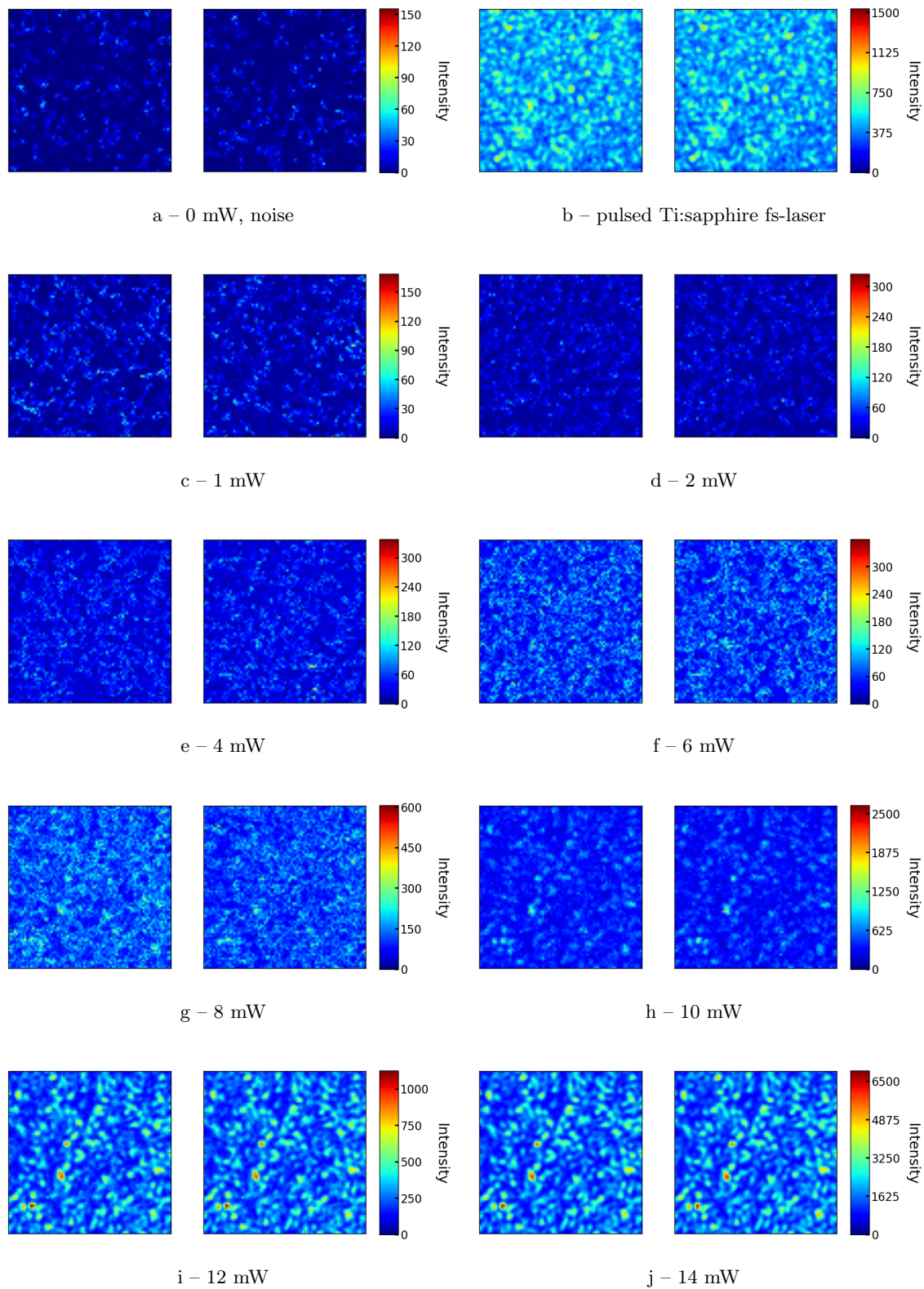


Figure 5.11: Imaging of scattered light on a 0.5 mm thick teflon plate. (a) The noise signal. (b) The speckles obtained with the pulsed Ti:sapphire laser. (c-j) The burst signals, corresponding to the burst shown in figure 5.8. For 0 to 10 mW excitation power the detection conditions are unchanged. Only the images (b), (i) and (j) have shorter integration times to compensate for the much more intense signals. Every two consecutive acquisitions are taken under exactly the same conditions. Their common colour scale goes from 0 to the maximal detected signal. If speckles are present, the case in the images (b, g-j), they are repeated in both images of a set, while noise is not, being random events.

For small excitation power the burst signals are very similar to the noise signal. Two consecutive images seem not to be correlated and noise fluctuations dominate. The average amplitude and maximal detected amplitude increase with the exciting laser power. Contrast between light and dark zones is weak. This is the regime of spontaneous emission and incoherent burst light. For higher excitation power, from 8 mW on, speckles get clearly visible and become more and more obvious with increasing laser power. This is in accordance with figure 5.9. Two consecutive images are clearly correlated and the contrast between light and dark zones increases with the laser power. Those speckled images resemble the speckled image of the pulsed Ti:sapphire fs-laser. The coherence of the lasing QD burst signal is even better than the coherence of the Ti:sapphire laser. This is consistent, as the pulse duration of the laser is much shorter (~ 200 fs).

These preliminary experiments give a first confirmation of the generation of ultrashort pulses of incoherent light as long as QD spontaneous emission dominates (< 6 mW in our experiments). At this stage, a more refined analysis of the correlation properties of images such as the one shown in figure 5.11 is necessary to confirm this conclusion. For the present data, we face two main problems in this prospect: the small speckle size and the rather low signal to noise ratio.

The size of the speckles is about one pixel, so the same size as the camera's noise. If the speckles would be bigger, an analysis of the size distribution could give valuable information. By replacing the 10x objective by a 40x objective, speckles of the laser are sufficiently resolved in space, while noise keeps the size of one pixel. Unfortunately, the QD signal was too low to be detected with the 40x objective. Several approaches may solve the problem: A much thinner teflon plate as diffuser may reduce the signal losses and is in production. Focusing the burst light on the teflon plate using a second objective or a lens would increase the local intensity of the scattered light and so of the detected signal, too.

Analysing speckles and the power-dependent intensity, both a low power regime of spontaneous emission and a high power regime of stimulated emission were identified. We were able to generate ultrashort and speckle-free spontaneous emission bursts.

5.2 Is there Purcell switching in the experiments?

With the ultrashort spontaneous emission bursts we gave a first example of switching the spontaneous emission. When a QD enters in resonance with a cavity mode, it emits into the cavity mode (in addition to the leaky modes). One can say that one switches the emission diagram of the QD. Ideally, we would like that all the spontaneous emission of the QD would be emitted into the cavity mode during the switch. This can (almost) be obtained if the Purcell effect plays an important role; and raises the question of whether Purcell switching is present in these experiments.

Purcell switching is an acceleration of a QD's spontaneous emission rate when the switched cavity mode is brought in resonance with a QD transition, combined with an accelerated decrease of the QD exciton population. In all the conducted experiments an intense burst is emitted when cavity and QDs come in resonance — the intensity is here proportional to the Purcell factor. Unfortunately one cannot conclude on Purcell switching: it is not a clear signature of Purcell switching but mainly due to the highly directive emission when signal is emitted through the cavity mode — increasing strongly the detected signal — at contrast with the emission through the leaky modes. An obvious signature of Purcell switching would be a decrease of the QD exciton population when the cavity mode and QD exciton enter in resonance.

The proper way to detect Purcell switching is to detect emission through the leaky modes only, as their intensity is proportional to the QD exciton population. A possible experimental arrangement is shown in figure 5.12. Purcell switching should lead to a step in the exponential decay of the leaky mode signal, as shown in the theory chapter 4.3.

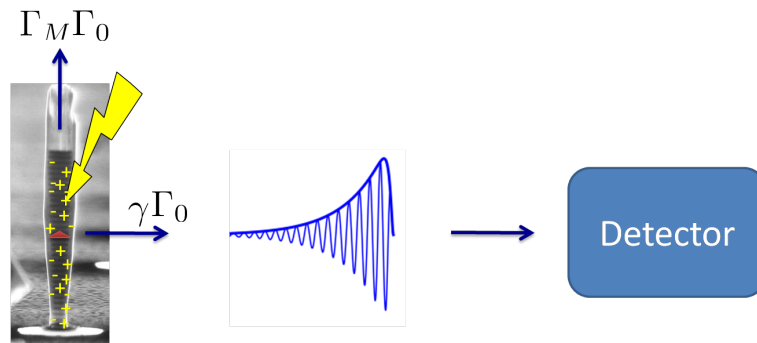


Figure 5.12: Detection of the leaky mode emission. Collection of the signal emitted only through the side-walls of a micropillar, enables us to select a pure leaky mode signal. Usually the detection is perpendicular to the micropillar's top facet to maximise the signal emitted through the cavity modes.

In our case, side detection was technically not possible, due to the available cryostats. We detected exclusively emission perpendicular to the sample surface. A new sample structure has been developed to solve this problem. Ovoid ring resonators, described in [132], show leaky mode emission perpendicular to the sample surface, thus ideal for the leaky mode detection using our cryostats. Switching them, instead of micropillar cavities, makes a Purcell switching experiment more realistic.

Two other parameters limit the feasibility of Purcell switching with the present micropillar samples. First, the maximal observed Purcell factor is of about 10 (*cf.* page 60). As the cavities have ensembles of QDs, spatially dispersed in the central plane of the cavity, the effective enhancement factor is $F_P/4 \leq 2.5$. Second, the spectral return of the cavity mode to its unswitched value happens in a few tens of picosecond. As shown in figure 4.4 under similar conditions, the effect on the QD exciton population is weak — it would be about 1% with the studied micropillar cavities — and Purcell switching could not be detected. A new sample should have a much larger Purcell factor and a slower spectral return of the cavity mode for significant and detectable Purcell switching. With higher quality GaAs, relaxation times of several hundred picosecond can be obtained. The simulations of figure 4.5 illustrate that Purcell switching is indeed realistic. Currently, Tobias SATTLE and Julien CLAUDON are processing samples grown by myself to obtain ovoid ring resonators with the needed parameters. With those samples, Tobias SATTLE and Joël BLEUSE will hopefully observe Purcell switching in the near future.

5.3 Switching a planar high- Q cavity with the application to change the colour of the trapped light

By applying cavity switching to a cavity where light is stored inside, one can modify the properties of the stored light. Notomi *et al.* explained in 2006 that a refractive index change in a microcavity can be used to change adiabatically its resonance and with it the colour of the light which is stored inside the cavity [78]. This adiabatic colour change was realised later by switching a ring cavity [11] or a photonic crystal cavity [15]. In this section, we show that it is possible to realise such conversion experiments with rather slow probe pulses (few tens of picoseconds) and a high conversion efficiency, using optimal planar cavities. As the presented method conserves the number of photons, it is also adapted to convert single photons in energy. Further high repetition rates are accessible.⁸

In this section, first the studied high- Q planar cavity will be introduced, then its light storage properties will be measured with the cavity ring-down experiment. For the same cavity, the colour changing experiment is simulated and its feasibility discussed, further the efficiency of the adiabatic conversion of a light pulse to a new energy. Finally we propose how to obtain a total conversion in energy of a tailored light pulse while switching an optimised and asymmetric planar cavity.

5.3.1 The high- Q planar cavity

In contrary to the previous studies on cavity switching, no internal light source like QDs was used to probe the cavity mode position. Light was injected from the outside using a pulsed or CW-laser (the probe), resonant to a cavity mode, so that we could probe the cavity modes with a transmission measurement. The properties of the light stored in the cavity mode m can only be modified, if the corresponding storage time τ_m is long, thus the quality factor Q_m high. We needed a high- Q filtering cavity.

A planar cavity seems to be ideal for transmission measurements and filtering of light. Its surface is usually much larger than a probing laser spot, what can prevent the laser light to transmit the sample if not resonant to a cavity mode. The main requirement to the cavity was a long storage time of tens of picosecond. The mode volume $V_{\text{eff},m}$ did not matter as no emitters were inside the cavity. A solution was to take a cavity with a very thick spacer. For a cavity mode which is centered inside the stopband, Q_m is proportional to the order of this cavity mode m (*cf.* equation 1.19). m increases with the thickness of the spacer L_{cav} (*cf.* equation 1.16). We chose $L_{\text{cav}} = 27\lambda_B/n_{\text{GaAs}}$. λ_B is the wavelength for which the cavity was designed, and n_{GaAs} the refractive index of the GaAs spacer. The cavity was made of altering GaAs and AlAs layers. The order of the central cavity mode was $m \approx 59$. This resulted in a 8.5 times higher order and quality factor of the central

⁸The simulation were conducted for GaAs/AlAs planar cavities. The free carriers injected in the GaAs layers, are responsible for the energy-shift of the cavity modes, and can have lifetimes down to few picoseconds. For an optimized experiment, repetition rates as high as 100 GHz may become possible.

cavity mode, than for the common cavity-design with a spacer thick as $L_{cav} = 1\lambda_B/n_{GaAs}$ (where $m \approx 5$). This high- Q cavity made of GaAs and AlAs was designed using the TMM simulations as discussed in section 2.5.1, see figure 2.17. The central cavity mode had in theory $Q_m = 65000$, $E_m = 1.3$ eV, so $\tau_m = 33$ ps. The bottom DBR, on the GaAs substrate, had 20 alternating layers, the top DBR 16. The fact that such cavity has many resonant modes did not trouble (their spectral separation was large enough). In contrary, it increased the spectral distribution of accessible modes with high Q_m .

In practice measurements have to confirm the Q_m . As stated in equation 1.11 and in figure 1.4, the spectral width of a cavity mode is the inverse of its storage time: $\Delta\omega_m = 1/\tau_m$ and Q_m can be measured either in the spectral or in the temporal domain. For high- Q cavities it is difficult to resolve the narrow spectral width of cavity modes $\Delta\omega_m$. But a study in the spectral domain, *e.g.* with a FTIR spectrometre, is still useful to check, for example, the spectral positions of cavity modes and stopband (see figure 5.13). To measure the quality factor of high- Q cavities (typically for $Q_m > 20000$ and $\tau_m > 10$ ps), the measurement of Q_m in the time-domain, *e.g.* with a cavity ring-down experiment, can be easier to realize [23].

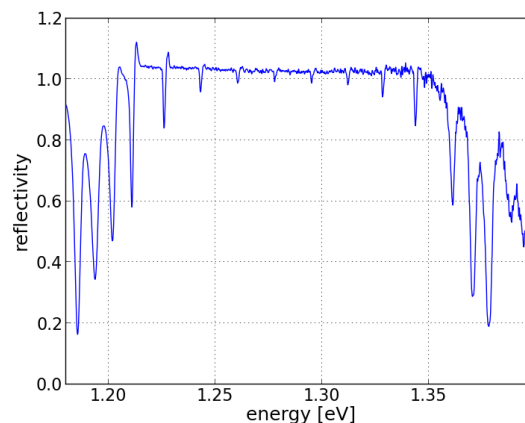


Figure 5.13: Reflectivity spectrum of the studied high- Q planar cavity, as obtained with the FTIR setup. We can observe the stopband, the different cavity modes, and their spectral positions. Unfortunately this spectrum is somehow limited. Due to the spectral resolution of the FTIR spectroscopy the widths of the modes are strongly broadened and no mode reaches close-to-zero reflectivity. In the ideal case, so if the necessary spectral resolution would have been accessible, the spectrum should look like in figure 2.17. Further the stopband has a reflectivity slightly above the value of 1. 1 is the reference of a gold mirror. That means the cavity has a better reflectivity than the used gold mirror. The peaks to the border of some cavity modes (*e.g.* at 1.21 eV and 1.212 eV), similar to oscillations, are an artefact of the FTIR spectrometre we couldn't eliminate.

5.3.2 The cavity ring-down measurement

The cavity ring-down experiment was necessary to characterise the light storage properties (*i.e.* Q_m and τ_m) of the above presented high- Q cavity. It was done in transmission. This had the advantage, that only the light which entered a cavity mode could cross, after storage, the sample. All other light was reflected and could not be detected. This made the transmission measurement better, as far as signal-to-noise ratio was concerned. It is a kind of “dark-field” measurement, as opposed to “bright-field” measurements for reflection.

To accomplish the transmission measurement, the backside of the sample, so the thick GaAs wafer, had to be transparent and free of reflection centres. GaAs is transparent at the studied wavelengths, but the backside of the sample had to be polished in order to establish a flat GaAs surface and limit reflection. A mechanical polishing took off the indium used to fix the substrate during the growth, and further flattened the so uncovered GaAs surface. A mixed mechanical and chemical polishing using bromine and methanol smoothed the remaining surface roughness. To limit internal reflection, an anti-reflection coating made of SiN_x was deposited on the polished backside of the sample.

We used the setup of the streak-camera, see figure 2.13, and put the planar cavity sample into the beam-path to make the transmission measurement possible. This allowed me to measure the temporal response of some modes of the planar cavity to a short laser pulse, and to deduce the cavity’s quality factor.

Each cavity mode has a spatial extension. In a planar cavity the confinement is only perpendicular to the surface. The lateral extension of a mode can be described with an effective surface $S_{\text{eff},m} = (Q_m/2)(\lambda_m/n)^2$ [133, 134]. For the central mode with $Q = 65000$ this results in a diameter $d_m = 4/\pi \cdot \sqrt{S_{\text{eff},m}}$ of about $62 \mu\text{m}$. For the cavity mode with $Q = 19000$ this results in a diameter of about $32 \mu\text{m}$. The necessary condition to probe only one spatial cavity mode — and not to average over eventual spatial inhomogeneities — is to focus the probing laser on the mode size or smaller.

The streak camera is mostly sensitive to visible light. From 1.4 eV to lower energies on (so for $\lambda > 880 \text{ nm}$), its response drops by a factor of 10 every 45 meV (equivalent to every 30 nm). Thus only cavity modes of the high-energy side of the stopband were accessible in terms of detection.

In a successful transmission measurement, we detected the three planar cavity modes of the high-energy side of the stopband (*cf.* figure 5.14). Those modes had simulated quality factors $Q_{m,\text{th}}$ equal to 40600, 19000 and 4100, respectively. The corresponding simulated values for τ_m were 20.5 ps, 10 ps and 2 ps, respectively. The 2 ps were at the limit of the streak-camera’s temporal resolution and thus too short for the study of light storage. We could measure the storage time τ_m of the two other modes and obtained 8.1 ps and 3.2 ps, respectively. Thus Q_m equal to 16000 and 6600, respectively. Those are smaller than the predicted values. Most probably a gradient in the cavity thickness, we estimate it to be 5 to 10 nm per mm, thus not negligible on the scale of d_m , limits the quality factors of the realized planar cavity.

Modes which are resonant to higher energies, and have larger $Q_{m,\text{th}}$ and $\tau_{m,\text{th}}$, were not detectable with the streak-camera.

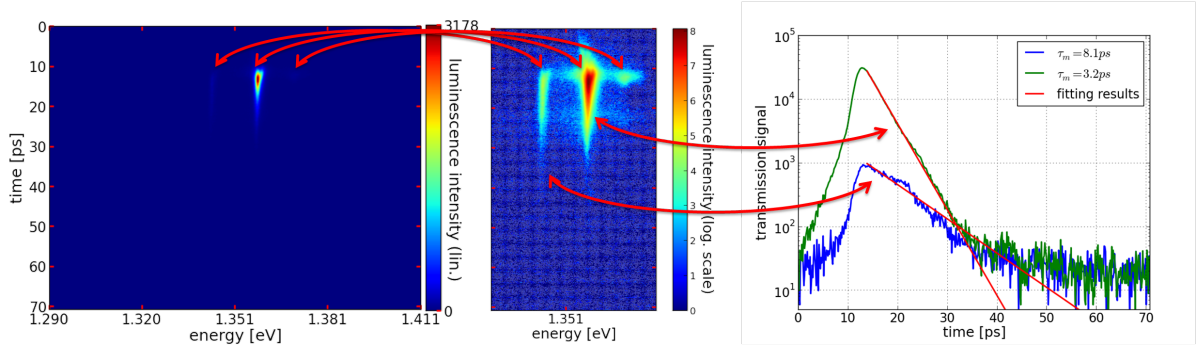


Figure 5.14: Cavity ring-down experiment. To the left is shown a streak-camera image in a linear scale, barely evidencing the transmission of light through three cavity modes. The central image shows a part of the left image in a logarithmic scale to better illustrate the cavity modes. The temporal storage, so the planar cavity's response to the probing 200 fs-long laser pulse, is highlighted with the time-profiles of the two high- Q modes in the right graph. The storage times and the corresponding adjustments to exponential decays are indicated. The red arrows link identical cavity modes in the three different illustrations.

With this demonstration of storing the light few tens of picoseconds inside a planar cavity, it became imaginable to switch the cavity while light is stored and escaping the cavity. A consequence would be the adiabatic colour change of the stored light.

5.3.3 Changing the colour of the light trapped in a planar cavity

Once light is stored in a cavity mode, a switch should change the mode's resonance and with it adiabatically the colour of the trapped light [78, 11, 15].

The experimental attempt of the colour changing experiment and its simulation

We tried to measure the changing of the colour of the light trapped in the above presented semiconductor microcavity. The corresponding experiment is sketched in figure 5.15. A resonant CW-laser should probe one high- Q cavity mode of the unswitched cavity. A short laser pulse is used to switch the cavity⁹. For sufficient switching amplitude the CW-laser will no more be resonant to the mode and cannot further inject light. If the stored light follows adiabatically the spectral cavity mode position, as predicted in reference [78], it should escape the cavity mode at the switched resonance.

⁹Its energy has to be tuned over the GaAs bandgap to excite free carriers in GaAs and switch the cavity resonances.

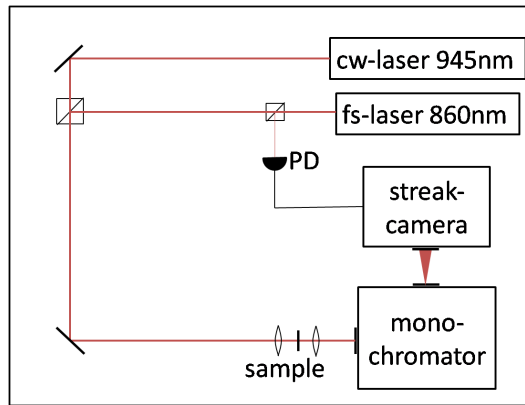


Figure 5.15: Setup of the colour changing experiment. We use a CW-laser (probe), resonant to a high- Q cavity mode, and a femtosecond-second laser (pump), situated above the GaAs bandgap in energy. A beam-splitter takes a very small part of the pulses light; it is detected by a photodiode (PD) to synchronise the detection in the streak camera with the laser’s repetition rate. The remaining part of the pulse’s signal and the CW-laser are focused on the sample. The CW-light probes one cavity mode, while the repeated femtosecond-pulses inject free carriers and switch the cavity. The outgoing transmitted light is spectrally resolved in a monochromator and detected in the streak camera. (The laser’s repetition rate is much slower that the spectral return of the cavity mode following the switching event.)

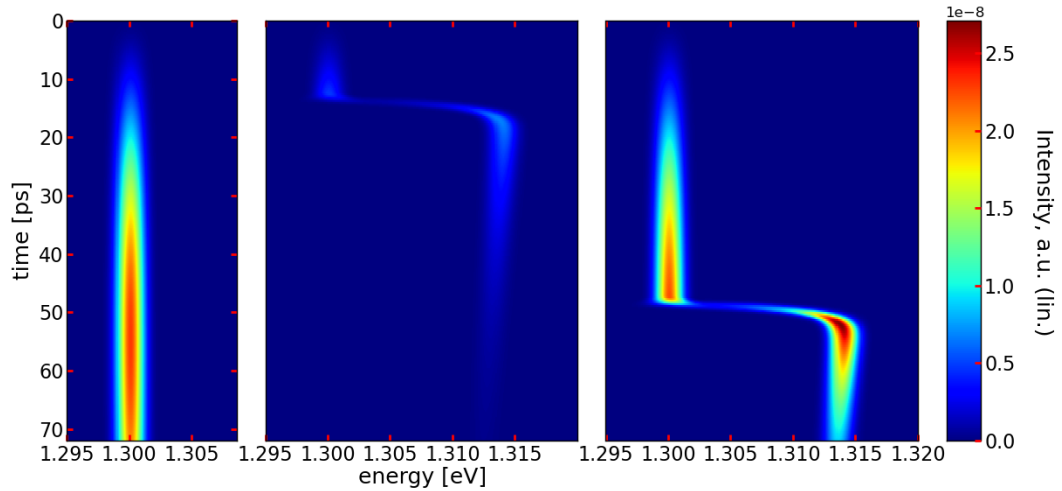
FDTD simulations were done to predict this adiabatic colour change. The simulated cavity was the same as the one used in the experiment¹⁰, but resonant to 1.3 eV. The central cavity mode had $Q_m = 65000$, $E_m = 1.3$ eV, and $\tau_m = 33$ ps, see figure 2.17.

The figure 5.16 shows the simulation’s results. The shown relative refractive index change of GaAs — responsible for the switch — was used as input for the simulation.

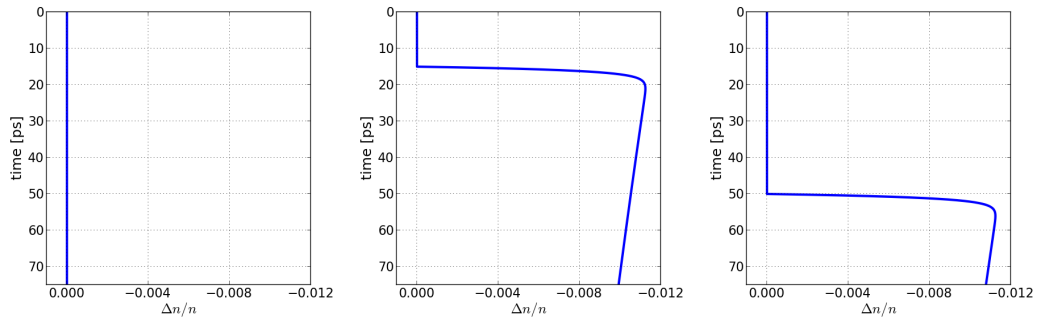
In the left subplots no switching occurred. The streak-camera image shows the transmitted light through the central cavity mode of the unswitched cavity. The CW-laser, which was resonant to the central cavity mode, started at the beginning of the simulation, *i.e.* at $t = 0$ ps. Before no light impinged on the cavity. Some time was needed to store light inside the cavity mode. Only once the maximum intensity of the stored light was established, the transmitted intensity was maximal. That is why the transmitted signal increases during the first 45 picoseconds.

In the central subplots switching occurred at $t = 15$ ps. The CW-laser stayed the same. For $t < 15$ ps the cavity was unswitched and the still resonant CW-laser could inject light in the central cavity mode. When the switching occurred, the refractive index of GaAs was strongly decreased — simulating a fast free carrier injection. Simultaneously all cavity modes were blue-shifted. All the stored light escaped now resonant to the blue-shifted

¹⁰Only the bottom DBR, composed of 20 Bragg layers and deposited on GaAs substrate, was replaced by a 16-layer thick DBR next to an air interface.



a – simulated streak-camera images



b – relative refractive index changes of GaAs

Figure 5.16: FDTD simulation of the colour changing experiment. CW-laser light, resonant to the unswitched central cavity mode, impinged on the cavity. From the left to the right: the cavity was not switch; it was switched at $t = 15$ ps; and at $t = 50$ ps. (a) The simulated streak-camera images show the transmitted light. In (b) the corresponding relative refractive index changes of GaAs are plotted. They were the origin of the switch.

central cavity mode. No more light could be injected in the cavity, as no modes were any more resonant to the CW-laser. Once the switch established, the free-carriers were supposed to recombine with the characteristic time $\tau_{e,h} = 424$ ps. Same was applied to the refractive index change. The escaping light followed the relaxing cavity mode and its intensity decreased exponentially with the storage time τ_m .

In the right subplots switching occurred at $t = 50$ ps. All other parameter were identical to the central subplots. As the intensity of the stored light was higher at $t = 50$ ps than at $t = 15$ ps, more light was converted to the switched energy than in the previous case. One can observe that the maximal transmitted intensity is slightly higher than the maximal transmitted intensity of the unswitched case. This occurs because the switch reduces the mode's quality factor — modifying only the refractive index of GaAs, and not of AlAs.

If one superposes the relative refractive index changes with the simulated streak-camera images, one sees that the central energy of the emitted light matches perfectly the time-dependent cavity mode position. According to this simulations, the colour of the stored light followed always the switched cavity mode — that means the colour change was adiabatic.

In the simulated streak-camera images the spectral and temporal resolutions were given by a 3 ps long sliding Hamming-window, on which was performed a Fourier-transformation. The so computed spectra constructed the simulated streak-camera images.¹¹ The chosen temporal resolution is very similar to the experimental streak-camera resolution.

The adiabatic colour change should be confirmed by an experiment, which should be very similar to the simulation. As all the input parameters are realistic, the experiment should be feasible. I attempted a first experimental realization during the first year of my PhD, which was not successful. With the knowledge on cavity-switching I acquired in between, the experimental realization became much more realistic. A new attempt to the colour changing experiment will follow soon.

Adiabatic conversion of a light pulse

We saw in figure 5.16 that, during the switching event, all the light stored in a cavity mode was converted to another energy. Thus this conversion was adiabatic. In view of practical applications it is interesting to consider the efficiency of the conversion of a light pulse to a new energy.

Sending a light pulse — resonant to the central cavity mode — on the cavity and observing its transmission, we want here to study which ratio of the transmitted light can be converted to the switched energy. (We used still the same cavity). To achieve a good coupling to the central cavity mode, we chose the light pulse to be resonant to the unswitched central cavity mode and its duration at FWHM to be equal to the mode storage time $\tau_m = 33$ ps. The pulse shape was chosen to be Gaussian. We observe the light transmitted through the unswitched cavity, and compare it to the light transmitted through the cavity which is switched at a given instant. We can then calculate the ratio between all the converted light, the total intensity of the original light pulse, and the total intensity of the transmitted light in the unswitched case.

In the figure 5.17 are shown — from the left to the right — the probing light pulse which propagated in air and where the cavity was replaced by air; the light which was transmitted through the unswitched central cavity mode; and the light which was transmitted through the central cavity mode when the cavity was switched at $t = 50$ ps. This time for the switching event is the time where the transmitted light in the unswitched case shows its maximum, *i.e.* when the stored light field inside the cavity is maximal.

Comparing the three images, the light which was transmitted through the cavity —

¹¹This made that every instant in the simulated streak-camera images is here retarded of 1.5 ps compared to the instantaneous data for the refractive index.

i.e. in the second and third image — arrived later on the detection and its duration is longer than in the first image.¹² Furthermore, its intensity is decreased. The delay in the detection results from the fact that the light which transmitted through the cavity was stored for a certain time inside the cavity. This also increased the detected pulse duration. Its intensity is reduced, because not all the light of the original pulse could enter the cavity mode. In the unswitched case, 52% of the original light pulse coupled into the cavity, while 48% were reflected by the cavity surface. Furthermore, the light which was stored in the cavity mode escaped from both sides of the symmetric cavity, reducing the detected signal by a factor of 2. Therefore the total amount of the transmitted light of the original pulse is 26% in the unswitched case. The third image differs from the second image only after the switching event, *i.e.* for $t > 50$ ps. The total total intensity of the third image — *i.e.* the case with switching — represents 88% of the total intensity of the second image — *i.e.* the case without switching. This result occurs, because from the switching event on no light can be injected anymore in the cavity mode, in contrast to the unswitched case. As a consequence, all further incoming light will be reflected. Finally, in the case with switching, 23% of the original light pulse were transmitted through the cavity.

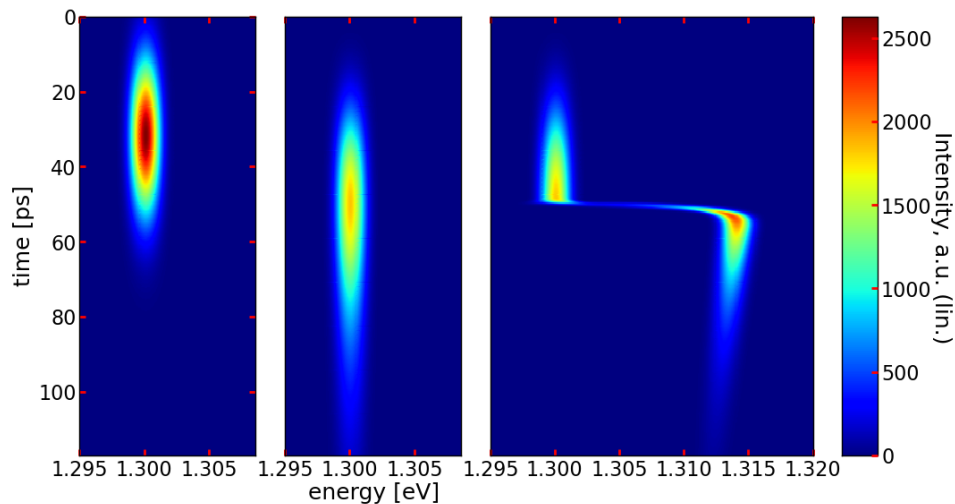


Figure 5.17: FDTD simulations: A Gaussian shaped laser pulse with a FWHM of 33 ps ($= \tau_m$), resonant to the unswitched central cavity mode, was sent on a cavity and its transmission was observed, shown in streak-camera images. Three different cases were studied — shown from the left to the right: no cavity was present and the pulse propagated in air; the pulse transmitted through the cavity which was not switched; the cavity was switched at $t = 50$ ps. For the left image the intensity of the colour-scale has to be multiplied by a factor of 4 — this adjustment ameliorated the visibility of the other subplots.

Of this 23% which were transmitted — including the transmission before and after the switching event — we want to know the conversion efficiency to the new energy: Before

¹²As one can see, at the end of the simulation remains some light inside the cavity. Its intensity is so weak, that the results remain unchanged if the duration of the simulation was increased.

the switching event the light escaped at the unswitched cavity resonance. Its integrated intensity represents 46% of total intensity of the third image. After the switching event the light escaped converted in energy. Its integrated intensity represents 54% of total intensity of the third image. Therefore 12.5% (equal to 0.54 times 0.23) of the original light pulse were transmitted through the cavity and adiabatically converted in energy. Another 12.5% were adiabatically converted in energy and escaped the cavity in the direction of the reflected light. Further 10.5% were transmitted before the switching event, remaining unconverted, and the lasting 64.5% represent the sum of the light reflected before and after the switching event, also not converted in energy. The total amount of light is conserved. We conclude that 12.5% of the original light pulse were both converted in energy and transmitted.

The obtained values for the conversion efficiency can also be illustrated with the time-profiles of the streak-camera images. The relevant ones are shown in the figure 5.18.

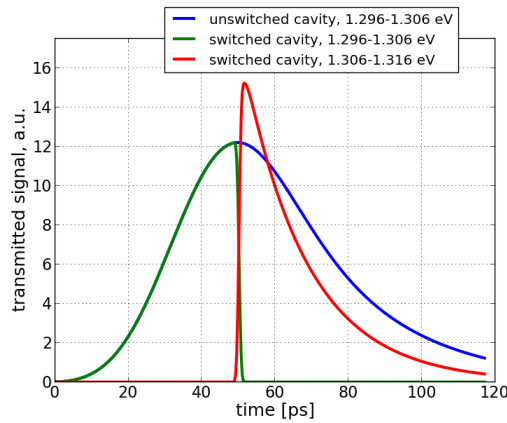


Figure 5.18: Time-profiles of the second and third streak-camera images of figure 5.17, integrated over the indicated energy ranges.

Before the switching event ($t < 50$ ps) the time-profiles of the light escaping the switched and unswitched cavity are exactly the same (green and blue line, respectively). They increase up to their maximum, reflecting the fact the cavity is charged by the light pulse. We chose the switching event to be at the maximum of unswitched time-profile, in order to maximise the light conversion efficiency.

After the switching event the time-profile of the light escaping the unswitched cavity (blue line) starts decaying, as we chose the switching event to be at the maximum of this time-profile. In contrast, the light escaping the switched cavity (red line) shows first an increased intensity and decays in the following. The light intensity is increased, because the quality factor of the cavity is decreased by the switch: from $Q_m = 65000$ ($\tau_m = 33$ ps) to Q_m about 40000 (τ_m about 20 ps). Light escapes faster the cavity, causing the increased intensity. Soon its intensity falls beneath the intensity in the unswitched case. The switched cavity is getting empty. Furthermore, no more light can be injected in the switched and energy shifted cavity mode, while light is still injected in the mode in the case where the cavity is not switched.

We showed here, using cavity switching and the adiabatic colour change, how to convert in energy 25% of a light pulse. One half of the converted light was transmitted through the planar cavity, the other half reflected.

Prospect of a perfect energy conversion of a light pulse

If one is able to perfectly match a light pulse to a cavity mode — which is theoretically possible — the pulse would be entirely stored inside the cavity, before being released. Switching at the right moment would allow to convert the entire light pulse in energy, as sketched in the figure 5.19. Let us note that the number of photons is conserved in such adiabatic colour change experiments [78]. The conversion of single photons is thus possible.

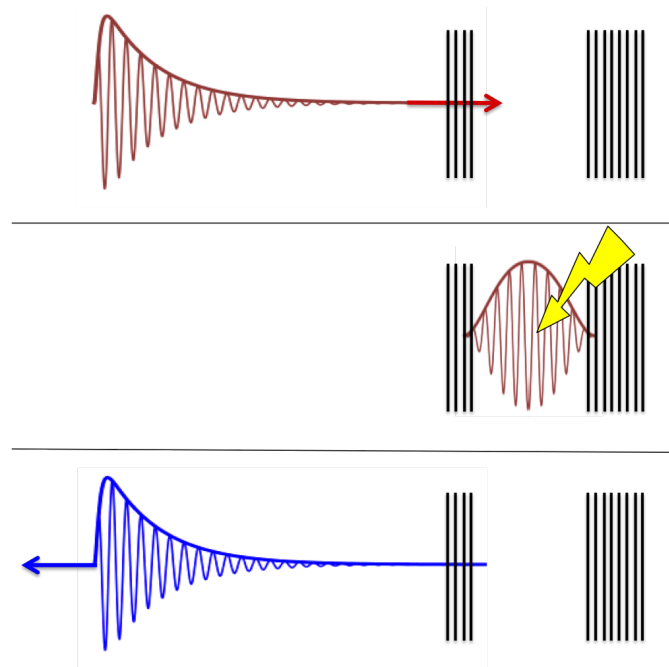


Figure 5.19: Sketch of the total conversion of a light pulse to a new energy, using cavity switching and an appropriate asymmetric planar cavity. The pulses are shown as a function of space (and not as a function of time).

For this purpose, our approach is to use a very asymmetric planar cavity, having a thin DBR at the cavity surface and a thick DBR at the backside of the cavity. The reflectance of the thin DBR will be smaller than the reflectance of the thick DBR, which ideally equals unity. In such cavity, the light which is stored in the cavity modes can escape only through the thin DBR. Sending the perfect time-reversal of such a pulse on the cavity, would result in perfect capture, as sketched in the first and second sequence of the figure 5.19. Once completely trapped, the pulse would be released, and result in the same — but not time-reversed — light pulse. Applying cavity switching at the time when all the light is stored inside the cavity, would allow to convert the entire pulse adiabatically to a new energy; as it is sketched in the second and third sequence of the figure 5.19.

Applying this procedure to cavities with a small volume, the needed light intensities for the all-optical switch can be reduced by orders of magnitude. For example, when switching a micropillar cavity of diameter $1\ \mu\text{m}$, an initial pulse energy of 0.6 pJ would convert the stored light stored by a relative energy change of 1% (*cf.* the calculations in chapter 3.3.3).

In this section we introduced a high- Q planar cavity and discussed the colour changing experiment. We showed that, using cavity switching, light stored in a cavity mode can be adiabatically converted to another energy. The experimental realization was discussed and seems to be very realistic. In this context we showed further that a light pulse can be partially converted to a new energy. Finally we gave a roadmap to the total energy conversion of a tailored light pulse, using a suitable asymmetric planar cavity and ultrafast all-optical cavity switching. This method is applicable to single photons and should be realisable with repetition rates higher than 10 GHz. When small microcavities are used, *e.g.* small micropillars, a relative energy conversion of 1% can be obtained, switching with 0.6 pJ per conversion event.

5.4 Conclusion

In this chapter, we presented three applications of all-optical cavity switching. 1.) The generation of ultrashort spontaneous emission bursts. 2.) The Purcell switching. 3.) The efficient conversion of the colour of a light pulse.

The ultrashort emission bursts were emitted by InAs QDs integrated in a micropillar cavity. Those QDs probed the spectral position of the switched, thus time-dependent, cavity modes. Spectral filtering enabled selecting several QD transitions, which were only during a very short time in resonance with one cavity mode. The duration (and spectral width) of the so obtained emission burst could be tailored. Successful preparation of ultrashort emission bursts as short as 3 ps was demonstrated. Switching spectrally close-by cavity modes, multiple bursts could also be generated. We demonstrated ultrashort double bursts, each a few picosecond-long and separated by 10 to 30 picoseconds; the burst durations and their temporal separation could be tailored. Depending on the experimental conditions, we found those ultrashort emission bursts to be either of spontaneous or of stimulated emission nature. To test this, we illuminated a scattering media with those bursts: if the resulting image was speckle-free, it proved that the studied burst was emitted by a spontaneous emission process. Such ultrashort spontaneous emission bursts may be useful for an ultrafast illumination.

If the Purcell factor of a studied micropillar was large enough, such ultrashort spontaneous emission burst could be combined with Purcell switching, *i.e.* a simultaneous decrease of the QD exciton population. Its detection is one of the future projects, with the long term aim of shaping the envelope of single photon pulses, as discussed in chapter 4.

Finally we studied a multi-modal high- Q planar cavity with long light storage times.

Simulations showed that, using cavity switching, it should be possible to adiabatically change the colour of the light trapped in a cavity mode. Making use of this, a light pulse can be partially converted to a new frequency. A conversion efficiency of 25% (that means 12.5% reflected, and 12.5% transmitted) has been predicted for our existing high- Q planar cavity, operating in the transmission geometry. The combination of an asymmetric high- Q cavity and tailored pulses with inverse exponential shape, would lead to a total conversion of the incoming light pulse to a new frequency. This method may be interesting for the energy conversion of single photons and possible high repetition rates.

CONCLUSION AND PERSPECTIVES

The subject of this thesis was to study the all-optical switching of semiconductor microcavities on the picosecond time-scale, and to investigate potential applications of this effect, such as the color conversion of light trapped in the cavity or the control in real time of the spontaneous emission rate of embedded emitters.

To this purpose, I focused my attention on microcavities fabricated in the well mastered GaAs/AlAs semiconductor system. Both planar microcavities defined by Bragg mirrors and grown by molecular beam epitaxy, and micropillar cavities providing full 3D confinement of light, defined through the etching of planar cavities, have been designed, fabricated and characterised. Noticeably, I have developed planar microcavities comprising a very thick cavity layer, which display very long photon storage times in the 10-40 ps range, as confirmed by cavity ring-down experiments. For experiments requiring only a high quality factor (such as color change experiments), this original design relaxes very significantly the constraints on the quality of the Bragg mirrors.

The switching of planar or micropillar cavities through the optical injection of free carriers had initially been studied to develop bistable devices for all-optical data processing and computing in the early 90's. Since then, most experimental investigations of switching behaviours had been performed using pump-probe spectroscopy. In this work, we implement a different approach, based on the integration of an ensemble of InAs quantum dots within our cavities. This collection of independent emitters acts as a broadband internal light source, which is used to monitor the time-dependent frequencies of the resonant modes of the micropillar throughout the switching events. A set-up comprising a monochromator and a streak camera is used to detect and analyse the photoluminescence from the QD-micropillar system. These experiments reveal a short "switch-on" delay after the pump pulse (around 7 ps, likely limited by the cooling of the injected electron-hole plasma). The return of the cavity modes toward their original frequency, which is governed by the recombination of these charge carriers in GaAs, occurs within a few-hundred picoseconds. This "switch-off" time becomes shorter for smaller micropillar cavities, due to increased non-radiative recombination at the micropillar's sidewall surface. I have modeled such

switching events, by taking into account the lateral diffusion of injected carriers and the recombination through bimolecular radiative recombination and non-radiative recombination within bulk GaAs or at pillar sidewalls. We extract from this study estimates for the surface recombination velocity at etched sidewalls $S = 1.33 \cdot 10^3$ m/s and for the non-radiative lifetime in bulk GaAs $\tau_{\text{bulk}} = 424$ ps for our structures. I have investigated the switching amplitude as a function of the frequency and power of the pump pulses. We show that a saturation occurs at large pump powers, due to the state filling effects. For this reason, we can increase the maximum switching amplitude obtained at saturation by raising the energy of pump photons. By using this strategy, I observe a switching amplitude as large as 13 meV, corresponding to about 34 mode linewidths, for the modes of a 3 μm diameter micropillar with a pump pulse energy around 130 pJ and photon energy of 1.7 eV. Interestingly, operation in the saturation regime should lead to a highly uniform distribution of the free carriers in GaAs sublayers, along the micropillar axis.

By using a tightly focused pump beam, one can achieve a local injection of free carriers. Drastically different switching behaviour are then observed for the different cavity modes. Switching can be induced with some mode selectivity by placing the pump spot at well defined locations with respect to the micropillar top facet. For a given pump pulse energy, free carriers induce a maximum shift at zero delay when injected close to an antinode of the mode of interest, and a much smaller shift when injected close to a node of the mode. While all modes shift the same way for a uniform injection of free carriers, either the fundamental or the first higher order modes display the largest switching amplitude, for a pump spot respectively close to the center or close to the edges of the micropillar. Due to the lateral diffusion of the free carriers, all modes recover the same “switching off” behaviour after around 100 ps. The differential switching behaviour of the first modes of the micropillar has been successfully modeled by taking into account the inhomogeneous injection of the free carriers, their lateral diffusion and their recombination.

One of the most promising application prospects of cavity switching is the control of emitter–cavity interactions in real time, which would represent a major milestone for solid-state cavity quantum electrodynamics (CQED). I have investigated theoretically the spontaneous emission of a two-level emitter (such as a QD exciton) in a microcavity, assuming a time-dependent detuning between the cavity mode and the emitter transition. The temporal evolution of the system has been described using both rate equations and quantum Langevin equations. I first simulated how to trigger efficiently, using cavity switching, the spontaneous emission of the two-level emitter at a well defined time. Then I studied how to control the emission of a single photon over its entire duration, so as to tailor its time-envelope in view of applications in the context of photonic quantum information processing. The simulation shows that, using cavity switching, the production of single photon pulses with Gaussian or exponential increasing time-envelope can be achieved with state of the art QD–microcavity systems, with combined high efficiency and high fidelity. Compared to the alternative approach based on a tuning of the emitter’s frequency (e.g. using Stark frequency tuning of the QD exciton), cavity switching does not induce a significant frequency chirp within the single photon pulses. The fidelity between a perfect 150 ps-FWHM Gaussian reference photon and the simulated emitted one was almost per-

fect and obtained independently for numerous emitting QD–cavity systems: I obtained $f \approx 99\%$ for κ/g in the range from 2 to 15; the overall efficiency of the emission process, the photon integral times fidelity If , varied between 98.6% and 99%. I also discussed the maximisation of the reabsorption probabilities for shaped single photon pulses. An overall efficiency for the emission–absorption process with two different cavity–QD systems of 96.7% could be obtained. This result is very attractive in view of the development of efficient (asymmetric) quantum optical links. For reversible quantum optical links a maximal efficiency of 90% was found.

As a first application of cavity switching to the tailoring of the spontaneous emission of embedded emitters, I present the generation of ultrashort (few picoseconds) light pulses by a collection of QDs in a switched micropillar. In our experiment, the same pump pulse is used to excite the QDs and to switch the pillar modes. Using spectral filtering, we select the QDs with transition energies within a chosen spectral window. During the return of the pillar modes to their original frequencies, one or several modes enter into resonance with these QDs in a transient way. Each resonance event generates an emission burst into the cavity mode, whose duration is defined by the width of the selected spectral window and by the mode’s switching speed. By playing with the switching parameters, emission bursts as short as 3 ps have been generated, as well as ultrashort double bursts, each a few picoseconds long and separated by 10 to 30 picoseconds. A transmission experiment through a scattering medium has been performed to probe the coherence of these light pulses. While speckle formation is detected for control laser pulses or QD micropillars in the lasing regime, this is not the case when the light bursts are generated under weak QD pumping conditions. This result demonstrates that ultrashort pulses of incoherent light can be emitted using the spontaneous emission of switched QD–micropillars.

The frequency-conversion (“color change”) of light pulses is another important application field for cavity switching, previously discussed in the literature. When cavity switching is performed on a picosecond time scale, adiabatic conversion of the frequency of the light trapped in a high- Q mode can be obtained. I have performed FDTD simulations of this effect for switched planar cavities, so as to find experimental protocols enabling efficient frequency conversion of short (~ 30 ps) light pulses, typical of telecom/datacom networks. For symmetric cavities operating in the transmission geometry, a conversion efficiency around 12.5% is obtained by matching the pulse length and the cavity storage time. Perfect frequency conversion is predicted for an asymmetric cavity working in the reflection mode, provided the time-envelope of the pulse is properly shaped.

Beyond the results presented in this work, cavity switching appears as a very attractive resource for quantum optics, which has barely been exploited until now. On one side, it is not yet clear whether cavity switching can compete with present approaches used in telecom networks for frequency translation, for instance in terms of energy per translated bit. However, this approach displays unique assets in view of the frequency conversion of single photons, since the number of photons is conserved by this adiabatic frequency conversion process. On the other side, the control in real-time of CQED effects is still in its infancy, despite its huge interest. Playing with higher Q micropillars would enable

a clean and clear observation of the “Purcell switching”. In a longer term, switching a cavity containing a single QD will be necessary to tailor the time envelope of single photon pulses, which represents an appealing and very challenging goal. In this context, extended cavities such as microrings look more attractive than micropillars as they enable to switch the mode and to pump the QD with two perfectly independent optical beams. Several experimental projects are presently under way in our laboratory along these lines.

- [1] S. HAROCHE et D. KLEPPNER : Cavity Quantum Electrodynamics. *physicstoday*, 24:24, 1989.
- [2] J. M. GÉRARD, B. SERMAGE, B. GAYRAL, B. LEGRAND, E. COSTARD et V. THIERRY-MIEG : Enhanced Spontaneous Emission by Quantum Boxes in a Monolithic Optical Microcavity. *Phys. Rev. Lett.*, 81:1110–1113, 1998.
- [3] Peter LODAHL, A. Floris van DRIEL, Ivan S. NIKOLAEV, Arie IRMAN, Karin OVERGAAG, Daniël VANMAEKELBERGH et Willem L. VOS : Controlling the dynamics of spontaneous emission from quantum dots by photonic crystals. *Nature*, 430:654–657, 2004.
- [4] S. NODA, M. FUJITA et T. ASANO : Spontaneous-emission control by photonic crystals and nanocavities. *Nature Photon.*, 1:449–458, 2007.
- [5] J. P. REITHMAIER, G. SEK, A. LÖFFLER, C. HOFMANN, S. KUHN, S. REITZENSTEIN, L. V. KELDYSH, V. D. KULAKOVSKII, T. L. REINECKE et A. FORCHEL : Strong coupling in a single quantum dot–semiconductor microcavity system. *Nature*, 432:197–200, 2004.
- [6] E. Peter et AL : Exciton-photon strong-coupling regime for a single quantum dot embedded in a microcavity. *Phys. Rev. Lett.*, 95(6), 2005.
- [7] J. CLAUDON, J. BLEUSE, N. S. MALIK, M. BAZIN, P. JAFFRENNOU, N. GREGERSEN, C. SAUVAN, P. LALANNE et J.-M. GÉRARD : A highly efficient single-photon source based on a quantum dot in a photonic nanowire. *Nature Photon.*, 4:174–177, 2010.
- [8] Michael E. REIMER, Gabriele BULGARINI, Nika AKOPIAN, Moïra HOCEVAR, Maaïke Bouwes BAVINCK, Marcel A. VERHEIJEN, Erik P.A.M. BAKKERS, Leo P. KOUWENHOVEN et Val ZWILLER : Bright single-photon sources in bottom-up tailored nanowires. *Nature Comm.*, 3:737, 2012.
- [9] O. GAZZANO, S. Michaelis de VASCONCELLOS, C. ARNOLD, A. NOWAK, E. GALOPIN,

- I. SAGNES, L. LANCO, A. LEMAITRE et P. SENELLART : Bright solid-state sources of indistinguishable single photons. *Nature Comm.*, 4:1425, 2013.
- [10] Qianfan XU, Bradley SCHMIDT, Sameer PRADHAN et Michal LIPSON : Micrometre-scale silicon electro-optic modulator. *Nature*, 435:325–327, 2005.
- [11] S.F. PREBLE, Q. XU et M. LIPSON : Changing the colour of light in a silicon resonator. *Nature Photon.*, 1:293–296, 2007.
- [12] Georgios CTISTIS, Emre YUCE, Alex HARTSUIKER, Julien CLAUDON, Maela BAZIN, Jean-Michel GÉRARD et Willem L. VOS : Ultimate fast optical switching of a planar microcavity in the telecom wavelength range. *Appl. Phys. Lett.*, 98:161114, 2011.
- [13] V. ECKHOUSE, I. CESTIER, G. EISENSTEIN, S. COMBRIÉ, G. LEHOUCQ et A. De ROSSI : Kerr-induced all-optical switching in a GaInP photonic crystal Fabry-Perot resonator. *Optics Express*, 20:8524–8534, 2012.
- [14] P. J. HARDING, H. J. BAKKER, A. HARTSUIKER, J. CLAUDON, A. P. MOSK, J. M. GÉRARD et W. L. VOS : Observation of a stronger-than-adiabatic change of light trapped in an ultrafast switched GaAs-AlAs microcavity. *JOSA B*, 29(2), 2012.
- [15] Takasumi TANABE, Masaya NOTOMI, Hideaki TANIYAMA et Eiichi KURAMOCHI : Dynamic release of trapped light from an ultrahigh-Q nanocavity via adiabatic frequency tuning. *Phys. Rev. Lett.*, 102:043907, 2009.
- [16] Emanuel PEINKE : Changing the colour of the light trapped in a semiconductor microcavity. Mémoire de D.E.A., Karlsruhe Institut für Technologie, 2013.
- [17] E. M. PURCELL : Proceedings of the american physical society. *Phys. Rev.*, 69:674, 1946.
- [18] E. BURSTEIN et C. WEISBUCH : *Confined Electrons and Photons*. Plenum Press, 1995.
- [19] Lord RAYLEIGH : The problem of the whispering gallery. *Scientific Papers*, 5:617, 1912.
- [20] P. LODAHL, A. Floris van DRIEL, I. NIKOLAEV, A. IRMAN, K. OVERGAAG, D. VAN-MAEKELBERGH et W. L. VOS : Controlling the dynamics of spontaneous emission from quantum dots by photonic crystals. *Nature*, 430:654–657, 2004.
- [21] J.-M. LOUTIOZ, H. BENISTY, V. BERGER, J.M. GÉRARD, D. MAUSTRE et A. TCHELNOKOV : *Photonic Crystals (2nd Edition)*. Springer, 2008.
- [22] R. P. FEYNMAN, R.B. LEIGHTON et M. SANDS : *The Feynman Lecture on Physics Vol. II*. Addison Wesley, 1964.
- [23] D. K. ARMANI, T. J. KIPPENBERG, S. M. SPILLANE et K. J. VAHALA : Ultra-high Q toroid micrtocavity on a chip. *Nature*, 421:925–928, 2003.
- [24] T. RIVERA, J.-P. DEBRAY, J. M. GÉRARD, B. LEGRAND, L. MANIN-FERLAZZO et

- J. L. OUDAR : Optical losses in plasma-etched algaas microresonators using reflection spectroscopy. *Appl. Phys. Lett.*, 74:911–913, 1999.
- [25] B. GAYRAL, J. M. GÉRARD, A. LEMAÎTRE, C. DUPUIS, L. MANIN et J. L. PELOUARD : High-Q wet-etched GaAs microdisks containing InAs quantum boxes. *Appl. Phys. Lett.*, 75:1908–1910, 1999.
- [26] Bryan ELLIS, Marie A. MAYER, Gary SHAMBAT, Tomas SARMIENTO, James HARRIS, Eugene E. HALLER et Jelena VUČKOVIĆ : Ultralow-threshold electrically pumped quantum-dot photonic-crystal nanocavity laser. *Nature Photon.*, 5:297–300, 2011.
- [27] K. SRINIVASAN, M. BORSELLI, T. J. JOHNSON, P. E. BARCLAY, O. PAINTER, A. STINTZ et S. KRISHNA : Optical loss and lasing characteristics of high-quality-factor AlGaAs microdisk resonators with embedded quantum dots. *Appl. Phys. Lett.*, 86:151106–3, 2005.
- [28] S. L. MCCALL, A. F. J. LEVI, R. E. SLUSHER, S. J. PEARTON et R. A. LOGAN : Whispering-gallery mode microdisk lasers. *Appl. Phys. Lett.*, 60:289–291, 1992.
- [29] Maela BAZIN : *Contrôle de l'émission spontanée de boîtes quantiques semiconductrices insérées dans des micro-structures à confinement optique originales*. Thèse de doctorat, Université de Grenoble, 2010.
- [30] J. S. FORESI, P. R. VILLENEUVE, J. FERRERA, E. R. THOEN, G. STEINMEYER, S. FAN, J. D. JOANNOPOULOS, L. C. KIMERLING, Henry I. SMITH et E. P. IPPEN : Photonic-bandgap microcavities in optical waveguides. *Nature*, 390:143–145, 1997.
- [31] D. LABILLOY, H. BENISTY, C. WEISBUCH, T. F. KRAUSS, C. J. M. SMITH, R. HOUDRÉ et U. OESTERLE : High-finesse disk microcavity based on a circular bragg reflector. *Appl. Phys. Lett.*, 73:1314, 1998.
- [32] Hiroshi SEKOGUCHI, Yasushi TAKAHASHI, Takashi ASANO et Susumu NODA : Photonic crystal nanocavity with a Q-factor of 9 million. *Opt. Express*, 22:916, 2014.
- [33] Christophe ARNOLD, Vivien LOO, Aristide LEMAÎTRE, Isabelle SAGNES, Olivier KREBS, Paul VOISIN, Pascale SENELLART et Loïc LANCO : Optical bistability in a quantum dots/micropillar device with a quality factor exceeding 200 000. *Appl. Phys. Lett.*, 100:111111, 2012.
- [34] J. L. JEWELL, A. SCHERER, S. L. MCCALL, Y. H. LEE, S. WALKER, J. P. HARBISON et L. T. FLOREZ : Low-threshold electrically pumped vertical-cavity surface emitting microlasers. *Electron. Lett.*, 25:1123–1125, 1989.
- [35] S. REITZENSTEIN, C. HOFMANN, A. GORBUNOV, M. STRAUSS, S. H. KWON, C. SCHNEIDER, A. LÖFFLER, S. HÖFLING, M. KAMP et A. FÖRCHEL : AlAs/GaAs micropillar cavities with quality factors exceeding 150.000. *Appl. Phys. Lett.*, 90:251109–3, 2007.
- [36] Pochi YEH : *Optical waves in Layered Media*. WILEY, Rockwell International

- Science Center, Thousand Oaks, California, 1988.
- [37] H. A. MACLEOD : *Thin film optical filters*. Adam Hilger, Bristol, 1969.
- [38] S. GEHRSTZ, F. K. REINHART, C. GOURGON, N. HERRES, A. VONLANTHEN et H. SIGGA : The refractive index of $\text{Al}_x\text{Ga}_{1-x}\text{As}$ below the band gap: Accurate determination and empirical modeling. *J. Appl. Phys.*, 87(11), 2000.
- [39] R. RAM, D. BABIC, R. YORK et J. BOWERS : Spontaneous emission in microcavities with distributed mirrors. *IEEE J. Quant. Electron.*, 31:399–410, 1995.
- [40] Susumu KINOSHITA : Surface emitting semiconductor lasers. *IEEE J. Quantum Electron.*, 1988.
- [41] T. BABA, T. HAMANO, F. KOYAMA et K. IGA : Spontaneous emission factor of a microcavity DBR surface-emitting laser. *IEEE J. Quant. Electron.*, 27:1347–1358, 1991.
- [42] J. M. GÉRARD, D. BARRIER, J. Y. MARZIN, R. KUSZELEWICZ, L. MANIN, E. COSTARD, V. THIERRY-MIEG et T. RIVERA : Quantum boxes as active probes for photonic microstructures: The pillar microcavity case. *Appl. Phys. Lett.*, 69:449–451, 1996.
- [43] P. LALANNE, J. P. HUGONIN et J. M. GÉRARD : Electromagnetic study of the quality factor of pillar microcavities in the small diameter limit. *Appl. Phys. Lett.*, 84(23):4726–8, 2004.
- [44] S. REITZENSTEIN et A. FORCHEL : Quantum dot micropillars. *J. Phys. D: Appl. Phys.*, 43:033001, 2010.
- [45] E.A.J. MARCATILI : Bends in optical dielectric guides. *Bell Syst. Tech. J.*, 48:2103–32, 1969.
- [46] F. XIA, L. SEKARIC et Y. VLASOV : Ultracompact optical buffers on a silicon chip. *Nature Photon.*, 1:65–71, 2007.
- [47] J.G. RARITY et Claude WEISBUCH : *Microcavities and Photonic Bandgaps: Physics and Applications*. Nato Science Series E. Kluwer Academic Publishers, 1996.
- [48] Jean-Michel GÉRARD et Bruno GAYRAL : *Semiconductor Microcavities, Quantum Boxes and the Purcell Effect in Confined Photon Systems*. Springer, 1998.
- [49] L. C. ANDREANI, G. PANZARINI et J. M. GÉRARD : Strong-coupling regime for quantum boxes in pillar microcavities: Theory. *Phys. Rev. B*, 60:13276–13279, 1999.
- [50] Alexia AUFFÈVES, Benjamin BESGA, Jean-Michel GÉRARD et Jean-Philippe POIZAT : Spontaneous emission spectrum of a two-level atom in a very-high-Q cavity. *Phys. Rev. A*, 77:63833, 2008.
- [51] R. J. THOMPSON, G. REMPE et H. J. KIMBLE : Observation of normal-mode splitting for an atom in an optical cavity. *Phys. Rev. Lett.*, 68:1132, 1992.

- [52] T. YOSHIE, A. SCHERER, J. HENDRICKSON, G. KHITROVA, H. M. GIBBS, G. RUPPER, C. ELL, O. B. SHCHEKIN et D. G. DEPPE : Vacuum rabi splitting with a single quantum dot in a photonic crystal nanocavity. *Nature*, 432:200–203, 2004.
- [53] M. BAYER, T. L. REINECKE, F. WEIDNER, A. LARIONOV, A. McDONALD et A. FORCHEL : Inhibition and Enhancement of the Spontaneous Emission of Quantum Dots in Structured Microresonators. *Phys. Rev. Lett.*, 86:3168–3171, 2001.
- [54] E. MOREAU, I. ROBERT, J. M. GÉRARD, I. ABRAM, L. MANIN et V. THIERRY-MIEG : Single-mode solid-state single photon source based on isolated quantum dots in pillar microcavities. *Appl. Phys. Lett.*, 79:2865–2867, 2001.
- [55] G. S. SOLOMON, M. PELTON et Y. YAMAMOTO : Single-mode Spontaneous Emission from a Single Quantum Dot in a Three-Dimensional Microcavity. *Phys. Rev. Lett.*, 86:3903–3906, 2001.
- [56] Ph. LELONG et G. BASTARD : Binding energies of excitons and charged excitons in GaAs/Ga(In)As quantum dots. *Solid State Communications*, 98:819–823, 1996.
- [57] C. KAMMERER, C. VOISIN, G. CASSABOIS, C. DELALANDE, Ph. ROUSSIGNOL, F. KLOPF, J. P. REITHMAIER, A. FORCHEL et J. M. GÉRARD : Line narrowing in single semiconductor quantum dots: Toward the control of environment effects. *Phys. Rev. B*, 66:041306, 2002.
- [58] I. FAVERO, G. CASSABOIS, R. FERREIRA, D. DARSON, C. VOISIN, J. TIGNON, C. DELALANDE, G. BASTARD, P. ROUSSIGNOL et J. M. GÉRARD : Acoustic phonon sidebands in the emission line of single InAs/GaAs quantum dots. *Phys. Rev. B*, 68:233301, 2003.
- [59] K. MATSUDA, K. IKEDA, T. SAIKI, H. TSUCHIYA, H. SAITO et K. NISHI : Homogeneous linewidth broadening in a In_{0.5}Ga_{0.5}As/GaAs single quantum dot at room temperature investigated using a highly sensitive near-field scanning optical microscope. *Phys. Rev. B*, 63:121304, 2001.
- [60] C. SANTORI, M. PELTON, G. SOLOMON, Y. DALE et E. YAMAMOTO : Triggered single photons from a quantum dot. *Phys. Rev. Lett.*, 86:1502–1505, 2001.
- [61] C. SANTORI, D. FATTAL, J. VUKOVIĆ, G. S. SOLOMON et Y. YAMAMOTO : Indistinguishable photons from a single-photon device. *Nature*, 419:594–597, 2002.
- [62] A. KIRAZ, P. MICHLER, C. BECHER, B. GAYRAL, A. IMAMOGLU, Lidong ZHANG, E. HU, W. V. SCHOENFELD et P. M. PETROFF : Cavity-quantum electrodynamics using a single InAs quantum dot in a microdisk structure. *Appl. Phys. Lett.*, 78:3932, 2001.
- [63] D. ENGLUND, D. FATTAL, E. WAKS, G. SOLOMON, B. Y. ZHANG, T. NAKAOKA, Y. ARAKAWA, Y. YAMAMOTO et J. VUCKOVIC : Controlling the Spontaneous Emission Rate of Single Quantum Dots in a Two-Dimensional Photonic Crystal. *Phys. Rev. Lett.*, 95:013904–4, 2005.

- [64] D. L. HUFFAKER et D. G. DEPPE : Improved performance of oxide-confined vertical-cavity surface-emitting lasers using a tunnel injection active region. *Appl. Phys. Lett.*, 71:1449, 1997.
- [65] M. FUJITA : Continuous wave lasing in GaInAsP injection laser with threshold current of μA . *IEEE*, 36:790–791, 2000.
- [66] Artur K. EKERT : Quantum cryptography based on Bell’s theorem. *Phys. Rev. Lett.*, 67:661, 1991.
- [67] Gilles BRASSARD, Norbert LÜTKENHAUS, Tal MO et Barry C. SANDERS : Limitations on Practical Quantum Cryptography. *Phys. Rev. Lett.*, 85:1330–1333, 2000.
- [68] A.J. SHIELDS : Semiconductor quantum light sources. *Nature Photon.*, 1:215–223, 2007.
- [69] R. BROURI, A. BEVERATOS, J. P. POIZAT et P. GRANGIER : Photon antibunching in the fluorescence of individual color centers in diamond. *Opt. Lett.*, 25:1294–1296, 2000.
- [70] C. KURTSIEFER, S. MAYER, P. ZARDA et H. WEINFURTER : Stable Solid-State Source of Single Photons. *Phys. Rev. Lett.*, 85:290–293, 2000.
- [71] P. MICHLER, A. IMAMOĞLU, M. D. MASON, P. J. CARSON, G. F. STROUSE et S. K. BURATTO : Quantum correlation among photons from a single quantum dot at room temperature. *Nature*, 406:968–970, 2000.
- [72] J. M. GÉRARD et B. GAYRAL : Strong Purcell effect for InAs quantum boxes in three-dimensional solid-state microcavities. *J. Lightwave Tech.*, 17:2089–2095, 1999.
- [73] A. ZRENNER, E. BEHAM, S. STUFLER, F. FINDEIS, M. BICHLER et G. ABSTREITER : Coherent properties of a two-level system based on a quantum-dot photodiode. *Nature*, 418:612–614, 2002.
- [74] C.-M. SIMON, T. BELHADJ, B. CHATEL, T. AMAND, P. RENUCCI, A. LEMAITRE, O. KREBS, P. A. DALGARNO, R. J. WARBURTON, X. MARIE et B. URBASZEK : Robust quantum dot exciton generation via adiabatic passage with frequency-swept optical pulses. *Phys. Rev. Lett.*, 106:166801, 2011.
- [75] J. L. JEWELL, S. L. MCCALL, A. SCHERER, H. H. HOUEH, N. A. WHITTAKER, Gossard A. C. et English J. H. : Transverse modes, waveguide dispersion, and 30 ps recovery in submicron GaAs/AlAs microresonators. *Appl. Phys. Lett.*, 55:22–24, 1989.
- [76] T. RIVERA, F. R. LADAN, A. IZRAËL, R. AZOULAY, R. KUSZELEWICZ et J. L. OUDAR : Reduced threshold all-optical bistability in etched quantum well microresonators. *Appl. Phys. Lett.*, 64(7):869–871, 1994.
- [77] Emre YÜCE, Georgios CTISTIS, Julien CLAUDON, Emmanuel DUPUY, Robin D. BUIJS, Bob de RONDE, Allard P. MOSK, Jean-Michel GÉRARD et Willem L. VOS

- : All-optical switching of a microcavity repeated at terahertz rates. *Opt. Lett.*, 38(3):374–376, 2013.
- [78] Masaya NOTOMI et Satoshi MITSUGI : Wavelength conversion via dynamic refractive index tuning of a cavity. *Phys. Rev. A*, 73:051803, 2006.
- [79] L. MIDOLO, F.M. PAGLIANO, T.B. HOANG, T. XIA, F.W.M. van OTTEN, L.H. LI, E.H. LINFIELD, M. LERMER, S. HÖFLING et A. FIORE : Spontaneous emission control of single quantum dots by electromechanical tuning of a photonic crystal cavity. *Appl. Phys. Lett.*, 101(9):091106, 2012.
- [80] Henri THYRRESTRUP, Alex HARTSUIKER, Jean-Michel GÉRARD et Willem L. VOS : Non-exponential spontaneous emission dynamics for emitters in a time-dependent optical cavity. *Opt. Express*, 21(20):23130–23144, 2013.
- [81] C.Y. JIN, R. JOHNE, M.Y. SWINKELS, T.B. HOANG, L. MIDOLO, P.J. van VELDHoven et A. FIORE : Ultrafast non-local control of spontaneous emission. *Nature Nano.*, 9:886–890, 2014.
- [82] Francesco PAGLIANO, YongJin CHO, Tian XIA, Frank van OTTEN, Robert JOHNE et Andrea FIORE : Dynamically controlling the emission of single excitons in photonic crystal cavities. *Nature C*, 5:5786, 2014.
- [83] Robert JOHNE, Ron SCHUTJENS, Sartoon Fattah POOR, Chao-Yuan JIN et Andrea FIORE : Control of the electromagnetic environment of a quantum emitter by shaping the vacuum field in a coupled-cavity system. *Phys. Rev. A*, 91:063807, 2015.
- [84] Henri THYRRESTRUP, Emre YÜCE, Georgios CTISTIS, Julien CLAUDON, Willem L. VOS et Jean-Michel GÉRARD : Differential ultrafast all-optical switching of the resonances of a micropillar cavity. *Appl. Phys. Lett.*, 105:111115, 2014.
- [85] Tanwin CHANG : *Optical Studies of Type-II GaAs/AlAs Superlattices: The Quantification of Heterointerfacial Quality*. Thèse de doctorat, Emory University, 1999.
- [86] L. GOLDSTEIN, F. GLAS, J. Y. MARZIN, M. N. CHARASSE et G. LE ROUX : Growth by molecular beam epitaxy and characterization on InAs/GaAs strained-layer superlattices. *Appl. Phys. Lett.*, 47:1099–1101, 1985.
- [87] J. M. MOISON, F. HOUZAY, F. BARTHE, L. LEPRINCE, E. ANDRÉ et O. VATEL : Self-organized growth of regular nanometer-scale InAs dots on GaAs. *Appl. Phys. Lett.*, 64:196–198, 1994.
- [88] D. LEONARD, M. KRISHNAMURTHY, C. M. REAVES, S. P. DENBAARS et P. M. PETROFF : Direct formation of quantum-sized dots from uniform coherent islands of InGaAs on GaAs surfaces. *Appl. Phys. L*, 63:3203–3205, 1993.
- [89] J. M. GÉRARD, J. B. GÉNIN, J. LEFÈVRE, J. M. MOISON, N. LÉBOUCHÉ et F. BARTHE : Optical investigation of the self-organized growth of InAs/GaAs quantum boxes. *Journal of Crystal growth*, 150:351–356, 1995.

- [90] Jürgen KLEIN : *Epitaktische Heterostrukturen aus dotierten Manganaten*. Thèse de doctorat, University of Cologne, 2001.
- [91] C.T. FOXON et B.A. JOYCE : Interaction kinetics of As 4 and Ga on (100) GaAs surfaces using a modulated molecular beam technique. *Surface Science*, 50:434, 1975.
- [92] T. WADAYAMA et co WORKERS : Reflection High Energy Electron Diffraction : RHEED. http://www.material.tohoku.ac.jp/~kaimenb/B_RHEED.html, August 14th, 2013.
- [93] J. M. GÉRARD, J. Y. MARZIN, G. ZIMMERMANN, A. PONCHET, O. CABROL, D. BARRIER, B. JUSSERAND et B. SERMAGE : InAs/GaAs quantum boxes obtained by self-organized growth: Intrinsic electronic properties and applications. *Solid State Electronics*, 40:807–814, 1996.
- [94] W. J. SCHAFFER, M. D. LIND, S. P.KOWALCZYK et R. W. GRANT : Nucleation and strain relaxation at the InAs/GaAs(100) heterojunction. *Journal of Vacuum Science and Technology B Microelectronics and Nonmeter Structures*, 1:741–746, 1983.
- [95] F. HOUZAY, G. GUILLE, J. M. MOISON, P. HENOC et T. BARTHE : First stage of MBE growth of InAs on (001)GaAs. *Journal of Crystal growth*, 81:67–72, 1987.
- [96] J. M. GÉRARD et J. Y. MARZIN : High quality ultrathin InAs/GaAs quantum wells grown by standard and low-temperature modulated-fluxes molecular beam epitaxy. *Appl. Phys. Lett.*, 53:568, 1988.
- [97] Jean-Michel GÉRARD : Prospects of high-efficiency quantum boxes obtained by direct epitaxial growth. In E. BURNSTEIN et C. Weisbuch EDITORS, éditeurs : *Confined electrons and photons: New physics and applications*, volume 340 de NATO ASI Series B: Physics, 1995.
- [98] BRUKER OPTICS INC. : VERTEX Series — Advanced Research FT-IR Spectrometers. http://www.bruker.com/fileadmin/user_upload/8-PDF-Docs/OpticalSpectroscopy/FT-IR/VERTEX/Brochures/VERTEXseries_brochure_EN.pdf, August 3rd, 2013.
- [99] T. MAKINO : Transfer matrix method with applications to distributed feedback optical devices. *PIER*, 10:271–319, 1995.
- [100] K. S. YEE : Numerical solution of initial boundary value problems involving Maxwell's equations in isotropic media. *IEEE Trans. Antennas Propagat.*, 14:302–307, 1966.
- [101] Hung LOUI : 1D-FDTD using MATLAB. *ECEN-6006 Num. Meth. in Photonics Proj. 1*, pages 1–13, 2004.
- [102] Gerrit MUR : Absorbing Boundary Conditions for the Finite-Difference Approximation of the Time-Domain Electromagnetic-Field Equations. *IEEE Transactions on Electromagnetic Compatibility*, EMC-23(4):377–382, 1981.

- [103] Georgios CTISTIS, Emre YUCE, Alex HARTSUIKER, Julien CLAUDON, Maela BAZIN, Jean-Michel GÉRARD et Willem L. VOS : Addendum: “Ultimate fast optical switching of a planar microcavity in the telecom wavelength range” [Appl. Phys. Lett. 98, 161114 (2011)]. *Appl. Phys. Lett.*, 99:199901, 2011.
- [104] Emre YÜCE, Georgios CTISTIS, Julien CLAUDON, Jean-Michel GÉRARD et Willem L VOS : Optimal all-optical switching of a microcavity resonance in the telecom range using the electronic Kerr effect. *Optics Express*, 24:239–253, 2016.
- [105] N. W. ASHCROFT et N.D. MERMIN : *Solid State Physics*. Saunders College Publishing, 1976.
- [106] P. DRUDE : Zur Elektronentheorie der Metalle. *Annalen der Physik*, 306:566–613, 1900.
- [107] E. YABLONOVITCH : Inhibited Spontaneous Emission in Solid-State Physics and Electronics. *Phys. Rev. Lett.*, 58:2059–2062, 1987.
- [108] Toshio MATSUSUE et Hiroyuki SAKAKI : Radiative recombination coefficient of free carriers in GaAs–AlGaAs quantum wells and its dependence on temperature. *Applied Physics Letters*, 50:1429, 1987.
- [109] Daniel STEIAUF, Emmanouil KIOUPAKIS et Chris G. Van de WALLE : Auger recombination in GaAs from first principles. *ACS Photonics*, 1:643–646, 2014.
- [110] S. GHOSH, P. BHATTACHARYA, E. STONER, J. SINGH, H. JIANG, S. NUTTINCK et J. LASKAR : Temperature-dependent measurement of Auger recombination in self-organized $\text{In}_{0.4}\text{Ga}_{0.6}\text{As}/\text{GaAs}$ quantum dots. *Appl. Phys. Lett.*, 79:722–4, 2001.
- [111] B. R. BENNETT, R. A. SOREF et J. A. Del ALAMO : Carrier-induced change in refractive index of InP, GaAs, and InGaAsP. *IEEE J. Quantum Electron.*, 26:113–122, 1990.
- [112] U. STRAUSS, W. W. RÜHLE et K. KÖHLER : Auger recombination in intrinsic GaAs. *Applied Physics Letters*, 62(1):55–57, 1993.
- [113] D. T. STEVENSON et R. J. KEYES : Measurement of carrier lifetimes in germanium and silicon. *Journal of Applied Physics*, 26:190–195, 1955.
- [114] E. YABLONOVITCH, C. J. SANDROFF, R. BHAT et T. GMITTER : Nearly ideal electronic properties of sulfide coated GaAs surfaces. *Appl. Phys. Lett.*, 51:439–441, 1987.
- [115] E. YABLONOVITCH, D. L. ALLARA, C. C. CHANG, T. GMITTER et T. B. BRIGHT : Unusually low surface-recombination velocity on Silicon and Germanium surfaces. *Phys. Rev. Lett.*, 57:249–252, 1986.
- [116] Brian A. RUZICKA, Lalani K. WERAKE, Hassana SAMASSEKOU et Hui ZHAO : Ambipolar diffusion of photoexcited carriers in bulk GaAs. *Appl. Phys. Lett.*, 97, 2010.
- [117] E. SNITZER : Cylindrical Dielectric Waveguide Modes. *JOSA*, 51:491, 1961.

-
- [118] Georgios CTISTIS, Alex HARTSUIKER, Edwin van der POL, Julien CLAUDON, Willem L. VOS et Jean-Michel GÉRARD : Optical characterization and selective addressing of the resonant modes of a micropillar cavity with a white light beam. *Phys. Rev. B*, 82:195330, 2010.
- [119] Peter P. ROHDE, Timothy C. RALPH et Michael A. NIELSEN : Optimal photons for quantum information processing. *Phys. Rev. A*, 72:52332, 2005.
- [120] M. STOBINSKA, G. ALBER et G. LEUCHS : Perfect excitation of a matter qubit by a single photon in free space. *Europhys. Letters*, 86:14007, 2009.
- [121] J. M. GÉRARD : Solid-State Cavity-Quantum Electrodynamics with Self-Assembled Quantum Dots. *Top. Appl. Phys.*, 90:269–314, 2003.
- [122] R. JOHNE et A. FIORE : Single-photon absorption and dynamic control of the exciton energy in a coupled quantum-dot—cavity system. *Phys. Rev. A*, 84:53850, 2011.
- [123] Gaston HORNECKER, Emanuel PEINKE, Julien CLAUDON, Alexia AUFFÈVES et Jean-Michel GÉRARD : Temporal shaping of single-photon pulses. *SPIE Proceedings*, 9505, 2015.
- [124] C. W. GARDINER et M. J. COLLETT : Input and output in damped quantum systems: Quantum stochastic differential equations and the master equation. *Phys. Rev. A*, 31:3761–3774, 1985.
- [125] Melvin LAX : Quantum Noise. IV. Quantum Theory of Noise Sources. *Phys. Rev.*, 145:110, 1966.
- [126] P. M. JOHNSON, A. F. KOENDERINK et W. L. VOS : Ultrafast switching of photonic density of states in photonic crystals. *Phys. Rev. B*, 66:81102, 2002.
- [127] E. KNILL, R. LAFLAMME et G. J. MILBURN : A scheme for efficient quantum computation with linear optics. *Nature*, 409:46–52, 2001.
- [128] J. L. O'BRIEN : Optical quantum computing. *Science*, 318:1567–1570, 2007.
- [129] Mark J. FERNÉE, Halina RUBINSZTEIN-DUNLOP et G. J. MILBURN : Improving single-photon sources with Stark tuning. *Phys. Rev. A*, 75:43815, 2007.
- [130] Matthias KELLER, Birgit LANGE, Kazuhiro HAYASAKA, Wolfgang LANGE et Herbert WALTHER : Continuous generation of single photons with controlled waveform in an ion-trap cavity system. *Nature*, 431:1075–1078, october 2004.
- [131] Brandon REDDING, Michael A. CHOMA et Hui CAO : Speckle-free laser imaging using random laser illumination. *Nature Photon.*, 6:355–359, 2012.
- [132] Tobias SATTLER : Ovoid ring resonators for microlasers and all-optical switches. Mémoire de D.E.A., Karlsruher Institut für Technologie, 2015.
- [133] K. UJIHARA : Spontaneous emission and the concept of effective area in a very short optical cavity with plane-parallel dielectric mirrors. *Jpn J. Appl. Phys.*, 30:L901,

1991.

- [134] G. BJORK, H. HEITMANN et Y. YAMAMOTO : Spontaneous-emission coupling factor and mode characteristics of planar dielectric microcavity lasers. *Phys. Rev. A*, 47: 4451, 1993.

Résumé

Il est possible de modifier en quelques picosecondes les fréquences de résonance d'une microcavité optique semiconductrice en injectant optiquement des porteurs de charge dans le semiconducteur. Dans cette thèse, nous étudions en détail de tels événements de commutation tout-optique pour des cavités planaires et des cavités en forme de micropilier à base de GaAs/AlAs, en utilisant l'émission de boîtes quantiques intégrées dans ces cavités comme source interne de lumière pour sonder la fréquence des modes résonnants en fonction du temps. Des décalages en fréquence très conséquents, de l'ordre de 34 fois la largeur du mode considéré, sont obtenus après optimisation. Nous réalisons une commutation différentielle des modes d'un micropilier en injectant les porteurs de manière très localisée, et modélisons les comportements observés en prenant en compte la distribution des porteurs injectés ainsi que leur diffusion et leur recombinaison en fonction du temps. Nous étudions par ailleurs deux applications potentielles importantes de la commutation ultra-rapide de cavité. D'une part, nous modélisons le changement de couleur qui est induit sur de la lumière piégée dans un mode de cavité lors d'un événement de commutation. Nous montrons que pour une cavité planaire optimisée, une telle conversion de fréquence peut être réalisée de façon très efficace. D'autre part, la commutation de cavité peut aussi être employée pour contrôler en temps réel l'émission spontanée d'émetteurs intégrés, et plus généralement tous les effets d'électrodynamique quantique en cavité. Nous présentons la génération d'impulsions de lumière incohérente de quelques picosecondes seulement, en utilisant l'émission spontanée de boîtes quantiques dans un micropilier commuté. Nous montrons aussi par une étude théorique qu'il est possible de donner une forme choisie aux impulsions à un photon émises par une boîte quantique, ce qui ouvre des applications intéressantes dans le domaine des liens optiques quantiques et du traitement quantique photonique de l'information.

Abstract

The resonance wavelengths of semiconductor optical microcavities can be changed within few picoseconds through the optical injection of free charge carriers. In this PhD thesis, we study in detail such “cavity switching” events for GaAs/AlAs planar and micropillar cavities, using the spontaneous emission of embedded QDs as an internal light source to probe the time-dependent frequencies of the cavity modes. Switching amplitudes as large as 34 mode linewidths are observed for optimized pumping conditions. Differential switching of micropillar modes is achieved by performing a localized injection of charge carriers, and modeled by taking into account their injection profile, diffusion and recombination processes. We investigate two important potential applications of cavity switching in the field of quantum optics. On one hand, we model the frequency conversion of light trapped in a cavity mode, which is induced by a switching event, and show that adiabatic and highly efficient frequency conversion can be achieved in properly designed planar cavities. On the other hand, cavity switching appears as a powerful resource to control in real-time the spontaneous emission of embedded emitters and more generally CQED effects. As a first example, we demonstrate the generation of few picosecond short pulses of incoherent light, using the spontaneous emission of switched QD-micropillars. We also show theoretically that cavity switching can be used to shape the time-envelope of single photon pulses emitted by a single QD, which is highly desirable for quantum-optical links and photonic quantum information processing.